

**Pilot Plant Analysis, Experiments, and Control for the Hybridization of
Transient Solar Heat with Conventional Utilities**

by

Scott Christian Rowe

B.A., Biology, Washington University St. Louis – St. Louis, 2007

M.S., Plant Biology, University of California – Berkeley, 2009

B.S., Chemical Engineering, University of Texas – Austin, 2013

M.S., Chemical Engineering, University of Colorado – Boulder, 2015



A thesis submitted to the

Faculty of the Graduate School of the

University of Colorado in partial fulfillment

of the requirements for the degree of

Doctor of Philosophy

Department of Chemical and Biological Engineering

2018

This thesis entitled:

**Pilot Plant Analysis, Experiments, and Control for the Hybridization of
Transient Solar Heat with Conventional Utilities**

written by Scott Christian Rowe

has been approved for the Department of Chemical and Biological Engineering

_____ Date_____

Dr. Alan W. Weimer

_____ Date_____

Dr. David E. Clough

The final copy of this thesis has been examined by the signatories, and we find that both the content and the form meet acceptable presentation standards of scholarly work in the above-mentioned discipline.

ABSTRACT

Rowe, Scott Christian

(Ph.D., Chemical Engineering, Department of Chemical and Biological Engineering)

Pilot Plant, Analysis, Experiments and Control for the Hybridization of Transient Solar Heat with Conventional Utilities

Thesis directed by Alan W. Weimer and David E. Clough

ABSTRACT

The direct capture of solar heat is now commercial for electrical generation at 550 °C (1000 °F), which has provoked interest in solar driven approaches to commodity and fuels production at higher temperatures. However, conventional commodity and fuels facilities often operate continuously regardless of weather and nighttime conditions. Conversely, direct sunlight is immediately lost upon shading by clouds and sunset. Beyond inconvenience, this intermittency has the potential to destroy high temperature equipment through thermal fatigue and thermal shock. To overcome interruptions in solar availability we propose the inclusion of direct sunlight in commodities and fuels production as a supplement to conventional electrical heating. Within this regime conventional utilities are ideally sourced from sustainable stored or orthogonal energy sources. Control is needed to substitute solar, which can be lost within seconds during transient weather, with electrical heat. To explore control strategies for the alternation of solar and electrical heat a new facility was constructed at the University of Colorado, Boulder. Specifically, a 45 kW 18 lamp high-flux solar simulator was erected that approximates the sunlight found in actual concentrated solar plants. Calorimetry was analyzed for the measurement of extreme radiance in this testbed. Results from calorimeter design were applied to radiation measurement from the lamps, which were capable of delivering 9.076 ± 0.190 kW of power to a $\varnothing 10$ cm target with a peak flux of 12.50 MW/m^2 (12,500 “suns”). During this characterization a previously unknown observer effect was seen that differentiates radiative heat from lamps and the energy delivered by sunlight in actual concentrated solar facilities. This characterization allowed confident experimentation within the lamp testbed for control studies on a 15 kW solar-electric tube furnace for commodities and fuels production. Furnace electric heat was manipulated by four different linear control strategies for the rejection weather transients reproduced by the high-flux solar simulator lamps. These included feedback, feedforward feedback, model predictive control, and model predictive control with a weather forecast. It was found that model predictive control with a forecast best maintained furnace conditions. Prior researchers have suggested that forecasts would be useful in solar control, which was shown across simulation and experiment.

ACKNOWLEDGMENTS

I acknowledge financial support from ARPA-E (Award AR0000404), NSF (Award 1622824) and the fellowship in Graduate Areas of National Need (GAANN, United States Department of Education). These programs continue to support difficult projects and promote industrially relevant research.

I am grateful for my advisors, Dr. Alan Weimer and Dr. David Clough, for the opportunity to study controls engineering and solar energy. I thank Team Weimer for their camaraderie and involvement in the execution of a multimillion dollar research project, especially Aaron Palumbo, Mark Wallace, and Boris Chubukov. Outside the lab, Dr. Pao's graduate student Arnold Braker provided invaluable advice. Furthermore, I am forever indebted to Carol Bender and Alia Lubers, whose support was essential to success. Finally, I thank my late father, whose graduation from the University of Colorado (1977) and fruitful doctoral career inspired long and persistent academic inquiry.

TABLE OF CONTENTS

Chapter 1: What is Solar-Thermal Energy?.....	1
1.1 Introduction	1
1.2 The Problem: Weather	4
1.3 A Solution: the Hybridization of Solar and Conventional Utilities	5
1.4 The Contents of this Thesis, an Experimental Approach to Utilities Hybridization.....	8
Chapter 2: How Accurate is High-Flux Solar Measurement?	10
2.1 Introduction	10
2.2 A Ray Tracer for Radiation Analysis.....	13
2.3 Calorimeter Finite Volume Simulation.....	14
2.4 Results	18
2.4.1 Observer Effects on the Solar Simulator Flux Profile.....	18
2.4.2 Calorimeter Accuracy and Robustness.....	19
2.4.3 Calorimeter Accuracy with a Conical Aperture	20
2.5 Conclusion.....	20
Chapter 3: Do High-Flux Solar Simulators Accurately Represent Real World Facilities?.....	25
3.1 Introduction	25
3.2 Results	27
3.2.1 Single Lamp Experiments for Model Development.....	27
3.2.2 Filament Modeling with Monte Carlo Analysis.....	32
3.2.3 Observer Effects in the Fully Assembled High-Flux Solar Simulator	35
3.2.4 Modeling Reproduces High-Flux Solar Simulator Results	43
3.3 Discussion	45
Chapter 4: Can Control Models be More Transparent?.....	47
4.1 Introduction	47
4.2 Methods.....	51
4.3 c-Optimality Preserves State Tracking Relative to Established Technique.....	51
4.3.1 Nonlinear Flash Model.....	51
4.3.2 State Space Modeling and Alignment for Estimation of the Nonlinear Flash System.....	54
4.3.3 Aligned Model Performance and Conditioning in Inferential Estimation	56
4.4 c-Optimality Preserves State Tracking for Accurate Process Forecasting.....	61
4.4.1 Experimental Carbon Gasifier	61
4.4.2 State Space Modeling and Alignment for Forecasting in the Carbon Gasifier	63

4.4.3 Model Alignment Performance in Process Forecasting	64
4.5 Conclusion.....	65
Chapter 5: Can Linear Models, with Forecasting, Achieve Solar-Electric Control?.....	67
5.1. Solar-Electric Reactor Design.....	67
5.2. Solar-Electric Reactor Modeling.....	69
5.3 Solar-Electric Reactor Chemistry and Distributed Control System.....	72
5.4. Solar-Electric Control Strategies and Tuning	75
5.4.1 Control Architectures	75
5.4.2 Controller Tuning	80
5.5 The Experimental Performance of Solar-Electric Control.....	82
5.6 Simulations for Optimal Forecasts in Solar-Electric Control	87
5.7 Conclusion.....	89
Chapter 6: What was Learned and What is Unanswered?.....	91
6.1 The Observer Effect in High-Flux Solar Simulators.....	91
6.2 The Hybridization of Solar and Electric Heat.....	92
Appendix A: A Tutorial Introduction to Subspace Identification	95
A.1. The State Space	95
A.2. The Estimation of State Space Models.....	100
Appendix B: An Exercise in Kalman Filtering and State Inference.....	125
B.1. Introduction	125
B.1.1 The Kalman Filter	125
B.1.2 The Steady State Kalman Filter	130
B.2. Exercise	133
B.2.1 Observability.....	133
B.2.2 Simulation Approach	135
B.2.3 State Estimation, Base Case.....	141
B.2.4 State Estimation without Access to the Process Noise Covariance Matrix	144
B.2.5 State Estimation with an Unobservable System	147
B.3. Conclusions	151
Appendix C: A Hill Equation for Heat Capacity Calculation	152
C.1. Introduction	152
C.2. Results	155
C.3 Discussion.....	160

Appendix D: Optimized Blocking in Nonlinear Model Predictive Control	163
D.1. Introduction	163
D.2. Multidimensional Shooting	166
D.3. Parallel Multiple Shooting	170
D.4. Results	176
References	182

Chapter 1: What is Solar-Thermal Energy?

1.1 Introduction

Concentrated solar technologies harness energy with mirrored heliostats, dishes, or troughs – optics that heat a boiler or reactor with reflected sunlight [9]. This “solar-thermal” premise dates to Archimedes’ supposed use of polished shields to concentrate (and weaponize) sunlight in 212 BCE [10]. Direct solar heat would later be used for the generation of steam in 1882 [11], and ironically, the study of combustion in 1774 [12]. The first substantial solar-thermal facility was reported in 1913 when reflective parabolic troughs were used to drive water flow for irrigation in Egypt [13] (Figure 1.1). This approach is now commercial for electrical generation wherein sunlight heats a working fluid, which could be air, a molten salt, or steam, to high temperature. Heat from the working fluid is then dispatched to drive electrical turbines directly or indirectly [14]. Notably, the fluid can be stored at temperatures of nearly 550° C (1000° F) for continuous operation overnight or during inclement weather [9]. Heat storage in these facilities has allowed capacity factors (uptimes) of 70-80%, making them baseload power plants [14]. Furthermore, the storage of solar energy as heat is substantially cheaper than batteries (Figure 1.2). Parabolic troughs (Figure 1.3), the most mature solar-thermal technology today, can reach a solar to electricity conversion comparable to photovoltaics (15%) [9]. More recently solar plants built around “power towers” (Figure 1.4), which harvest light from vast fields of mirrors, have achieved 35% efficiency [15]. Various authors believe that a 65% ultimate efficiency is possible in power tower facilities [15], although only through operation at higher temperatures (higher Carnot Efficiency).

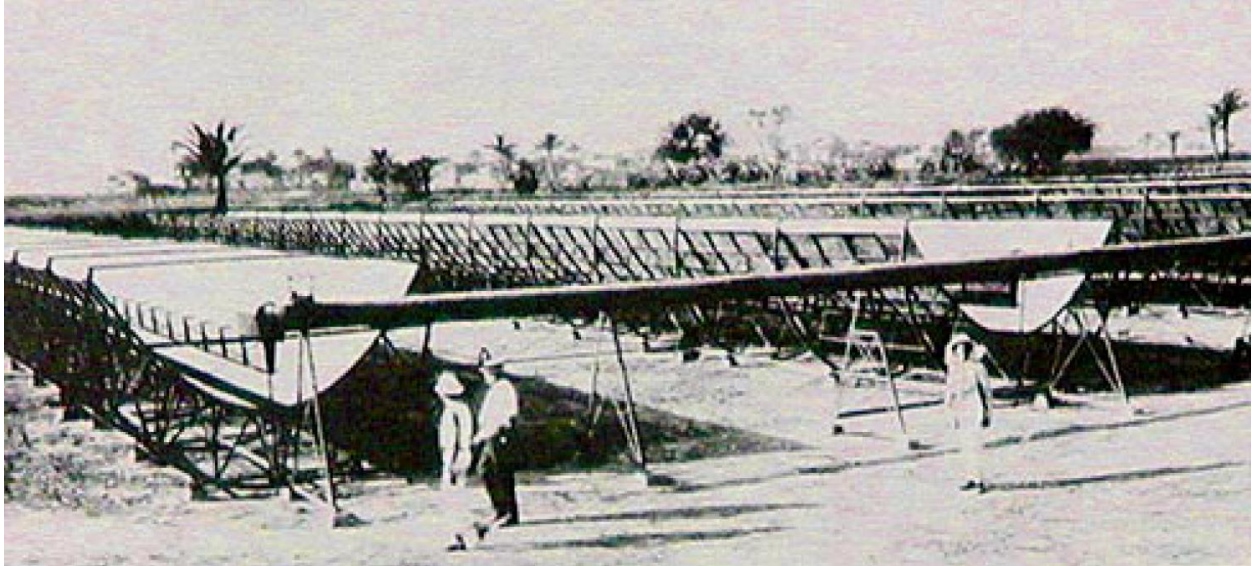


Figure 1.1: “That mechanical power was without limit contained in the sun’s rays has been known to scientists for many years” [13]. The world’s first substantial solar-thermal power plant in Egypt, 1913. It is, in all fundamental aspects, similar to a modern parabolic trough power plant.

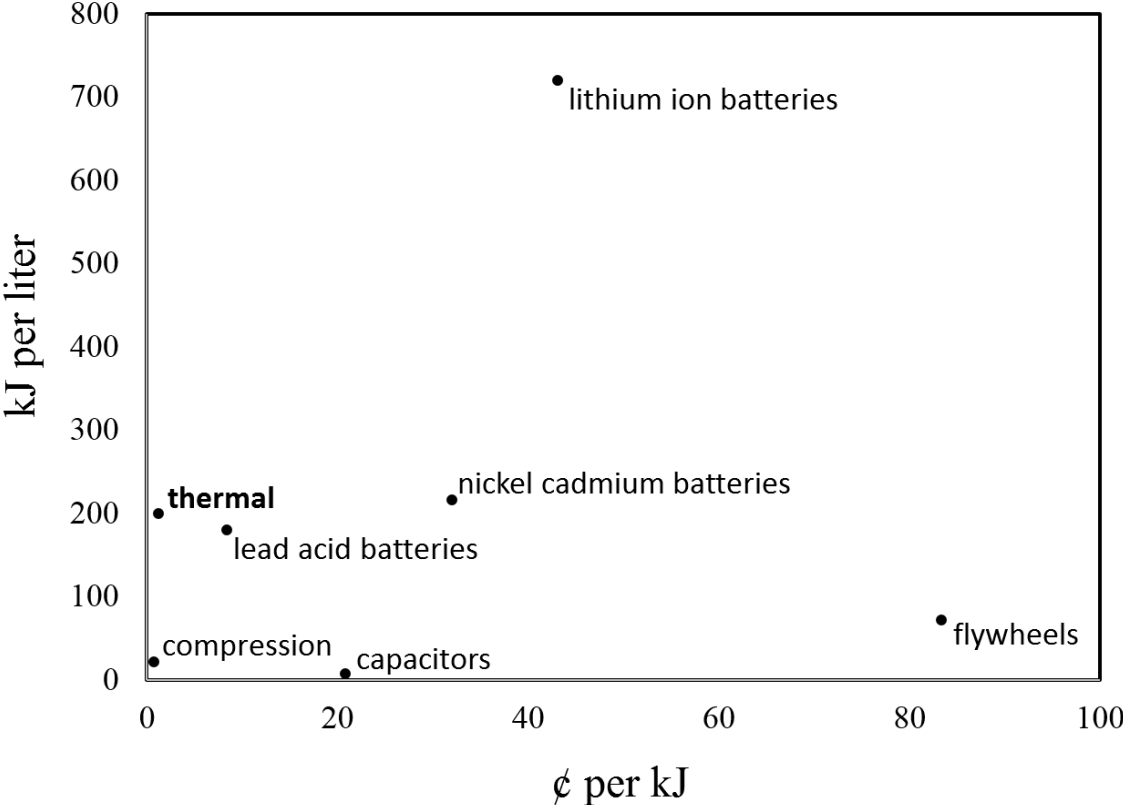


Figure 1.2: The relative cost and energy density of different power storage technologies circa 2013 [16]. Thermal storage, as is practiced by solar-thermal facilities, is remarkably dense and inexpensive.

The success of concentrated solar power has piqued interest in the use of sunlight to heat commodities and fuel production (“chemical processes”). Many endothermic energy intensive manufacturing processes could benefit from the inclusion of solar heating, including biomass gasification, metals manufacture and hydrogen production [17-20]. However, like newly proposed power plants these systems require operation at higher temperatures. Table 1.1 summarizes the temperatures that solar heat likely must achieve in these new applications.

Table 1.1 Likely future solar-thermal energy applications.

process	temperature	notes:
Rakine powerplant* [9]	550° C (1000° F)	nitrate salt working fluid
Brayton powerplant [21]	>800° C (1450° F)	supercritical CO ₂ working fluid
Gasification [22]	>850° C (1550° F)	solid carbonaceous feeds
methane splitting [23]	>1000° C (1800° F)	without greenhouse gas generation
H ₂ production [9]	>1200° C (2200° F)	metal oxide chemical looping
metals manufacture [24]	>1350° C (2500° F)	smelting by carbothermal reduction

*commercial

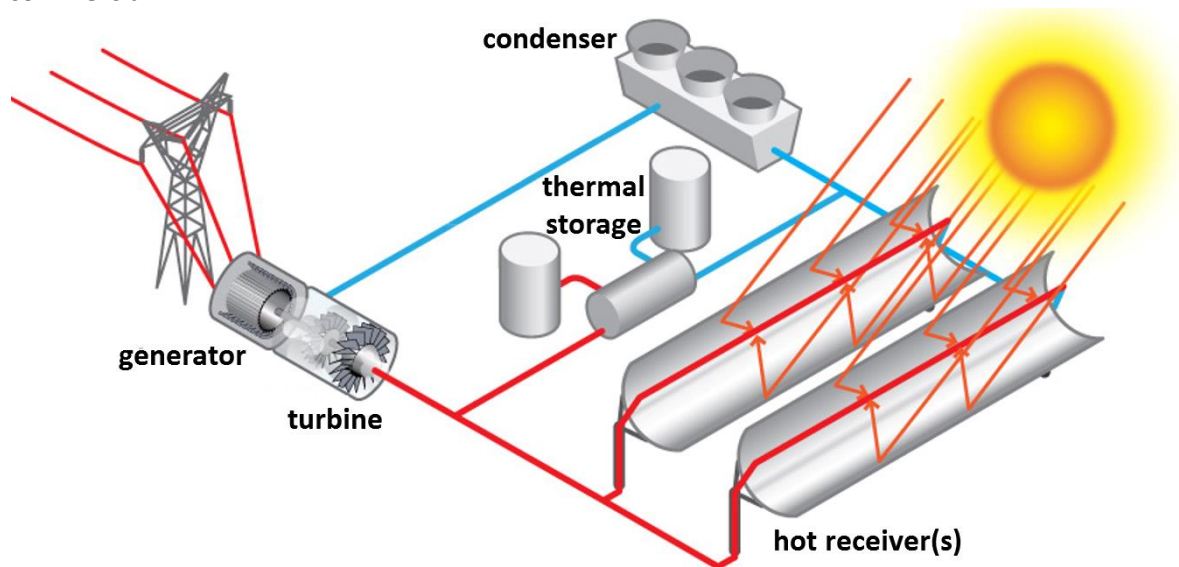


Figure 1.3 The parabolic trough solar-thermal concept for electrical generation (image courtesy of the United States Department of Energy). Long tube runs could be adapted to plug flow reactions in commodities and fuels production, assuming that the troughs are wide enough to collect solar heat sufficient to achieve the necessary temperatures.

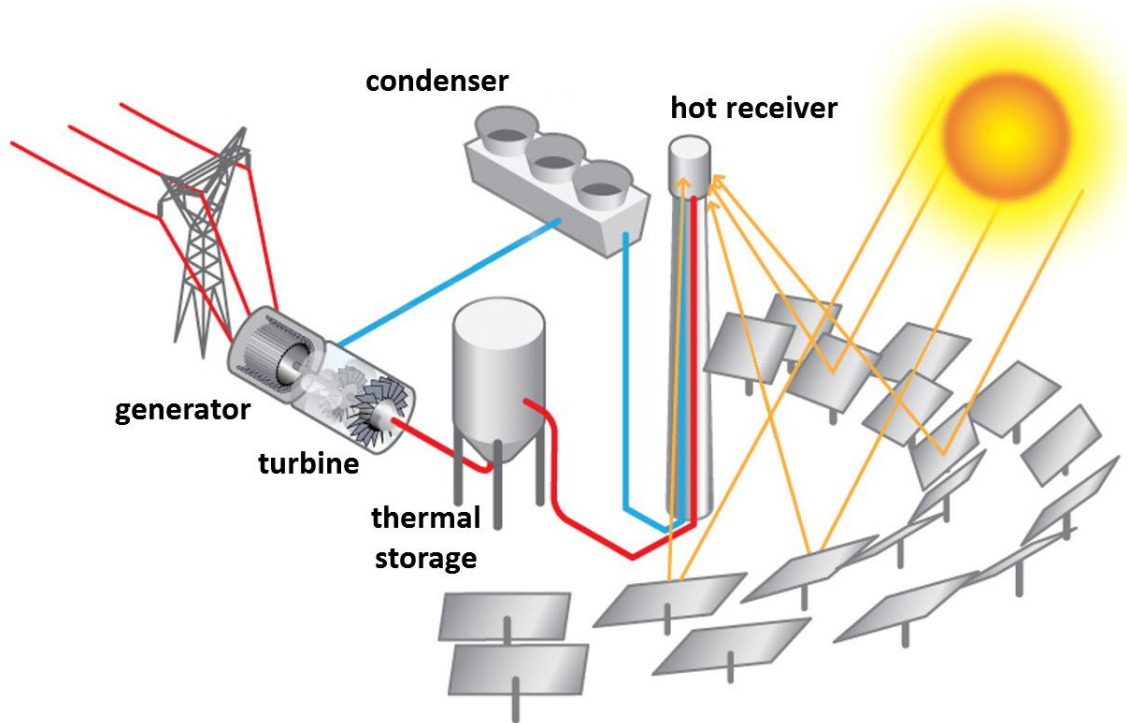


Figure 1.4: The power tower solar-thermal concept for electrical generation (image courtesy of the United States Department of Energy). With sufficient mirrored heliostats power towers can achieve the temperatures expected in next-generation solar-thermal applications (Table 1.1).

1.2 The Problem: Weather

There is an increasing awareness that clouding and weather, which can cause a total (100%) loss of direct sunlight within seconds, threatens reliable solar facility performance [25]. Weather is especially problematic in high-temperature facilities where transient solar heat can induce thermal shock and fatigue. Indeed, concentrated solar facilities are known as ideal testbeds for studying shock behavior [26-29]. Fortunately, controls engineering has the potential to combat thermal shock, maintain facility conditions, and allow robust operation despite weather interruptions.

Table 1.2 summarizes prior concentrated solar control studies for commodities and fuels production. Compensation for weather and diurnal disturbances can be approached from different perspectives. We define process compensation as the manipulation of system flowrates to reject weather transients. Examples include autothermal heating in gasification [2] or heat storage in

electrical generation [30]. Not all systems allow process compensation, either due to their chemistry, due to slow dynamics, or due to the presence of recycle streams that can propagate disturbances [31]. However, where possible this approach has been successful [2, 8, 9, 14, 15].

We define facility compensation as manipulations that act on sunlight concentration directly. These include heliostat movement to defocus or redirect sunlight and/or shutters that block excessive solar heat. Prior academic authors have used these approaches for the rejection of weather disturbances [4, 5]. However, these techniques are problematic at scale. In solar-thermal plants the heliostat field is 30-50% of total facility costs, contains thousands of actuators, and is only 65% efficient [32-34]. Oversizing a heliostat field to contend with clouding will lower efficiency, will incur additional cost, and increases parasitic actuator losses, which are already 3.8% of facility power [35]. Furthermore, heliostat actuation for weather compensation likely induces offsets in equipment that require additional heliostat aiming, a task that remains burdensome [36, 37]. The use of a shutter implies that the solar field is already oversized to reject clouding effects. Current shutters are fabricated from metals that may melt at the elevated process temperatures sought in proposed solar-thermal applications (Table 1.1) [7, 38]. Scalable ceramic or actively cooled shutters likely require further development. Ultimately, the shutter, versus other equipment, becomes the site of potential thermal fatigue and thermal shock.

1.3 A Solution: the Hybridization of Solar and Conventional Utilities

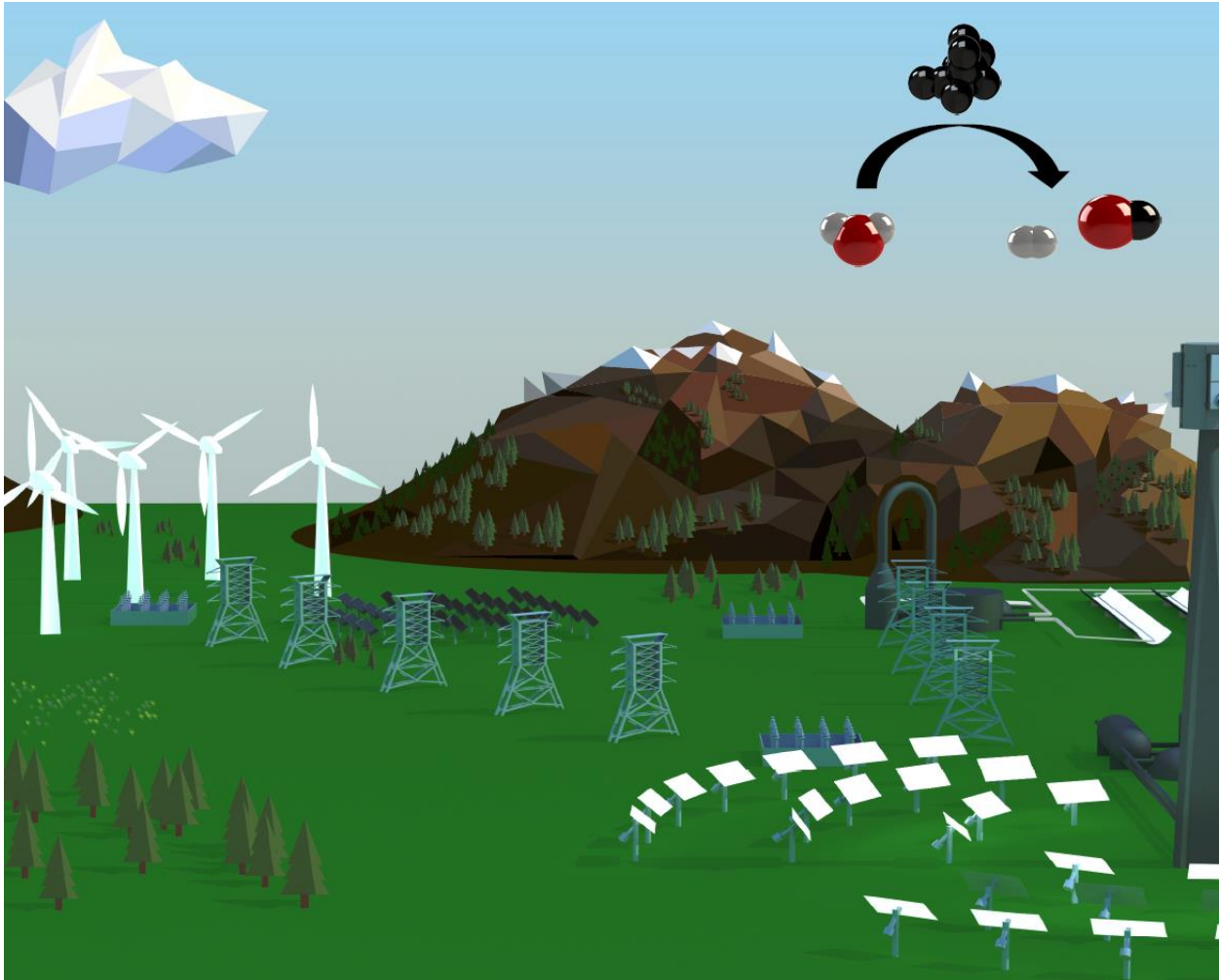
We propose an alternative approach to weather compensation. Namely, we seek to add electrical heating to solar commodities or fuels facilities (Figure 1.5). Within this scheme waste heat, likely from product streams, can be stored in a working fluid as per current commercial practice. That heat can then be used to drive electrical turbines to power heaters during cloud transients or overnight. Alternatively, the facility could be integrated into the electrical grid [39]. Power for

electrical heating would then be sourced from elsewhere during weather or night, ideally from orthogonal renewable sources (wind, geothermal, wave) or stored energy supplies. Supplementary electrical heat could smoothly maintain facility conditions, avert thermal shock, and allow an undersized heliostat field.

Table 1.2 prior studies on the control of solar heat in commodities and fuels production processes.

process	control simulations	control experiments	manipulated variable	feed forward	forecast	disturbances (% sun)	controller	reference
gasification	✓	✓	electricity	✓	✓	~100%	PI, MPC	Chapter 5
gasification	✓		flowrate(s)			~100%	LQG/LQR	[1]
gasification	✓		flowrate(s)	✓		~100%	PI	[2]
gasification	✓		flowrate(s)			~20%	PI, MPC	[3]
H ₂ looping	✓	✓	heliostats			~25%	PI	[4]
H ₂ looping	✓	✓	heliostats	✓		~100%	PI	[5]
sintering	✓	✓	shutters			~20%	GPC, PI	[6]
gasification	✓		shutters			~100%	NMPC, PI	[7]
superheating	✓	✓	flowrate(s)	✓		~10%	LQR	[8]

Figure 1.5: The integration of sustainable commodities and fuels production with other renewables that supply electrical heat during weather and overnight. The gasification of carbon, tested in Chapter 5, is depicted in the upper right.



1.4 The Contents of this Thesis, an Experimental Approach to Utilities Hybridization

To study the hybridization of solar and electric utilities a “high-flux solar simulator,” an assembly of eighteen lamps whose irradiance mimics concentrated sunlight, was erected at the University of Colorado. High-flux solar simulators are platforms for the evaluation of new solar-thermal technologies under tightly controlled and well-characterized conditions. Presently, at least twelve high-flux solar simulators are available worldwide for academic studies [40, 41]. Chapter 2 and 3

characterize the new high-flux solar simulator at the University of Colorado with ray tracing and experiments, work prerequisite to solar-electric control studies.

State space models were then used for solar-electric control, but only after modification by a technique described in Chapter 4 for process alignment. Aligned state space models were then employed to control a solar-electric reactor for gasification studies. The 15 kW reactor is described in Chapter 5. Four different linear control schemes manipulated electric heaters to maintain facility conditions despite clouds programmed onto the high-flux solar simulator lamps (Chapter 5). The best results were achieved via model predictive control with a weather forecast. Researchers have theorized that weather forecasts could improve solar facility control (reviewed in [42]). Chapter 5 contains the first online evidence that weather forecasts are highly effective in practice.

Chapter 2: How Accurate is High-Flux Solar Measurement?

Content within Chapter 2 was previously published as “Worst-case losses from a cylindrical calorimeter for solar simulator calibration” by Scott C. Rowe, Arto J. Groehn, Aaron W. Palumbo, Boris A. Chubukov, David E. Clough, Alan W. Weimer and Ilias Hischer in *Optics Express* (2015).

2.1 Introduction

Knowledge of the radiative power and flux available from a given high-flux solar simulator is prerequisite to its use, including use in solar-electric control studies with reproduced weather. Water cooled cylindrical calorimeters, which consist of a radial aperture affixed to a cylindrical cavity, can be used to acquire this information [43-45]. The irradiance a calorimeter intercepts is dependent on aperture diameter, and a range of aperture sizes can characterize a solar simulator flux profile. However, it is recommended that the ratio of calorimeter cavity length to aperture diameter always exceed 4:1 [46]. At lower ratios, emission and reflective losses can significantly degrade calorimeter power measurements. The fidelity of calorimeters in flux measurement is unclear. Previous work has shown that different flux measurement techniques, which included a cylindrical calorimeter, yield disparate readings [47]. The cause of these measurement discrepancies, which spanned nearly 10%, was nonobvious [47].

This chapter examines a well-insulated calorimeter design with detachable faceplates similar to Diver et al 1983 [48]. Figure 2.1 shows how the absorptive body and detachable faceplate are separately cooled to avert heat exchange between these components. Radiation that enters the calorimeter through the faceplate aperture, Q_{in} , heats the circulating coolant within the body, causing a coolant temperature rise that reveals the intercepted irradiance [44]:

$$Q_{in} \approx \dot{m} C_p \Delta T \quad 2.1$$

where \dot{m} is the coolant mass flowrate, C_p is the coolant heat capacity and ΔT is the coolant temperature rise. Although faceplate coolant temperature could be instrumented, only heating of the body coolant was considered a measure of incident power [48]. Equation 2.1 is not a strict equality because some energy entering the calorimeter is reflected or scattered ($Q_{\text{reflective}}$), some energy is lost by thermal emission (Q_{emissive}), and some energy is lost by convection to the ambient air ($Q_{\text{convective}}$). Furthermore, the calorimeter can induce an observer effect that alters the solar simulator flux profile (Q_{observer}). Thus, minimally the calorimeter heat balance harbors five terms:

$$Q_{\text{in}} = \dot{m}C_p \Delta T + Q_{\text{reflective}} + Q_{\text{emissive}} + Q_{\text{convective}} + Q_{\text{observer}} \quad 2.2$$

Radiative, conductive, and convective losses from the calorimeter exterior may be considered negligible provided the coolant is sufficiently insulated. Beyond these losses, calorimeter accuracy can be affected by measurement error and drift. However, this chapter focuses on physical calorimeter losses, not measurement errors induced by specific instrumentation.

Herein the effect of calorimeter design attributes on thermal losses was explored with Monte Carlo ray tracing and computer simulation. CUtrace, a parallel, grey body, Monte Carlo ray tracer was written to represent the solar simulator design planned for the University of Colorado [41]. CUtrace is freely available online at Matlab Central (Mathworks Incorporated) and features a graphical user interface. Cylindrical calorimeter designs were traced in the solar simulator and the results were processed by finite volume simulation. Simulations were performed over a range of optical properties to evaluate calorimeter robustness against radiative losses, emissive losses, convective losses and the observer effect.

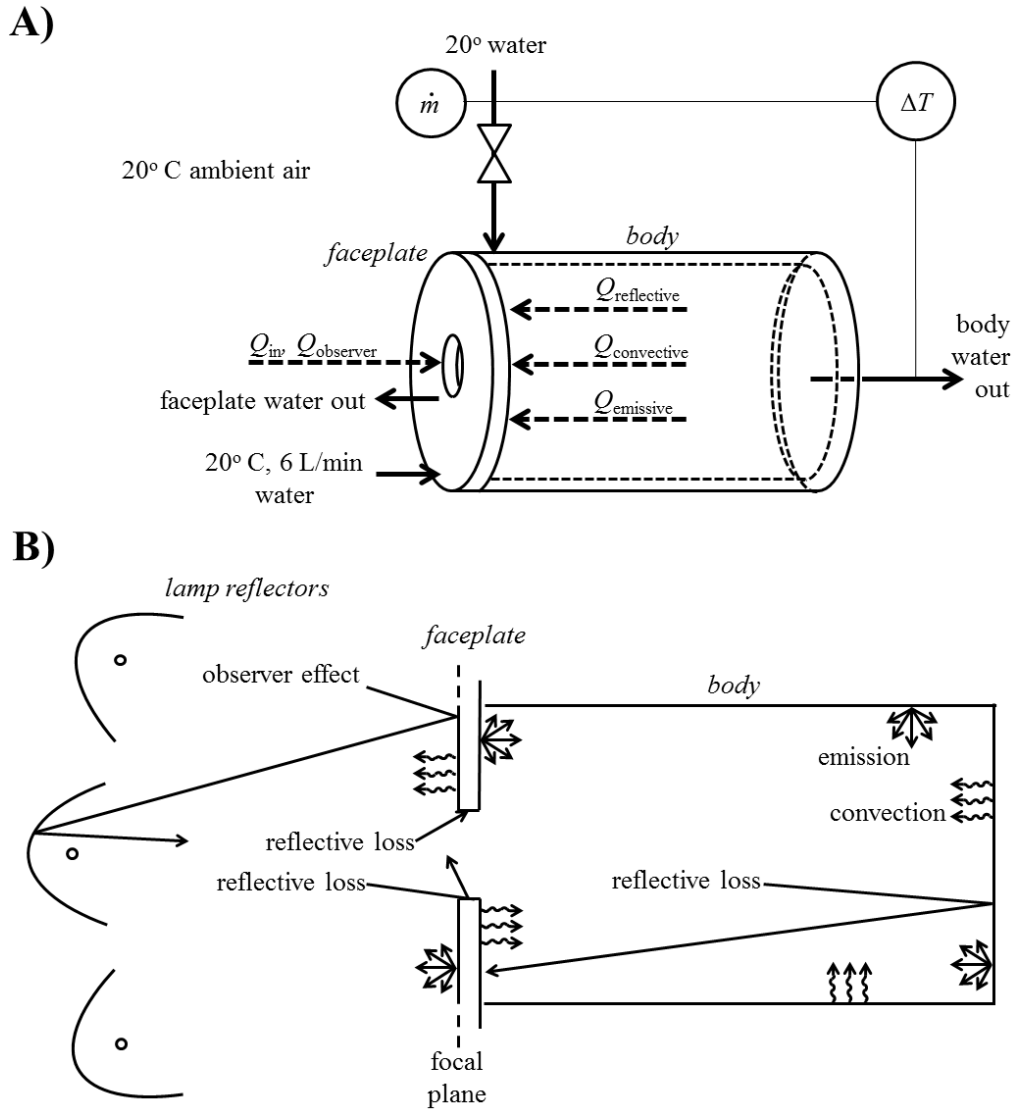


Figure 2.1: A simulation framework for calorimeter evaluation. A) piping and instrumentation diagram of the calorimeter cooling flows showing confounding radiation effects. The operational temperature target was $\Delta T = 25^\circ\text{C}$. The faceplate coolant flowrate was fixed at 6 L/min. B) Radiative and thermal phenomena within and outside the calorimeter.

2.2 A Ray Tracer for Radiation Analysis

A software package, CUtrace, was written using Matlab's Parallel Programming Toolbox [49]. The grey body ray tracer implements 14 geometric primitives and three filaments (ray sources). The code is freely available for detailed inspection online at Matlab Central (Mathworks Incorporated). In brief, the object-oriented program traces rays through a given user defined scene by affine reflections [50, 51] (Figure 2.2). To determine where a ray terminates, a random number is drawn [0-1] upon each ray-shape intersection. If the random number is greater than the incident surface reflectivity, the ray is absorbed. Otherwise the ray is reflected in analogy with Phong Illumination [52]. Specifically, a second random number [0-1] is drawn. Reflection is Lambertian if the number is less than a user inputted fraction for the incident surface. Otherwise, reflection is specular with error bounded by a user inputted angular standard deviation [53]. All random numbers originate from the Mersenne Twister algorithm for a uniform distribution. Each geometric object maintains a private record of absorbed rays. Each new ray intersection is discovered by scanning objects in the scene for the nearest parametric ray-shape collision.

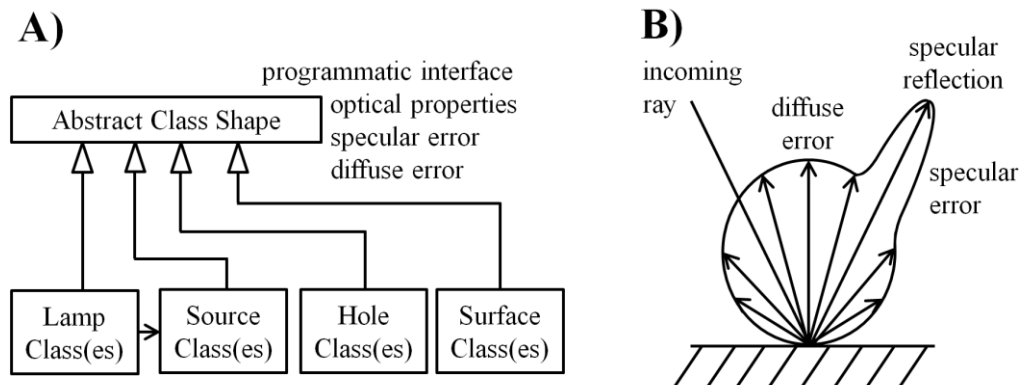


Figure 2.2: features of the new parallel ray tracer. **A)** object oriented inheritance framework. **B)** the CUtrace reflection model.

CUtrace was validated by simulating radiation exchange in three test systems. Additionally, the tracer was used to generate view factors with known analytical solutions. Figure 2.3 shows the

validations. Radiation exchange in the planned 18 lamp University of Colorado high-flux solar simulator served as the first test case [41]. CUtrace matched an existing code for modeling this design (Figure 2.3A) [41]. Next the VEGAS ray tracer was used to model radiation exchange within the 18 lamp solar simulator [54]. VEGAS can only approximate radiation exchange within this facility because the program lacks an exact model of the xenon filaments used in the solar simulator design. CUtrace matched VEGAS when cylindrical radiation sources were substituted for rigorous filament modeling (Figure 2.3B). Of the objects implemented in the new tracer, the compound parabola was most complicated. This solid of revolution harbors four nontrivial roots [55]. A compound parabola was drawn in both Soltrace, a tool for the design of commercial solar facilities [56], and the new tracer. CUtrace reproduced the Soltrace output (Figure 2.3C). In a final test, the ray tracer was used to generate view factors. For a myriad of view factors, the new tracer matched known analytical solutions (Figure 2.3D) [50]. Although it is impossible to test the new tracer exhaustively, it successfully recapitulates results from proven computer codes and documented view factors.

Figure 2.4 shows the calorimeter in simulation at the focus of the planned University of Colorado 18 lamp solar simulator [41]. One million rays were used to simulate 1.05 kW from each lamp. Unless noted, all calorimeter surfaces were diffusely reflective.

2.3 Calorimeter Finite Volume Simulation

Monte Carlo ray tracing results were fed to a 2D finite volume calorimeter simulation by applying annularly the peak axial and radial fluxes (Figure 2.5). This results in a slightly higher radiative power input, higher surface temperatures, and consequently higher losses consistent with worst-case calorimeter performance.

Figure 2.6 details the calorimeter design. Two detachable faceplates were modeled, each with a different aperture diameter and independent coolant system. Coolant flow was modeled by convective upwinding assuming a water inlet temperature of 20°C. For the range of flowrates examined, the Dean number was consistently turbulent ($Dean > 500$). Thus, the simulation implemented turbulent heat transfer relationships for cylindrical and spiral ducts. Temperature dependent physical properties were implemented for the copper calorimeter body, water coolant, and ambient air [57]. Body outer surfaces, which are typically insulated, were assumed adiabatic. Convection to ambient air employed a heat transfer coefficient for cylindrical calorimeters [58]. Air was assumed to be optically transparent. Equation 58 of Mori and Nakayama (1967) served as the heat transfer coefficient to coolant in spiral ducts [59]. Equation 45 of Kaya and Teke (2005) served as the heat transfer coefficient in cylindrical coolant ducts [60]. Thermal emission between and within cylindrical and radial annuli was modeled using analytical view factors [50]. In all cases, the view factors of a radial or cylindrical annulus summed to unity. Simulation physicality was supported by energy closure. The mesh was refined until power lost through the aperture was statistically invariant (95% confidence), yielding a 540 element grid (Figure 2.6).

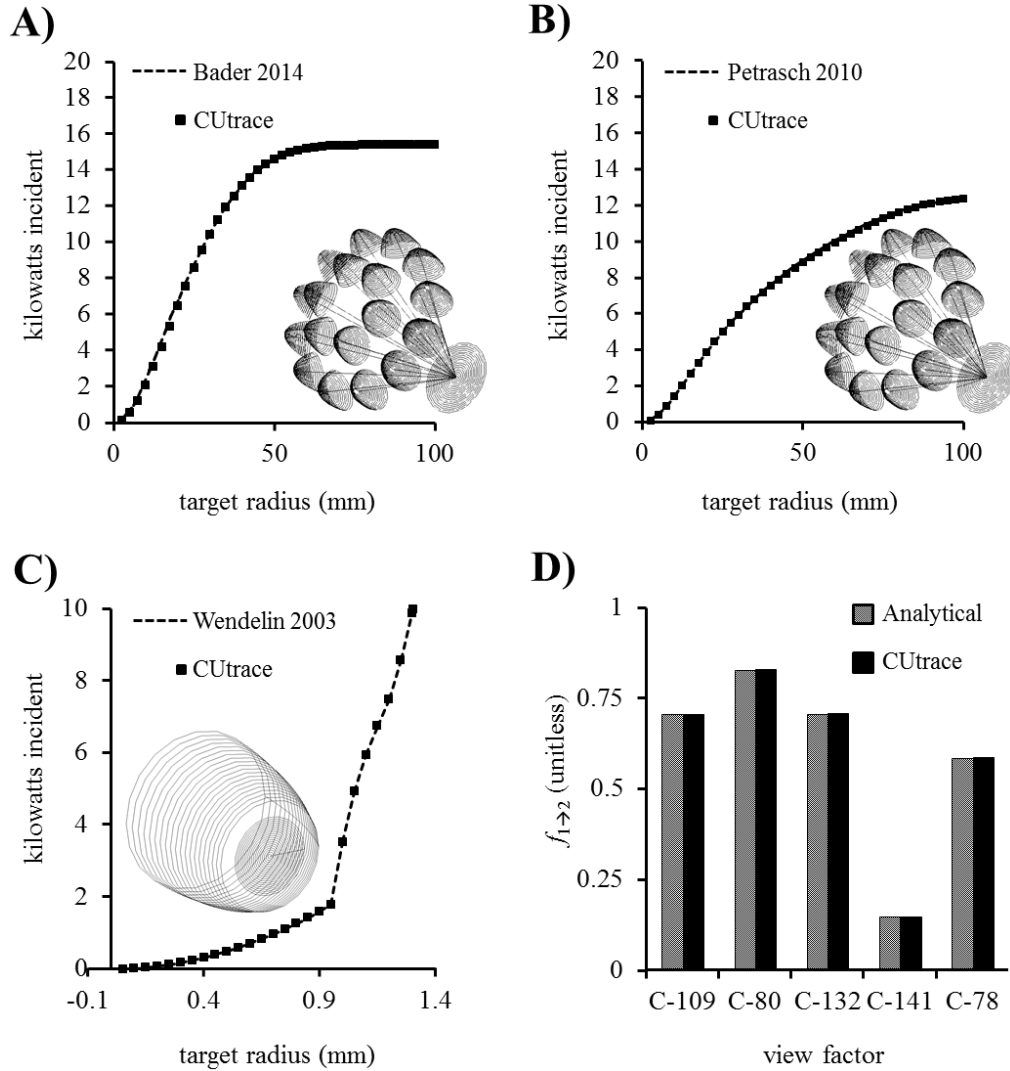


Figure 2.3: Validation of the new, parallel, grey body Monte Carlo ray tracer (CUtrace). **A)** Predicted power intercepted by a disc at a solar simulator focus. Trace was of the projected University of Colorado solar simulator with rigorous xenon filament modeling as described by Bader 2014 [41]. **B)** Predicted power intercepted by a disc at a solar simulator focus. Trace was of the University of Colorado solar simulator with simplified volumetric cylindrical sources in each lamp [41, 54]. Source cylinder length was 0.0045 meters and radius was 0.00075 meters. **C)** Predicted power intercepted by a disc at a compound parabola outlet [56]. The compound parabola acceptance angle was 35° and the outlet radius was 1.3 meters. **D)** Analytical view factors from Appendix C of Howell 2010 [50] are reproduced by CUtrace, wherein any surface can act as a diffuse source of radiation.

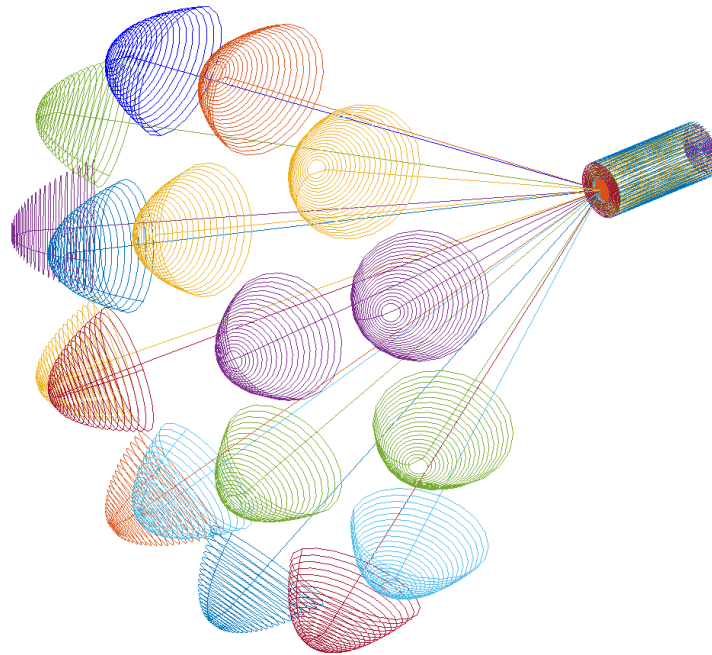


Figure 2.4: CUtrace depiction of the calorimeter design at the high-flux solar simulator focus [41].

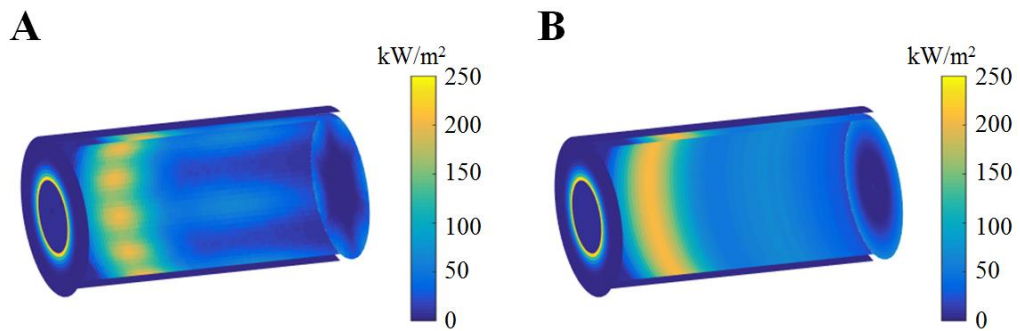


Figure 2.5: Peak Monte Carlo fluxes were mapped annularly around exposed calorimeter surfaces. **A)** Actual fluxes and **B)** Mapped fluxes.

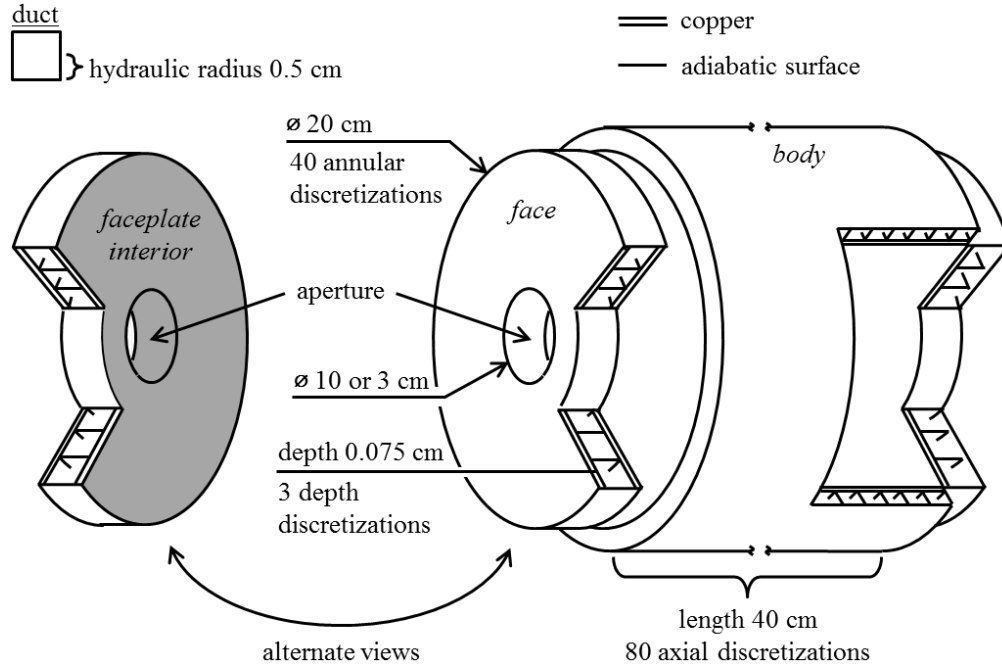


Figure 2.6: Details of the dimensions and discretization used in Monte Carlo ray tracing and finite volume simulation. Unless otherwise specified body cavity reflectivity was 0.05 diffuse, faceplate interior reflectivity was 0.95 diffuse, and face reflectivity was 0.05 diffuse.

2.4 Results

2.4.1 Observer Effects on the Solar Simulator Flux Profile

Monte Carlo simulations performed with a perfectly absorbing calorimeter face resulted in $Q_{\text{observer}} = 0$ kW for both the large ($\varnothing 10$ cm) and small ($\varnothing 3$ cm) aperture faceplates. Any face reflectivity greater than zero caused radiation exchange between the calorimeter and lamp reflectors (Figure 2.7), exchange that distorted the native solar simulator flux profile. When the calorimeter face had a reflectivity of 0.95 more radiation was intercepted irrespective of whether that surface was diffuse ($Q_{\text{observer}} = 0.20$ kW) or specular ($Q_{\text{observer}} = 1.6$ kW). Thus, a significant fraction of radiation that reflected off the face ultimately returned to the calorimeter aperture. Calorimeter face reflectivity presents a tradeoff. A highly reflective face will absorb little heat, but can perturb the solar simulator flux profile. Conversely, an absorptive face preserves the flux profile, but can

overheat. Based on these results a diffusely reflective calorimeter face with a reflectivity of 0.05 was adopted in subsequent simulations.

2.4.2 Calorimeter Accuracy and Robustness

Figure 2.8 shows coolant temperature rise and calorimeter losses for a range of coolant flowrates and body reflectivities. Predictably, Q_{emissive} was a function of coolant flow and reflectivity, $Q_{\text{reflective}}$ was solely a function of reflectivity, and $Q_{\text{convective}}$ was solely a function of coolant flow. At low coolant flowrates high calorimeter temperatures drove significant convection (Figure 2.8). Convective losses were always higher for the large ($\varnothing 10$ cm) aperture calorimeter, consistent with natural convection through a larger outlet. For moderate coolant flowrates reflective losses always dominated emissive and convective losses (Figure 2.8). A reflective calorimeter body induced higher reflective losses because light was not immediately absorbed by the cavity surfaces. Losses were significant relative to the inlet irradiance, which was $Q_{\text{in}} = 14.51$ kW and 4.16 kW for the large ($\varnothing 10$ cm) and small ($\varnothing 3$ cm) aperture faceplates, respectively. This was especially true of the small aperture calorimeter, which intercepted more radiation on the aperture lip. This radiation was scattered or absorbed before it could reach the calorimeter cavity for detection, commensurate with high ($Q_{\text{reflective}} > 0.5$ kW) reflective losses.

Figure 2.9 shows coolant temperature rise and calorimeter losses for a range of coolant flowrates and faceplate interior reflectivities. Again, convective losses dominated at low coolant flowrates and reflective losses dominated at moderate coolant flowrates. Reflective losses due to light adsorption by the aperture lip were pronounced, especially for the small aperture calorimeter. To test the importance of the aperture lip, a beveled aperture was simulated.

2.4.3 Calorimeter Accuracy with a Conical Aperture

Beveled (conical) apertures were explored as a means of making the calorimeter more accurate and robust. Figure 2.10 compares losses from the different calorimeter designs for a coolant temperature rise of $\Delta T = 25^\circ\text{C}$. The beveled (conical) aperture design featured an acceptance angle that matched that of the planned University of Colorado high-flux solar simulator (45°). Thus, light entered the calorimeter directly without reflecting off the faceplate aperture. In all cases this modification rendered reflective losses, which were consistently dominant, nearly insubstantial (Figure 2.10). Notably, losses from the small ($\varnothing 3$ cm) aperture calorimeter dropped from approximately 15% of the incident flux (Q_{in}) to less than 2% due to use of a beveled aperture. This modification reveals that calorimeter losses are a strong function of calorimeter geometry, not necessarily calorimeter coolant flow or reflectivity.

2.5 Conclusion

A grey body Monte Carlo ray tracer was developed and used to analyze a cylindrical calorimeter for solar simulator calibration. Worst-case emissive and convective losses from the calorimeter were predicted by finite volume simulation. The calorimeter was most accurate when mounted with a beveled (conical) aperture. For both a large aperture and small aperture this geometry brought calorimeter losses within 1.2% of the incident power. Conversely, in select cases calorimeter losses could be nearly 15%. Generally, calorimeter performance was robust to mild changes in cavity reflectivity. It is noteworthy that the calorimeter, like any radiation target, can alter the solar simulator flux profile significantly. This effect should be considered when studying any device within a high-flux solar simulator.

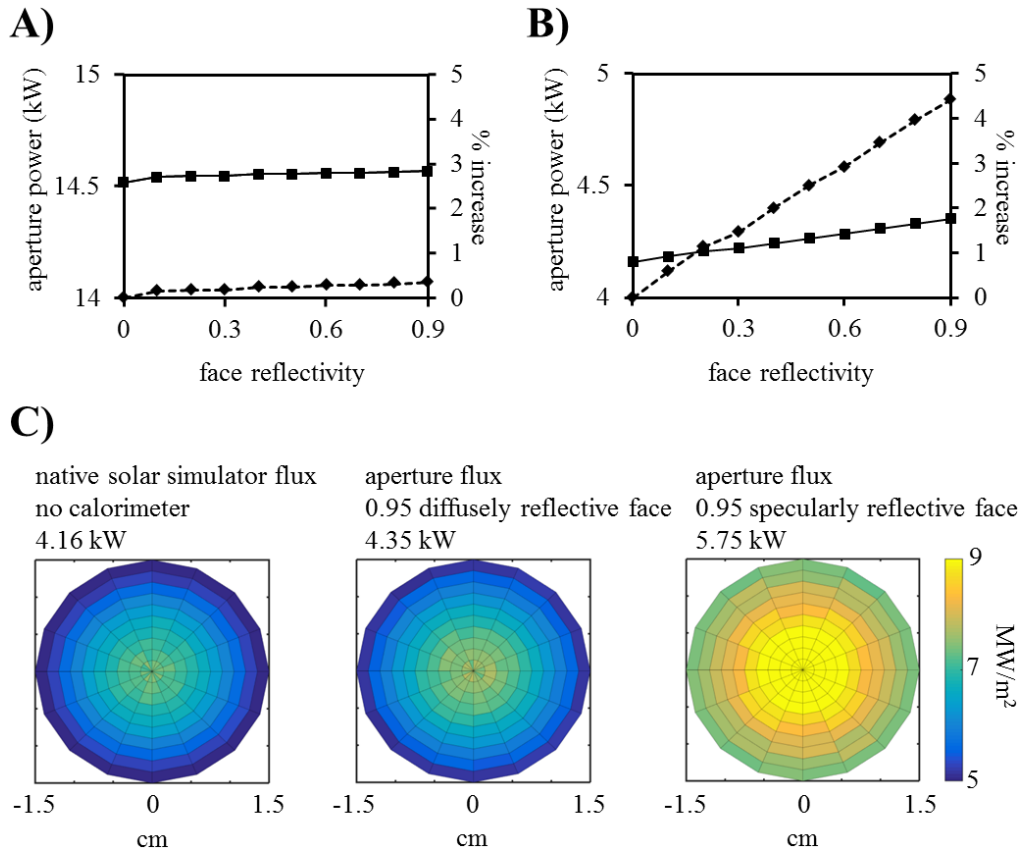


Figure 2.7: The calorimeter induces an observer effect. **A)** Percent distortion (◆) and power intercepted (■) by the large (∅10 cm) aperture faceplate as calorimeter face reflectivity increased. **B)** Percent distortion (◆) and power intercepted (■) by the small (∅3 cm) aperture faceplate as calorimeter face reflectivity increased. **C)** Flux distortion at the small (∅3 cm) calorimeter aperture induced by different face reflectivities.

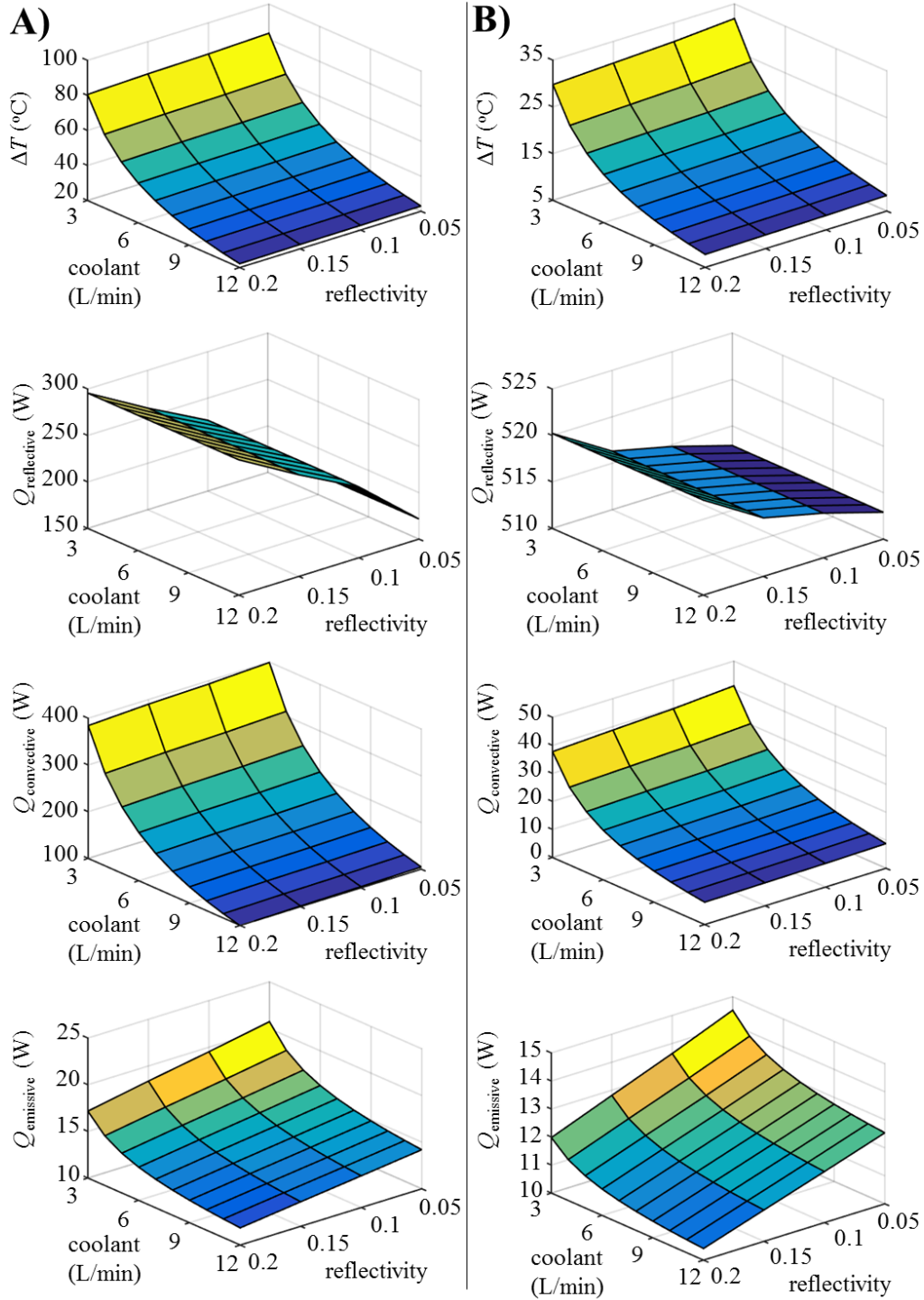


Fig. 2.8: Simulation results for variations in body reflectivity. A) Results for the large ($\varnothing 10$ cm) aperture faceplate. B) Results for the small ($\varnothing 3$ cm) aperture faceplate.

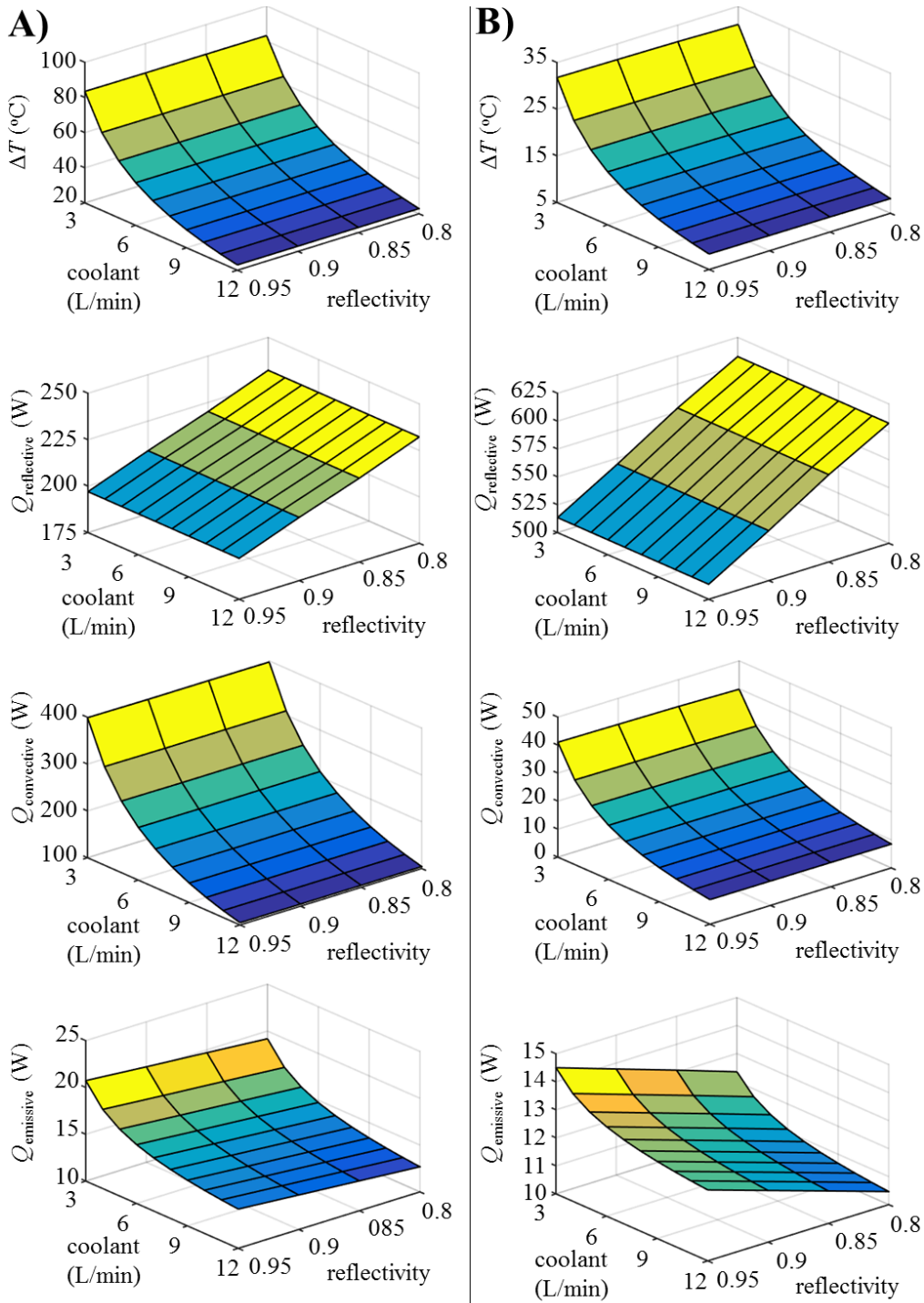


Fig. 2.9: Simulation results for variations in interior faceplate reflectivity. A) Results for the large ($\varnothing 10$ cm) aperture faceplate. B) Results for the small ($\varnothing 3$ cm) aperture faceplate.

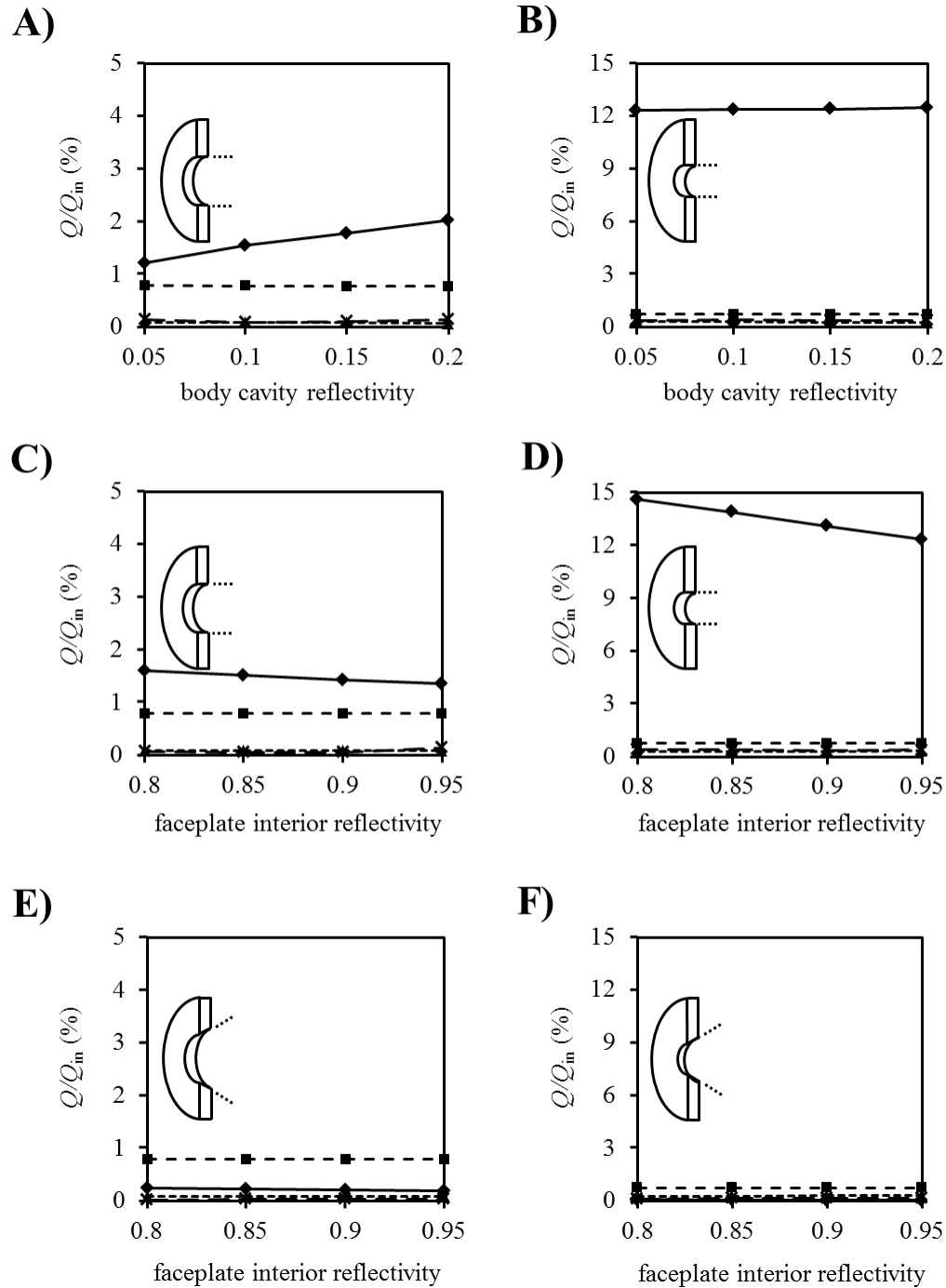


Fig. 2.10: Losses as a percentage of Q_{in} for a calorimeter coolant temperature rise of $\Delta T = 25^\circ\text{C}$. Symbols across all graphs: $Q = Q_{reflective}$ (\blacklozenge), $Q = Q_{convective}$ (\blacksquare), $Q = Q_{emissive}$ (\blacktriangle) and $Q = Q_{observer}$ (\times). **A)** Large (ø10 cm) square aperture faceplate. **B)** Small (ø3 cm) square aperture faceplate. **C)** Large (ø10 cm) square aperture faceplate. **D)** Small (ø3 cm) square aperture faceplate. **E)** Large (ø10 cm) beveled aperture faceplate. **F)** Small (ø3 cm) beveled aperture faceplate.

Chapter 3: Do High-Flux Solar Simulators Accurately Represent Real World Facilities?

Content within Chapter 3 was previously published as “Experimental evidence of an observer effect in high-flux solar simulators” by Scott C. Rowe, Mark A. Wallace, Allan Lewandowski, Richard P. Fisher, W. Ray Cravey, David E. Clough, Illias Hischer and Alan W. Weimer in *Solar Energy* (2017).

3.1 Introduction

In principle, high-flux solar simulators should closely approximate the conditions found in solar furnaces, facilities that use actual sunlight. Relative to this setting, any artifacts in high-flux solar simulator operation could distort the evaluation of solar-thermal designs, especially when assessing solar-electric control strategies. In Chapter 2 an observer effect was noted in simulations of the anticipated University of Colorado high-flux solar simulator design. More detail is provided in Figure 3.1, which shows how reflection and emission from the target of a high-flux solar simulator can be refocused, a trait attributable to the geometry of ellipsoidal reflectors [61, 62]. Conversely, the flat and/or parabolic heliostat(s) that concentrate energy in solar furnaces [48, 63-67] direct light reflected or emitted from a radiation target back towards the sun (Figure 3.1). Although Figure 3.1 suggests a slight optical difference between solar furnaces and high-flux solar simulators, Rowe et al. 2015 predicted that refocusing in simulator facilities could inflate target power by 20% depending on whether the wider environment was specularly reflective or diffusely absorptive. This issue is likely compounded in large high-flux solar simulators that present substantial solid angles to the radiation target. The new high-flux solar simulator at the University of Colorado, built from the dimensions of Bader et al. 2015, presents 2.97 steradians to the radiation target. To test for an observer effect in this setup a cavity calorimeter was built with interchangeable faceplates, whereby solar-simulator power measurement was coincident with different optical environments. It was expected that a specular and reflective calorimeter face

would induce more radiation exchange between the target and simulator, altering calorimeter power measurements relative to a diffuse and absorptive face. Thus, calorimeter faces, but not measurement surfaces, were rendered either specularly reflective or diffusely absorptive. The observer effect was further characterized with a Gardon gauge embedded in alternatively specularly reflective or diffusely absorptive surfaces at the focal plane.

Artifacts in high-flux solar simulator operation can be parsed through computational characterization. In pursuit of characterization many groups analyze their installations via Monte-Carlo ray tracing [41, 54, 62, 68-70]. When the fates of light within a given simulator are predictable the study of high-flux receivers, reactors, and thermal systems is enhanced. Filament modeling within these simulations has a substantive effect on ray tracing fidelity [71, 72], and prior filament modeling has predicted the peak radiant flux from a high-flux solar simulator within 4.2% of experimental measurements [41]. In these Monte Carlo traces model parameters were iterating *in silico*, either manually or through derivative-free optimization, until results approximated the images cast from reflector-filament assemble(s) [68, 72, 73]. Initially, filament modeling research focused on volumetric or surface ray emission from single geometric primitives that approximate lamp arc plasma (reviewed in Dong et al., 2015). More recently, an accurate halide filament model was developed from suites of nine emitting geometric primitives [71]. Ray emission from short-arc xenon filaments, as used in the new University of Colorado solar simulator, have been accurately simulated by probabilistic basis functions for ray emission with three fitted parameters [68]. The use of emitting geometric primitives to approximate xenon filaments has also been attempted [72, 73], and this approach remains attractive for its computational simplicity. Here, we built a short-arc xenon filament model from geometric

primitives that reproduced the results of high-flux solar simulator experiments, including the observer effect.

3.2 Results

3.2.1 Single Lamp Experiments for Model Development

Previous work has shown that the performance of high-flux solar simulators, including the 18 lamp design installed at the University of Colorado, can be analyzed as the superposition of simulator reflector(s) and filament(s) [68, 73]. Thus, single lamp experiments were performed for initial characterization and modeling of the new high-flux solar simulator, efforts prerequisite to the analysis of observer effects. A test lamp built to the dimensions of Bader et al. 2015 was assembled around an Osram GmbH XBO 2500W/HS OFR filament, which was actuated along Cartesian axes at the reflector focus to achieve peak flux on a diffuse planar quartz target (20x20x0.2 cm, United Silica Products). Peak flux was taken as maximal pixel intensity from CCD camera imaging (Coherent Lasercam Hr 1098577 camera) after voltage and amperage to the filament had stabilized (15 minutes). Three reflectors were available for use in single lamp testing: an aluminized reflector, a silvered reflector, and an uncoated reflector. The elemental treatments, protected by quartz overcoats, were applied by Optiforms Incorporated in Temecula, CA.

Figure 3.2 shows how the entire reflector-filament system was aimed at either the diffuse quartz target or a Vatell 1000-4 Gardon flux gauge. This alternation allowed the calibration and integration of flux images as has been previously described [68]. In brief, perspective projection was used to correct minor off axis distortion from the camera [73], which brought distortion across the entire 1280x1024 image within ± 1 pixel (± 0.00027 meters) when imaging a rectangular grid. The Vatell flux gauge was analyzed as recommended by previous studies [72, 74, 75]. To assess gauge accuracy, given the inaccuracies typical of Vatell gauge measurement [47, 74], the device

was further instrumented as a power meter wherein gauge coolant reported the incident radiation. An energy balance on the circular gauge yielded [76]:

$$\alpha Q_{incident} = \dot{m} C_p \Delta T + \frac{2\pi k A \Delta T_{insul.}}{\ln(R_o / R_i)} \quad 3.1$$

Where $Q_{incident}$ is the power intercepted, α is the gauge effective absorptivity, \dot{m} is coolant mass flowrate, C_p is the coolant heat capacity, k is the annular thermal conductivity, R_o/R_i is the divisor of annular insulation radii, ΔT is the coolant temperature rise and $\Delta T_{insul.}$ is the insulation temperature drop. The Vatell gauge effective absorptivity was $\alpha = 0.83$ for the xenon spectrum reflected off aluminum and $\alpha = 0.82$ for the xenon spectrum reflected off silver, which was similar to that previously determined for a Vatell gauge and raw xenon spectrum ($\alpha = 0.8125$) [72, 77]. Table 3.1 gives numerical values of the remaining equation parameters. Although not an exhaustive evaluation of the losses associated with Vatell gauge measurement, results from Equation 3.1 should match flux integration over the gauge face. Figure 3.3 shows this correspondence across all single lamp experiments. This dual analysis provided a fortified approach for assessing the power in single lamp experiments.

Figure 3.4 shows the radial variation in flux and power for the different reflector treatments (aluminized, silvered, uncoated) at the nominal filament operating current (90 amps) for the single 2.5kW_{electric} lamp. Overall, the aluminized reflector was most efficient in delivering electrical power optically onto a Ø10cm target (35% efficient, 1.523 MW/m² peak flux). The silvered reflector was 33% efficient and the uncoated reflector was 25% efficient, with peak fluxes of 1.179 MW/m² and 0.986 MW/m² respectively. Given that the aluminized reflector was most efficient, computational modeling focused on this result.

Table 3.1	Parameters in Equation 3.1
A	$3.21 \cdot 10^{-6}$ meters (Vatell Inc.)
C_p	$4186.6 \text{ J}(\text{kgK})^{-1}$ [57]
k	$0.0721 \text{ W}(\text{mK})^{-1}$ (Zircar Inc.)
R_o/R_i	2

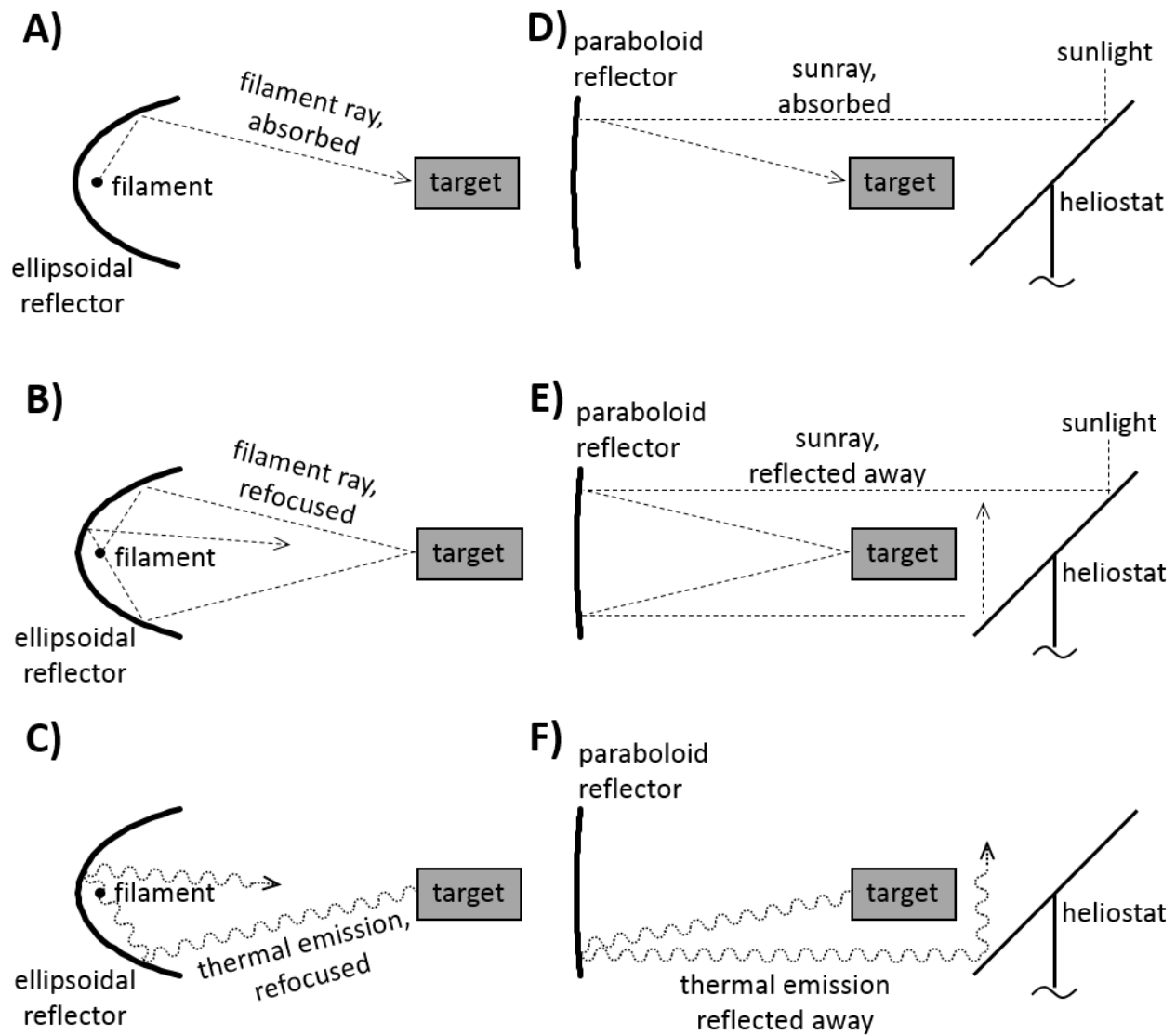


Figure 3.1: A) Radiation without observer effects in point-focused solar simulators. B) Reflection with observer effects in point-focused solar simulators. C) Emission with observer effects in point-focused solar simulators. D) Radiation lacks observer effects in point-focused solar furnaces. E) reflection lacks observer effects in point-focused solar furnaces. F) Emission likely lacks observer effects in point-focused solar furnaces.

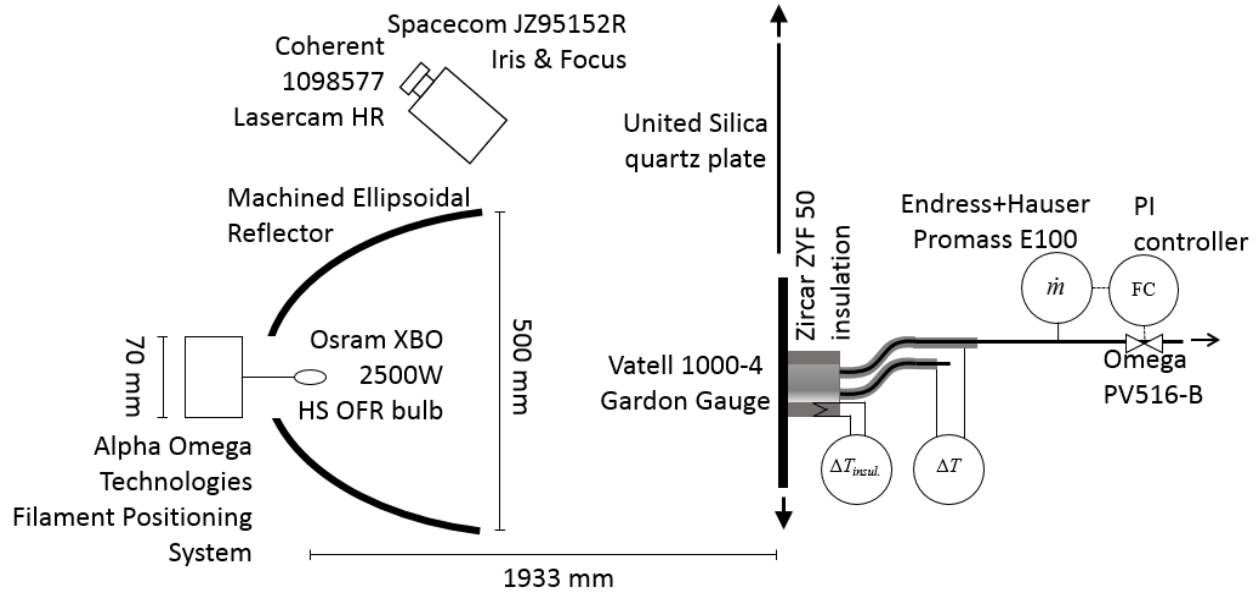


Figure 3.2: Experimental setup for single lamp flux imaging from the diffusely reflective quartz plate, which was displaced linearly to accommodate flux measurement instrumentation. Lamp and reflector dimensions matched those of Bader et al. 2015 [41].

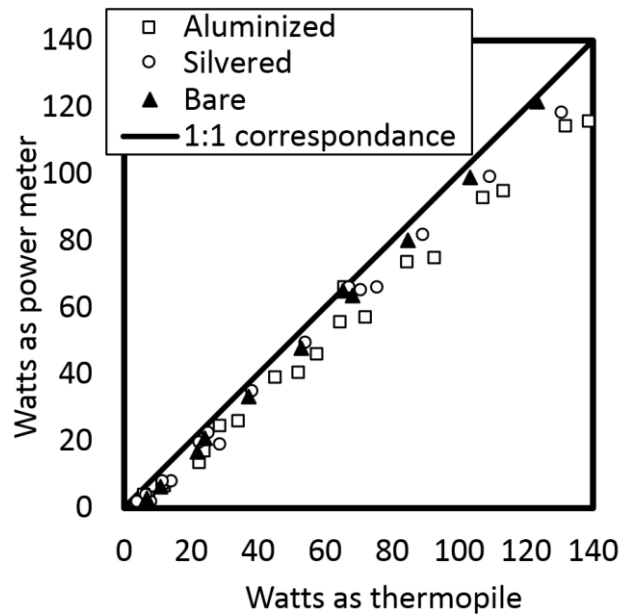


Figure 3.3: Results from integrating imaged flux on the Vatall gauge face (x-ordinate) versus gauge power measured by thermocouple instrumentation (y-ordinate).

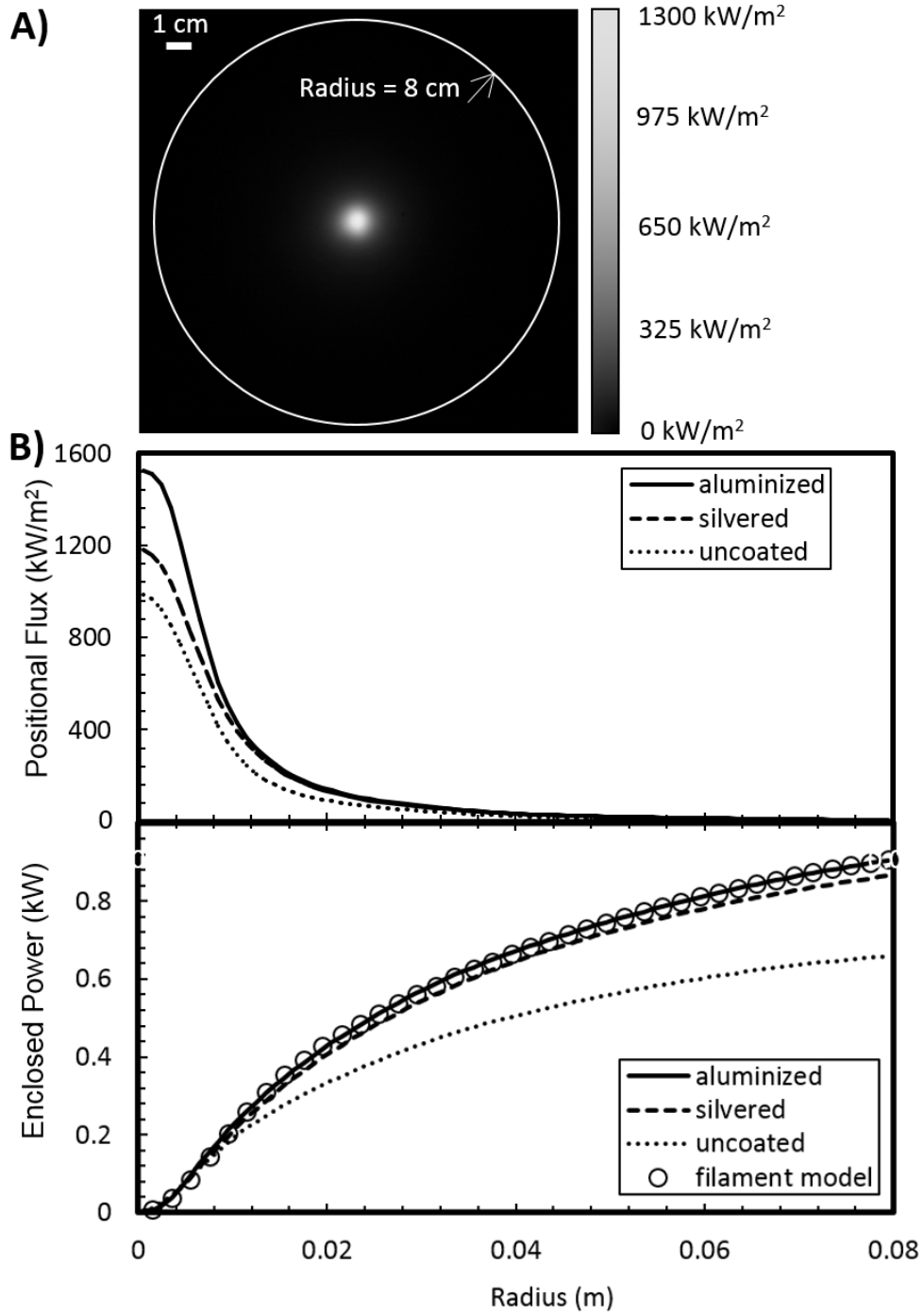


Figure 3.4: A) Representative target flux image. B) Reflector coating performance; instantaneous flux & power on target at or within a given radius, respectively.

3.2.2 Filament Modeling with Monte Carlo Analysis

The grey body Monte Carlo ray tracer for modeling work, which is freely available online (matlabcentral.com), was previously validated against analytical view factors and published ray tracing software [62]. The new Monte Carlo xenon filament model was built from four concentric cylinders that featured uniform volumetric ray emission. Ray origination from each cylindrical source was performed as described by Bader et al. 2015, but without any attempt to truncate the direction rays assume upon emission [41]. Figure 3.5 shows how the basis cylinders were arranged at the reflector focus to mimic the intensity profile of xenon lamp arcs [78]. Five adjustable parameters were varied until simulation approximated the normalized power profile cast by the aluminized reflector in single lamp experiments. Figure 3.4 shows the fit after further optimization via a Nelder-Meade algorithm, which yielded the final model parameters ($R^2 = 0.999$, Table 3.2) [79]. The probability of ray emission from each of the concentric cylinders provided three degrees of freedom. The filament radius and reflector specular error provided two further degrees of freedom. The final model inputs are summarized in Table 3.2 with confidence intervals on the parameter estimates. All traces were with 10^6 rays, which was shown to bring reproducibility within 0.2% in a Monte Carlo convergence study of this optical configuration [68].

To further validate the filament model, results were compared when lamp filament placement was varied in Monte Carlo simulations and on the actual experiment. Filament motion within single lamp tests was achieved with stepper motor actuators that moved the bulb in x, y, and z displacements about the reflector focus (0.2 mm gradations). Figure 3.6 shows the effect of moving the filament along the reflector major axis and minor axis across three experimental replicates with aluminized reflectors. Notably, millimeter adjustments in filament position had substantive effects on optical flux and power. The power on target declined by up to 20% as the

filament was moved a millimeter off center. Unexpectedly, the peak flux and peak power did not coincide as the filament moved along the reflector semi-major axis (Figure 3.6). These experiments were reproduced in Monte Carlo simulations with the new computational filament model. Model results matched experiment with one exception -- when the filament was pushed axially into the reflector there was a 15% discrepancy between model and experimental power results, which brought model predictions outside experimental error. However, the model did recapitulate the disparate axial power and flux peaks observed in experiment.

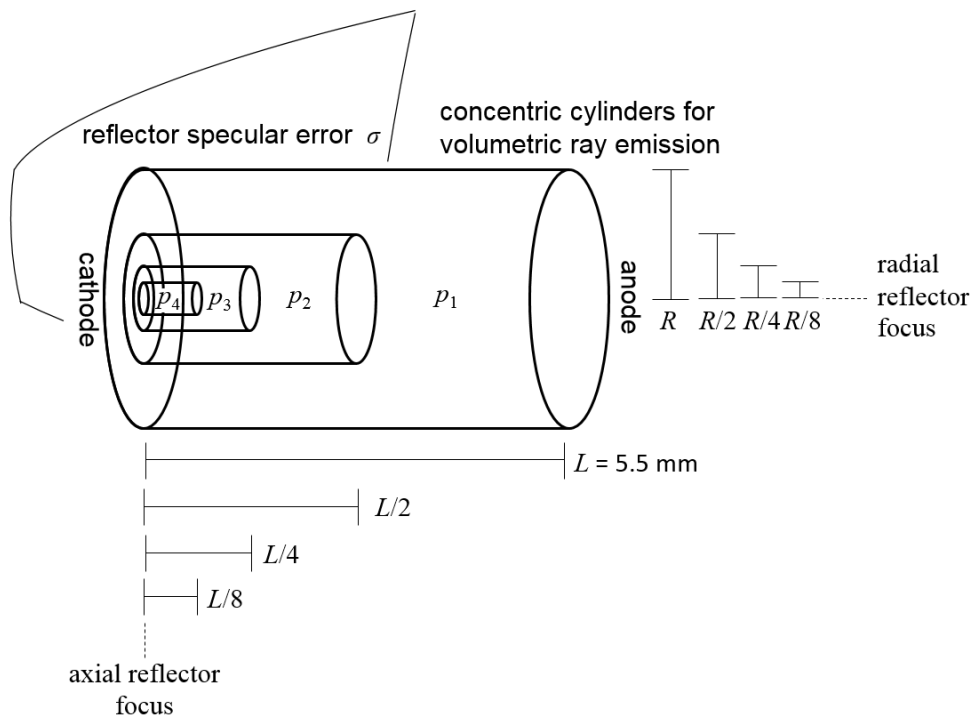


Figure 3.5: Geometry of the filament model (not to scale). Parameter estimates R , σ , p_1 , p_2 , p_3 and p_4 are listed in Table 3.2.

Table 3.2 | Fitted parameter estimates within the filament model \pm 95% confidence.

p_1	54.0 \pm 1.4%	probability of ray emission from cylinder 1 (Figure 3.5)
p_2	16.4 \pm 1.2%	probability of ray emission from cylinder 2 (Figure 3.5)
p_3	9.8 \pm 1.8%	probability of ray emission from cylinder 3 (Figure 3.5)
p_4	19.7 \pm 1.8%	probability of ray emission from cylinder 4 (Figure 3.5)
R	3.5 \pm 0.3 mm	effective filament radius (Figure 3.5)
σ	3.0 \pm 0.3 mRad	reflector specular error (Figure 3.5)

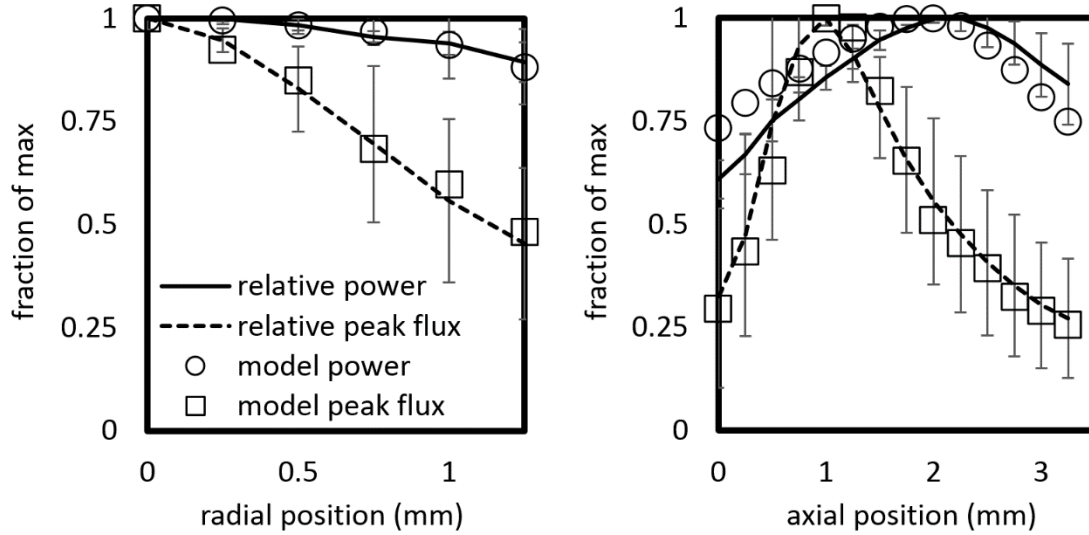


Figure 3.6: The effect of moving the filament radially and axially in a reflector for three replicate lamps with aluminized reflectors. Error bars are 95% confidence intervals of three independent experimental replicates (separate lamps).

3.2.3 Observer Effects in the Fully Assembled High-Flux Solar Simulator

Based on the results of single lamp experimentation (section 3.2.2), aluminized reflectors were chosen to direct emission from the fully assembled high-flux simulator to radiation measurement equipment. It was hypothesized that radiation measurement instrumentation, under different optical regimes, would show an observer effect predicted in simulation [62]. To evaluate this possibility, power from the 18 lamp device, which was built from the geometry of Bader et al. 2015, was measured by a cavity calorimeter with interchangeable faceplates [48, 62]. Figure 3.7 shows a rendering of the calorimeter design, which was analyzed in detail by Rowe et al. 2015 (Chapter 2), alongside calorimeter modeling *in silico*. All simulator filaments were positioned as described in section 3.2.1.

Calorimeter coolant flows were instrumented with resistance temperature thermometers and an Endress-Hausser Promass E100 Coriolis mass flow meter. Figure 3.8 details the calorimeter faceplate designs and cooling channel arrangement. It was found that during illumination 6-7

L/min of water flow was needed to actively cool and avert deterioration of the calorimeter faces. A Ø10cm aperture and Ø3cm aperture faceplate were available for light entry into the 40cm deep cylindrical calorimeter cavity.

Prior work has shown that, in the absence of instrumentation error, calorimeter performance can be highly accurate [62]. Theoretically, measurement error for the calorimeter design herein is <1% of the recorded optical power [62]. Thus, 1% error was added to the instrumentation error, where calorimeter power was calculated from measurements as:

$$Q = \dot{m}C_p\Delta T - \frac{\dot{m}\Delta P}{\rho} \quad 3.2$$

Here, ΔP is the coolant pressure drop, ρ is the coolant water density (998.0 kg/m³, [57]), and all other symbols are as shown in Equation 3.1. Instrumentation error was given by partial derivatives on Equation 3.2:

$$dQ = \sqrt{\left(\frac{\partial Q}{\partial \dot{m}} d\dot{m}\right)^2 + \left(\frac{\partial Q}{\partial C_p} dC_p\right)^2 + \left(\frac{\partial Q}{\partial \Delta T} d(\Delta T)\right)^2 + \left(\frac{\partial Q}{\partial \rho} d\rho\right)^2 + \left(\frac{\partial Q}{\partial \Delta P} d(\Delta P)\right)^2} \quad 3.3$$

Table 3.3 lists accuracy of the calorimeter sensors for use in Equation 3.3.

The calorimeter interior was painted with ThurmaloX Black while the interchangeable calorimeter faces were polished to specularity. Figure 3.9A shows the wavelength specific reflectivity of the calorimeter faces from PE Lambda 1050 and Cary 500 spectrophotometers. After the reflective calorimeter faces were subjected to triplicate measurements under illumination from all 18 lamps the polished faces were roughened, painted with ThurmaloX Black, and retested under the same conditions. Figure 3.10 shows the baseline for high-flux solar simulator

performance, which was evaluated for $2.25 \text{ kW}_{\text{electric}}$ from each lamp into the $\varnothing 10\text{cm}$ aperture ThurmaloX coated calorimeter faceplate. Under these conditions the high-flux solar simulator directed $9.076 \pm 0.190 \text{ kW}$ of optical power into the $\varnothing 10\text{cm}$ target and imaging indicated a peak flux 12.50 MW/m^2 , where calorimetric flux mapping was performed as described by Gill et al. 2015, but with the camera and quartz target from Section 3.2.1.

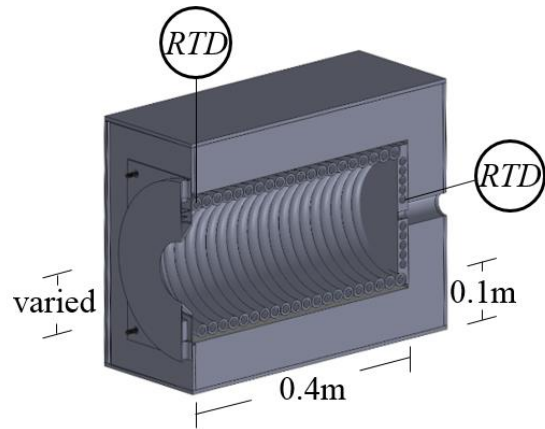
Relative to the absorptive calorimeter faceplates, it was expected that the polished calorimeter faceplates would inflate calorimeter power measurements because radiation exchange between the high-flux simulator and target refocuses light. This effect was experimentally significant for the smaller calorimeter aperture, as shown in Figure 3.9C, and less pronounced for the larger aperture. Specifically, when the calorimeter faceplates were polished to specularity 11.1% and 2.7% more power was intercepted by the $\varnothing 3\text{cm}$ and $\varnothing 10\text{cm}$ aperture calorimeters, respectively. Thus, optical properties of the radiation environment, here the calorimeter face, altered the incident simulator power.

Table 3.3	Instrumentation uncertainty.
$d\dot{m}$	0.15% (Endress Hauser Inc.)
dT	$0.03+0.0005T$ °C (Omega Inc.)
$d\rho$	1% [57]
dC_p	1% [57]
$d(\Delta P)$	0.25% (Omega Inc.)

Calorimeter results suggested that incident flux was either higher overall, or reshaped, when reflective surfaces were present at the high-flux solar simulator target. To explore these possibilities a Gardon flux gauge (Vatell 1000-1) was embedded in either a specularly reflective

or diffusely absorptive plate and subjected to $1.75 \text{ kW}_{\text{electric}}$ on all high-flux solar simulator lamps. The $\varnothing 28 \text{ cm}$ plates were water cooled and prepared identically to the cavity calorimeter faceplates, where the surfaces were either polished or coated with ThurmaloX Black. Figure 3.11A shows gauge holders and relative increase in gauge output when sampling fluxes at the high-flux solar simulator focus. Notably, damage to the absorptive ThurmaloX plate was evident, likely because cooling was insufficient for the preservation of surfaces exposed directly to peak solar simulator fluxes. However, despite the deterioration of this optical coating the observer effect remained evident. Figure 3.11B shows that, relative to the absorptive plate, fluxes were higher on the specular plate. As the flux gauge sampled points further from the high-flux solar simulator focus, the relative increase in flux grew, with a maximal inflation of $23 \pm 4\%$. This result is consistent with light exchange between the high-flux solar simulator and target, where specular reflection from the target is refocused by the high-flux solar simulator.

A)



B)

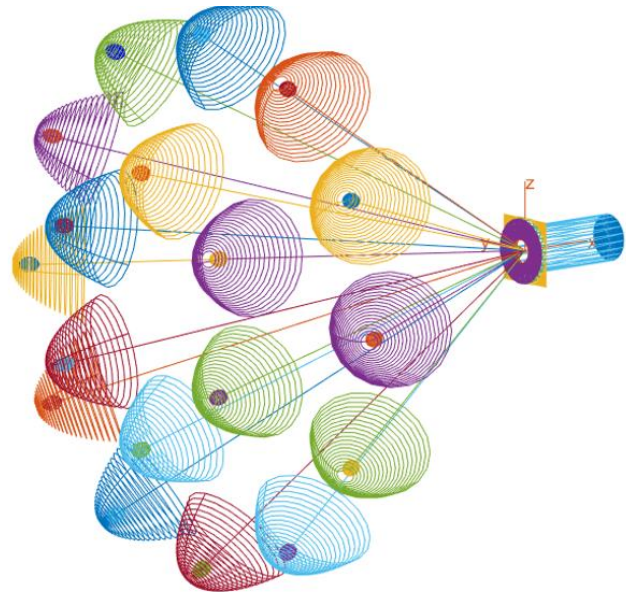


Figure 3.7: A) Cutaway of the calorimeter design showing internal cooling channels and the detachable, $\varnothing 10\text{cm}$ aperture, faceplate. Additional details and analysis of this design is available in Rowe et al. 2015. B) the calorimeter and simulator in computer simulation.

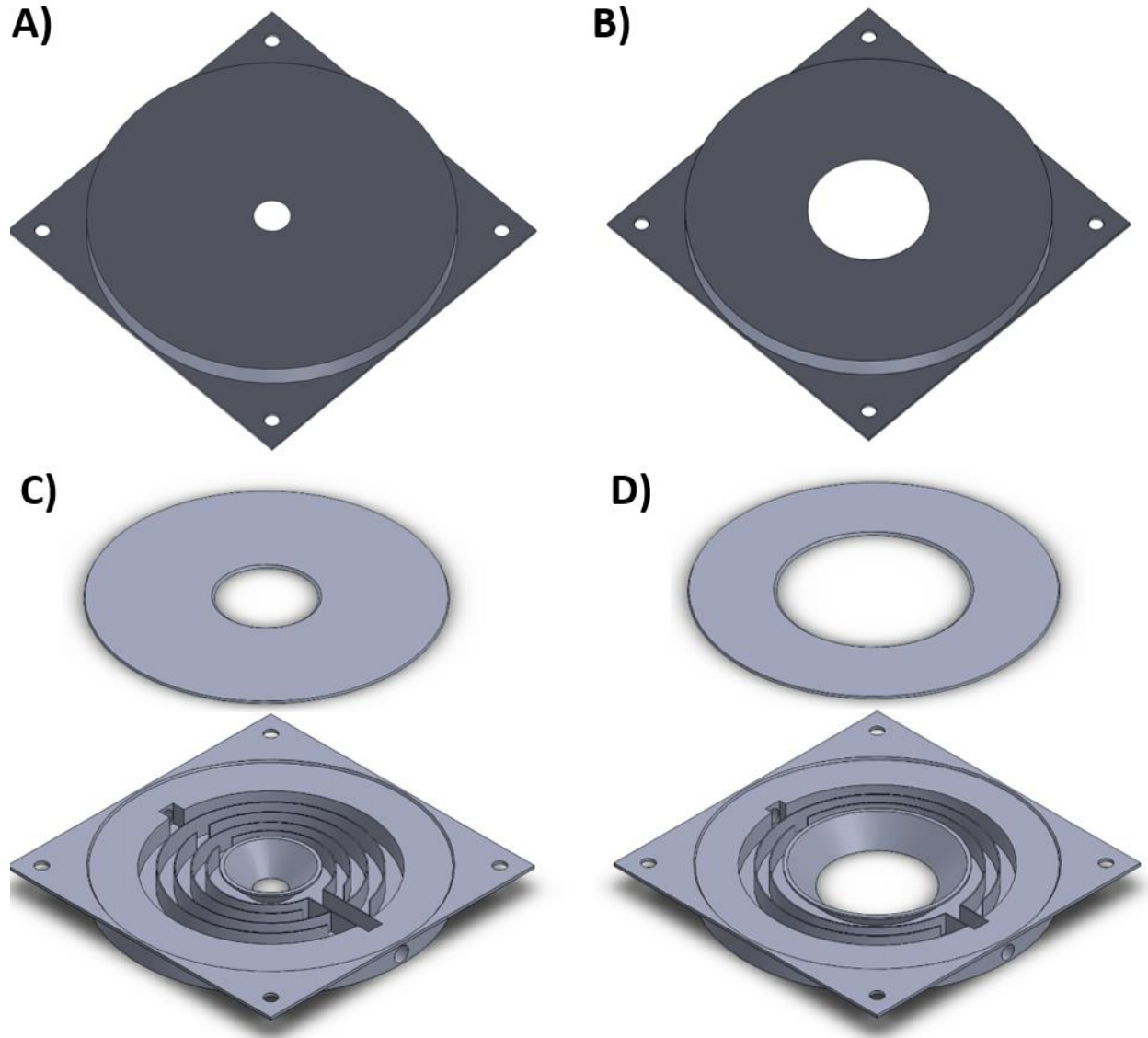


Figure 3.8: A) Front of the $\varnothing 3\text{cm}$ aperture calorimeter faceplate. B) Front of the $\varnothing 10\text{cm}$ aperture calorimeter faceplate. C) Cutaway of cooling channels embedded in the $\varnothing 3\text{cm}$ aperture calorimeter faceplate. D) Cutaway of cooling channels embedded in the $\varnothing 10\text{cm}$ aperture calorimeter faceplate.

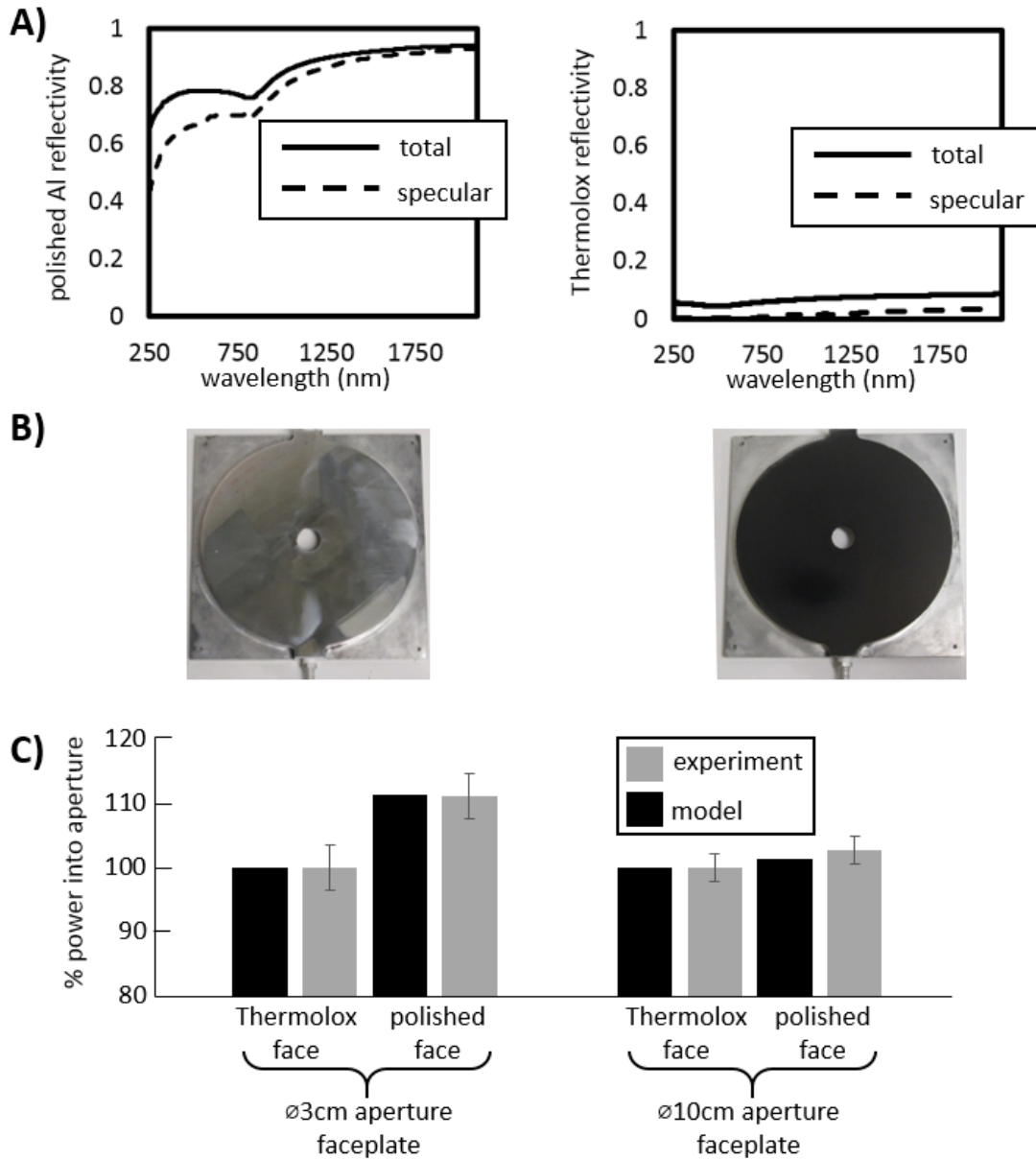


Figure 3.9: A) Total and specular reflectivity of the faceplate treatments. B) The $\varnothing 3\text{cm}$ faceplate, polished (left) or ThurmaloX coated (right). C) Observer effect results showing inflated simulator power when the calorimeter faces were polished.

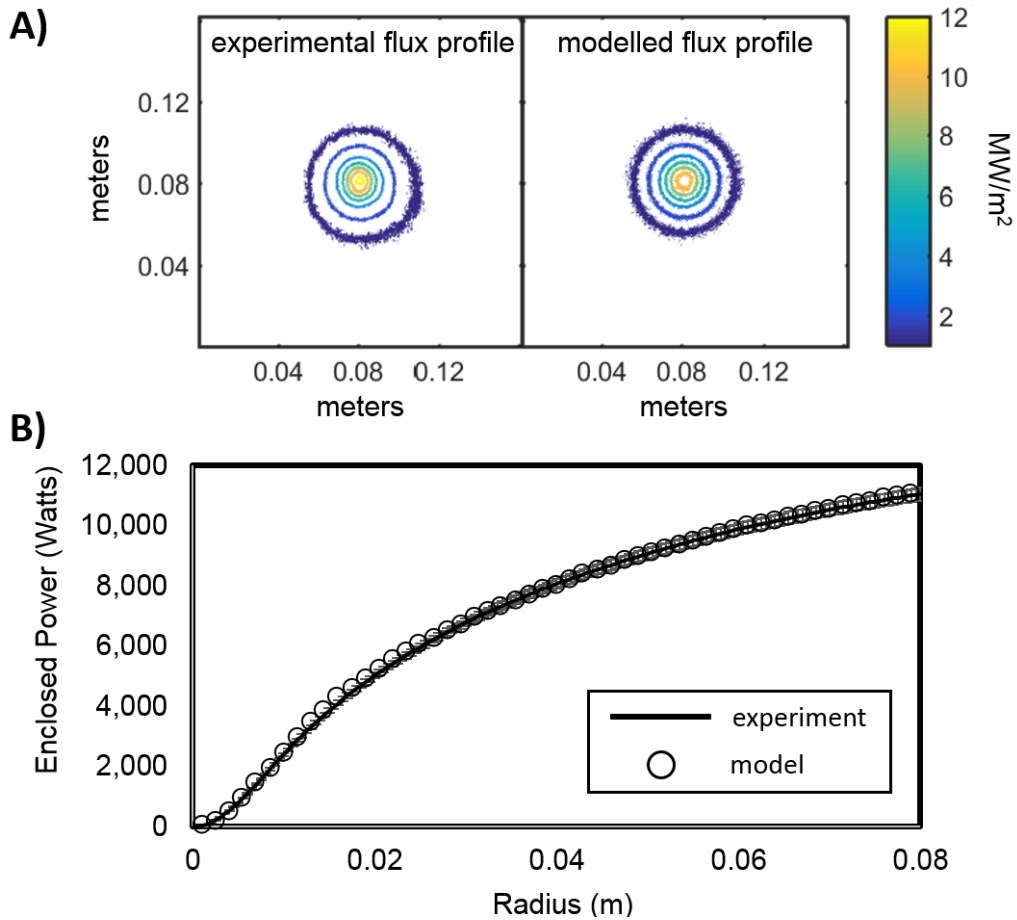


Figure 3.10: A) Monte Carlo flux profile compared to the experimental flux profile of the entire, 18 lamp, high-flux solar simulator. B) Monte Carlo power profile compared to the experimental power profile of the entire, 18 lamp, high-flux solar simulator. The simulator achieved a peak flux of 12.507 MW/m² and delivered 9.076±0.190 kW onto a Ø10cm target for a mean flux of 1.155 MW/m².

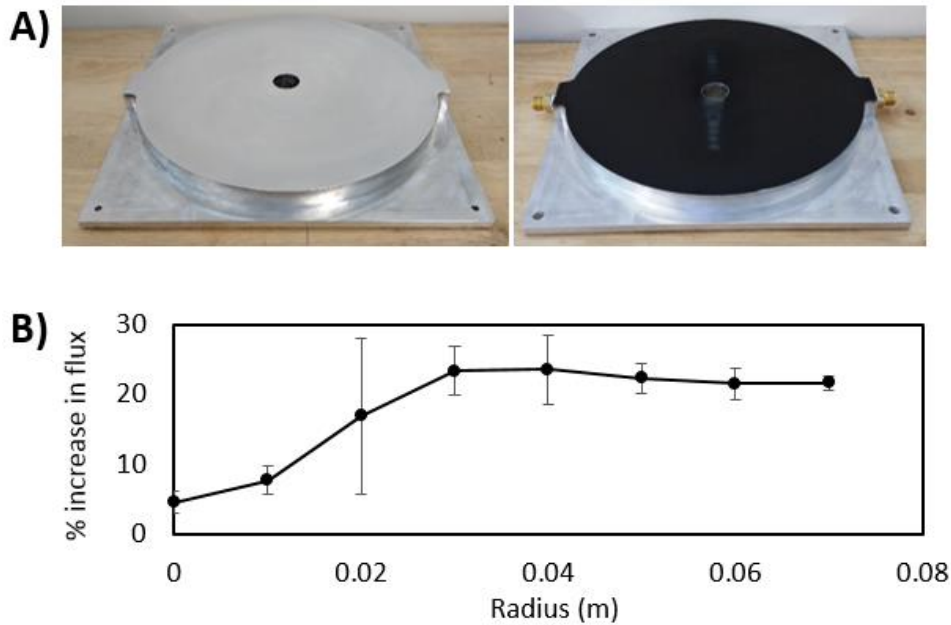


Figure 3.11: A) flux gauge plates, polished (left) and ThurmaloX coated (right). Note damage on the ThurmaloX coated plate. B) Increase in flux as sampled outwardly from the high-flux solar simulator focus.

3.2.4 Modeling Reproduces High-Flux Solar Simulator Results

Through superposition, the computational filament model from single lamp experimentation should reproduce results from the fully assembled high-flux solar simulator, including observer effects [68, 73]. To test this possibility, the entire high-flux solar simulator was represented in Monte Carlo ray traces. All traces were done with 10^6 rays per lamp, which has been shown to be repeatable within $<0.2\%$ for Monte Carlo traces of this high-flux solar simulator configuration [68]. Figure 3.10 shows that experimental power into the $\varnothing 10\text{cm}$ aperture calorimeter, 9.076 ± 0.190 kW, closely matched the result from Monte Carlo simulation, 9.086 kW. Furthermore, Figure 3.10 shows that flux profile imaging at the solar simulator focus was similar to that found *in silico*. The error in peak flux between experiment and simulation, 4.0%, was similar to that for a filament model based on probabilistic basis functions, which gave a 4.2% discrepancy [68]. Specifically, a maximum flux of 12.50 MW/m^2 was seen in experiment, while

a maximum flux of 12.02 MW/m² was predicted in simulation. Overall, given the quantitative and qualitative similarities seen across experiment and simulation, we conclude that the filament model likely captures general system behavior.

Before the observer effect could be examined in grey Monte Carlo ray traces, the effective reflectivity of target surfaces required evaluation. The reflectivities of polished aluminum and ThurmaloX black, as determined on PE Lambda 1050 and Cary 500 spectrophotometers (Figure 3.9A), were integrated given the wavelength specific intensity of the xenon filament source.

$$r = \frac{\int_{250nm}^{1650nm} r_{\lambda} I_{\lambda} d\lambda}{\int_{250nm}^{1650nm} I_{\lambda} d\lambda} \quad 3.4$$

Here, I_{λ} is the source wavelength specific intensity after reflection off aluminum, r_{λ} is the measured wavelength specific reflectivity of the surface from Figure 3.9A, and r is the effective reflectivity of the surface in simulation. The difference between effective specular to effective total reflectivity was used as the diffuse reflection fraction Monte Carlo tracing. As in prior work source intensities outside 250 nm and 1650 nm were unavailable [75]. The specular aluminum polish showed an effective total reflectivity of 0.902 with a specular reflectivity of 0.812. ThurmaloX black showed an effective total reflectivity of 0.151 with a specular reflectivity of 0.023.

Initially, Monte Carlo ray traces substantially overestimated the observer effect and yielded results outside experimental error. Although the lamp filament was modelled, other bulb structures were likely involved in light exchange with the high-flux solar simulator target. Any light refocused by a lamp likely passes through the bulb glass, which may absorb light and attenuate the observer effect. This was tested by adding ellipsoids to the filament model with a transmittivity

characteristic of glass ($t = 0.88$ [80]) and dimensions consistent with the bulbs of OSRAM XBO 2500W/HS OFR xenon sources (3.8 cm semi-major axis and 3.2 cm semi-minor axis). Figure 3.9C shows that, with this addition, the observer effects shown by the cavity calorimeter were reproduced in Monte Carlo ray traces. No attempt was made to reproduce Gardon gauge results given the heterogeneous deterioration of optical surfaces in flux experiments.

3.3 Discussion

Previous computational work has shown that high-flux solar simulators, unlike solar-furnaces, can show an observer effect [62]. This was confirmed experimentally through the use of a cylindrical calorimeter with interchangeable faceplates. Relative to a diffusely absorptive faceplate, when a specular and reflective $\varnothing 3\text{cm}$ aperture faceplate was mounted on the calorimeter 11.1% more power was intercepted. This effect was attenuated, but still present, for a $\varnothing 10\text{cm}$ faceplate. Thus, in high-flux solar simulators the overall optical environment can alter the incident power and flux. Distortion of the flux profile was observed with a Gardon gauge, which indicated that higher fluxes were present at the simulator target when the overall environment was specularly reflective, versus diffusely absorptive. These results were supported with Monte Carlo ray traces that reproduced experiment.

To attenuate any observer effects when evaluating different targets within a high-flux solar simulator we recommend that power and flux measurement instrumentation optically and geometrically resemble other experimental equipment (reactors, concentrators, collectors). This insures that all equipment similarly interacts and exchanges light with a high-flux solar simulator. To the extent possible, high-flux solar simulator targets should be rendered diffusely absorptive to prevent reflections and spurious light exchange. A survey of existing simulators showed that many

place experimental equipment close to simulator lamps [40] and future designs might consider longer focal lengths to ameliorate observer effects. Alternatively, high performance flux measurement and calibration systems may compensate for observer effects in software, perhaps with model-based Monte Carlo corrections [81]. In some fields the measured efficiency of experimental solar-thermal systems is at or below 15% [9]. Adding observer effect uncertainty to low efficiency calculations is clearly undesirable, but can likely be avoided with analysis and experimental care.

Chapter 4: Can Control Models be More Transparent?

4.1 Introduction

During the evaluation of various strategies for use in solar-electric control, state space models appeared to represent the state-of-art in applied chemical engineering. Relative to alternatives, various authors have advanced state space models as the most natural basis for controls analysis and practice in the chemical industry [82-85]. Select control vendors have adopted the state space and multiple techniques are now available for fitting these models to system data (Appendix A, [86-89]). This approach is derived as a 1st order Taylor linearization of system dynamics, is a Markov chain for facile analysis, and allows fault detection and inference in chemical processes [84]. However, unlike transfer function and autoregressive moving average (ARMA) models, which operate on inputs and outputs, this representation uses internal states to propagate system dynamics. The compartmentalization of system dynamics within the state space can make these models less intuitive, especially for facility operators accustomed to pure input-output representations [85, 87, 90]. The state space can be rendered more transparent by model realignment where, when possible, internal states identically match measured outputs. Such an approach can frame the state space in a manner that befits reduced order estimation. Prior to state space development for the solar-electric reactor, we sought to develop a general method for state space alignment.

To illustrate, consider the discrete time state space without feedthrough (Appendix A):

$$\bar{x}_{k+1} = A\bar{x}_k + B\bar{u}_k \quad 4.1$$

$$\bar{y}_k = C\bar{x}_k \quad 4.2$$

Where at time k an $n \times 1$ state vector \bar{x}_k propagates system dynamics, an $m \times 1$ vector \bar{u}_k of control inputs impinges on the system, and an $r \times 1$ measurement vector \bar{y}_k is observed from the chemical

process. In cases where $n = r$, whereby the number of states and measurements are equal, inversion of matrix C can reveal the current system state \vec{x}_k :

$$C^{-1}\vec{y}_k = \vec{x}_k \quad 4.3$$

However, in cases where $n > r$ and/or matrix C is poorly conditioned direct observation of the system state may be lost. Sophisticated techniques exist for recovering the system state in these cases [91, 92], although select authors consider these methods inaccessible to practicing control engineers [93]. Alternatively, formulations exist wherein the system state consists solely of the outputs and inputs:

$$T\vec{x}_k = \begin{bmatrix} \vec{y}_k \\ \vec{u}_k \end{bmatrix} \quad 4.4$$

Where transform T converts an identified model of the system dynamics to the aligned model. Unfortunately, the resultant state space model is likely non-minimal and may be unobservable [94]. Furthermore, there is no assurance that, when limiting the state to consist of inputs and outputs, the model will capture full system dynamics. Thus, we consider an alternative approach to model alignment that was formalized by Franklin, Powell, and Workman [95]. Here, the system state is coerced to align only with the measurements:

$$T\vec{x}_k = \begin{bmatrix} \vec{y}_k \\ \vec{z}_k \end{bmatrix} \quad 4.5$$

Where \vec{z}_k is an $n-r \times 1$ vector of opaque states needed for the full representation of system dynamics. The resultant, partitioned, state space has the following form:

$$\begin{bmatrix} \bar{y}_{k+1} \\ \bar{z}_{k+1} \end{bmatrix} = \begin{bmatrix} A_{yy} & A_{yz} \\ A_{zy} & A_{zz} \end{bmatrix} \begin{bmatrix} \bar{y}_k \\ \bar{z}_k \end{bmatrix} + \begin{bmatrix} B_y \\ B_z \end{bmatrix} \bar{u}_k \quad 4.6$$

$$\bar{y}_k = \begin{bmatrix} I & 0 \\ 0 & \bar{z}_k \end{bmatrix} \quad 4.7$$

Where:

$$T^{-1}AT = \begin{bmatrix} A_{yy} & A_{yz} \\ A_{zy} & A_{zz} \end{bmatrix} \quad 4.8$$

$$T^{-1}B = \begin{bmatrix} B_y \\ B_z \end{bmatrix} \quad 4.9$$

$$CT = \begin{bmatrix} I & 0 \end{bmatrix} \quad 4.10$$

The opaque states \bar{z}_k can be readily discovered by reduced order estimation with a Luenberger observer [95], or alternatively the Kalman gain (Appendix B).

Model realignment can degrade conditioning of the state space, which may compromise model utility in predictive control applications [96-100]. Thus, any transformation T for model realignment should preserve numerical properties of the initial state space. Currently, there is no systematic way of choosing transform T [101]. We propose an established technique from statistics, c-optimality [102], for the maintenance of model condition upon state space realignment:

$$\begin{aligned} T &= \arg \min \text{cond}(T^{-1}AT) \\ &\text{s.t. } \begin{bmatrix} I & 0 \end{bmatrix} = CT \end{aligned} \quad 4.11$$

Where *cond* refers to the condition number of $T^{-1}AT$, the divisor of the largest over smallest matrix eigenvalues (modes):

$$\text{cond}(T^{-1}AT) = \frac{\lambda_{\text{largest}}}{\lambda_{\text{smallest}}} \quad 4.12$$

By minimizing the condition number, transform T minimally inflates timescale separation between the output equated states \bar{y}_k and opaque states \bar{z}_k . Although a feasible minimization cannot be

guaranteed, this approach is highly general and automatic. The optimization can be started with any invertible matrix, although we recommend initialization with the orthonormal matrix $T = Q^T$ from LQ decomposition on the output matrix C :

$$C = LQ \tag{4.13}$$

Note that the LQ decomposition can be found as the transpose of QR decomposition on C^T . This initialization is convenient because setting $T = Q^T$ immediately satisfies $r^*(n-r-1)/2$ of the optimization equality constraints:

$$\begin{bmatrix} L & 0_{r \times n-r} \end{bmatrix} = CQ^T \tag{4.14}$$

Furthermore, as an orthonormal matrix selecting $T = Q^T$ has initial no effect on open-loop system eigenvalues (conditioning).

Tractability of the c-optimal approach was assessed on two systems that harbored opaque states. It was expected that model realignment by c-optimal transformation would preserve accurate state estimation in these systems. Successful state tracking was first judged by inferential composition estimation in a simulated nonlinear binary flash separation. Performance of the c-optimal aligned models was compared against inference using the unaligned models with established Sylvester observers [92]. Next successful state estimation was explored for process forecasting in an experimental carbon gasifier. A reasonable model realignment, including through c-optimal transformation, should allow state tracking in this system that preserves accurate process forecasting for model predictive control applications.

4.2 Methods

4.3 c-Optimality Preserves State Tracking Relative to Established Technique

4.3.1 Nonlinear Flash Model

A nonlinear binary flash simulation was used to validate the c-optimal model alignment technique, especially with respect to state estimation relative to established methods. Figure 4.1 shows the binary flash and Table 4.1 defines the system variables. In this case the nonlinear differential equations were developed from Baldea et. al. [103]:

$$\dot{M}_v = N_l + N_h - V \quad 4.15$$

$$\dot{y} = M_v^{-1}(N_l - yN) \quad 4.16$$

$$\dot{M}_B = F - N - B \quad 4.17$$

$$\dot{x} = M_B^{-1}(F(x_{in} - x) - N_l + xN) \quad 4.18$$

$$\dot{T} = [C_p(M_v + M_B)]^{-1} \begin{pmatrix} C_p F(T_{in} - T) + \dots \\ Q - \Delta H_l N_l - \Delta H_h N_h \end{pmatrix} \quad 4.19$$

The lumped energy balance assumes that the chemical constituents have similar heat capacities. System behavior also conforms to six algebraic equations. Antoine relations express the saturation pressure of the light and heavy components:

$$P_l^{sat}(T) = e^{A_l - B_l/T} \quad 4.20$$

$$P_h^{sat}(T) = e^{A_h - B_h/T} \quad 4.21$$

In addition, the interfacial fluxes are driven by departures from Raoult's law:

$$N_l = k_l a \left(\frac{P_l^{sat}(T)}{P} x - y \right) \frac{M_B}{\rho} \quad 4.22$$

$$N_h = k_h a \left(\frac{P_h^{sat}(T)}{P} (1-x) - (1-y) \right) \frac{M_B}{\rho} \quad 4.23$$

Finally, system pressure and liquid density are a function the ideal gas law and composition respectively:

$$P[v - M_B / \rho] = M_v RT \quad 4.24$$

$$\rho = \rho_l x + \rho_h (1-x) \quad 4.25$$

It was assumed that a gain only inventory controller was already active, as is common prior to the identification of system models [104]:

$$B = \bar{B} - 10(\bar{M}_B / \bar{\rho} - M_B / \rho) \quad 4.26$$

The overbars refer to the steady-state quantities from Table 4.1.

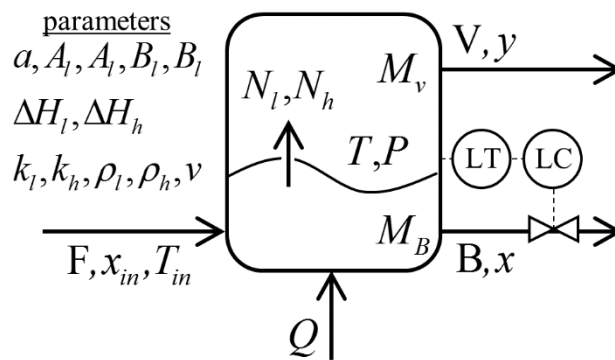


Fig. 4.1: Nonlinear chemical flash simulation variables and flows. LT refers to level transducer and LC to level controller.

TABLE 4.1

vectors	Quantity	
F	vector of state functions f	
d	d x1 disturbance vector	
G	vector of output functions g	
u	m x1 input vector	
y	r x1 output vector	
x	n x1 state vector	
z	$n-r$ x1 vector of opaque states that remain after c-optimal transform	
matrices	Quantity	
0	matrix of zeros	
A	discrete time state transition matrix	
A'	A with appended states	
B	discrete time input matrix	
B'	B with appended states	
C	discrete time output matrix	
C'	C with appended states	
I	identity matrix	
L	Leunberger Gain	
L	lower diagonal matrix	
Q	orthonormal rotation matrix	
T	c-optimal transform matrix	
nonlinear states	Quantity	steady state
M_B	liquid holdup (moles)	2,366
M_V	vapor holdup (moles)	22
T	temperature (Kelvins)	291
x	light liquid fraction (unitless)	0.13
y	light vapor fraction (unitless)	0.84
algebraic variables	Quantity	steady state
N_h	heavy species flux (mole/sec)	0.66
N_l	light species flux (mole/sec)	4.33
P_h^{sat}	heavy species saturation pressure (Pa)	9,618
P_l^{sat}	light species saturation pressure (Pa)	38,353
P	system pressure (Pa)	5,361
ρ	liquid density (mole/m ³)	2,366
process flows	Quantity	steady state
B	liquid rate (mole/sec)	5
Q	heat rate (watts)	10,000
V	vapor rate (mole/sec)	5
parameters	Quantity	steady state
a	specific interfacial area (m ² /m ³)	5
A_h	heavy Antoine coefficient (unitless)	15
A_l	light Antoine coefficient (unitless)	18
B_h	heavy Antoine coefficient (Kelvins)	1700
B_l	light Antoine coefficient (Kelvins)	1500
ΔH_h	heavy vaporization energy (J/mole)	1000
ΔH_l	light vaporization energy (J/mole)	250
k_h	heavy transfer coefficient (mol/m ² sec)	6
k_l	light transfer coefficient (mol/m ² sec)	10
ρ_h	heavy species density (mole/m ³)	2,500
ρ_l	light species density (mole/m ³)	1,500
v	flash volume (m ³)	2
disturbances	Quantity	steady state
F	feed rate (mol/sec)	10
ρ_{in}	feed density (mole/m ³)	2000
T_{in}	feed temperature (Kelvins)	300

4.3.2 State Space Modeling and Alignment for Estimation of the Nonlinear Flash System

The nonlinear flash described in section 4.2 was linearized about the operating point shown in Table 4.1 via n4sid subspace identification [88]. Figure 4.2 shows the identification workflow. In brief, identification data was collected from the nonlinear model with a pseudorandom binary sequence of $\pm 5\%$ perturbations in the process inputs (Q , V) and disturbances (x_{in} , T_{in} , F). An 8.4 minute PRBS duty cycle was chosen based on the recommendations of Gaiwak and Rivera [105].

The resultant state models had the following form:

$$\bar{x}_{k+1} = A\bar{x}_k + [B_d \quad B] \begin{bmatrix} \bar{d}_k \\ \bar{u}_k \end{bmatrix} \quad 4.27$$

$$\bar{y}_k = C\bar{x}_k \quad 4.28$$

Where the measured disturbances \bar{d}_k , inputs \bar{u}_k and measured outputs \bar{y}_k were as follows:

$$\bar{d}_k := \begin{bmatrix} T_{in} \\ F \\ \rho_{in} \end{bmatrix}_k, \quad \bar{u}_k := \begin{bmatrix} Q \\ V \end{bmatrix}_k, \quad \bar{y}_k := \begin{bmatrix} T \\ P \\ \rho \\ y \end{bmatrix}_k$$

In subsequent discussions we refer to this as the identified state model. Note the distinction between the output measurement vector \bar{y}_k and the scalar vapor mole fraction y (Table 4.1).

Chemical process models can readily accept upstream conditions as measured disturbances. These can be incorporated into the state space by appending the state vector:

$$\begin{bmatrix} \bar{d}_{k+1} \\ \bar{x}_{k+1} \end{bmatrix} = \begin{bmatrix} I & 0 \\ B_d & A \end{bmatrix} \begin{bmatrix} \bar{d}_k \\ \bar{x}_k \end{bmatrix} + \begin{bmatrix} 0 \\ B \end{bmatrix} \bar{u}_k \quad 4.29$$

$$\begin{bmatrix} \bar{d}_k \\ \bar{y}_k \end{bmatrix} = \begin{bmatrix} I & 0 \\ 0 & C \end{bmatrix} \begin{bmatrix} \bar{d}_k \\ \bar{x}_k \end{bmatrix} \quad 4.30$$

For clarity the appended state matrices are primed:

$$A' := \begin{bmatrix} I & 0 \\ B_d & A \end{bmatrix}, \quad B' := \begin{bmatrix} 0 \\ B \end{bmatrix}, \quad C' := \begin{bmatrix} I & 0 \\ 0 & C \end{bmatrix}$$

We refer to this structure as the appended state model.

The appended state model was subjected to c-optimal transform via interior-point optimization such that all disturbances and output measurements were aligned:

$$\begin{bmatrix} \vec{d}_{k+1} \\ \vec{y}_{k+1} \\ \vec{z}_{k+1} \end{bmatrix} = T^{-1} A' T \begin{bmatrix} \vec{d}_k \\ \vec{y}_k \\ \vec{z}_k \end{bmatrix} + T^{-1} B' \vec{u}_k \quad 4.31$$

$$\begin{bmatrix} \vec{d}_k \\ \vec{y}_k \end{bmatrix} = \begin{bmatrix} I & 0 \end{bmatrix} \begin{bmatrix} \vec{d}_k \\ \vec{y}_k \\ \vec{z}_k \end{bmatrix} \quad 4.32$$

We refer to this model as the aligned state model.

It was assumed that vapor composition measurement, although used for model identification, would be unavailable or unreliable during routine process operation. An observer for the aligned model was built by expanding \vec{z}_k to include vapor composition y :

$$\vec{z}_k := \begin{bmatrix} y \\ z \end{bmatrix}_k \quad 4.33$$

Again, vapor composition y and the measurement output vector \vec{y}_k were distinct. The resultant inferential model excludes vapor composition as a measured output, but otherwise retains all matrices of the aligned state model:

$$\vec{y}_k := \begin{bmatrix} T \\ P \\ \rho \end{bmatrix}_k \quad 4.34$$

The Luenberger gain was designed to place the two estimator eigenvalues (poles) at 7.5/seconds, with a 10 second process sampling interval.

4.3.3 Aligned Model Performance and Conditioning in Inferential Estimation

The model identification procedure from Figure 4.2 was performed 100 times for the Monte Carlo analysis of c-optimality in state space transformation and model alignment. Error in composition estimation for the c-optimal aligned models and the unaligned appended models was evaluated. Figure 4.3 shows characteristic results for inferential composition measurement from a c-optimal aligned state model ($R^2=0.98$). Figure 4.4 shows R^2 and integral squared error values for vapor composition estimates across all 100 aligned state models. Overall, when c-optimality was used to build models for vapor composition estimation $R^2 = 0.68\pm 0.05$ and integral squared error was 0.31 ± 0.04 . Select aligned state models accurately predicted vapor composition (Figure 4.3) while other attempts at reduced order estimation were wholly inaccurate (Figure 4.4).

To gauge the success of inferential estimation with the aligned state models, the unaligned appended state models were also used for vapor composition prediction. Here, estimator construction followed the Sylvester Equation [92]. For comparability with the aligned state models, eigenvalues of the Sylvester estimators matched those from pole placement via the Luenberger gain. Figure 4.4 shows similar vapor composition estimation via c-optimal aligned models with Luenberger estimators and the unaligned models with Sylvester observers. When the models were unaligned, the average R^2 of 0.70 ± 0.05 and integral squared error of 0.35 ± 0.05 were statistically indistinct the aligned state spaces ($p=0.36$ and $p=0.183$ respectively). This suggests that c-optimality is likely a tractable means of model alignment for inferential estimation.

The identified state models, found through n4sid subspace identification [88], featured consistently low condition numbers. Interestingly, model conditioning deteriorated considerably when the identified state models were recast as an appended state models. Figure 4.5 shows condition numbers for the identified state models, the appended state models, and the aligned state models. Condition number of the state transition matrix was greatly improved after c-optimal transformation into an aligned state form. Indeed, frequently condition numbers of the aligned state models were lower than those of their corresponding identified state models. However, in four instances c-optimality could not recondition the appended state model ($\text{cond}(T^{-1}AT) > 100$). Although a weak metric [106], all models showed full rank of the observability matrix.

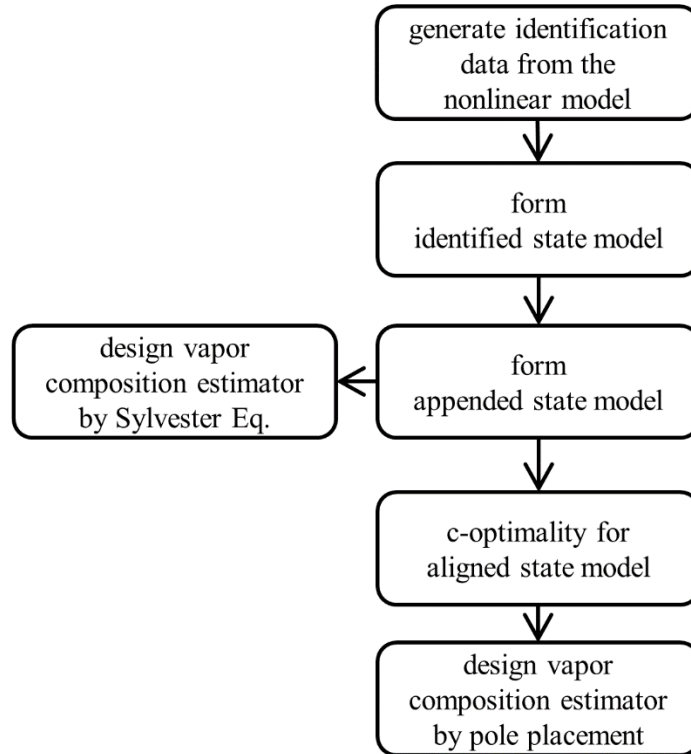


Fig. 4.2: Workflow for each Monte Carlo simulation. Identification data was generated by pseudorandom binary sequences on the nonlinear process model inputs and disturbances, then fit to a state space model for inferential vapor composition determination.

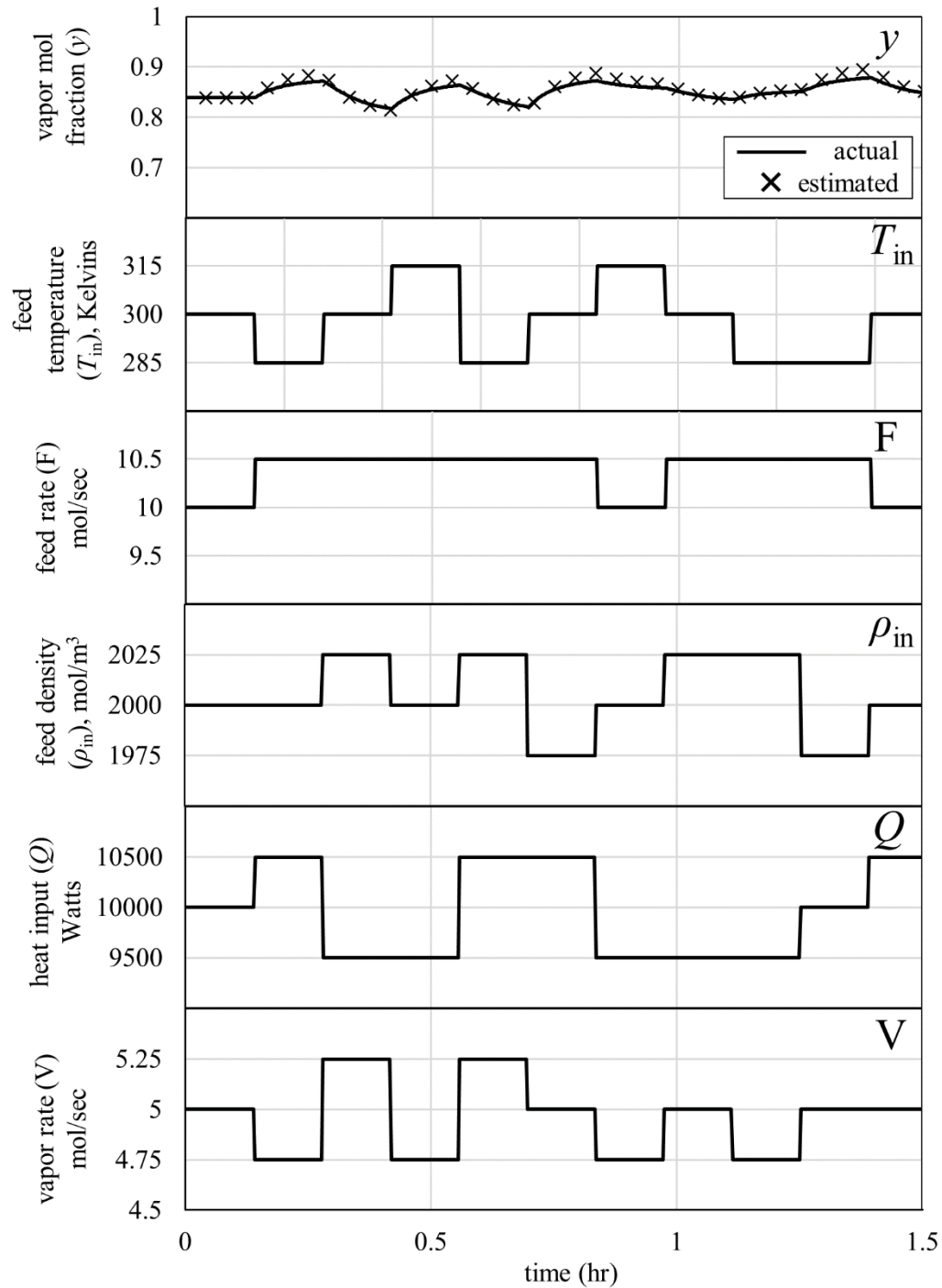


Fig. 4.3: Illustrative case of vapor inferential composition determination from an aligned state model for manipulations in the process inputs and disturbances ($R^2 = 0.98$).

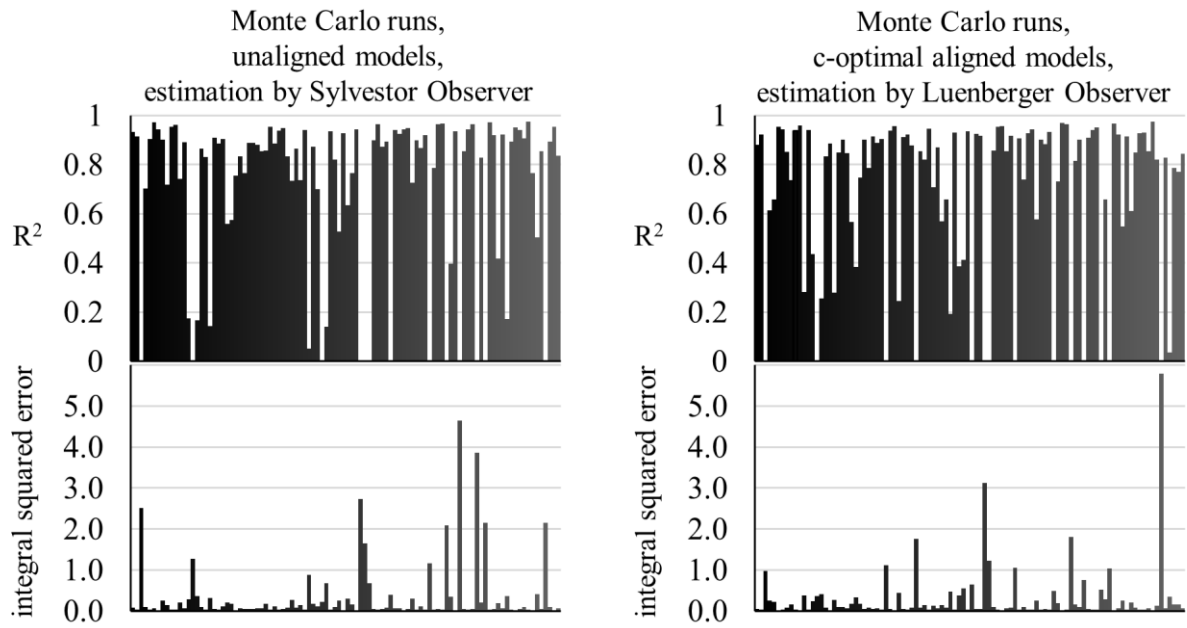


Fig. 4.4: Measures of success and failure in inferential composition measurement across all the generated state space models. Estimation proceeded via pole placement on the aligned state models, or Sylvester estimation on the appended state models.

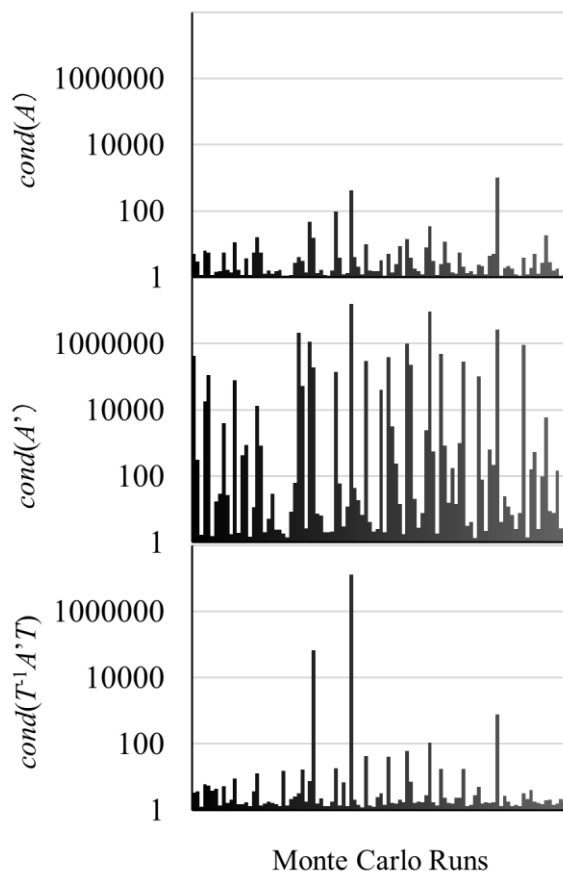


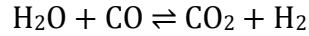
Fig. 4.5: Condition numbers across all generated state space models; top shows condition number of the identified model forms, middle shows condition number of the appended model forms, and bottom shows condition number of the aligned model forms.

4.4 c-Optimality Preserves State Tracking for Accurate Process Forecasting

4.4.1 Experimental Carbon Gasifier

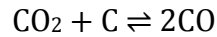
An experimental carbon gasifier was used to validate the c-optimal model alignment technique, especially with respect to accurate state tracking for process forecasting. Figure 4.6 shows the gasifier P&ID, which included upstream MKS GE50A mass flow controllers for gas metering and a downstream MKS T3Bi valve for pressure regulation at 0.9 bar. As in industrial gasification [107], steam injection at high temperature drove the oxidation of carbon for hydrogen generation:





$$\Delta H = -41 \text{ kJ/mol}$$

Specifically, steam was provided to the carbon by a heated bubbler and 1.5 L/min of argon sweep gas. The 0.600 kg carbon bed (Figure 4.6) was maintained at 925° C in a heated vertical tube furnace whose thermal mass (15.25 kg) mitigated temperature transients. Additionally, carbon dioxide flowed through the system and split into carbon monoxide:



$$\Delta H = 183 \text{ kJ/mol}$$

The batch system showed a pseudo steady-state where 0.3 L/min of hydrogen was produced at a H₂:CO ratio of 0.9:1, as determined by a NOVA N4X gas analyzer.

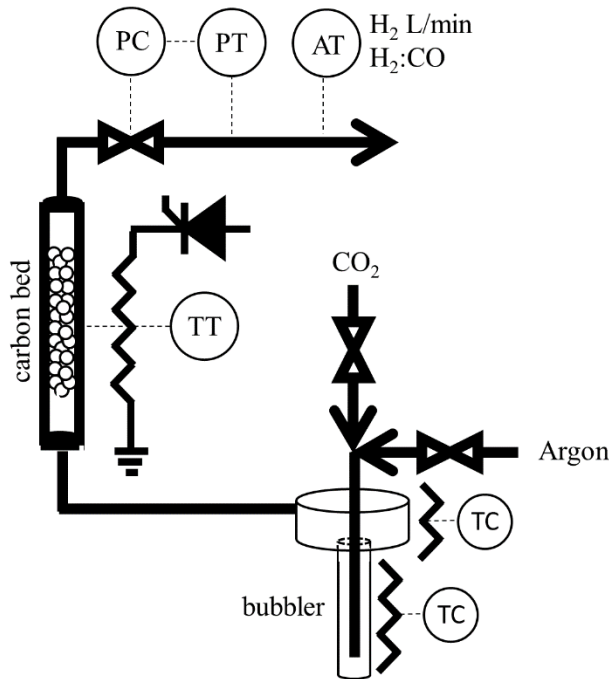


Fig. 4.6: Gasifier experimental apparatus. The pressure controller was characterized and tuned as described by Lee et al. [108]. Bubbler temperature controllers were characterized and tuned by internal model control for a 1st order plus deadtime process. PC refers to pressure controller, PT refers to pressure transducer, AT refers to analytical transducer, TT refers to temperature transducer, and TC refers to temperature controller.

4.4.2 State Space Modeling and Alignment for Forecasting in the Carbon Gasifier

Figure 4.7 shows the system response to changes in bubbler temperature and carbon dioxide flowrate. Transfer function models (1st order plus time delay) were fit to operating data for hydrogen production and H₂:CO ratio via interior point optimization:

$$Y(s) = \begin{bmatrix} \frac{0.015e^{-\frac{5}{3}s}}{14s+1} & \frac{-1e^{-\frac{5}{3}s}}{0.5s+1} \\ \frac{0.011e^{-\frac{5}{3}s}}{7s+1} & 0 \end{bmatrix} U(s) \quad 4.35$$

Where:

$$\vec{y}(t) = \begin{bmatrix} \Delta(L/min H_2) \\ \Delta(H_2 : CO) \end{bmatrix}, \quad \vec{u}(t) = \begin{bmatrix} \Delta(^{\circ}C bubbler) \\ \Delta(L/min CO_2) \end{bmatrix}$$

The transfer function was converted to a minimal discrete time state space for predictive control applications with a 20 second sample interval [101]:

$$\vec{x}_{k+1} = \begin{bmatrix} 0.9765 & 0 & 0 \\ 0 & 0.9535 & 0 \\ 0 & 0 & 0.5134 \end{bmatrix} \vec{x}_k + \begin{bmatrix} 0.0772 & 0 \\ 0.0763 & 0 \\ 0 & 3.6494 \end{bmatrix} \vec{u}_k \quad 4.36$$

$$\vec{y}_k = \begin{bmatrix} 0.0046 & 0 & 0 \\ 0 & 0.0067 & -0.1333 \end{bmatrix} \vec{u}_k \quad 4.37$$

The state space was then subjected to c-optimal transformation for model alignment, leaving a single opaque state, $\vec{z} = z$:

$$\begin{bmatrix} \vec{y} \\ \vec{z} \end{bmatrix}_{k+1} = \begin{bmatrix} 0.97 & 0 & 0 \\ 0 & 0.5134 & 0.0033 \\ 0 & 0.0033 & 0.59535 \end{bmatrix} \begin{bmatrix} \vec{y} \\ \vec{z} \end{bmatrix}_k + \begin{bmatrix} 0.0004 & 0 \\ 0.0004 & 0.4866 \\ 0.0692 & 0.0036 \end{bmatrix} \vec{u}_k \quad 4.38$$

$$\begin{bmatrix} \vec{y} \\ \vec{z} \end{bmatrix}_k = \begin{bmatrix} 1 & 0 & 0 \\ 0 & 1 & 0 \end{bmatrix} \begin{bmatrix} \vec{y} \\ \vec{z} \end{bmatrix}_k \quad 4.39$$

The associated Luenberger estimator featured a pole at 0.95.

4.4.3 Model Alignment Performance in Process Forecasting

Successful process forecasting hinges on accurate state estimation. To evaluate the performance of state estimation by c-optimal aligned process models, the experimental gasification process was subjected to step changes in the inputs. Figure 4.8 shows how bubbler temperature and carbon dioxide flow rate were manipulated over the course of 80 minutes. Every five minutes the current state estimate, based off estimation on the c-optimal aligned model, was used to predict future process movement given planned changes in the inputs. Overall, the forecasts were highly accurate despite constant process movement and noisy measurements (Figure 4.8). Notably, the inputs were manipulated between their actuator extremes at maximum slew.

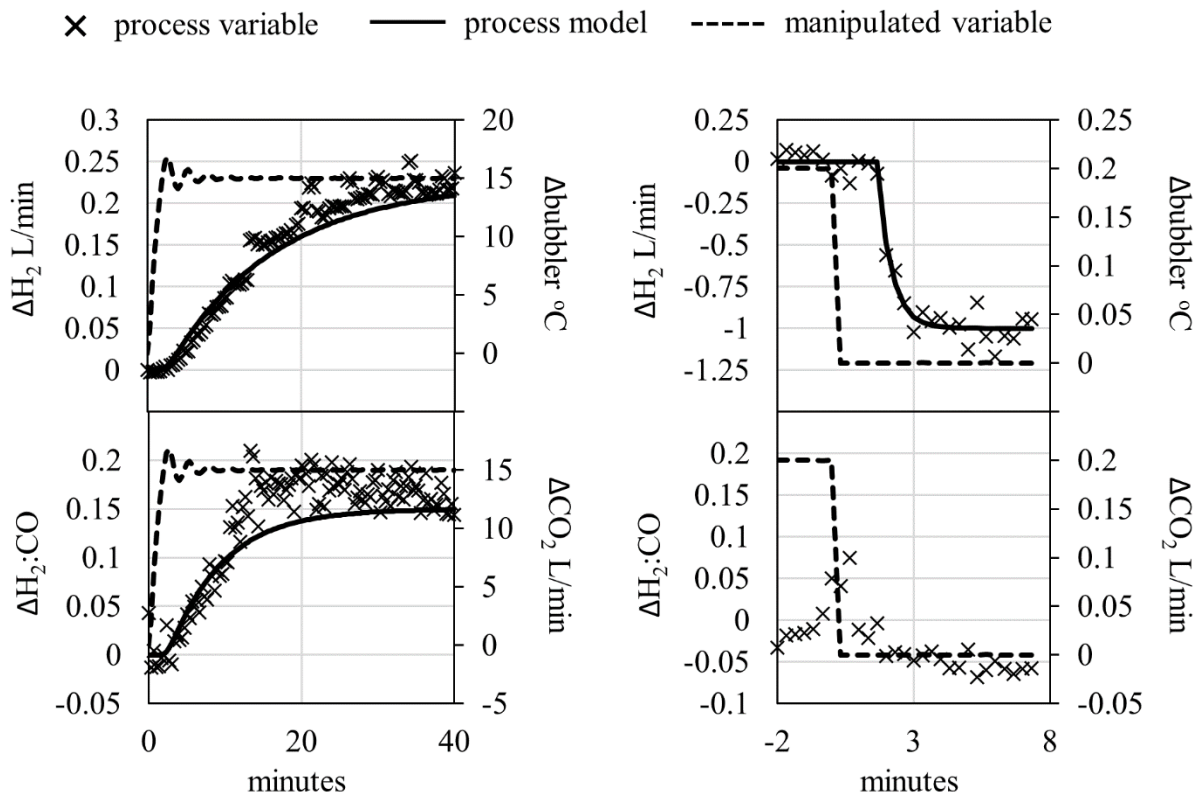


Fig.4.7: Model identification of the experimental gasifier.

4.5 Conclusion

C-optimality was proposed to enhance the input-output correspondence of state space models. Within this regime the state space is transformed such that states and output measurements are equated. In selecting the necessary transform, condition number of the state transition matrix A was minimized. The resultant models benefit reduced state estimation with a Luenberger observer, which was shown using simulation and experimental examples common to the chemical process industries. Namely, the state space was aligned for inferential composition measurement in a chemical separation and process forecasting in a chemical reaction. In simulations Monte Carlo analysis showed that, c-optimality restored system conditioning after manipulations that degraded numerical properties of the original model. Furthermore, aligned models could faithfully track an unmeasured system output similar to tracking by an advanced technique [92]. State tracking with c-optimal aligned models was accurate in a gasification reaction, where a c-optimal aligned model successfully predicted future process trajectories based on the current state estimate. However, we caution against the naive use of c-optimality because, although the technique worked in these chemical engineering case studies, its success may be situation dependent and likely requires application specific development.

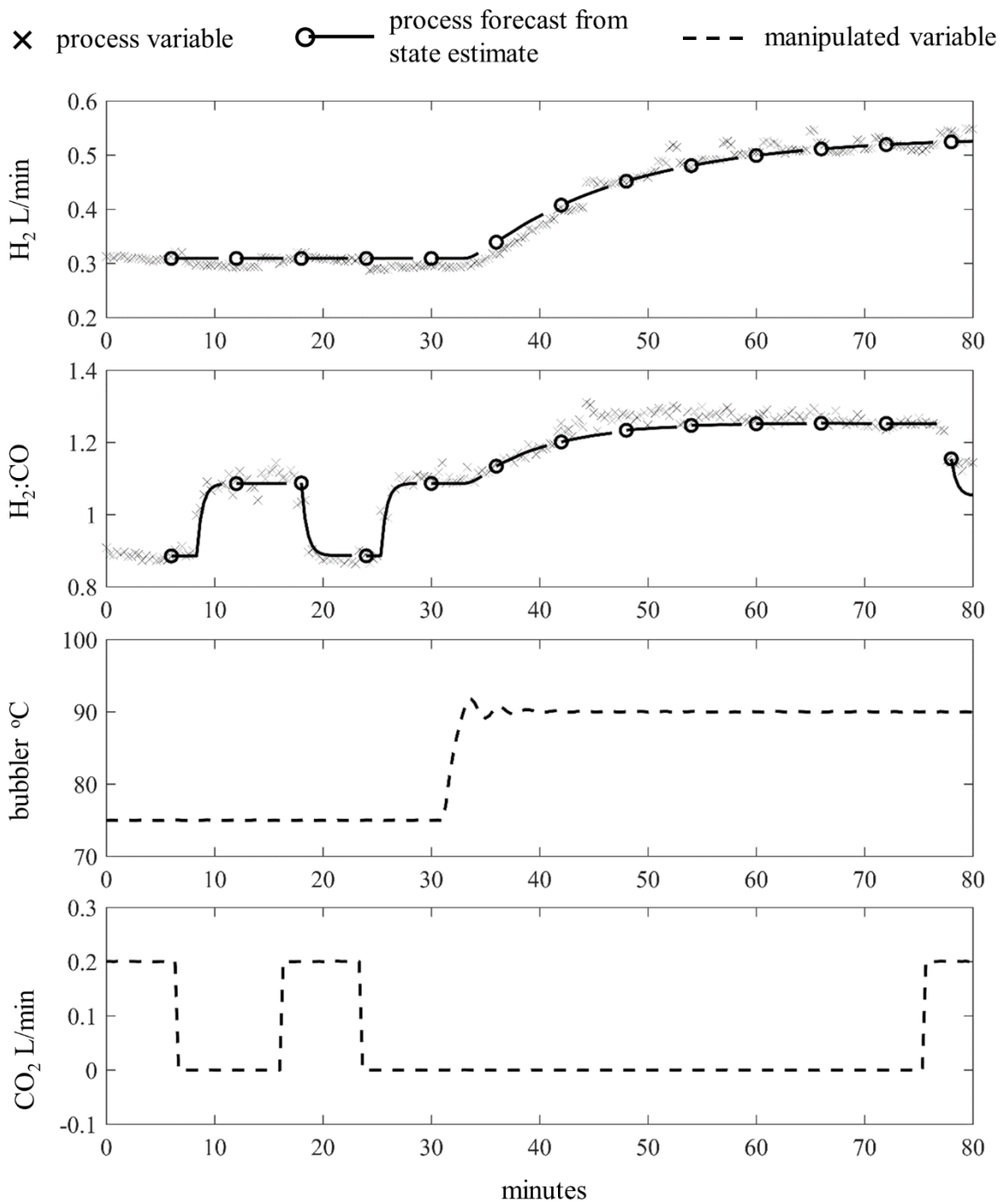


Fig. 4.8: Output forecasts based on the current state estimate from the c-optimal model and planned input action.

Chapter 5: Can Linear Models, with Forecasting, Achieve Solar-Electric Control?

5.1. Solar-Electric Reactor Design

A prototype reactor, envisioned for operation on a power tower (Chapter 1), was fabricated for use in solar-electric control studies. Figure 5.1 and Figure 5.2 show the device, which closely approximated a design built at the Swiss Federal Institute of Technology [109, 110]. As in prior work [109-111], the reactor contained a single vertical transport tube housed within an insulated cavity. A cavity-mounted Type B thermocouple was available for reactor temperature control. Unlike previous studies, the reactor cavity included six molydisilicide heating elements capable of supplying electrical heat at temperatures up to 1700° C (3100° F). Furthermore, the reactor featured a water cooled jacket, which pinned exterior insulation temperatures at approximately 15° C. In experiment light from high-flux solar simulator lamps entered the cavity through concentrating optics, whereas in practice sunlight would be funneled into the reactor from heliostats.

The inclusion of concentrating optics to harvest light from a high-flux solar simulator is inconsistent across the academic literature [109, 111-114]. Thus, a design study was pursued to guide the construction of polished aluminum optics for the new solar-electric reactor. Figure 5.3 shows how variations in the acceptance angle and inlet diameter of the concentrating optics, a compound paraboloid [115], effected light ingress into the reactor cavity. Net energy into the reactor was dependent on cavity conditions, given that high temperatures can cause thermal reradiation. This effect was included by tracing view factors for emissive losses from the reactor to the wider environment [50, 116]. Notably, although the optical design was sensitive to inlet diameter, acceptance angle of the compound paraboloid had negligible effects on light entry (Figure 5.3). Lamp light was already tightly focused by the high-flux solar simulator (Chapter 2),

which suggests that acceptance angle and concentrating optics were dispensable in this reactor design. To confirm these simulation results a compromise optical design, with an acceptance angle of 45° and inlet aperture of $\varnothing 8$ cm, was fabricated and polished to specularity. Before use on the reactor, this water cooled aluminum device (Figure 5.4) was mounted on a calorimeter for solar measurement [62, 116]. Measurements in Figure 5.5 show that the concentrating optics failed to funnel additional light relative to a $\varnothing 8$ cm aperture mounted on the calorimeter. These results indicate that concentrating optics, although likely useful at commercial scale, are unnecessary in experiments on tightly focused high-flux solar simulators.

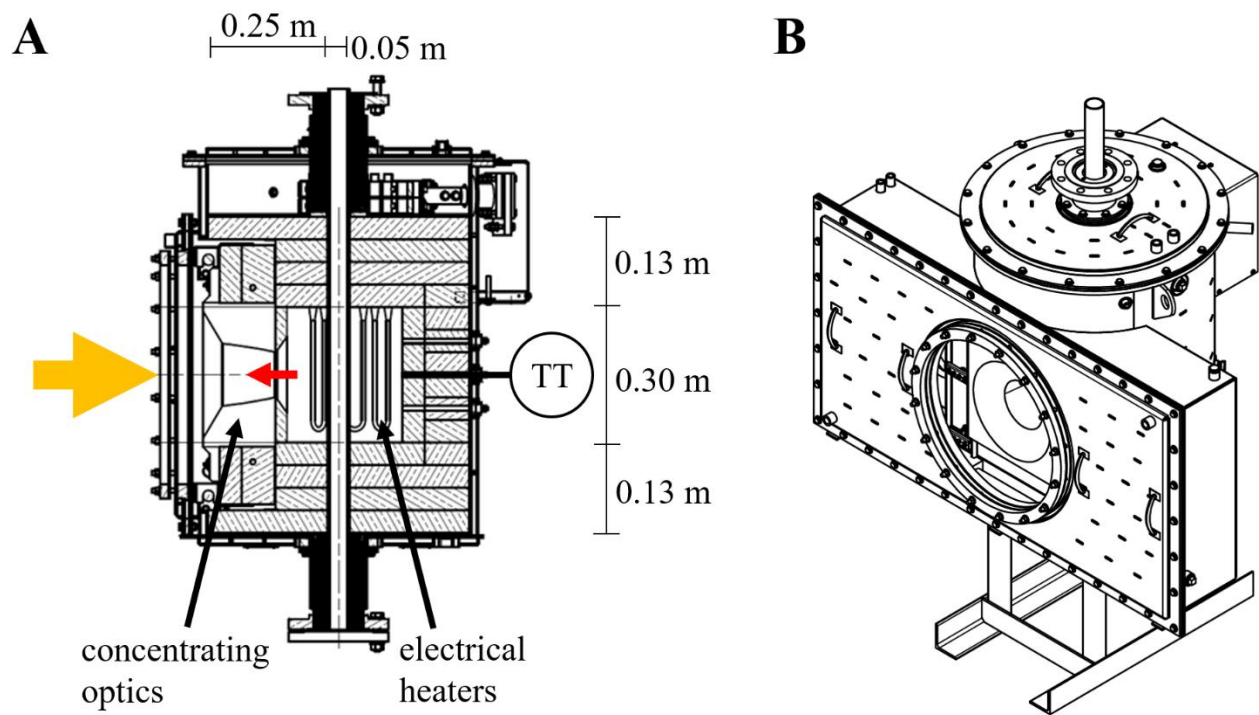


Figure 5.1: A) Cutaway of the solar-electric reactor. The orange arrow represents solar entry while the red arrow represents thermal reradiation. TT indicates temperature transducer (b-type thermocouple). B) Rendering of the solar-electric reactor.



Figure 5.2: The fully fabricated solar-electric reactor at the focus of high-flux solar simulator lamps.

5.2. Solar-Electric Reactor Modeling

To assist the design of solar-electric controllers, a dynamic model of the solar-electric reactor was formulated and coded in Matlab. The radially symmetric reactor design was represented in finite volume simulation in full cylindrical coordinates and integrated through time with the method of lines [117]. The resultant model featured thermal conduction, radiative forcing from ray tracing simulation (Chapter 2), lumped convection to the ambient air, electrical forcing, and radiative exchange via traced view factors (Chapter 1 and 2) [50]. A stainless steel water cooled jacket enveloped the reactor, which fixed exterior insulation temperatures at $\sim 15^{\circ}$ C based on observed average coolant temperatures in experiment. Thermal conductivity, density, and heat capacity of the 310 stainless steel reactor tube were taken from the literature [118-121]. Temperature dependent heat capacity of the alumina insulation was also literature sourced [57] and fit to the Hill Equation (Appendix C). The mesh granularity was increased until the simulation time reflected realtime (3344 element mesh), where rapid computation was considered more practical for controls development relative to model precision. Five parameters were fitted to operating data from the solar-electric reactor for steps in solar or electric heat (Figure 5.7). Figure 5.6 shows the model after interior-point optimization to minimize the squared error between temperature data

from the furnace thermocouple and temperature predictions. Figure 5.7 shows the final model parameters, which included the insulation emissivity, the tube emissivity, the insulation density, the insulation thermal conductivity, and the cavity convective heat transfer coefficient. Estimated values of emissivity were high and may represent effective emissivity, versus physical emissivity of the actual materials.

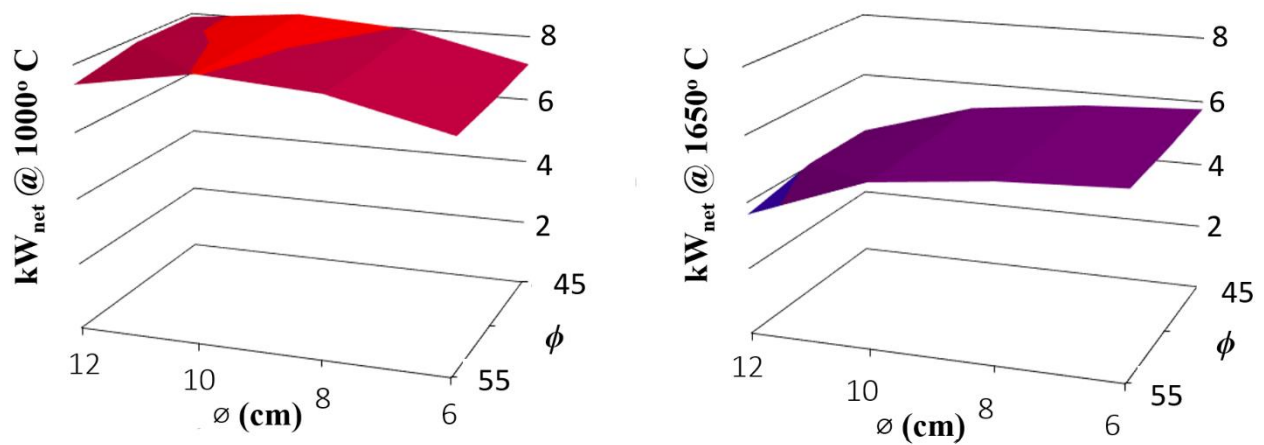


Figure 5.3: Net power into the solar-electric reactor for operation at two cavity temperatures and a range of outlet diameters and acceptance angles ϕ . Traces were for all eighteen high-flux solar simulator lamps at 90 amps (40.5 kW).

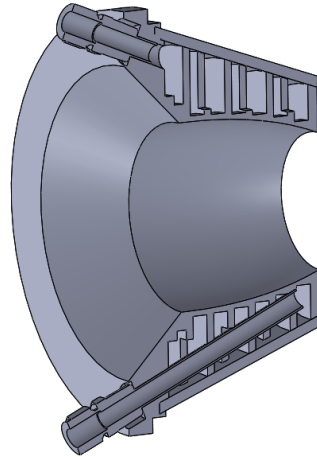


Figure 5.4: Rendering of the compromise optics design for light entry into the solar-electric reactor. Channels are for water cooling. See also Figure 5.2. The compound parabolic section featured an acceptance angle of 45° , an inlet diameter of $\varnothing 11$, and an outlet of diameter of $\varnothing 8$ cm.

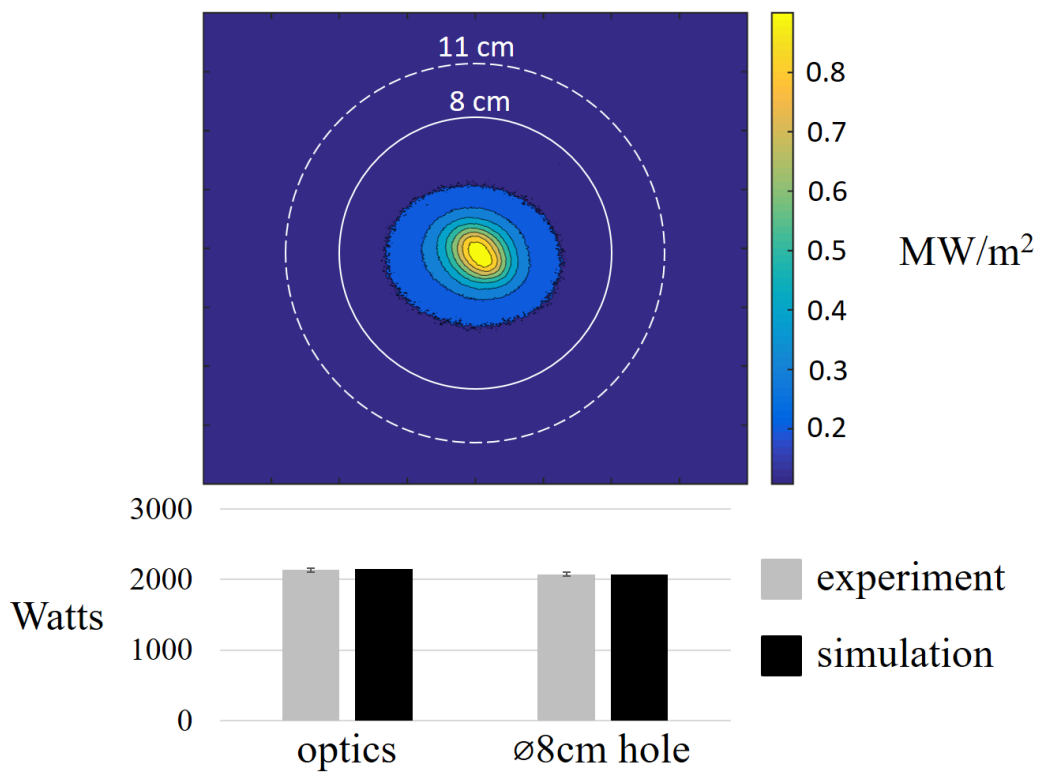


Figure 5.5: Experimental flux profile for six lamps operating at 70 amps (10.5 kW), as used in control experiments. The inlet (dashed line) and outlet (solid line) diameters of the concentrating optics are shown. The graph shows total optical power through the concentrating optics, or through an equivalent $\varnothing 8$ cm hole, as measured by a calorimeter (Chapter 2 and 3).

5.3 Solar-Electric Reactor Chemistry and Distributed Control System

The thermochemical conversion of solid carbonaceous feedstocks using solar-thermal reactor systems represents a promising pathway for storing renewable energy as chemical energy [9]. One thermochemical conversion process, gasification, has served as a testbed for solar-thermal system control in at least five previous studies (Table 1.2) [22]. In this process carbonaceous feeds are converted to H₂ and CO with steam, an endothermic reaction that can be driven allothermally with solar heat or autothermally through oxygen combustion of the feedstock [22]. At commercial scale the resultant H₂/CO product mixture (syngas) can be converted to a range of chemicals or commodity fuels via subsequent processing. If bio-based feedstocks are employed, gasification has the potential to supplant conventional fossil fuel supplies [122]. However, successful solar-thermal processing requires a steady syngas flow with an H₂/CO ratio tailored to downstream equipment that converts gases to fungible liquid products [123-126]. Flowrate manipulation, which has been previously used for the control of solar-thermal syngas production, may be incompatible with the needs of gas-to-liquid reactors and distillation trains. Conversely, solar-electric control has the potential to minimize flowrate disturbances by maintaining process temperatures, which are a proxy for product rate and composition [22].

To test solar-electric control strategies the reactor system was instrumented for carbon gasification. Table 5.1 lists composition of the feedstock, a highly pure activated carbon for minimal reactor fouling over the course of experiments. Figure 5.8 shows how 1.5 L/min of argon sweep flow delivered steam from a 2 L bubbler to the 600 gram carbon bed inside a \varnothing 5 cm 310 stainless steel reaction tube situated within the solar-electric reactor cavity. The bubbler, line heaters, and MKS T3Bi throttle valve were subjected to step tests for process modeling with

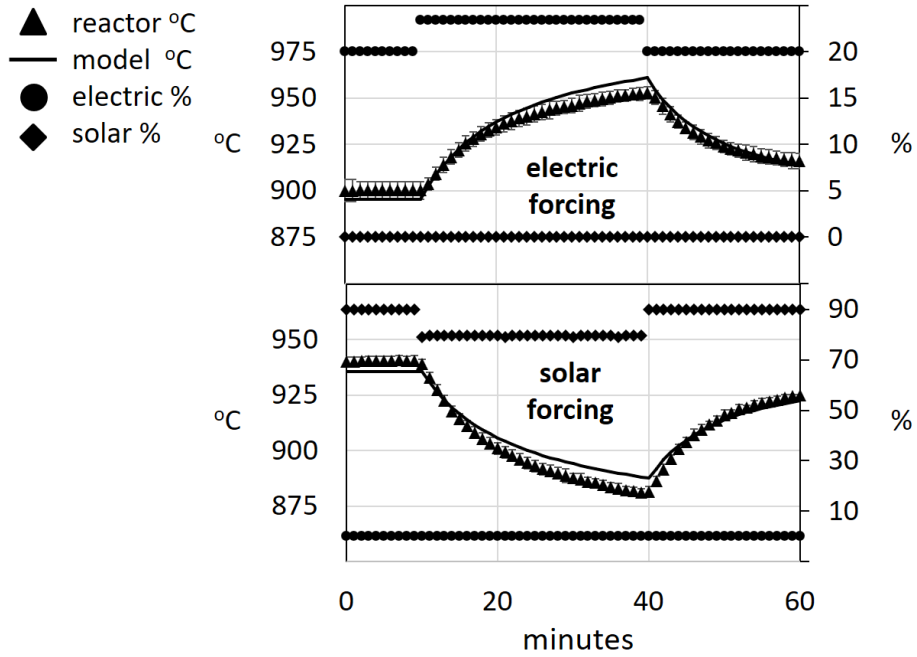


Figure 5.6: Finite volume model fit to temperature data from the solar-electric Type B thermocouple in reactor steps tests in electric heat (top) or solar heat (bottom).

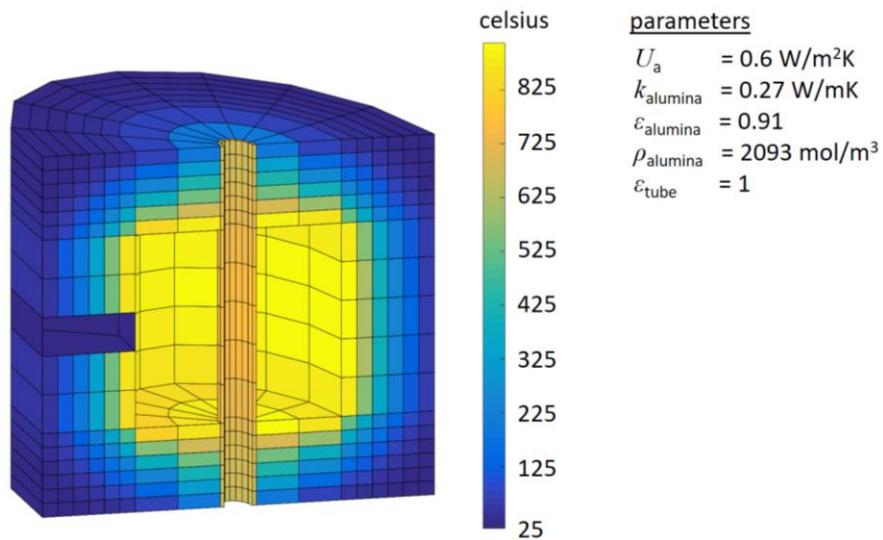
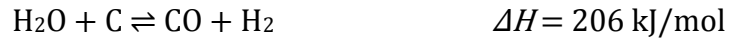


Figure 5.7: Depiction of and fitted parameters in the solar-electric reactor finite volume simulation.

transfer functions (Figure 5.9). Feedback PID tuning parameters for line heater and bubbler temperature regulation were then chosen by internal model control with $\tau_c = \tau_p/2$ [127]. A PI controller for pressure regulation at 0.9 bar was designed according to the tuning recommendations of Lee et al. [108]. In addition to argon, 0-0.3 L/min of CO₂ could flow through the system. Thus, three chemical reactions were likely active in the solar-electric reactor:



The relative gain array indicated that CO₂ flow could control of H₂/CO ratio [128], which was maintained at 1/1, while bubbler temperature could control overall syngas productivity, which was maintained at 0.3 L/min. To pair these manipulated and controlled variables distributed PI feedback was implemented with internal model control tunings ($\tau_c = \tau_p/2$) [127].

Table 5.1: Ultimate (dry and ash free), proximate, and heating value (as received) analyses for activated carbon used in solar-electric experimentation.

<i>Component</i>	<i>wt%</i>	<i>mol%</i>
C	94.24%	92.30%
H	< 0.55%	< 0.05%
O	4.25%	5.54%
N	0.27%	0.31%
S	0.69%	1.80%
Fixed Carbon	85.21%	
Volatile Matter	3.40%	
Loss of Drying	0.31%	
Ash	11.08%	
LHV [MJ/kg]	28.64	

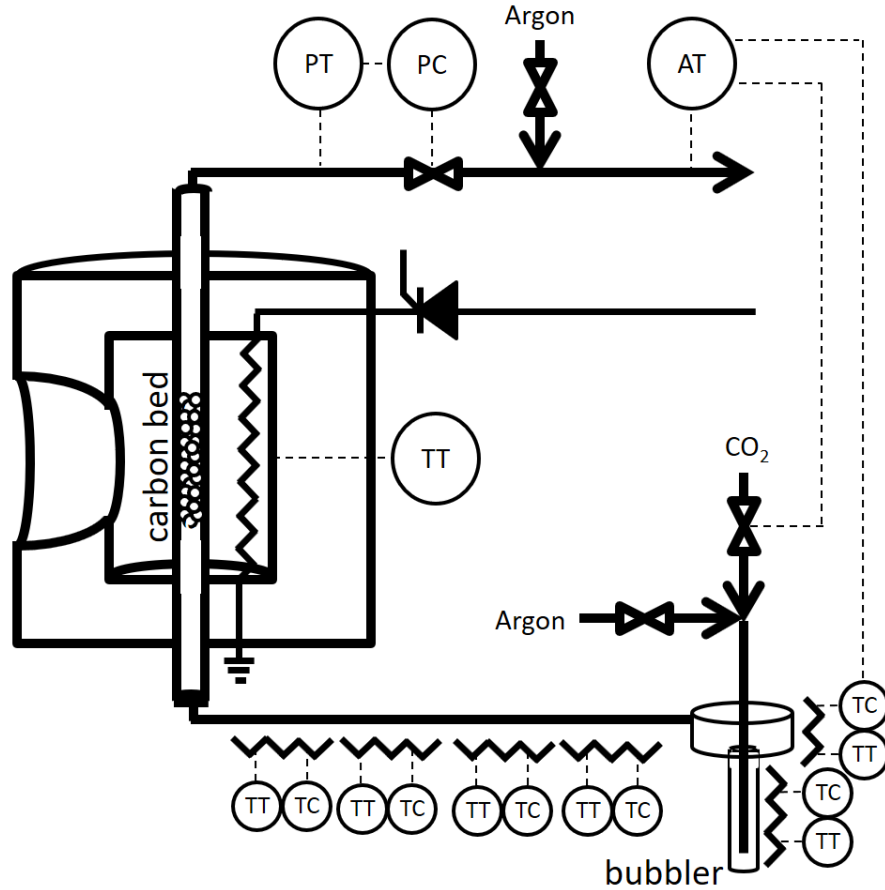


Figure 5.8: distributed control system for gasification studies on the solar-electric reactor. PT is pressure transducer, PC is pressure controller, AT analytical transducer, TT is temperature transducer and TC is temperature controller.

5.4. Solar-Electric Control Strategies and Tuning

5.4.1 Control Architectures

Given the potential for destructive thermal shock and fatigue in concentrated solar facilities, solar-electric reactor temperature control regimes of varied sophistication were evaluated. Although solar heat and chemical processing are highly nonlinear, only linear controllers were explored given their online tractability [89]. Figure 5.10 shows the tested control architectures. First feedback controllers were built and tested with and without of feedforward action from the solar disturbance, d_k [129]:

$$\Delta u_k = K_C \left[(e_k - e_{k-1}) + \frac{\Delta t}{\tau_I} e_k + \frac{\tau_D}{\Delta t} (e_k - 2e_{k-1} - e_{k-2}) \right] - \frac{K_p}{K_d} \Delta d_k \quad 5.1$$

Here, Δu_k is the change in electrical duty applied to the system at time k (0-15 kW), e_k is the temperature setpoint departure at time k and d_k is the solar disturbance at time k (0-15 kW). K_p and K_d were the process and disturbance gains identified from 1st order transfer function models fit to reactor step tests (Figure 5.6) [127]. The sampling interval, $\Delta t = 25$ seconds, was constrained by the rate of information acquisition from the experimental equipment.

Based on the success of prior model predictive controllers in solar furnace temperature regulation (Table 1.1), a linear model predictive controller was built for the solar-electric reactor. Figure 5.11 summarizes trajectories relevant to the predictive control architecture. In brief, a minimal state space model of the reactor system was distilled from 1st order transfer function models built off system step responses (Figure 5.6) [101]. The resultant 2nd order discrete time state space assumed the following form:

$$\bar{x}_{k+1} = A\bar{x}_k + [B_d \quad B] \begin{bmatrix} d_k \\ u_k \end{bmatrix} \quad 5.2$$

$$y_k = C\bar{x}_k \quad 5.3$$

Here, a 2x1 vector \bar{x}_k was needed to propagate system dynamics through the 2x2 state transition matrix A . The output transition matrix C converts the state into the system deviation temperature y_k . B_d and B form a block matrix that describes how the solar disturbances d_k and electrical duty u_k impinge on the system state (dynamics). For convenience, c-optimality was used to align the model as described in Chapter 4.

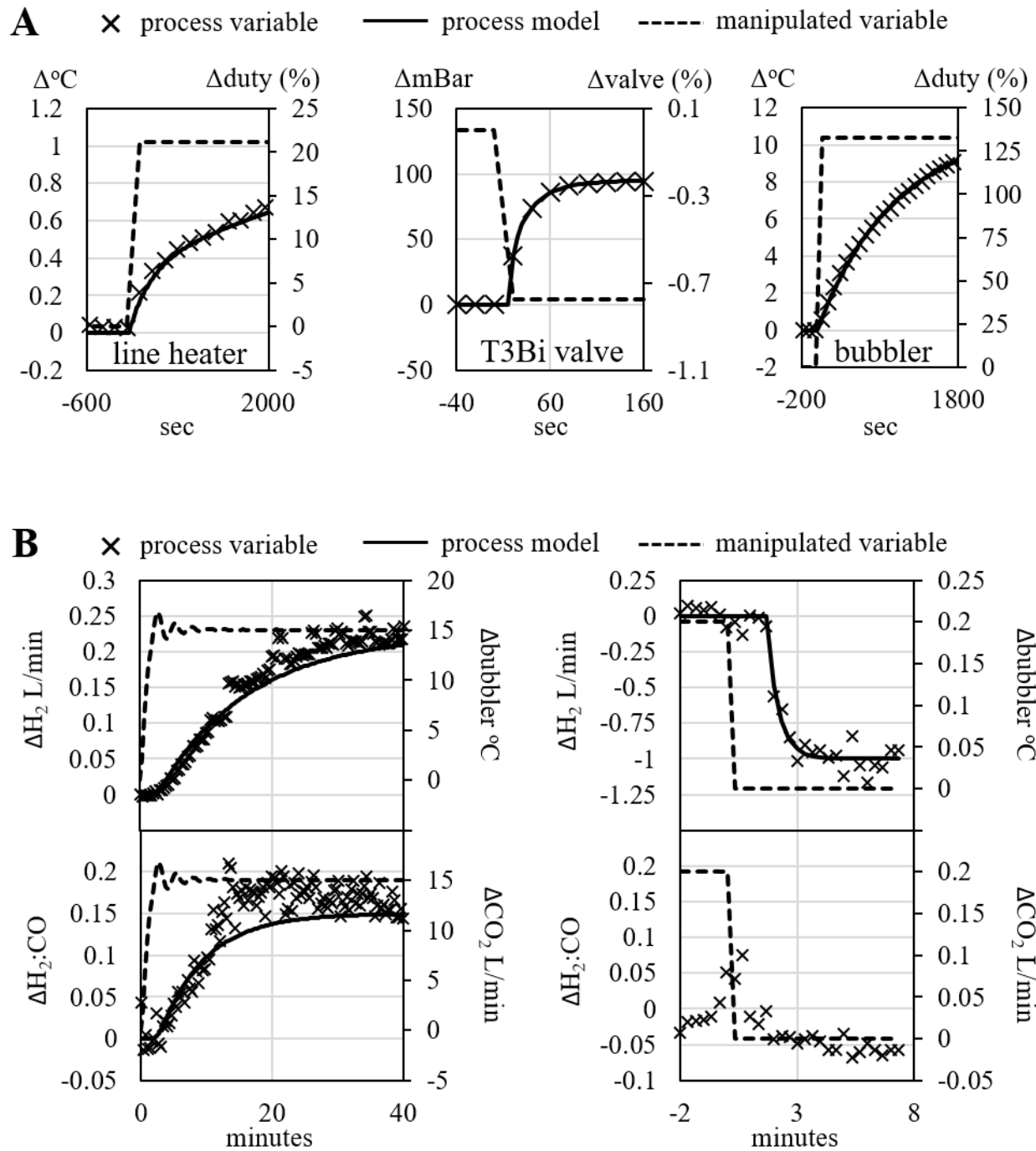


Figure 5.9: A) Step tests and transfer function modeling for pressure and heater control. B) Step tests and transfer function modeling for gasification control.

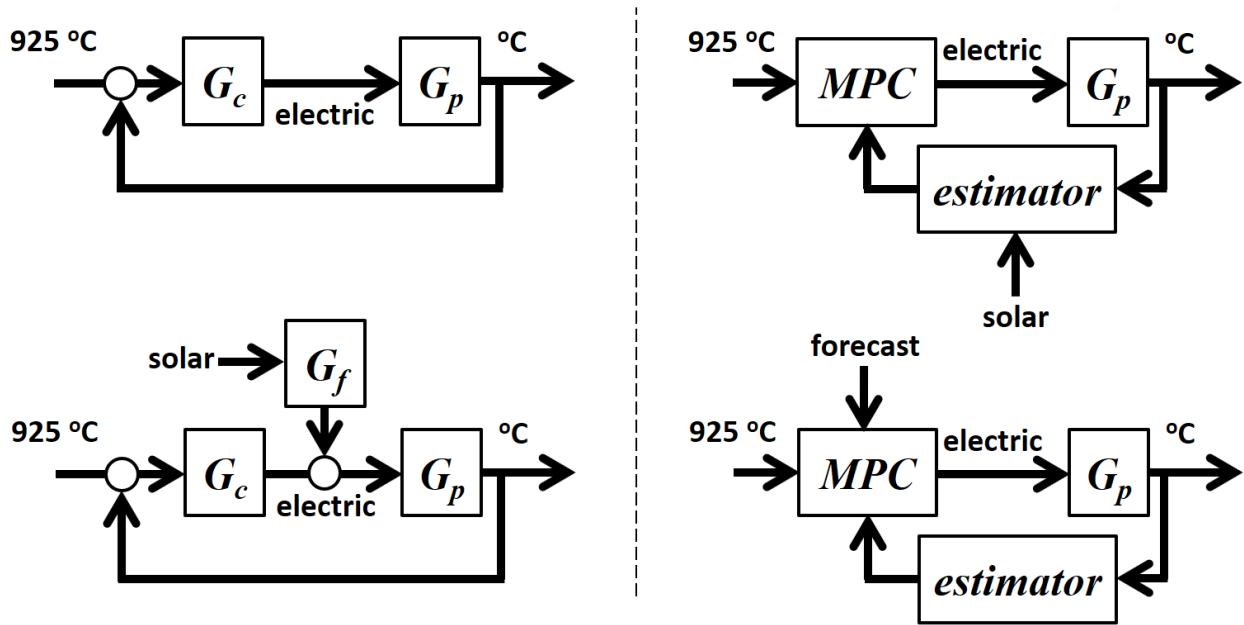


Figure 5.10: Feedback controller architectures (left) and model predictive controller (MPC) architectures (right) implemented for the solar-electric temperature regulation in experiments.

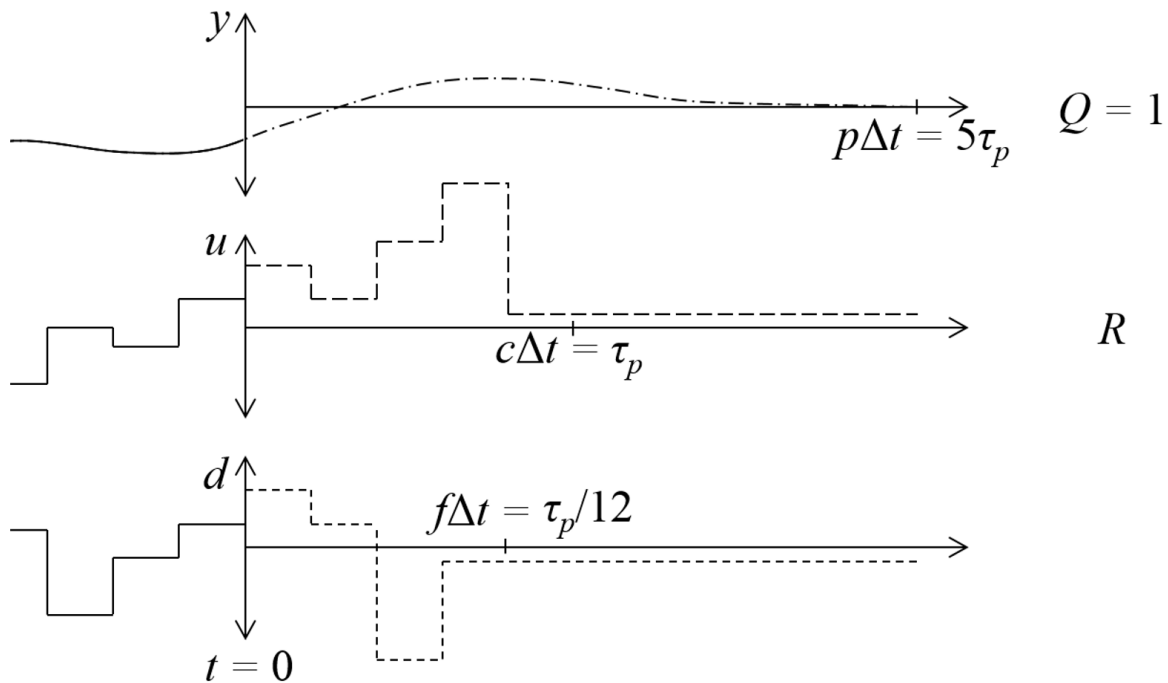


Figure 5.11: Trajectories relevant to the model predictive controller. y is the controlled variable (temperature) which can be tuned by an output weight matrix Q . In this work, $Q = 1$. u is the manipulated variable (electric heat), which can be tuned by the move suppression matrix R . d is the disturbance variable (solar heat). The horizon lengths are p (prediction), c (input), and f (disturbance), which were multiples of the dominant process time constant τ_p in experiment.

The model was converted to an observer form for use with a state estimator and cast into velocity mode for enhanced controller integral action [94, 95]:

$$\begin{bmatrix} \Delta \bar{x}_{k+1} \\ y_{k+1} \end{bmatrix} = \tilde{A} \begin{bmatrix} \Delta \bar{x}_{k+1} \\ y_k \end{bmatrix} + \begin{bmatrix} \tilde{B}_d & \tilde{B} \end{bmatrix} \begin{bmatrix} \Delta d_k \\ \Delta u_k \end{bmatrix} \quad 5.4$$

$$y_k = \tilde{C} \begin{bmatrix} \Delta \bar{x}_k \\ y_k \end{bmatrix}, \quad \tilde{C} = [0 \quad 0 \quad 1] \quad 5.5$$

The model predictive controller assumed a standard quadratic form with the output weight matrix $Q = 1$ [127]:

$$\Delta U = \arg \min Y^T Y + \Delta U^T R \Delta U \quad 5.8$$

Where $\Delta U^T = [\Delta u_k \quad \Delta u_{k+1} \quad \dots]^T$ for a control horizon of length c and $Y^T = [y_k \quad y_{k+1} \quad \dots]^T$ for a prediction horizon of length p . Figure 5.11 details the horizons used in model predictive control. The move suppression matrix R can moderate and detune controller aggression. The extended state space equations formed an objective function that was amenable to rapid solution by quadratic minimization [94, 95]:

$$\Delta U = \arg \min 2 \left(\begin{bmatrix} \Delta \bar{x}_k^T & y_k \end{bmatrix} \mathcal{G}^T H + S \Delta D^T P^T H \right) \Delta U + \Delta U^T (H^T H + R) \Delta U \quad 5.9$$

The linear term on ΔU depends only on the current state $[\Delta \bar{x}_k \quad y_k]^T$ and a weather forecast $\Delta D^T = [\Delta d_k \quad \Delta d_{k+1} \quad \dots]^T$ of length f . \mathcal{G} is the observability matrix. H and P are Teoplitz matrices on the state and forecast respectively [95]:

$$H = \begin{bmatrix} \tilde{C}\tilde{B} & 0 & 0 & \dots \\ \tilde{C}\tilde{A}\tilde{B} & \tilde{C}\tilde{B} & 0 & \dots \\ \tilde{C}\tilde{A}^2\tilde{B} & \tilde{C}\tilde{A}\tilde{B} & \tilde{C}\tilde{B} & \ddots \\ \vdots & \vdots & \ddots & \ddots \end{bmatrix} \quad P = \begin{bmatrix} \tilde{C}\tilde{B}_d & 0 & 0 & \dots \\ \tilde{C}\tilde{A}\tilde{B}_d & \tilde{C}\tilde{B}_d & 0 & \dots \\ \tilde{C}\tilde{A}^2\tilde{B}_d & \tilde{C}\tilde{A}\tilde{B}_d & \tilde{C}\tilde{B}_d & \ddots \\ \vdots & \vdots & \ddots & \ddots \end{bmatrix}$$

[95]. A sample time of $\Delta t = 30$ seconds was adopted to allow the use of forecasts within the model predictive controller, since forecasts were only available in 30 second gradations [130] (http://midcdmz.nrel.gov/srrl_bms/).

5.4.2 Controller Tuning

The feedback controller [129], without feedforward action, was tuned by minimizing simulated departures from a 925°C temperature setpoint on the solar-electric reactor. Three days of diverse weather from Sunspot 2 in Colorado [25], chosen by manual inspection, served as disturbances in the interior-point optimization (Nov 1st 2010, Jan 16th 2010, and May 20th 2009, http://midcdmz.nrel.gov/srrl_bms/) [130]. Figure 5.12 shows controller sensitivity to the PID tuning parameters K_c , τ_I and τ_D from these computations. The nonlinear process model indicated that the optimal tuning would be bounded and stable on the actual equipment. However, once online minor oscillations were observed, likely due to plant model mismatch and/or unseen delays in hardware. These oscillations that were eliminated by detuning the optimal controller gain K_c by 3X. Table 5.2 shows the final feedback controller parameters.

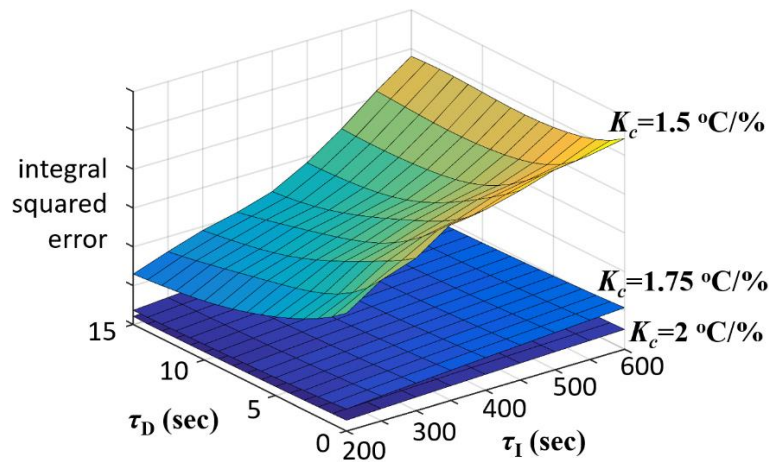


Figure 5.12: Relative feedback controller tuning effects on solar-electric temperature regulation.

Table 5.2

feedback controller parameters				
K_c	K_f	τ_I	τ_D	Δt
0.66 C° C/%	0.35 C° C/%	200 sec	0 sec	25 sec

Model predictive control relied on an estimate of the current facility state (dynamics). To track the facility state a Luenberger observer was designed that conservatively placed the estimator pole at 0.92 [95]. Standard values were chosen for the prediction ($p=5\tau_p/\Delta t$) and control ($c=\tau_p/\Delta t$) horizons. Move suppression within the predictive controller was then tuned without a forecast by minimizing simulated departures from a 925° C temperature setpoint on the solar-electric reactor. Again, three days of diverse weather from Sunspot 2 in Colorado served as disturbances in the interior-point optimization (Nov 1st 2010, Jan 16th 2010, and May 20th 2009, http://midcdmz.nrel.gov/srrl_bms/) [130]. Figure 5.13 shows controller sensitivity to move suppression in these computations. The nonlinear process model indicated that the optimal tuning would be bounded and stable on the actual equipment. However, as for the feedback controller minor oscillations were observed when the predictive controller was online. These oscillations were eliminated by detuning the move suppression factor R by 3X. Table 5.3 shows the final model predictive controller parameters.

Table 5.3

model predictive controller parameters					
c	p	f	Q	R	Δt
$\tau_p = 12$ min	$5\tau_p = 60$ min	$\tau_p/12 = 1$ min	1	100	30 sec

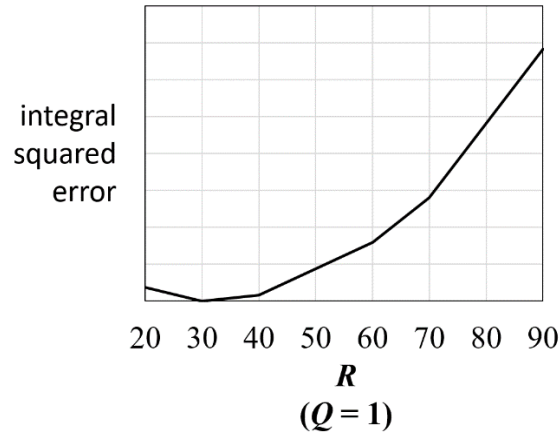


Figure 5.13: Relative model predictive controller tuning effects on solar-electric temperature regulation.

5.5 The Experimental Performance of Solar-Electric Control

To challenge the control architectures described in Section 5.4 a thirty minute solar transient was replicated on the high-flux solar simulator lamps. The chosen transient featured high frequency features characteristic of cloud arrival and departure and low frequency features likely induced by general light scattering in the atmosphere [25]. Figure 5.14 compares the transient, which was taken from weather on September 5th at Sunspot 2 in Colorado (http://midcdmz.nrel.gov/srri_bms/) [130], against power output by six lamps on the high-flux solar simulator. In all tests the same six lamps were used.

Initially, the solar-electric reactor was ramped to 925° C by electric heating with all distributed controllers set to regulate batch gasification as described in Section 5.3. Once the reactor was at a steady state the 30 minute solar transient commenced. This experiment was performed in triplicate for each control architecture (Figure 5.10).

Figure 5.15 shows results for solar-electric reactor temperature control with PID feedback. The distributed control system successfully regulated the gasification reaction despite disturbances of $\pm 25^\circ\text{C}$ ($\pm 60^\circ\text{F}$) in solar-electric furnace temperature, which occurred upon 100% disturbances

in solar heat. Figure 5.16 shows that feedforward feedback improved this result and brought disturbances within $\pm 20^{\circ}$ C. When the model predictive controller was used for solar-electric furnace regulation, Figure 5.17 shows that temperature excursions were similar to control by feedback alone. The model predictive controller relies on a feedback estimator of the system state, which may have compromised performance. However, only the model predictive controller can incorporate a projected forecast of future cloud transients.

A one minute forecast was incorporated in the model predictive controller as recommended by previous work [42]. Figure 5.18 shows that use of a forecast in the controls architecture yielded performance that was substantially better than feedback and feedforward feedback. In this case, only $\pm 10^{\circ}$ C excursions occurred in furnace temperature.

Performance results were summarized by the integral squared error of controlled variable excursions from their setpoints [129]. Relative to feedback, Figure 5.19 shows that feedforward feedback reduced integral squared error by 50% in solar-electric temperature control. Model predictive control with a forecast further reduced the integral squared error. Relative to feedback alone, model predictive control showed a 75% reduction in integral squared error (Figure 5.19). Regulation of the gasification reaction by the distributed control system was similar across the different solar-electric control architectures (Figure 5.19). Likely, the reaction was similarly controlled despite furnace temperature excursions and performance differences across the experiments arose from noise.

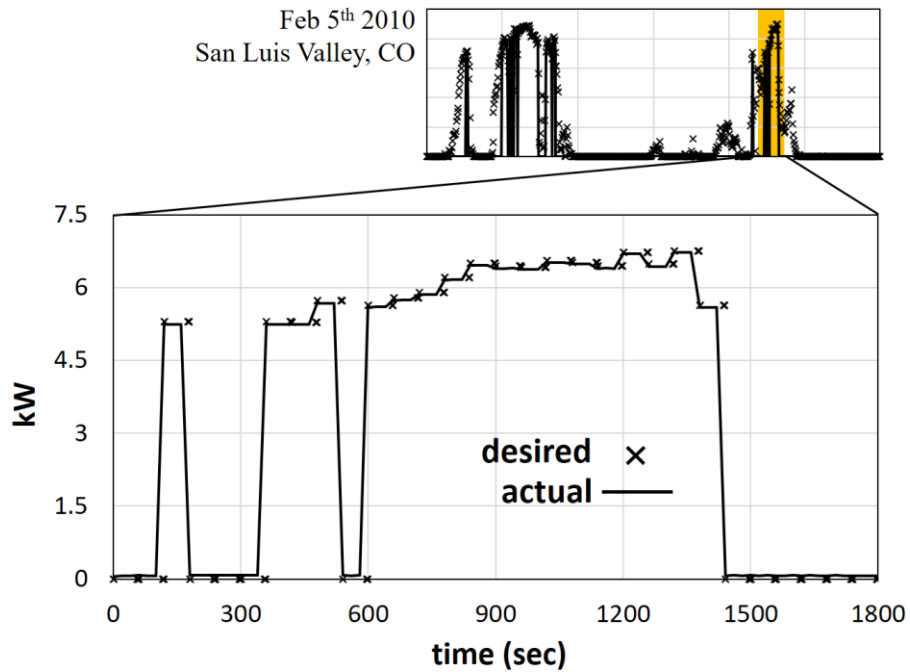


Figure 5.14: The weather transient for experimental control studies, taken from February 5th 2010 at Sunspot 2 in Colorado (http://midcdmz.nrel.gov/srrl_bms/) [130].

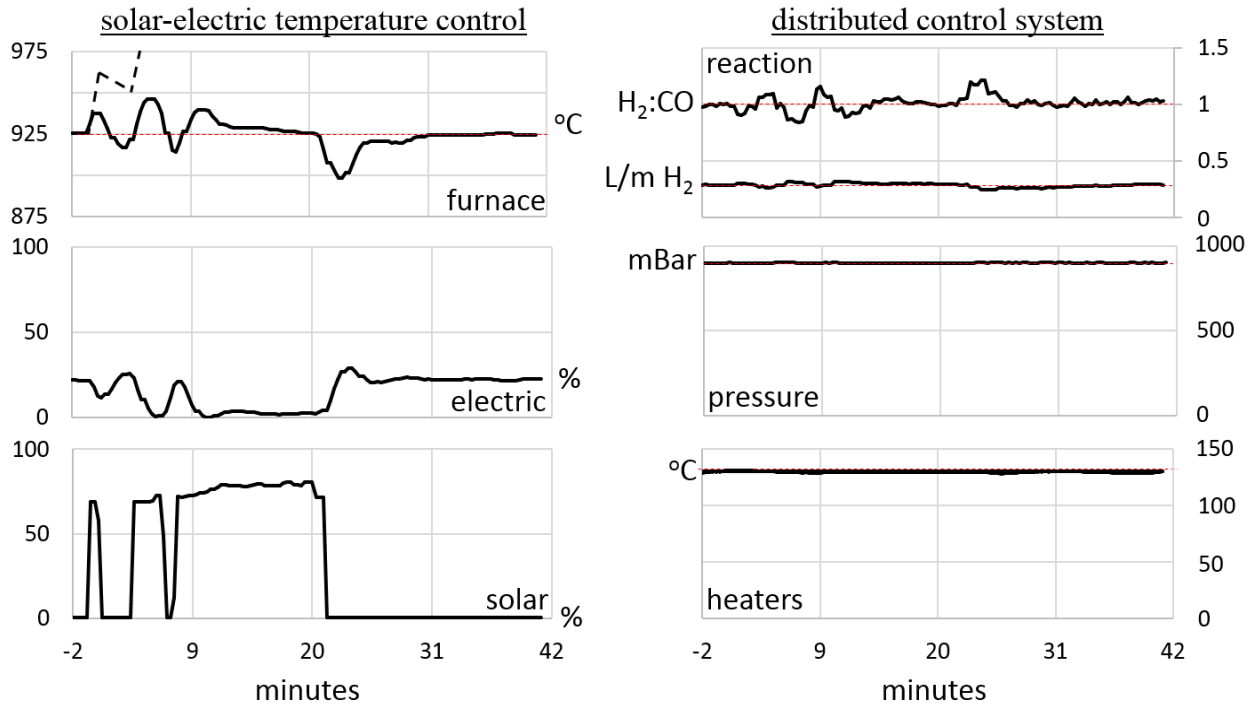


Figure 5.15: Performance of feedback control on the 30 minute weather transient reproduced by the high-flux solar simulator lamps in experiment. Dashed line shows the simulated uncontrolled temperature response.

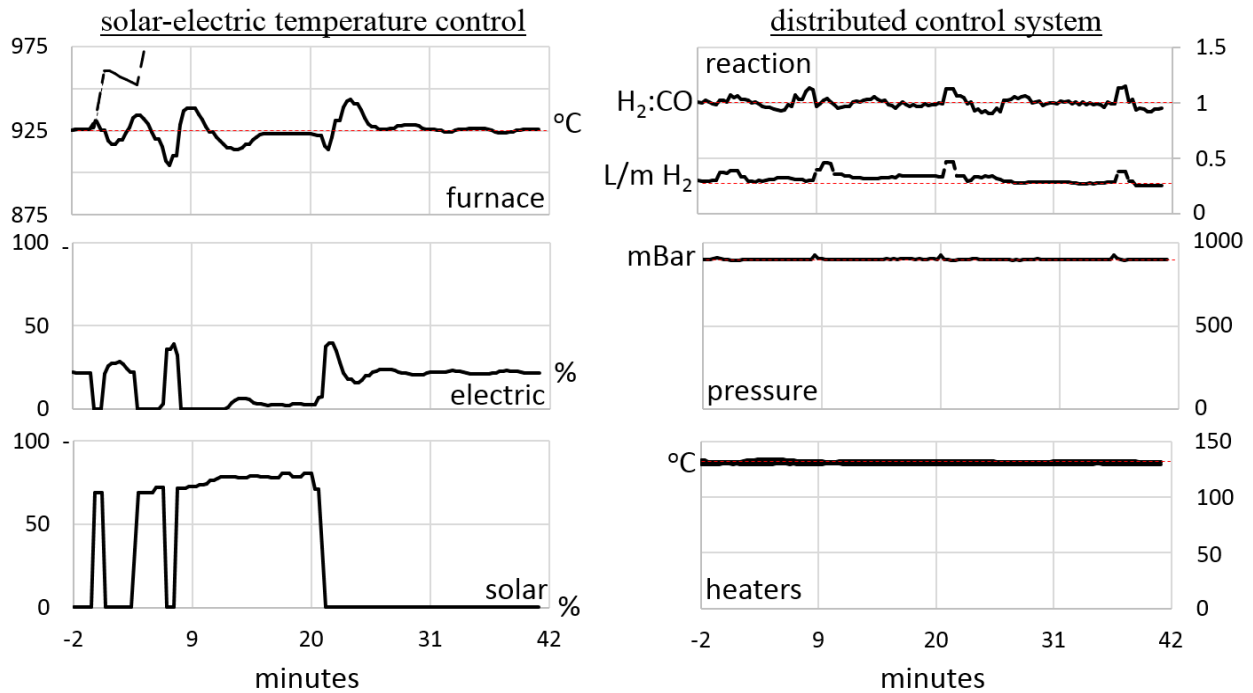


Figure 5.16: Performance of feedforward feedback control on the 30 minute weather transient reproduced by the high-flux solar simulator lamps in experiment. Dashed line shows the simulated uncontrolled temperature response.

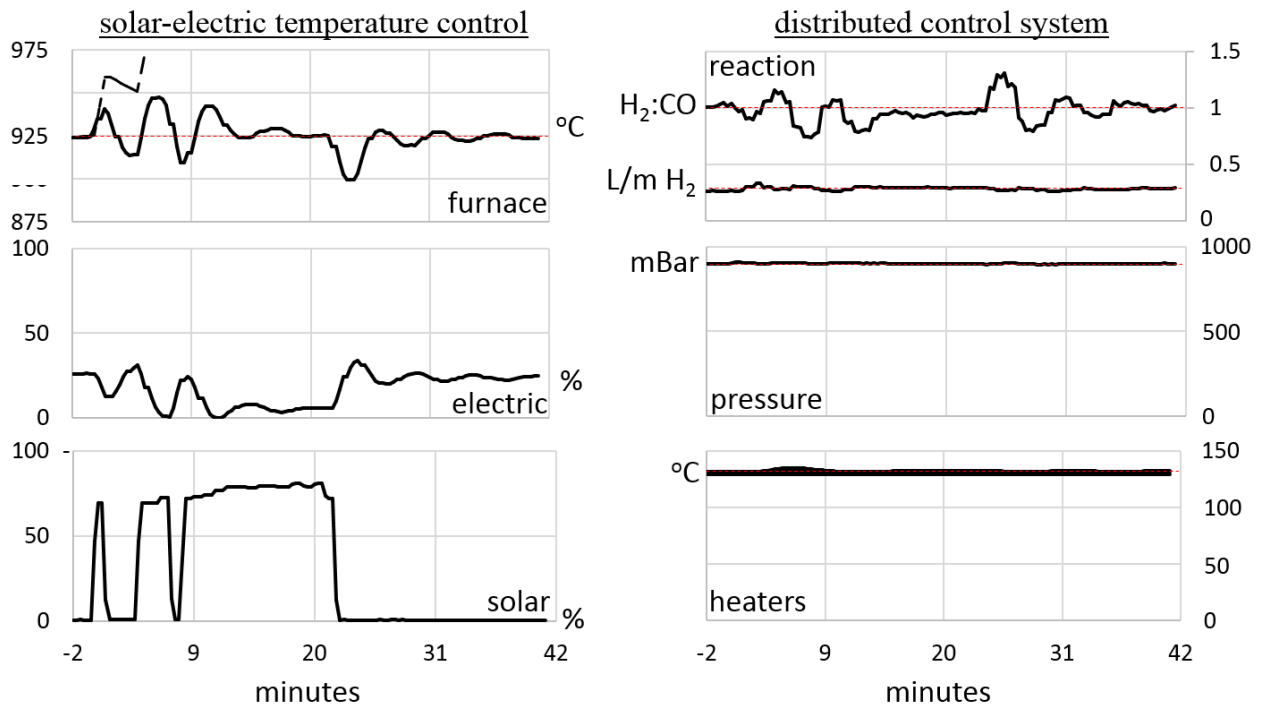


Figure 5.17: Performance of model predictive control *without a forecast* on the 30 minute transient reproduced by the high-flux solar simulator lamps in experiment. Dashed line shows the simulated uncontrolled temperature response.

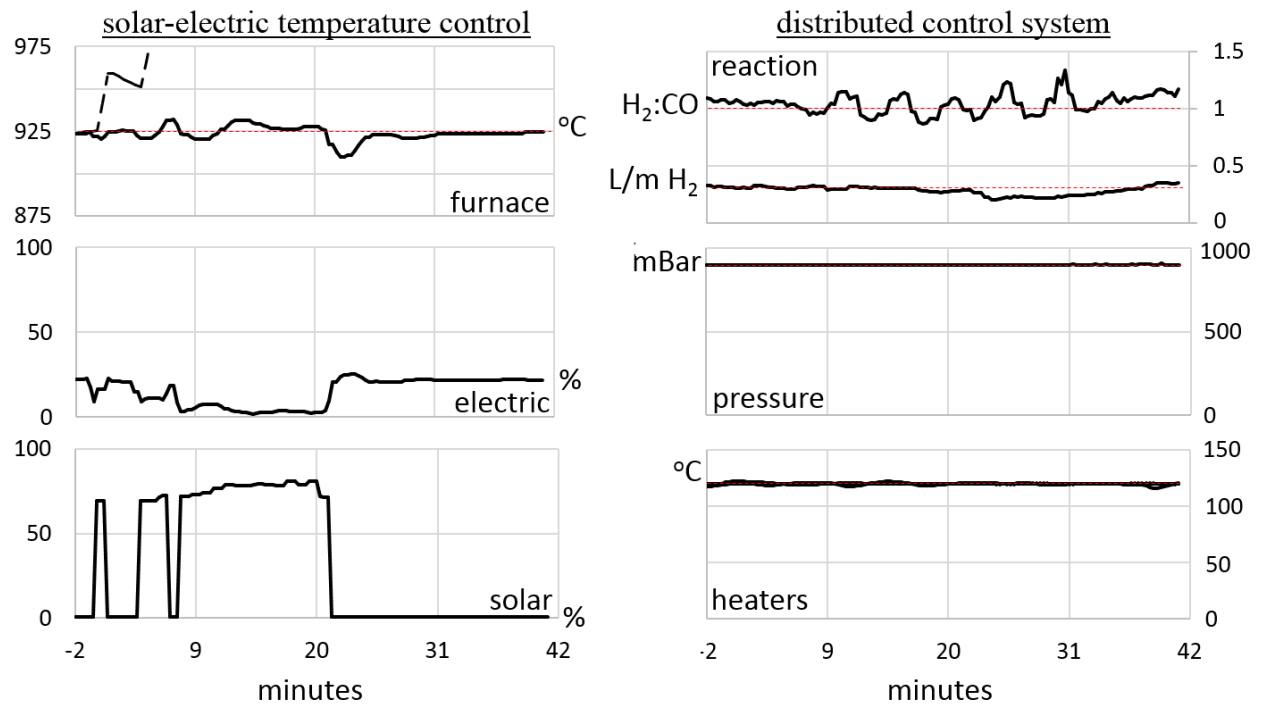


Figure 5.18: Performance of model predictive control *with a 1 minute forecast* on the 30 minute transient reproduced by the high-flux solar simulator lamps in experiment. Dashed line shows the simulated uncontrolled temperature response.

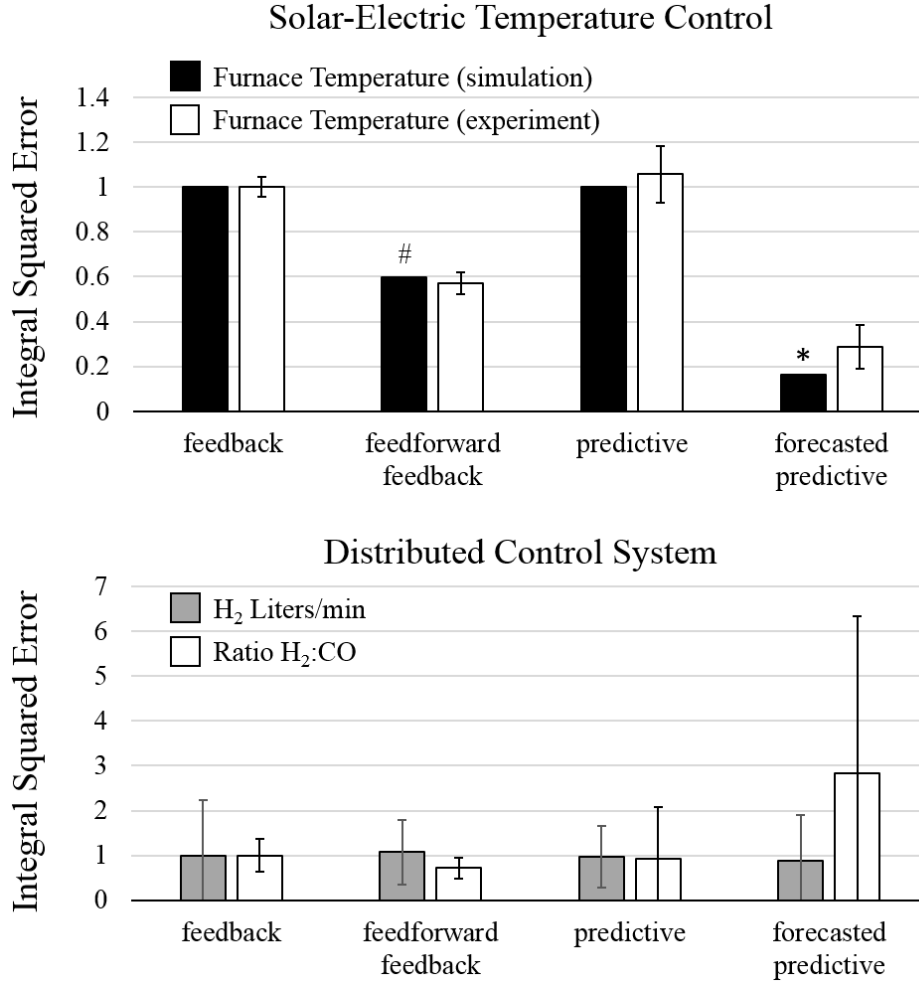


Figure 5.19: Performance of the controllers in solar-electric reactor temperature regulation (top) and gasification control (bottom). All experimental results normalized to feedback. Predictive refers to model predictive control, forecasted predictive refers to model predictive control with a forecast one minute forecast of future weather.

*simulation normalized to feedback, # simulation normalized to model predictive control.

5.6 Simulations for Optimal Forecasts in Solar-Electric Control

The success of model predictive control with a forecast provoked interest in the ideal length and necessary accuracy of weather predictions. In reactor experiments a perfect forecast was available whose length was suggested by prior work (1 minutes, $\tau_p/12$) [42]. To further explore optimal forecast length in solar-electric reactor temperature regulation, model predictive control

performance was examined in simulation with different forecast lengths and accuracy. Figure 5.20 shows that a one minute forecast was best among the cases examined (integral squared error). Longer forecasts likely cause the controller to react to conditions beyond immediate system dynamics. A forecast that spanned the duration of the system dominant time constant (τ_p) severely degraded control performance. A tradeoff was evident between the forecast length used for control and forecast accuracy. Specifically, Figure 5.21 shows that control with a short one minute forecast was sensitive to forecast amplitude inaccuracy. Conversely, control with a long three minute forecast, although less efficacious, was robust to and benefitted from forecast amplitude inaccuracy (Figure 5.21). In both cases temporal forecast accuracy was essential. Figure 5.22 shows that for both long forecasts and short forecasts weather prediction errors of $\pm\Delta t = \tau_p/24$ completely obviated the benefits of model predictive control.

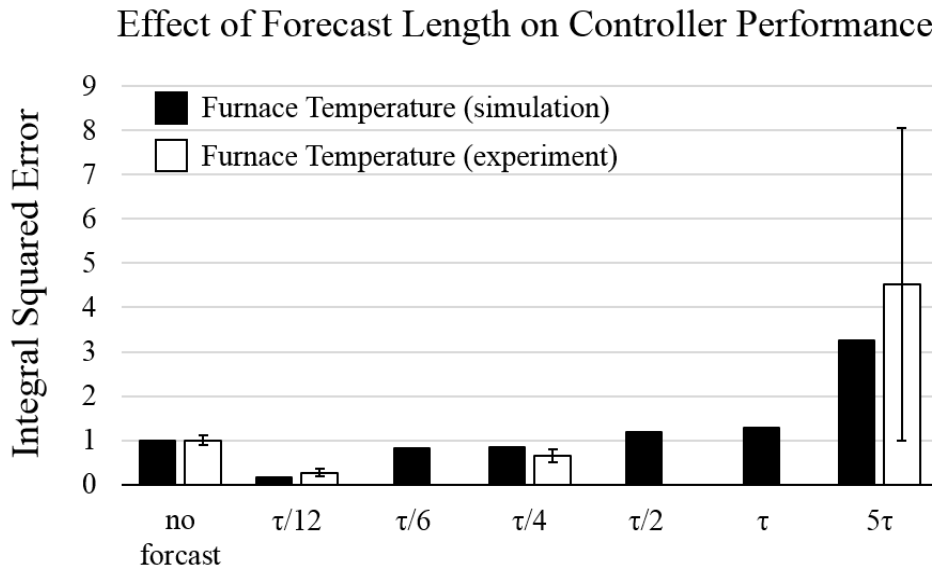


Figure 5.20: Simulation results (black bars) and experimental results (white bars) show the effect of forecast length on solar-electric reactor temperature regulation with model predictive control. Figure 5.14 shows the weather challenge used to assess control performance.

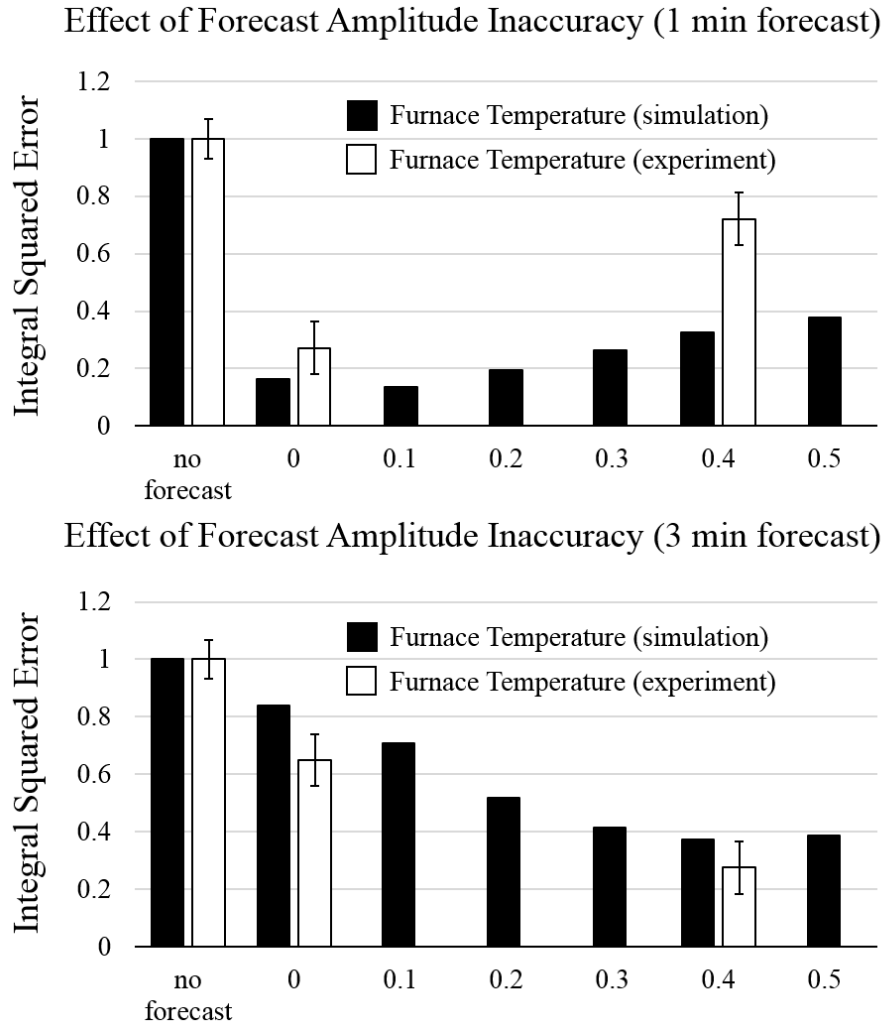


Figure 5.21: Simulation results (black bars) and experimental results (white bars) show the effect of forecast amplitude inaccuracy on solar-electric reactor temperature regulation by model predictive control. Numbers 0 through 0.5 indicate the fractional decrease between forecasted cloud intensity used within the controller and actual cloud intensity. Figure 5.14 shows the weather challenge used to assess control performance.

5.7 Conclusion

A solar-electric reactor design was modeled in simulation and fabricated for control experiments. The use of concentrated optics to funnel renewable solar energy into this device was unnecessary within the experimental facility, a tightly focused high-flux solar simulator, but may be needed when light is delivered by heliostat(s). Different temperature control strategies were implemented on the solar-electric reactor, which operated at 925° C for carbon gasification studies. Control

architectures included feedback and model predictive control. Model predictive control outperformed feedback and feedforward feedback when a one minute forecast of future weather was available. In this case, a 75% improvement in performance (integral squared error) was observed over standard feedback control in experiments with a weather transient that was produced by the high-flux solar simulator lamps. An ideal forecast length for this system was explored in simulation and verified with experiments. Notably, shorter forecasts were highly effective in model predictive control, but longer forecasts were more robust to weather forecast amplitude inaccuracy. In all cases temporal forecast inaccuracy completely negated model predictive control benefits.

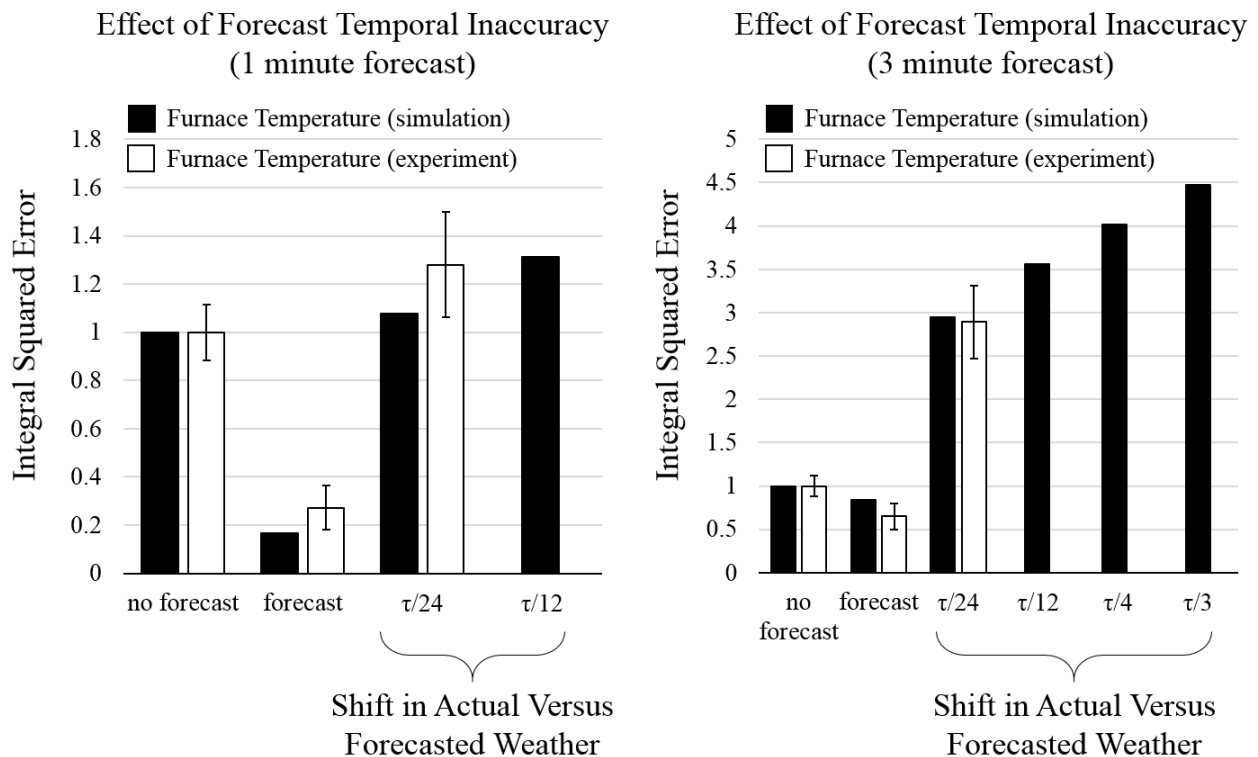


Figure 5.21: Simulation results (black bars) and experimental results (white bars) show the effect of forecast temporal inaccuracy on solar-electric reactor temperature regulation by model predictive control. Figure 5.14 shows the weather challenge used to assess control performance.

Chapter 6: What was Learned and What is Unanswered?

In this thesis a high-flux solar simulator was analyzed (Chapter 2), built (Chapter 3), and used to execute control experiments for the hybridization of solar and electric heat (Chapter 5). In these experiments weather transients were rejected by automated electric heaters, control that relied on c-optimal aligned models (Chapter 4). To our knowledge, this is the first use of a high-flux solar simulator to reproduce actual weather, although more than twelve high-flux solar simulators are available worldwide for experimental studies [40, 41]. In preparation for control experiments an artifact likely common to all extant high-flux solar simulators, specifically an observer effect, was discovered.

6.1 The Observer Effect in High-Flux Solar Simulators

In general, high-flux solar simulators are difficult to analyze and characterize because the absolute volume of energy they deliver, here 12,000 suns, can readily destroy sensitive flux and power measurement equipment. Despite these challenges, software from Chapter 2 and experiments from Chapter 3 identified a subtle observer effect in high-flux simulators that distinguishes these devices from the solar furnace facilities they recapitulate. If ignored, the observer effect can distort efficiency measurements during tests of solar-driven process equipment, potentially inflating the performance of solar designs. Recommendations for minimizing observer effects in high-flux solar simulators include:

- 1) Decreasing the solid angle a high-flux solar simulator presents to experimental equipment, which can be achieved by increasing the high-flux solar simulator focal length.

- 2) Insuring experimental equipment and flux measurement instrumentation present a similar or identical optical environment to high-flux solar simulators.
- 3) Insuring that experimental equipment and flux measurement instrumentation is diffusely absorbing and not specularly reflective.
- 4) Using facility characterization and software to correct for observer effects upon data analysis.

It could be worthwhile to investigate the experimental efficiency and performance of prior solar process equipment, reviewed in Chapter 5, to see if the observer effect significantly affected previously published experimental results.

6.2 The Hybridization of Solar and Electric Heat

Once observer effects were fully understood, the high-flux solar simulator was used to challenge automated controllers for temperature regulation of a solar-electric furnace (Chapter 5). It was found that linear model predictive control with a weather forecast of incipient clouding maintained furnace temperature setpoints despite weather transients. That forecasts could be useful in solar control has been recognized in simulation [42], although until now forecast efficacy was unproven in experiment. Model predictive control with a forecast was compared against standard model predictive control, feedback control, and feedforward feedback control. When compared to feedback, feedforward feedback halved the control residuals (integral squared error) for furnace temperature regulation. Forecasted model predictive control reduced that metric three-fourths – it outperformed alternatives. However, the inclusion of a forecast complicates control. Atop hardware and software additions, forecast length and intensity must be determined, which was further explored in validated simulations of the solar-electric furnace. Simulations showed that,

at least in this application, shorter weather forecasts was most effective in solar-electric control. It was found that a forecast horizon of $\tau/12$ was best, where τ was the dominant process time constant.

Additional theoretical and applied research is needed to move model predictive control with a forecast from the lab to actual solar applications. Notably, the experimental furnace studied herein was only 4% efficient in converting solar heat to chemical energy via gasification, whereas actual industrial equipment should be more effective. Inefficiency likely owed to the use of a single transport tube within the reactor system. Presumably, were the system to incorporate fourteen reaction tubes along the reactor cavity, the maximal number of $\varnothing 50\text{mm}$ tubes that can be accommodated, higher efficiencies would be observed [131]. More effective equipment would couple thermal effects from solar and electric heating to reaction kinetics, which could confound controller performance. Thus, although a thermal model was sufficient in Chapter 5, more complicated engineering models will likely be needed in efficient reactor systems. Given that reaction kinetics are highly nonlinear, nonlinear control algorithms (Appendix D) may be worthwhile in future solar-electric research and development.

Overall, this research establishes an approach to solar and electric heating for renewable chemicals and commodities manufacture. As described in Chapter 1, there is strong interest in high-temperature solar heat integration for the production of fuels, electricity, and chemicals. The ultimate success of these proposals relies on minimal equipment wear in the face of thermal heat transients that accompany weather, sundown and sunrise. This thesis demonstrates that solar and electric heat can be controlled to maintain facility temperatures despite extreme disturbances, but quantifying success in this endeavor requires further study. In the future thermal shock and fatigue could be measured during the course of reactor operation to actually assess equipment wear, or the mitigation of equipment wear, under different control regimes. The study of material fatigue,

which includes acoustic emission, imaging, simulation and impedance spectroscopy, is a field onto itself [132-134]. However, the prospect of analyzing control success and predicting facility failure remains a tantalizing area for new research. With this information scaled solar-electric facilities could be pursued with added confidence by and in industry.

Appendix A: A Tutorial Introduction to Subspace Identification

A.1. The State Space

“The best material model of a cat is another, or preferably the same, cat.”

-Norbert Wiener, 1945

Generally fundamental system physics – mass, energy, and momentum balances – can be framed as a set of 1st order differential equations [84]:

$$\frac{d\vec{x}}{dt} = f(\vec{x}, \vec{u}, t) \quad \text{A.1}$$

Here \vec{x} is a vector of variables (states) that drive system dynamics and \vec{u} is a vector of time varying control inputs. The state space is a natural extension of this framework. To derive the state space, we first assume that the system is time invariant:

$$\frac{d\vec{x}}{dt} = f(\vec{x}, \vec{u}) \quad \text{A.2}$$

Figure A.1 shows how system behavior can be analyzed by expanding Equation A.2 with a 1st order Taylor series:

$$\begin{aligned} \Delta \frac{d\vec{x}}{dt} &= f(\vec{x} + \Delta\vec{x}, \vec{u} + \Delta\vec{u}) - f(\vec{x}, \vec{u}) \\ &= \frac{\partial f(\vec{x}, \vec{u})}{\partial \vec{x}} \Delta\vec{x} + \frac{\partial f(\vec{x}, \vec{u})}{\partial \vec{u}} \Delta\vec{u} \end{aligned} \quad \text{A.3}$$

Here $\frac{\partial f(\vec{x}, \vec{u})}{\partial \vec{x}}$ and $\frac{\partial f(\vec{x}, \vec{u})}{\partial \vec{u}}$ are Jacobians with respect to the states and inputs. Equation A.3

describes departures from a reference trajectory owing to perturbations in \vec{x} and \vec{u} . This analysis underlies the calculus of variations. If we use deviation variables from a steady-state ($f(\vec{x}, \vec{u}) = 0$) Equation A.3 simplifies:

$$\frac{d\bar{x}}{dt} = \frac{\partial f(\bar{x}, \bar{u})}{\partial \bar{x}} \bar{x} + \frac{\partial f(\bar{x}, \bar{u})}{\partial \bar{u}} \bar{u} \quad \text{A.4}$$

This is the classical continuous-time “state space” representation of a system:

$$\dot{\bar{x}} = A\bar{x} + B\bar{u} \quad \text{A.5}$$

$$A = \frac{\partial f(\bar{x}, \bar{u})}{\partial \bar{x}}, \quad B = \frac{\partial f(\bar{x}, \bar{u})}{\partial \bar{u}} \quad \text{A.6}$$

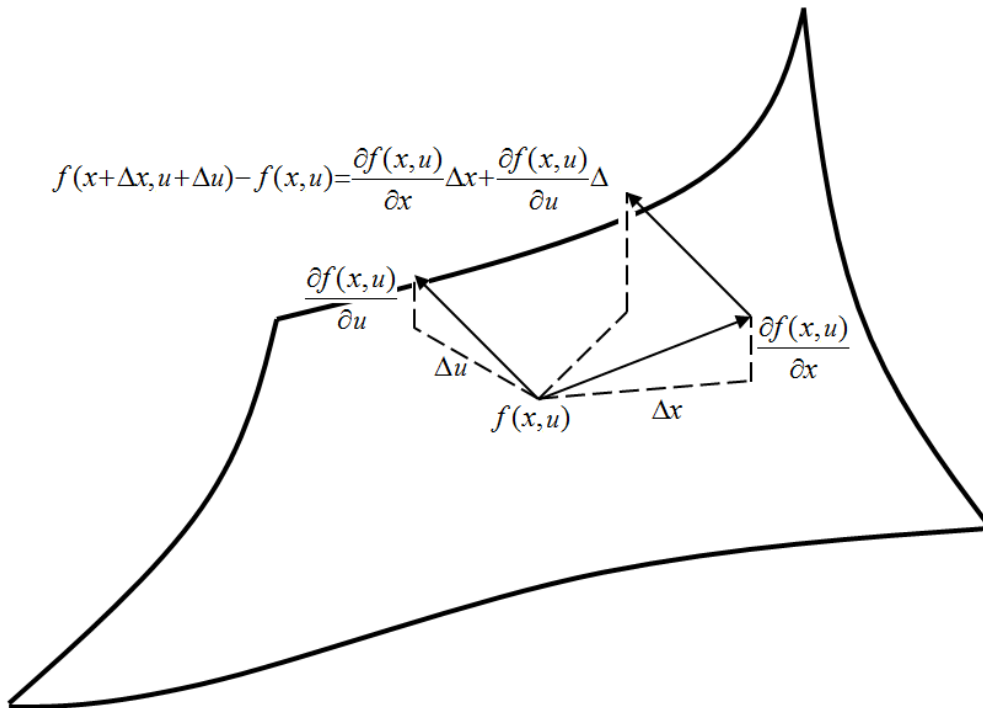
The state space is convenient because it describes the system trajectory exclusively with respect to current process conditions, \bar{x} , not a long history of system behavior (the “Markov property”).

This simplifies mathematical analysis [84]. The continuous state space can be discretized into a difference equation that is executed at regular intervals:

$$\bar{x}_{k+1} = \Phi \bar{x}_k + \Gamma \bar{u}_k \quad \text{A.7}$$

Mappings between Equation A.5 and Equation A.7 can be deduced with simple calculus.

Figure A.1: The 1st order Taylor series of a function.



Recall that 1st order linear differential equations are typically presented in a canonical form:

$$\dot{\vec{x}} - A\vec{x} = B\vec{u} \quad \text{A.8}$$

Formally, \vec{x} has two solutions:

$$\vec{x}(t) = \vec{x}(t)_{homogeneous} + \vec{x}(t)_{particular} \quad \text{A.9}$$

In the homogenous solution we consider underlying system behavior in the absence of external stimuli (the “free” response):

$$\dot{\vec{x}} - A\vec{x} = 0 \quad \text{A.10}$$

The homogenous solution follows immediately from properties of Napier’s constant:

$$\vec{x}(t)_{homogeneous} = e^{A(t-t_0)}\vec{x}(t_0) \quad \text{A.11}$$

The validity of this solution is immediately proven upon the insertion of $\vec{x}(t)_{homogeneous}$ and its derivative into Equation A.10 for initial time $t_0 = 0$.

The particular solution depends on external input. Thus its “particularity” – it is situation specific. We discover the particular solution via the integrating factor method:

$$\dot{\vec{x}} - A\vec{x} = B\vec{u} \quad \text{A.8}$$

$$e^{-At}\dot{\vec{x}} - e^{-At}A\vec{x} = e^{-At}B\vec{u} \quad \text{A.12}$$

$$\frac{d[e^{-At}\vec{x}]}{dt} = e^{-At}B\vec{u} \quad \text{A.13}$$

$$\vec{x}(t) = e^{At} \int_{t_0}^t e^{-A\tau} B\vec{u} d\tau \quad \text{A.14}$$

$$\vec{x}(t)_{particular} = \int_{t_0}^t e^{A(t-\tau)} B\vec{u} d\tau \quad \text{A.15}$$

Thus, we can assemble the complete solution via superposition (Equation A.9):

$$\begin{aligned}
\vec{x}(t) &= \vec{x}(t)_{homogeneous} + \vec{x}(t)_{particular} \\
&= e^{A(t-t_0)} \vec{x}(t_0) + \int_{t_0}^t e^{A(t-\tau)} B \vec{u} d\tau
\end{aligned} \tag{A.16}$$

Let us consider \vec{u} piecewise invariant over each interval $t_{0+} \Delta t, t_1+\Delta t \dots t_k+\Delta t$ (the so called “zero order hold”). \vec{u} is no longer time varying within a given interval and can then be removed from the integral, which is evaluated exclusively over Δt . This reveals the discretization matrices for Equation A.7:

$$\begin{aligned}
\vec{x}_{k+1} &= \Phi \vec{x}_k + \Gamma \vec{u}_k \\
&= \vec{x}(t)_{homogeneous} + \vec{x}(t)_{particular} \\
&= e^{A\Delta t} \vec{x}_k + \left(\int_0^{\Delta t} e^{A\tau} d\tau \right) B \vec{u}_k
\end{aligned}$$

$$\begin{aligned}
\Phi &= e^{A\Delta t} \\
\Gamma &= \left[\int_0^{\Delta t} e^{A\tau} d\tau \right] B
\end{aligned}$$

The discretized matrices are readily calculable via a Taylor series and integral respectively:

$$\Phi = e^{A\Delta t} \approx \frac{I}{0!} + \frac{A}{1!} \Delta t + \frac{A^2}{2!} \Delta t^2 + \frac{A^3}{3!} \Delta t^3 \dots \tag{A.17}$$

$$\Gamma = \int_0^{\Delta t} e^{A\tau} d\tau B \tag{A.18}$$

We have shown how the fundamental variables of any physical system relate to a 1st order Taylor approximate, namely the state space. However, in a given facility fundamental physical phenomenon are rarely measured directly. Thus, the states are usually unavailable. Instead, measurements are some function of the underlying system fundamentals:

$$\vec{y} = g(\vec{x}) \tag{A.19}$$

Again we use a Taylor series to predict measurement variation as a function of system conditions:

$$\Delta \vec{y} = \frac{\partial g(\vec{x})}{\partial \vec{x}} \Delta \vec{x} \quad \text{A.20}$$

If we use deviation variables from a steady-state Equation A.20 simplifies:

$$\vec{y} = H\vec{x} \quad \text{A.21}$$

$$H = \frac{\partial g(\vec{x})}{\partial \vec{x}} \quad \text{A.22}$$

This completes our state space view of physical phenomena, systems, and facilities:

$$\vec{x}_{k+1} = \Phi \vec{x}_k + \Gamma \vec{u}_k \quad \text{A.7}$$

$$\vec{y}_k = H\vec{x}_k \quad \text{A.21}$$

Although beyond the scope of this work, occasionally direct inputs, \vec{u}_k , are measured:

$$\vec{y}_k = H\vec{x}_k + D\vec{u}_k \quad \text{A.22}$$

Thus, one can confirm from the vector of outputs, \vec{y}_k , that the inputs are as expected. This formulation enters into fault detection and analysis. The entire framework can be viewed in a condensed, matrix, format:

$$\begin{bmatrix} \vec{x}_{k+1} \\ \vec{y}_k \end{bmatrix} = \begin{bmatrix} \Phi & \Gamma \\ H & D \end{bmatrix} \begin{bmatrix} \vec{x}_k \\ \vec{u}_k \end{bmatrix} \quad \text{A.23}$$

A.2. The Estimation of State Space Models

“The truth is out there.”

-Fox Mulder, 1993

The estimation of state space models is nontrivial, but also flexible. To illustrate this flexibility, consider a grand statement on Equation A.23:

$$\begin{bmatrix} \bar{x}_{k+1} & \bar{x}_k & \bar{x}_{k-1} & \cdots & \bar{x}_1 \\ \bar{y}_k & \bar{y}_{k-1} & \bar{y}_{k-2} & \cdots & \bar{y}_0 \end{bmatrix} = \begin{bmatrix} \Phi & \Gamma \\ H & D \end{bmatrix} \begin{bmatrix} \bar{x}_k & \bar{x}_{k-1} & \bar{x}_{k-2} & \cdots & \bar{x}_0 \\ \bar{u}_k & \bar{u}_{k-1} & \bar{u}_{k-2} & \cdots & \bar{u}_0 \end{bmatrix} \quad \text{A.24}$$

We can arbitrarily multiply this statement by a transform:

$$\begin{bmatrix} T & 0 \\ 0 & I \end{bmatrix} \begin{bmatrix} \bar{x}_{k+1} & \bar{x}_k & \cdots \\ \bar{y}_k & \bar{y}_{k-1} & \cdots \end{bmatrix} = \begin{bmatrix} T & 0 \\ 0 & I \end{bmatrix} \begin{bmatrix} \Phi & \Gamma \\ H & D \end{bmatrix} \begin{bmatrix} \bar{x}_k & \bar{x}_{k-1} & \cdots \\ \bar{u}_k & \bar{u}_{k-1} & \cdots \end{bmatrix} \quad \text{A.25}$$

$$\begin{bmatrix} T\bar{x}_{k+1} & T\bar{x}_k & \cdots & T\bar{x}_1 \\ \bar{y}_k & \bar{y}_{k-1} & \cdots & \bar{y}_0 \end{bmatrix} = \begin{bmatrix} T\Phi & T\Gamma \\ H & D \end{bmatrix} \begin{bmatrix} \bar{x}_k & \bar{x}_{k-1} & \cdots & \bar{x}_0 \\ \bar{u}_k & \bar{u}_{k-1} & \cdots & \bar{u}_0 \end{bmatrix} \quad \text{A.26}$$

Now we introduce an “identity” matrix into the rightmost expression:

$$\begin{bmatrix} T\bar{x}_{k+1} & T\bar{x}_k & \cdots \\ \bar{y}_k & \bar{y}_{k-1} & \cdots \end{bmatrix} = \begin{bmatrix} T\Phi & T\Gamma \\ H & D \end{bmatrix} \begin{bmatrix} T^{-1} & 0 \\ 0 & I \end{bmatrix} \begin{bmatrix} T & 0 \\ 0 & I \end{bmatrix} \begin{bmatrix} T\bar{x}_k & T\bar{x}_{k-1} & \cdots \\ \bar{u}_k & \bar{u}_{k-1} & \cdots \end{bmatrix} \quad \text{A.27}$$

$$\begin{bmatrix} T\bar{x}_{k+1} & T\bar{x}_k & \cdots \\ \bar{y}_k & \bar{y}_{k-1} & \cdots \end{bmatrix} = \begin{bmatrix} T\Phi T^{-1} & T\Gamma T^{-1} \\ HT^{-1} & DT^{-1} \end{bmatrix} \begin{bmatrix} T\bar{x}_k & T\bar{x}_{k-1} & \cdots \\ \bar{u}_k & \bar{u}_{k-1} & \cdots \end{bmatrix} \quad \text{A.28}$$

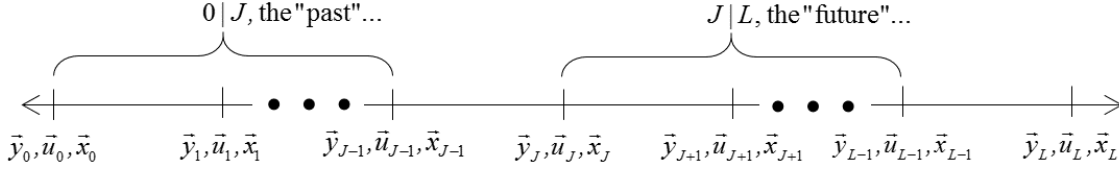
We have a new set of matrices that are related to actual system dynamics by a similarity transform,

T . Furthermore, our revised state sequence is linearly coupled to the true states:

$$\bar{w}_k = T\bar{x}_k \quad \text{A.29}$$

This is exceptional – any series of states that we might discover is related directly to physical phenomena. The observability principle dictates whether we can discover a viable state sequence from system outputs. We can formalize this principle on a timeline (Figure A.2).

Figure A.2: A state timeline originating at time $k = 0$. We adopt the peculiar notation of David Di Rusico [86], not Peter Van Overschee [135].



Consider a case wherein we have eliminated the inputs mathematically, or by holding all system controls invariant:

$$\vec{x}_{k+1} = \Phi \vec{x}_k \quad \text{A.30}$$

$$\vec{y}_k = H \vec{x}_k \quad \text{A.21}$$

Simple recursion reveals that the inputs and outputs are related by a particular matrix:

$$\begin{bmatrix} \vec{y}_0 \\ \vec{y}_1 \\ \vec{y}_2 \\ \vdots \\ \vec{y}_J \end{bmatrix} = \begin{bmatrix} H \\ H\Phi \\ H\Phi^2 \\ \vdots \\ H\Phi^J \end{bmatrix} \vec{x}_0 \quad \text{A.31}$$

We call this the “observability” matrix:

$$\mathcal{G}_J = \begin{bmatrix} H \\ H\Phi \\ H\Phi^2 \\ \vdots \\ H\Phi^J \end{bmatrix} \quad \text{A.32}$$

All columns of the observability matrix must be unique to truly relate \vec{x}_k to system outputs (full rank).

We are also interested in controllability – how to move from some initial state x_0 to any arbitrary final state x_J . Motion through time is entirely described by Equation A.7:

$$\vec{x}_{k+1} = \Phi \vec{x}_k + \Gamma \vec{u}_k \quad \text{A.7}$$

From our initial state, we have:

$$\begin{aligned} \vec{x}_1 &= \Phi \vec{x}_0 + \Gamma \vec{u}_0 \\ \vec{x}_2 &= \Phi \vec{x}_1 + \Gamma \vec{u}_1 \\ &\vdots \\ \vec{x}_J &= \Phi \vec{x}_{J-1} + \Gamma \vec{u}_{J-1} \end{aligned}$$

Backsubstitution to eliminate the intermediate states gives:

$$\begin{aligned} \vec{x}_1 &= \Phi \vec{x}_0 + \Gamma \vec{u}_0 \\ \vec{x}_2 &= \Phi \vec{x}_1 + \Gamma \vec{u}_1 \\ &= \Phi(\Phi \vec{x}_0 + \Gamma \vec{u}_0) + \Gamma \vec{u}_1 = \Phi^2 \vec{x}_0 + \begin{bmatrix} \Phi \Gamma & \Gamma \end{bmatrix} \begin{bmatrix} \vec{u}_0 \\ \vec{u}_1 \end{bmatrix} \\ \vec{x}_3 &= \Phi \vec{x}_2 + \Gamma \vec{u}_2 \\ &= \Phi(\Phi^2 \vec{x}_0 + \Phi \Gamma \vec{u}_0 + \Gamma \vec{u}_1) + \Gamma \vec{u}_2 = \Phi^3 \vec{x}_0 + \begin{bmatrix} \Phi^2 \Gamma & \Phi \Gamma & \Gamma \end{bmatrix} \begin{bmatrix} \vec{u}_0 \\ \vec{u}_1 \\ \vec{u}_2 \end{bmatrix} \\ &\vdots \\ \vec{x}_J &= \Phi^J \vec{x}_0 + \Delta_J \begin{bmatrix} \vec{u}_0 \\ \vec{u}_1 \\ \vdots \\ \vec{u}_{J-1} \end{bmatrix} \end{aligned} \quad \text{A.33}$$

Here, the relationship between the states and inputs is termed the “reverse controllability matrix.”

If the transform matrix is nonsingular (does not destroy information, is full rank) control actions exist for moving between the initial state and a general future state. The system is “controllable.”

We give the deterministic reverse controllability matrix a specific symbol:

$$\Delta_J = [\Phi^{J-1}\Gamma \quad \Phi^{J-2}\Gamma \quad \dots \quad \Phi\Gamma \quad \Gamma] \quad \text{A.34}$$

We can use Equation A.7 and Equation A.22 to write a unified statement on future outputs:

$$\begin{aligned}
\bar{y}_0 &= H\bar{x}_0 + D\bar{u}_0 \\
\bar{x}_1 &= [\Phi]\bar{x}_0 + [\Gamma]\bar{u}_0 & \bar{y}_1 &= H\bar{x}_1 + D\bar{u}_1 \\
& & &= [H\Phi]\bar{x}_0 + [H\Gamma]\bar{u}_0 + D\bar{u}_1 \\
& & &= [H\Phi]\bar{x}_0 + [H\Gamma \quad D] \begin{bmatrix} \bar{u}_0 \\ \bar{u}_1 \end{bmatrix} \\
\bar{x}_2 &= [\Phi^2]\bar{x}_0 + [\Phi\Gamma \quad \Gamma] \begin{bmatrix} \bar{u}_0 \\ \bar{u}_1 \end{bmatrix} & \bar{y}_2 &= H\bar{x}_2 + D\bar{u}_2 \\
& & &= [H\Phi^2]\bar{x}_0 + [H\Phi\Gamma \quad H\Gamma] \begin{bmatrix} \bar{u}_0 \\ \bar{u}_1 \end{bmatrix} + D\bar{u}_2 \\
& & &= [H\Phi^2]\bar{x}_0 + [H\Phi\Gamma \quad H\Gamma \quad D] \begin{bmatrix} \bar{u}_0 \\ \bar{u}_1 \\ \bar{u}_2 \end{bmatrix} \\
\bar{x}_3 &= [\Phi^3]\bar{x}_0 + [\Phi^2\Gamma \quad \Phi\Gamma \quad \Gamma] \begin{bmatrix} \bar{u}_0 \\ \bar{u}_1 \\ \bar{u}_2 \end{bmatrix} & \bar{y}_3 &= H\bar{x}_3 + D\bar{u}_3 \\
& & &= [H\Phi^3]\bar{x}_0 + [H\Phi^2\Gamma \quad H\Phi\Gamma \quad H\Gamma] \begin{bmatrix} \bar{u}_0 \\ \bar{u}_1 \\ \bar{u}_2 \end{bmatrix} + D\bar{u}_3 \\
& & &= [H\Phi^3]\bar{x}_0 + [H\Phi^2\Gamma \quad H\Phi\Gamma \quad H\Gamma \quad D] \begin{bmatrix} \bar{u}_0 \\ \bar{u}_1 \\ \bar{u}_2 \\ \bar{u}_3 \end{bmatrix} \\
& \vdots & & \vdots \\
& & & \vdots
\end{aligned}$$

$$\begin{bmatrix} \bar{y}_0 \\ \bar{y}_1 \\ \vdots \\ \bar{y}_J \end{bmatrix} = \begin{bmatrix} H \\ H\Phi \\ \vdots \\ H\Phi^J \end{bmatrix} \bar{x}_0 + \begin{bmatrix} D & 0 & 0 & 0 \\ H\Gamma & D & 0 & 0 \\ \vdots & \vdots & \ddots & \vdots \\ H\Phi^{J-1}\Gamma & H\Phi^{J-2}\Gamma & \dots & D \end{bmatrix} \begin{bmatrix} \bar{u}_0 \\ \bar{u}_1 \\ \vdots \\ \bar{u}_J \end{bmatrix} \quad \text{A.35}$$

Notice that the initial state is multiplied by the observability matrix. This represents the “free response” in dynamic matrix control – how the system will move without intervention. It is a component of the response irrespective of our control actions. The Toeplitz diagonal matrix is the “forced response,” the response we influence. The Toeplitz matrix is given its own symbol:

$$H_J = \begin{bmatrix} D & 0 & 0 & 0 \\ H\Gamma & D & 0 & 0 \\ \vdots & \vdots & \ddots & \vdots \\ H\Phi^{J-1}\Gamma & H\Phi^{J-2}\Gamma & \cdots & D \end{bmatrix} \quad \text{A.36}$$

Equation A.33 and Equation A.35 are the “extended state space equations:”

$$\vec{x}_J = \Phi^J \vec{x}_0 + \Delta_J \begin{bmatrix} \vec{u}_0 \\ \vec{u}_1 \\ \vdots \\ \vec{u}_{J-1} \end{bmatrix} \quad \text{A.37}$$

$$\begin{bmatrix} \vec{y}_0 \\ \vec{y}_1 \\ \vdots \\ \vec{y}_J \end{bmatrix} = \mathcal{G}_J \vec{x}_0 + H_J \begin{bmatrix} \vec{u}_0 \\ \vec{u}_1 \\ \vdots \\ \vec{u}_J \end{bmatrix} \quad \text{A.38}$$

We can elaborate these equations on data-rich “Hankel” matrices. For example, a given “past” horizon length of $J=2$ (Figure A.3) starting at $k=0$ would yield the following output matrix:

$$Y_{0|J} = \begin{bmatrix} \vec{y}_0 & \vec{y}_1 & \vec{y}_2 & \cdots \\ \vec{y}_{0+1} & \vec{y}_2 & \vec{y}_3 & \cdots \\ \vdots & \vdots & \vdots & \cdots \\ \vec{y}_{0+J-1} & \vec{y}_{1+J-1} & \vec{y}_{2+J-1} & \cdots \end{bmatrix} = \left[\begin{bmatrix} \vec{y}_0 & \vec{y}_1 & \vec{y}_2 & \cdots \\ \vec{y}_1 & \vec{y}_2 & \vec{y}_3 & \cdots \end{bmatrix} \right] \Bigg\} J = 2$$

The number of columns is solely dependent on the amount of data available for organization into a feasible horizon of interest. Thus, the Hankel matrices respect our horizon lengths (number or rows) while representing long history of process data across their columns:

$$\begin{bmatrix} \vec{y}_2 & \vec{y}_3 & \vec{y}_4 & \vec{y}_5 \\ \vec{y}_3 & \vec{y}_4 & \vec{y}_5 & \vec{y}_6 \end{bmatrix} = \begin{bmatrix} H \\ H\Phi \end{bmatrix} \begin{bmatrix} \vec{x}_2 & \vec{x}_3 & \vec{x}_4 & \vec{x}_5 \end{bmatrix} + \begin{bmatrix} D & 0 \\ H\Gamma & D \end{bmatrix} \begin{bmatrix} \vec{u}_2 & \vec{u}_3 & \vec{u}_4 & \vec{u}_5 \\ \vec{u}_3 & \vec{u}_4 & \vec{u}_5 & \vec{u}_6 \end{bmatrix}$$

$$\begin{aligned} Y_{\text{future}} &= \mathcal{G}_L X_{\text{future}} + H_L U_{\text{future}} \\ Y_{J|L} &= \mathcal{G}_L X_{J|L} + H_L U_{J|L} \end{aligned} \quad \text{A.39}$$

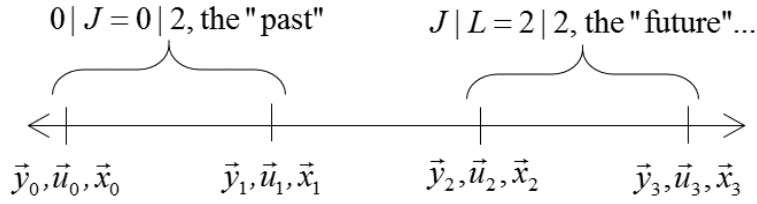
$$\begin{bmatrix} \bar{y}_0 & \bar{y}_1 & \bar{y}_2 & \bar{y}_4 \\ \bar{y}_1 & \bar{y}_2 & \bar{y}_3 & \bar{y}_5 \end{bmatrix} = \begin{bmatrix} H \\ H\Phi \end{bmatrix} \begin{bmatrix} \bar{x}_0 & \bar{x}_1 & \bar{x}_2 & \bar{x}_3 \end{bmatrix} + \begin{bmatrix} D & 0 \\ H\Gamma & D \end{bmatrix} \begin{bmatrix} \bar{u}_0 & \bar{u}_1 & \bar{u}_2 & \bar{u}_4 \\ \bar{u}_1 & \bar{u}_2 & \bar{u}_3 & \bar{u}_5 \end{bmatrix}$$

$$Y_{"past"} = \mathcal{G}_J X_{"past"} + H_J U_{"past"}$$

$$Y_{0J} = \mathcal{G}_J X_{01} + H_J U_{0J}$$
A.40

Here, the notation of David Di Rusico has been emphasized.

Figure A.3: a state timeline originating at time $k = 0$ with $J=2$ and $L=2$.



We can also use Hankel matrices within Equation A.37:

$$\begin{bmatrix} \bar{x}_2 & \bar{x}_3 & \bar{x}_4 & \bar{x}_5 \end{bmatrix} = \Phi^2 \begin{bmatrix} \bar{x}_0 & \bar{x}_1 & \bar{x}_2 & \bar{x}_3 \end{bmatrix} + \begin{bmatrix} \Phi\Gamma & \Gamma \end{bmatrix} \begin{bmatrix} \bar{u}_0 & \bar{u}_1 & \bar{u}_2 & \bar{u}_3 \\ \bar{u}_1 & \bar{u}_2 & \bar{u}_3 & \bar{u}_4 \end{bmatrix}$$

$$X_{"future"} = \Phi^J X_{"past"} + \Delta_J U_{"past"}$$

$$X_{J1} = \Phi^J X_{01} + \Delta_J U_{0J}$$
A.41

Together, we have three Hankel equations:

$$Y_{"future"} = \mathcal{G}_L X_{"future"} + H_L U_{"future"} \quad \text{A.39}$$

$$Y_{"past"} = \mathcal{G}_J X_{"past"} + H_J U_{"past"} \quad \text{A.40}$$

$$X_{"future"} = \Phi^J X_{"past"} + \Delta_J U_{"past"} \quad \text{A.41}$$

With this, we can completely eliminate the states. Specifically, substitute Equation A.40 into

Equation A.41, then insert into Equation A.39:

$$Y_{"future"} = \mathcal{G}_L \left[\Phi^J \left(\mathcal{G}_J^{-1} Y_{"past"} - \mathcal{G}_J^{-1} H_J U_{"past"} \right) + \Delta_J U_{"past"} \right] + H_L U_{"future"} \quad \text{A.42}$$

We have arrived at a statement wholly on known inputs and outputs, without any reference to the states. Lets carefully restructure the “nested Russian dolls” inside this expression (Figure A.4):

$$Y_{"future"} = \mathcal{G}_L \left[\Delta_J - \Phi^J \mathcal{G}_J^{-1} H_J \quad \Phi^J \mathcal{G}_J^{-1} \right] \begin{bmatrix} U_{"past"} \\ Y_{"past"} \end{bmatrix} + H_L U_{"future"} \quad \text{A.42}$$

Given Equation A.41 and Equation A.40 we can see that the 1st term of Equation A.42 represents the future states:

$$X_{"future"} = \left[\Delta_J - \Phi^J \mathcal{G}_J^{-1} H_J \quad \Phi^J \mathcal{G}_J^{-1} \right] \begin{bmatrix} U_{"past"} \\ Y_{"past"} \end{bmatrix} \quad \text{A.43}$$

For clarity, lets give the two matrices in Equation A.43 symbols:

$$X_{"future"} = MW_{"past"} \quad \text{A.44}$$

To summarize, we have an expression that harbors the state sequence (Equation A.43), but is written wholly on the known inputs and outputs:

$$Y_{"future"} = \mathcal{G}_L MW_{"past"} + H_L U_{"future"} \quad \text{A.42}$$

Superficially, we are no closer to finding the system matrices or state sequence ($\Phi, \Gamma, H, D, X_{"future"}$). However, for uncontrolled (open loop) systems the future inputs, the rightmost term in Equation A.42, have *no* direct correlation with the past inputs embedded within $W_{"past"}$. To move towards a straightforward identification algorithm we discard future inputs from our analysis. We want to work in a space that is wholly orthogonal to the future inputs, thereby isolating the output behavior that has propagated forward through the states. This is achieved by projecting our data into the space perpendicular to the future inputs, $U_{"future"}^\perp$:

$$Y_{"future"} / U_{"future"}^\perp$$

When applied to Equation A.42, we have:

$$\begin{aligned}
Y_{"future"} / U_{"future"}^\perp &= \mathcal{G}_L M W_{"past"} / U_{"future"}^\perp + H_L U_{"future"} / U_{"future"}^\perp \\
&= \mathcal{G}_L M W_{"past"} / U_{"future"}^\perp
\end{aligned} \tag{A.42}$$

(because $U_{"future"} / U_{"future"}^\perp = 0$)

We have eliminated the troublesome sum from Equation A.42, but a decomposition for identification remains mysterious. The smoke clears after some matrix algebra:

$$Y_{"future"} / U_{"future"}^\perp = \mathcal{G}_L M W_{"past"} / U_{"future"}^\perp \tag{A.43}$$

$$\left[Y_{"future"} / U_{"future"}^\perp \right] \left[W_{"past"} / U_{"future"}^\perp \right]^{-1} = \mathcal{G}_L M$$

$$\left[Y_{"future"} / U_{"future"}^\perp \right] \left[W_{"past"} / U_{"future"}^\perp \right]^{-1} W_{"past"} = \mathcal{G}_L M W_{"past"} \tag{A.44}$$

The rightmost expression contains Equation A.44, which reveals that Equation A.44 is a statement wholly on known data and a convenient decomposition of the states:

$$\left[Y_{"future"} / U_{"future"}^\perp \right] \left[W_{"past"} / U_{"future"}^\perp \right]^{-1} W_{"past"} = \mathcal{G}_L X_{"future"} \tag{A.44}$$

We use singular value decomposition to discover both the future state sequence *and* the observability matrix, which makes identification of the remaining system matrices trivial:

$$\begin{aligned}
\left[Y_{"future"} / U_{"future"}^\perp \right] \left[W_{"past"} / U_{"future"}^\perp \right]^{-1} W_{"past"} &= U \Sigma V^T \\
&= \mathcal{G}_L T^{-1} \Sigma T X_{"future"}
\end{aligned} \tag{A.45}$$

Or written more explicitly:

$$U \Sigma V^T = \begin{bmatrix} HT^{-1} \\ HT^{-1} T \Phi T^{-1} \\ HT^{-1} T \Phi T^{-1} T \Phi T^{-1} \\ \vdots \end{bmatrix} \begin{bmatrix} \lambda_1 & 0 & \cdots \\ 0 & \lambda_2 & \cdots \\ \vdots & \vdots & \ddots \end{bmatrix} \begin{bmatrix} T \bar{x}_0 & T \bar{x}_1 & \cdots \end{bmatrix}$$

As promised, we have identified a valid state sequence within the bounds of a similarity transform, T , of the physical states. The singular values reveal the system order, the number of states that play significant roles in the system dynamics.

The system identification algorithm we have described is appropriate for uncontrolled systems (open-loop systems). It is the basis for many subspace identification routines (n4sid, moesp). However, if controllers are active there is a correlation between the past and future, which is problematic in these regimes because they rely on uncorrelated past and future inputs.

Figure A.4: Nested Russian dolls *are* subspace identification.



We would like to identify our systems while controllers are active (closed-loop identification) or phenomena strongly links the past and future. This is akin to parsing attributes of acceleration in a car with cruise control engaged – some acceleration owes to system characteristics (the engine) while other aspects result from controller behavior. We also wish to avoid excessive matrix multiplication, which is numerically unsafe and inherent to orthogonal

projection. David Di Rusico has focused on these issues and his algorithm is described henceforth [86].

The DSRe algorithm is based on different views of the state space, views that incorporate stochastic noise. To represent noise consider a vector \vec{e}_k of white noise with variance $E[\vec{e}_k \vec{e}_k^T] = I$. This “generic” noise (Figure A.5) can be transformed into our systems by appending Equations A.7 and A.22:

$$\vec{x}_{k+1} = \Phi \vec{x}_k + \Gamma \vec{u}_k + C \vec{e}_k \quad \text{A.46}$$

$$\vec{y}_k = H \vec{x}_k + F \vec{e}_k \quad \text{A.47}$$

The process noise covariance is $E[C \vec{e}_k \vec{e}_k^T C^T] = E[CC^T]$ and the sensor noise covariance is

$E[F \vec{e}_k \vec{e}_k^T F^T] = E[FF^T]$. The system can also be structured from a control perspective, where

any noise (“surprises”) in the output are fed into the state. Presumably, this feedback can control the state at a desired setpoint:

$$\vec{x}_{k+1} = \Phi \vec{x}_k + \Gamma \vec{u}_k + K \vec{\varepsilon}_k \quad \text{A.48}$$

$$\vec{y}_k = H \vec{x}_k + \vec{\varepsilon}_k \quad \text{A.49}$$

The innovations, $\vec{\varepsilon}_k$, bridge random disturbances and controller feedback. The stochastic and

innovations structures are actually identical with $F \vec{e}_k = \vec{\varepsilon}_k$ and $K = CF$.

Figure A.5: Kenny G., an example of generic “white” noise.



To arrive at an effective identification algorithm, we build an extended state space from these equations. Using the innovations form we have:

$$\begin{aligned}
 \vec{x}_1 &= \Phi \vec{x}_0 + \Gamma \vec{u}_0 + K \vec{\varepsilon}_0 && = \Phi \vec{x}_0 + \Gamma \vec{u}_0 + K(\vec{y}_0 - H\vec{x}_0) \\
 &= (\Phi - KH)\vec{x}_0 + \Gamma \vec{u}_0 + K\vec{y}_0 \\
 \vec{x}_2 &= \Phi \vec{x}_1 + \Gamma \vec{u}_1 + K \vec{\varepsilon}_1 && = \Phi \vec{x}_1 + \Gamma \vec{u}_1 + K(\vec{y}_1 - H\vec{x}_1) \\
 &= \Phi \left\{ (\Phi - KH)\vec{x}_0 + \Gamma \vec{u}_0 + K\vec{y}_0 \right\} + \Gamma \vec{u}_1 + K \left\{ \vec{y}_1 - H((\Phi - KH)\vec{x}_0 + \Gamma \vec{u}_0 + K\vec{y}_0) \right\} \\
 &= \left\{ \Phi^2 - \Phi KH - KH\Phi + (KH)^2 \right\} \vec{x}_0 + \Gamma \vec{u}_1 + K\vec{y}_1 + (\Phi - KH)\Gamma \vec{u}_0 + (\Phi - KH)K\vec{y}_0 \\
 &= (\Phi - KH)^2 \vec{x}_0 + \left[\begin{array}{cc|cc}
 (\Phi - KH)^1 \Gamma & \Gamma & (\Phi - KH)^1 K & K
 \end{array} \right] \begin{bmatrix} \vec{u}_0 \\ \vec{u}_1 \\ \vec{y}_0 \\ \vec{y}_1 \end{bmatrix}
 \end{aligned}$$

Or, without belabouring the derivation:

$$\bar{x}_J = (\Phi - KH)^J \bar{x}_0 + \begin{bmatrix} \Delta_J^d & \Delta_J^s \end{bmatrix} \begin{bmatrix} \bar{u}_0 \\ \bar{u}_1 \\ \vdots \\ \bar{y}_0 \\ \bar{y}_1 \\ \vdots \end{bmatrix} \quad \text{A.50}$$

$$\Delta_J^d = \begin{bmatrix} (\Phi - KH)^{J-1} \Gamma & (\Phi - KH)^{J-2} \Gamma & \dots & \Gamma \end{bmatrix} \quad \text{A.51}$$

$$\Delta_J^s = \begin{bmatrix} (\Phi - KH)^{J-1} K & (\Phi - KH)^{J-2} K & \dots & K \end{bmatrix} \quad \text{A.52}$$

We have developed an expression for a future state at time J , the end of our horizon, given the initial state and a history of control moves and outputs. A new reverse controllability matrix (Equation A.50) is evident, which is split into deterministic (superscript d) and stochastic (superscript s) components. This expression is valid for Hankel matrices:

$$X_{J|1} = (\Phi - KH)^J X_{0|1} + \begin{bmatrix} \Delta_J^d & \Delta_J^s \end{bmatrix} \begin{bmatrix} U_{0,J} \\ Y_{0,J} \end{bmatrix} \quad \text{A.53}$$

We have found an expression analogous to Equation A.41. To complete an extended state space for closed-loop systems we need expressions similar to Equations A.39 and A.40. This is found through manipulation of the stochastic state space:

$$\begin{aligned}
\bar{y}_0 &= H\bar{x}_0 + F\bar{e}_0 \\
\bar{x}_1 &= [\Phi]\bar{x}_0 + [\Gamma]\bar{u}_0 + [C]\bar{e}_0 & \bar{y}_1 &= H\bar{x}_1 + F\bar{e}_1 \\
& & &= [H\Phi]\bar{x}_0 + [H\Gamma]\bar{u}_0 + [HC]\bar{e}_0 + F\bar{e}_1 \\
& & &= [H\Phi]\bar{x}_0 + [H\Gamma \quad 0] \begin{bmatrix} \bar{u}_0 \\ \bar{u}_1 \end{bmatrix} + [HC \quad F] \begin{bmatrix} \bar{e}_0 \\ \bar{e}_1 \end{bmatrix} \\
\bar{x}_2 &= [\Phi^2]\bar{x}_0 + [\Phi\Gamma \quad \Gamma] \begin{bmatrix} \bar{u}_0 \\ \bar{u}_1 \end{bmatrix} + [\Phi C \quad C] \begin{bmatrix} \bar{e}_0 \\ \bar{e}_1 \end{bmatrix} & \bar{y}_2 &= H\bar{x}_2 + F\bar{e}_2 \\
& & &= [H\Phi^2]\bar{x}_0 + [H\Phi\Gamma \quad H\Gamma] \begin{bmatrix} \bar{u}_0 \\ \bar{u}_1 \end{bmatrix} + [H\Phi C \quad HC] \begin{bmatrix} \bar{e}_0 \\ \bar{e}_1 \end{bmatrix} + F\bar{e}_2 \\
& & &= [H\Phi^2]\bar{x}_0 + [H\Phi\Gamma \quad H\Gamma \quad 0] \begin{bmatrix} \bar{u}_0 \\ \bar{u}_1 \\ \bar{u}_2 \end{bmatrix} + [H\Phi C \quad HC \quad F] \begin{bmatrix} \bar{e}_0 \\ \bar{e}_1 \\ \bar{e}_2 \end{bmatrix} \\
& \vdots & & \vdots
\end{aligned}$$

We are, again, building a Teoplitz matrix:

$$\begin{aligned}
\begin{bmatrix} \bar{y}_0 \\ \bar{y}_1 \\ \vdots \\ \bar{y}_J \end{bmatrix} &= \begin{bmatrix} H \\ H\Phi \\ \vdots \\ H\Phi^J \end{bmatrix} \bar{x}_0 + \dots \\
& \quad \begin{bmatrix} 0 & 0 & 0 & 0 \\ H\Gamma & 0 & 0 & 0 \\ \vdots & \vdots & \ddots & \vdots \\ H\Phi^{J-1}\Gamma & H\Phi^{J-2}\Gamma & \dots & 0 \end{bmatrix} \begin{bmatrix} \bar{u}_0 \\ \bar{u}_1 \\ \vdots \\ \bar{u}_J \end{bmatrix} + \dots \\
& \quad \begin{bmatrix} F & 0 & 0 & 0 \\ HC & F & 0 & 0 \\ \vdots & \vdots & \ddots & \vdots \\ H\Phi^{J-1}C & H\Phi^{J-2}C & \dots & F \end{bmatrix} \begin{bmatrix} \bar{e}_0 \\ \bar{e}_1 \\ \vdots \\ \bar{e}_J \end{bmatrix}
\end{aligned} \tag{A.54}$$

Note that the control Teoplitz matrix has a diagonal of zeros, unlike Equation A.35, because there is no direct feedthrough of control actions on the measured outputs. We adopt the same shorthand as Equation A.39 for this expression:

$$\begin{bmatrix} \bar{y}_0 \\ \bar{y}_1 \\ \vdots \\ \bar{y}_J \end{bmatrix} = \mathcal{G}_J \bar{x}_0 + \mathbf{H}_J^d \begin{bmatrix} \bar{u}_0 \\ \bar{u}_1 \\ \vdots \\ \bar{u}_J \end{bmatrix} + \mathbf{H}_J^s \begin{bmatrix} \bar{e}_0 \\ \bar{e}_1 \\ \vdots \\ \bar{e}_J \end{bmatrix} \quad \text{A.54}$$

Finally, using Hankel matrices we can assemble an extended state space for closed-loop identification analogous to Equations A.41 and A.39:

$$X_{J|1} = (\Phi - KH)^J X_{0|1} + \begin{bmatrix} \Delta_J^d & \Delta_J^s \end{bmatrix} \begin{bmatrix} U_{0,J} \\ Y_{0,J} \end{bmatrix} \quad \text{A.53}$$

$$Y_{0,J} = \mathcal{G}_J X_{0|1} + \mathbf{H}_J^d U_{0,J} + \mathbf{H}_J^s E_{0,J} \quad \text{A.54}$$

We can readily write Equation A.54 on the future horizon:

$$Y_{J|L} = \mathcal{G}_L X_{J|1} + \mathbf{H}_L^d U_{J|L} + \mathbf{H}_L^s E_{J|L} \quad \text{A.54}$$

Manipulating this extended state space yields the DSRe “past-future” equation:

$$Y_{J|L} = \mathcal{G}_L (\Phi - KH)^J X_{0|1} + \mathcal{G}_L \begin{bmatrix} \Delta_J^d & \Delta_J^s \end{bmatrix} \begin{bmatrix} U_{0,J} \\ Y_{0,J} \end{bmatrix} + \mathbf{H}_L^d U_{J|L} + \mathbf{H}_L^s E_{J|L} \quad \text{A.55}$$

After rearrangement, we have:

$$Y_{J|L} = \mathcal{G}_L (\Phi - KH)^J X_{0|1} + \begin{bmatrix} \mathbf{H}_L^d & \mathcal{G}_L \Delta_J^d & \mathcal{G}_L \Delta_J^s \end{bmatrix} \begin{bmatrix} U_{J|L} \\ U_{0,J} \\ Y_{0,J} \end{bmatrix} + \mathbf{H}_L^s E_{J|L} \quad \text{A.55}$$

This statement indicates that future outputs are a function of some array of initial states $X_{0|1} = [\bar{x}_0 \quad \bar{x}_1 \quad \bar{x}_2 \quad \dots]$, future inputs, past input-output pairs, and future noise. David Di Rusico argues that the state dependent term is irrelevant as the past horizon grows ($J \gg 0$). Certainly, if the linear combination $\Phi - KH$ is nilpotent this term will zero as J grows. We expect this behavior in any system with feedback controllers active, given that K is chosen to zero state deviations. Furthermore, if the system is controlled or stable around a steady state most values in

X_{01} will average to zero (we drive the state to zero). Thus, we have strong intuitive reasons to believe that the initial states are irrelevant. In DSRe the butterfly effect does not exist (Figure A.6). We are left with a simpler Equation:

$$Y_{J/L} = \begin{bmatrix} H_L^d & \mathcal{G}_L \Delta_J^d & \mathcal{G}_L \Delta_J^s \end{bmatrix} \begin{bmatrix} U_{J/L} \\ U_{0/J} \\ Y_{0/J} \end{bmatrix} + H_L^s E_{J/L}, \quad J \gg 1 \quad \text{A.56}$$

Finally, we choose a narrow future horizon of $L = 1$. Note that in this case $H_1^d = 0$, $\mathcal{G}_L = \Gamma$, and $H_1^s = F$ (from Equation A.54). We are left with:

$$Y_{J/1} = \begin{bmatrix} \Gamma \Delta_J^d & \Gamma \Delta_J^s \end{bmatrix} \begin{bmatrix} U_{0/J} \\ Y_{0/J} \end{bmatrix} + F E_{J/1} \quad \text{A.57}$$

This is a relatively simple expression. The future outputs are a function of past input-output pairs and the future innovation sequence.

Figure A.6: According to David Di Rusico, this butterfly *doesn't matter*.



Linear regression is a useful framework for viewing Equation A.57, but we must recognize that we're working with long arrays, not tall vectors. That is, we're concerned with rowspaces and not column spaces. For illustration, in typical linear regression ($b = Ax$) we have:

$$\begin{matrix} \text{tall} \\ \left[\begin{array}{c} \\ \\ \\ \end{array} \right] \end{matrix} = \begin{matrix} \\ \left[\begin{array}{c} \\ \\ \\ \end{array} \right] \\ \text{long} \end{matrix} \begin{matrix} \text{tall} \\ \left[\begin{array}{c} \\ \\ \\ \end{array} \right] \end{matrix}$$

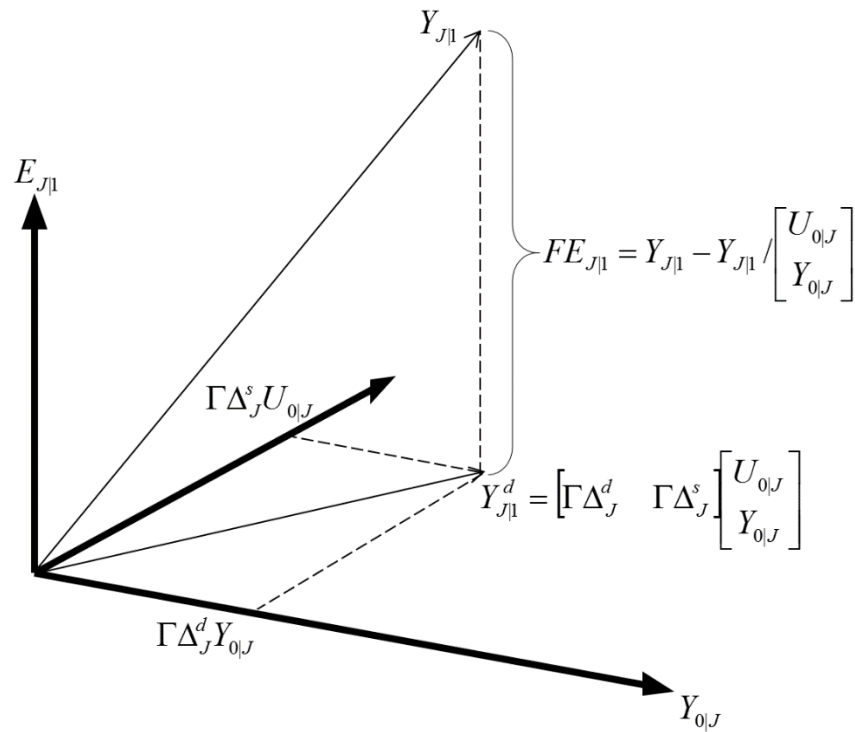
A “tall” set of weights is collapsed over a long matrix of basis vectors, usually composed of descriptor data, into a tall vector of results. Unfortunately, unlike most engineering the formalisms around subspace identification are built on rowspaces:

$$\begin{matrix} \left[\begin{array}{c} \\ \\ \\ \end{array} \right] \\ \text{long} \end{matrix} = \begin{matrix} \left[\begin{array}{c} \\ \\ \\ \end{array} \right] \\ \text{long} \end{matrix} \begin{matrix} \left[\begin{array}{c} \\ \\ \\ \end{array} \right] \\ \text{tall} \end{matrix}$$

Now a “long” matrix of weights are collapsed over a tall matrix of basis rows, which consists of I/O data, to yield a long array of results. Each view of the universe is equally valid, the choice in subspace identification is simply atypical.

With a firm view of the problem inhand, from Equation A.57 we see that past input-output data is a basis for future outputs (Figure A.7). The unknown reverse controllability matrices weight this basis to yield the future outputs. However, due to feedback and stochasticity the future cannot be fully predicted on this basis alone – the innovations push future observations away from complete determinism.

Figure A.7: Projection as regression, the case of Equation A.57, Y_{J1}^d is the deterministic portion of the outputs.



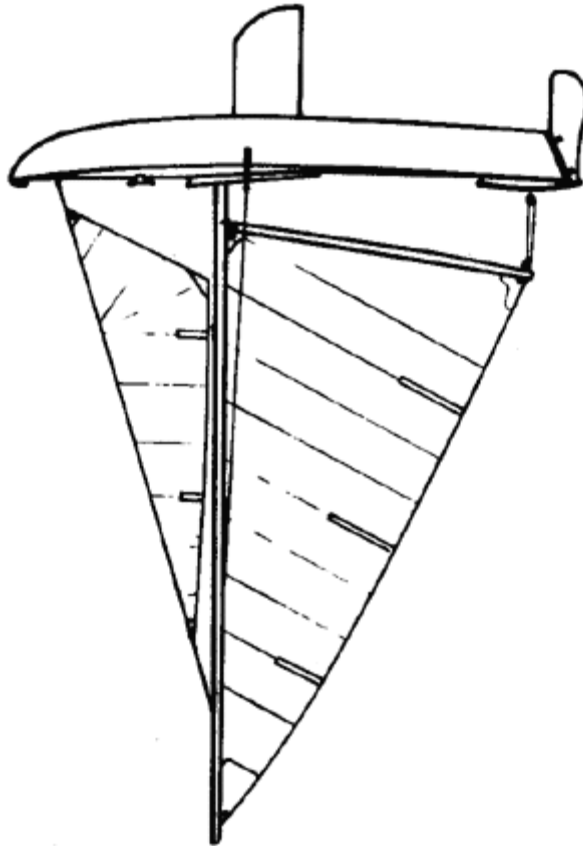
In traditional linear regression, the results and descriptor variables are available. The basis vectors (A in $b = Ax$) are found by minimizing a sum of squares:

$$(Ax - b)^2$$

Alternatively, the minimization can be found through projections. In either case, a basis is discovered.

In Equation A.57 two bases are known, $U_{0,J}$ and $Y_{0,J}$. A third basis, the future innovations (the future noise) E_{J1} , are orthogonal to the past (Figure A.7). However, the descriptor variables Δ_J^d , Δ_J^s and F are mysterious. This inverts our usual view of linear regression (Figure A.8), where descriptors are abundant. DSRe, like other subspace methods, contends with this challenge via LQ decomposition, the rowspace equivalent of QR decomposition (cite appendix).

Figure A.8: We face linear regression, capsized.



First we assemble our data into a matrix for LQ (QR) decomposition, which serves to structure and compress the data:

$$\begin{bmatrix} U_{0,J} \\ Y_{0,J} \\ Y_{J||} \end{bmatrix} = \begin{bmatrix} R_{11} & 0 & 0 \\ R_{21} & R_{22} & 0 \\ R_{31} & R_{32} & R_{33} \end{bmatrix} \begin{bmatrix} Q_1 \\ Q_2 \\ Q_3 \end{bmatrix} \quad \text{A.58}$$

We can see very clearly that:

$$\begin{aligned} U_{0,J} &= [R_{11} \quad 0 \quad 0]Q \\ Y_{0,J} &= [R_{21} \quad R_{22} \quad 0]Q \\ Y_{J||} &= [R_{31} \quad R_{32} \quad R_{33}]Q \end{aligned} \quad \text{A.59}$$

To find the deterministic portion of our future outputs, $Y_{J||}$, we take an orthogonal projection:

$$Y_{J|I}^d = Y_{J|I} \begin{bmatrix} U_{0,J}^T & Y_{0,J}^T \end{bmatrix} \left(\begin{bmatrix} U_{0,J} \\ Y_{0,J} \end{bmatrix} \begin{bmatrix} U_{0,J}^T & Y_{0,J}^T \end{bmatrix} \right)^{-1} \begin{bmatrix} U_{0,J} \\ Y_{0,J} \end{bmatrix} \quad \text{A.60}$$

Inserting our definitions from LQ (QR) decomposition, we get:

$$Y_{J|I}^d = \begin{bmatrix} R_{31} & R_{32} & R_{33} \end{bmatrix} Q Q^T \begin{bmatrix} R_{11} & R_{21} \\ 0 & R_{22} \\ 0 & 0 \end{bmatrix} \left(\begin{bmatrix} R_{11} & 0 & 0 \\ R_{21} & R_{22} & 0 \end{bmatrix} Q Q^T \begin{bmatrix} R_{11} & R_{21} \\ 0 & R_{22} \\ 0 & 0 \end{bmatrix} \right)^{-1} \begin{bmatrix} R_{11} & 0 & 0 \\ R_{21} & R_{22} & 0 \end{bmatrix} Q$$

Given that Q is orthonormal, $Q Q^T = I$:

$$Y_{J|I}^d = \begin{bmatrix} R_{31} & R_{32} & R_{33} \end{bmatrix} R^T (R R^T)^{-1} R Q \quad \text{A.61}$$

$$R = \begin{bmatrix} r & 0 \end{bmatrix} = \begin{bmatrix} R_{11} & 0 & 0 \\ R_{21} & R_{22} & 0 \end{bmatrix}$$

We can distribute the inverse for the special case of diagonal matrices:

$$Y_{J|I}^d = \begin{bmatrix} R_{31} & R_{32} & R_{33} \end{bmatrix} R^T (R^T)^{-1} R^{-1} R Q \quad \text{A.62}$$

$$Y_{J|I}^d = \begin{bmatrix} R_{31} & R_{32} & R_{33} \end{bmatrix} \begin{bmatrix} I & 0 \\ 0 & 0 \end{bmatrix} \begin{bmatrix} I & 0 \\ 0 & 0 \end{bmatrix} Q \quad \text{A.63}$$

$$Y_{J|I}^d = \begin{bmatrix} R_{31} & R_{32} \end{bmatrix} \begin{bmatrix} Q_1 \\ Q_2 \end{bmatrix} \quad \text{A.64}$$

Note that for our nonsquare matrices the penrose pseudoinverse substitutes for the inverse. From

Figure A.7 we know that the future response is the sum of two tensors:

$$\begin{aligned} Y_{J|I} &= Y_{J|I}^d + E_{J|I} \\ &= \begin{bmatrix} R_{31} & R_{32} \end{bmatrix} \begin{bmatrix} Q_1 \\ Q_2 \end{bmatrix} + E_{J|I} \\ &= \begin{bmatrix} R_{31} & R_{32} \end{bmatrix} \begin{bmatrix} Q_1 \\ Q_2 \end{bmatrix} + R_{33} Q_3 \end{aligned} \quad \text{A.65}$$

Thus, the innovations are also available from the LQ (QR) decomposition:

$$E_{J|I} = R_{33} Q_3 \quad \text{A.67}$$

Here R_{33} can be taken as F , where FF^T gives the measurement noise covariance. Now equipped with the expected responses and innovations we can formulate a deterministic subspace identification problem:

$$\bar{x}_{k+1} = \Phi \bar{x}_k + \begin{bmatrix} \Gamma & K \end{bmatrix} \begin{bmatrix} \bar{u}_k \\ \bar{\varepsilon}_k \end{bmatrix} \quad \text{A.48}$$

$$\bar{y}_k - \bar{\varepsilon}_k = H \bar{x}_k \quad \text{A.49}$$

Here, we have recast our view of what constitutes a response (left side of Equation A.49) and input (rightmost column of Equation A.48).

The deterministic identification relies on a particular view of the state space. Recall the DSRe formulation of the extended state space equations:

$$X_{J\ell} = (\Phi - KH)^J X_{0\ell} + \begin{bmatrix} \Delta_J^d & \Delta_J^s \end{bmatrix} \begin{bmatrix} U_{0,J} \\ Y_{0,J} \end{bmatrix} \quad \text{A.53}$$

$$Y_{0,J} = \mathcal{G}_J X_{0\ell} + H_J^d U_{0,J} + H_J^s E_{0,J} \quad \text{A.54}$$

We can readily cast these equations on the future horizon, for which we have identified the innovations:

$$X_{L\ell} = (\Phi - KH)^L X_{J\ell} + \begin{bmatrix} \Delta_L^d & \Delta_L^s \end{bmatrix} \begin{bmatrix} U_{J/L} \\ Y_{J/L} \end{bmatrix} \quad \text{A.53}$$

$$Y_{J/L} = \mathcal{G}_L X_{J\ell} + H_L^d U_{J/L} + H_L^s E_{J/L} \quad \text{A.54}$$

The identification problem was restructured to place innovations inside the input given our knowledge of the noise (Equations A.48, A.49, and A.67), thus we can remove stochastic terms:

$$X_{L\ell} = \Phi^L X_{J\ell} + \Delta_L U_{J/L} \quad \text{A.68}$$

$$Y_{J/L} = \mathcal{G}_L X_{J\ell} + H_L U_{J/L} \quad \text{A.69}$$

We can also displace our timeline by some arbitrary index M :

$$X_{J+M/L} = \Phi^M X_{J/L} + \Delta_M U_{J/M} \quad \text{A.70}$$

$$Y_{J+M/L} = \mathcal{G}_L X_{J+M/L} + H_L U_{J+M/L} \quad \text{A.71}$$

We can combine the displaced equations:

$$Y_{J+M/L} = \mathcal{G}_L (\Phi^M X_{J/L} + \Delta_M U_{J/M}) + H_L U_{J+M/L} \quad \text{A.72}$$

Finally, we can insert Equation A.69 into Equation A.72:

$$Y_{J+M/L} = \mathcal{G}_L \left\{ \Phi^M \mathcal{G}_L^{-1} (Y_{J/L} - H_L U_{J/L}) + \Delta_M U_{J/M} \right\} + H_L U_{J+M/L} \quad \text{A.73}$$

Rearrangement gives a matrix dense equation with no direct dependence on the states:

$$Y_{J+M/L} = \mathcal{G}_L \Phi^M \mathcal{G}_L^{-1} Y_{J/L} + \left[\begin{array}{cc} \mathcal{G}_L \Delta_M & H_L \end{array} \right] - \left[\begin{array}{cc} \mathcal{G}_L \Phi^M \mathcal{G}_L^{-1} H_L & 0 \end{array} \right] \left[\begin{array}{c} U_{J/M} \\ U_{J+M/L} \end{array} \right] \quad \text{A.74}$$

$$Y_{J+M/L} = \mathcal{G}_L \Phi^M \mathcal{G}_L^{-1} Y_{J/L} + \left[\begin{array}{cc} \mathcal{G}_L \Delta_M & H_L \end{array} \right] - \left[\begin{array}{cc} \mathcal{G}_L \Phi^M \mathcal{G}_L^{-1} H_L & 0 \end{array} \right] U_{J/L+M} \quad \text{A.75}$$

We simplify this equation by introducing notation:

$$Y_{J+M/L} = \tilde{A} Y_{J/L} + \tilde{B} U_{J/L+M} \quad \text{A.76}$$

With:

$$\tilde{A} = \mathcal{G}_L \Phi^M \mathcal{G}_L^{-1} \quad \text{A.77}$$

$$\tilde{B} = \left[\begin{array}{cc} \mathcal{G}_L \Delta_M & H_L \end{array} \right] - \left[\begin{array}{cc} \tilde{A} H_L & 0 \end{array} \right] \quad \text{A.78}$$

DSR assumes that the inverse observability matrix can be described as a least squares optimization on the true (albeit unknown) states:

$$\min \left\{ \mathcal{G}_L X_{L/L} - (Y_{J/L} - H_L U_{J/L}) \right\}^2 \quad \text{A.79}$$

In analogy with $\min \{Ax - b\}^2$ and the normal equation we have:

$$\mathcal{G}_L^{-1} = (\mathcal{G}_L^T \mathcal{G}_L)^{-1} \mathcal{G}_L^T \quad \text{A.80}$$

Thus, we are left with:

$$Y_{J+M/L} = \tilde{A} Y_{J/L} + \tilde{B} U_{J/L+M} \quad \text{A.81}$$

$$\tilde{A} = \mathcal{G}_L \Phi^M (\mathcal{G}_L^T \mathcal{G}_L)^{-1} \mathcal{G}_L^T \quad \text{A.82}$$

$$\tilde{B} = \begin{bmatrix} \mathcal{G}_L \Delta_M & \mathbf{H}_L \end{bmatrix} - \begin{bmatrix} \tilde{A} \mathbf{H}_L & \mathbf{0} \end{bmatrix} \quad \text{A.83}$$

We eliminate the inputs through postmultiplication by the space orthogonal to the inputs.

$$Y_{J+M|L} U_{J|L+M}^\perp = \tilde{A} Y_{J|L} U_{J|L+M}^\perp + \tilde{B} U_{J|L+M} U_{J|L+M}^\perp \quad \text{A.84}$$

$$U_{J|L+M} U_{J|L+M}^\perp = \mathbf{0}$$

$$Y_{J+M|L} U_{J|L+M}^\perp = \tilde{A} Y_{J|L} U_{J|L+M}^\perp \quad \text{A.85}$$

Projection onto the orthogonal subspace is given its own symbol:

$$Z_{J+M|L} = \tilde{A} Z_{J|L} \quad \text{A.86}$$

We can write a second expression on $Z_{J|L}$ based on Equation A.69 written M steps ahead.

$$Y_{J|L} = \mathcal{G}_L X_{J|1} + \begin{bmatrix} \mathbf{H}_L & \mathbf{0} \end{bmatrix} U_{J|L+M} \quad \text{A.87}$$

By post multiplying by $U_{J|L+M}^\perp$ we find:

$$Z_{J|L} = Y_{J|L} U_{J|L+M}^\perp = \mathcal{G}_L X_{J|1} U_{J|L+M}^\perp \quad \text{A.88}$$

For the purposes of data integrity, we do LQ (QR) decomposition on the inputs and outputs:

$$\begin{bmatrix} U_{J|L+M} \\ Y_{J+M|L} \end{bmatrix} = \begin{bmatrix} R_{11} & \mathbf{0} \\ R_{21} & R_{22} \end{bmatrix} \begin{bmatrix} Q_1 \\ Q_2 \end{bmatrix} \quad \text{A.89}$$

Insertion of the matrix multiplicands from Equation A.89 into Equation A.81 gives:

$$\begin{bmatrix} \bar{R}_{21} & \bar{R}_{22} \end{bmatrix} Q = \tilde{A} \begin{bmatrix} R_{21} & R_{22} \end{bmatrix} Q + \tilde{B} \begin{bmatrix} R_{11} & \mathbf{0} \end{bmatrix} Q \quad \text{A.90}$$

$$\begin{bmatrix} \bar{R}_{21} & \bar{R}_{22} \end{bmatrix} = \tilde{A} \begin{bmatrix} R_{21} & R_{22} \end{bmatrix} + \tilde{B} \begin{bmatrix} R_{11} & \mathbf{0} \end{bmatrix} \quad \text{A.91}$$

Here the overbars and underbars refer to deletion of the first or last M block rows respectively.

We can see Equation A.86 within this expression:

$$\begin{aligned} \bar{R}_{22} &= \tilde{A} \underline{R}_{22} \\ &= \tilde{A} Z_{J|L} \\ &= \tilde{A} \mathcal{G}_L X_{J|1} U_{J|L+M}^\perp \end{aligned} \quad \text{A.92}$$

We know that the observability matrix is “tall,” meaning that it can be parsed as the column space of the singular value decomposition (U):

$$\underline{R}_{22} = Z_{J|L} = USV^T \quad \text{A.93}$$

Thus we choose some n number of columns from U , corresponding to significant singular values, as the observability matrix:

$$\mathcal{G}_L = U_n \quad \text{A.94}$$

Recall our definition of \tilde{A} :

$$\tilde{A} = \mathcal{G}_L \Phi^M (\mathcal{G}_L^T \mathcal{G}_L)^{-1} \mathcal{G}_L^T = U_n \Phi^M (U_n^T U_n)^{-1} U_n^T \quad \text{A.82}$$

Inserting this into Equation A.92 (note that $U_n^T = U_n^{-1}$):

$$\bar{R}_{22} = U_n \Phi^M S_n V_n^T \quad \text{A.95}$$

Thus, we can pull the state transition matrix as:

$$\Phi^M = U_n^T \bar{R}_{22} V_n^{-1} \quad \text{A.96}$$

This is especially simple if $M=1$ (the recommended value). The system output matrix H is taken from the first rows of U_n (Equation A.32), where the number of rows harvested is the dimension of y .

For matrix Γ and K we return to Equations A.84 and A.91:

$$\bar{R}_{21} = \tilde{A} \underline{R}_{21} + \tilde{B} R_{11} \quad \text{A.97}$$

Thus, we can find \tilde{B} we can rearrange Equation A.97 (invert R_{11}) or form the following products from Equation A.84:

$$\tilde{B} U_{J|L+M} U_{J|L+M}^T = (Y_{J+M|L} - \tilde{A} Y_{J|L}) U_{J|L+M}^T \quad \text{A.98}$$

$$\tilde{B} = (Y_{J+M|L} - \tilde{A} Y_{J|L}) U_{J|L+M}^T$$

To extract Γ we carefully contemplate matrix \tilde{B} . Consider the case with $L = 3, M = 1$ (thereby $\Delta^d = \Gamma$) and no direct feedthrough:

$$\begin{aligned} \tilde{B} &= \left[\begin{array}{c|c} \mathcal{G}_L \Delta_M & H_L \end{array} \right] - \left[\begin{array}{c|c} \tilde{A} H_L & 0 \end{array} \right] \\ &= \left[\begin{array}{c|c} \left[\begin{array}{cccc} 0 & 0 & 0 & 0 \\ H\Gamma & 0 & 0 & 0 \\ H\Phi\Gamma & H\Gamma & 0 & 0 \\ H\Phi^2\Gamma & H\Phi\Gamma & H\Gamma & 0 \end{array} \right] & \left[\begin{array}{c} 0 \\ 0 \\ 0 \\ 0 \end{array} \right] \end{array} \right] - \left[\begin{array}{c|c} \tilde{A} \left[\begin{array}{cccc} 0 & 0 & 0 & 0 \\ H\Gamma & 0 & 0 & 0 \\ H\Phi\Gamma & H\Gamma & 0 & 0 \\ H\Phi^2\Gamma & H\Phi\Gamma & H\Gamma & 0 \end{array} \right] & 0 \end{array} \right] \end{aligned}$$

We can reorganize the columns to detect a matrix recursion:

$$\begin{aligned} \tilde{B} &= \left[\begin{array}{c|c} \mathcal{G}_L \Delta_M & H_L \end{array} \right] - \left[\begin{array}{c|c} \tilde{A} H_L & 0 \end{array} \right] \\ &= \left[\begin{array}{c|c} \left[\begin{array}{c} 0 \\ H\Gamma \\ H\Phi\Gamma \\ H\Phi^2\Gamma \end{array} \right] & \left[\begin{array}{c} 0 \\ H\Gamma \\ H\Phi\Gamma \\ H\Phi^2\Gamma \end{array} \right] \end{array} \right] - \tilde{A} \left[\begin{array}{c|c} \left[\begin{array}{c} 0 \\ 0 \\ H\Gamma \\ H\Phi\Gamma \end{array} \right] & \left[\begin{array}{c} 0 \\ 0 \\ 0 \\ H\Gamma \end{array} \right] \end{array} \right] \end{aligned}$$

We can see a recursive relationship across block columns of \tilde{B} :

$$\tilde{B} = \left[\begin{array}{c|c} \mathcal{G}_L \Gamma - \tilde{A} [b_{L+M-2}] & [b_{L+M-2} - \tilde{A} b_{L+M-1}] \end{array} \right] \left[\begin{array}{c|c} [b_{L+M-1} - \tilde{A} b_{L+M}] & b_{L+M} \end{array} \right]$$

Which yields the statement, where the subscripts refer to block columns across \tilde{B} :

$$b_i = \tilde{B}_i + \tilde{A} b_{i+1} \quad \text{A.99}$$

Or algorithmically:

$$\begin{aligned} b_{L+M} &= \tilde{B}_{L+M} \\ \text{for } i &= (L+M):1 \\ b_i &= \tilde{B}_i + \tilde{A} b_{i+1} \\ \text{end} \\ \Gamma &= \mathcal{G}_L^{-1} \tilde{A} b_1 = U_n^T \tilde{A} b_1 \end{aligned}$$

The feedback gain K is parsed as the last columns of Γ that correspond to the innovations, while the open loop Γ is the foremost columns.

Appendix B: An Exercise in Kalman Filtering and State Inference

B.1. Introduction

B.1.1 The Kalman Filter

Appendix A described an estimation framework, the “state space.” It is worth reviewing assumptions within this framework:

- 1) Linear time-invariance adequately represents the system.
- 2) $E[\vec{r}] = 0$, sensor noise is mean zero.
- 3) $E[\vec{q}] = 0$, process noise is mean zero.
- 4) $E[\vec{r}\vec{q}^T] = 0$, sensor and process noise are uncorrelated.
- 5) $E[\vec{r}\vec{x}^T] = 0$, sensor noise and process conditions are uncorrelated.
- 6) $E[\vec{q}\vec{x}^T] = 0$, process noise and process conditions are uncorrelated.

The Kalman filter uses the state space to infer truth from noisy operating data [136]. It is built on a Bayesian equation of estimation:

$$\hat{\vec{x}}_{\vec{x}|\vec{y}} = \hat{\vec{x}} + \Sigma_{\vec{x}\vec{y}} \Sigma_{\vec{y}\vec{y}}^{-1} (\vec{y} - \hat{\vec{y}}) \quad \text{B.1}$$

This expression arises from the probability of seeing a joint vector of \vec{x} & \vec{y} . It yields the most likely \vec{x} conditioned on the covariances $(\Sigma_{xy}, \Sigma_{yy}^{-1})$, the current estimate of $\hat{\vec{x}}$, and the observed value of \vec{y} . We must infuse temporal character into Equation B.1:

$$\hat{\vec{x}}_{k+1 \text{ given } \vec{y}_{k+1}} = \hat{\vec{x}}_{k+1} + \Sigma_{xy_{k+1}} \Sigma_{yy_{k+1}}^{-1} (\vec{y}_{k+1} - \hat{\vec{y}}_{k+1}) \quad \text{B.2}$$

Equation B.2 modifies the current state estimate given a new measurement \vec{y}_{k+1} . The covariance matrices, $\hat{\vec{x}}$ and $\hat{\vec{y}}$ are what we expect to see at $k+1$ based on our truth model, the state space:

$$\vec{x}_{k+1} = \Phi \vec{x}_k + \Gamma \vec{u}_k + \vec{q}_k \quad \text{B.3}$$

$$\vec{y}_k = H \vec{x}_k + \vec{r}_k$$

In the following derivations we assume that the estimates $\hat{\vec{x}}$ and $\hat{\vec{y}}$ closely approximate their expected values. Using assumption 3 ($E[\vec{q}] = 0$) native noise about the state is:

$$\begin{aligned} \hat{\vec{x}}_{k+1} &\approx E[\Phi \vec{x}_k + \vec{q}_k] \\ \hat{\vec{x}}_{k+1} &= \Phi \hat{\vec{x}}_k \end{aligned} \quad \text{B.4}$$

We can estimate future measurements similarly ($E[\vec{r}] = 0$):

$$\begin{aligned} \hat{\vec{y}}_{k+1} &\approx E[H \vec{x}_{k+1} + \vec{r}_{k+1}] \\ \hat{\vec{y}}_{k+1} &= H \hat{\vec{x}}_{k+1} = H \Phi \hat{\vec{x}}_k \end{aligned} \quad \text{B.5}$$

Since we believe that our estimates approximate the expected values of \vec{x} and \vec{y} , the expected covariance of \vec{x} and \vec{y} is:

$$\Sigma_{xy,k+1} = E[(\vec{x}_{k+1} - \hat{\vec{x}}_{k+1})(\vec{y}_{k+1} - \hat{\vec{y}}_{k+1})^T] \quad \text{B.6}$$

Equation B.6 requires significant manipulation:

$$\begin{aligned} \Sigma_{xy,k+1} &= E[(\Phi \vec{x}_k + \vec{q}_k - \Phi \hat{\vec{x}}_k)(H(\Phi \vec{x}_k + \vec{q}_k) + \vec{r}_k - H\Phi \hat{\vec{x}}_k)^T] \\ &= E[(\Phi(\vec{x}_k - \hat{\vec{x}}_k) + \vec{q}_k)(H\Phi(\vec{x}_k - \hat{\vec{x}}_k) + H\vec{q}_k + \vec{r}_k)^T] \\ &= E[(\Phi(\vec{x}_k - \hat{\vec{x}}_k) + \vec{q}_k)((\vec{x}_k - \hat{\vec{x}}_k)^T \Phi^T H^T + \vec{q}_k^T H^T + \vec{r}_k^T)] \\ &= E[\Phi(\vec{x}_k - \hat{\vec{x}}_k)(\vec{x}_k - \hat{\vec{x}}_k)^T \Phi^T H^T + \vec{q}_k \vec{q}_k^T H^T] \\ &= \Phi E[(\vec{x}_k - \hat{\vec{x}}_k)(\vec{x}_k - \hat{\vec{x}}_k)^T] \Phi^T H^T + E[\vec{q}_k \vec{q}_k^T] H^T \\ &= \underline{(\Phi \Sigma_{xx,k} \Phi + Q) H^T} \end{aligned} \quad \text{B.6}$$

Cross terms are absent because the noise and process behavior are supposedly uncorrelated. Furthermore, the sources of noise (process and measurement) have no correlation. Estimating the measurement covariance proceeds similarly:

$$\begin{aligned}
\Sigma_{yy,k+1} &= E[(\bar{y}_{k+1} - \hat{\bar{y}}_{k+1})(\bar{y}_{k+1} - \hat{\bar{y}}_{k+1})^T] \\
&= E[(H(\Phi\bar{x}_k + \bar{q}_k) + \bar{r}_k - H\Phi\hat{x}_k)(H(\Phi\bar{x}_k + \bar{q}_k) + \bar{r}_k - H\Phi\hat{x}_k)^T] \\
&= E[(H\Phi(\bar{x}_k - \hat{x}_k) + H\bar{q}_k + \bar{r}_k)(H\Phi(\bar{x}_k - \hat{x}_k) + H\bar{q}_k + \bar{r}_k)^T] \\
&= E[(H\Phi(\bar{x}_k - \hat{x}_k) + H\bar{q}_k + \bar{r}_k)(\bar{x}_k - \hat{x}_k)^T \Phi^T H^T + \bar{q}_k^T H^T + \bar{r}_k^T)] \\
&= H\Phi E[(\bar{x}_k - \hat{x}_k)(\bar{x}_k - \hat{x}_k)^T] \Phi^T H^T + HE[\bar{q}_k \bar{q}_k^T] H^T + E[\bar{r}_k \bar{r}_k^T] \\
&= H\Phi \Sigma_{xx,k} \Phi^T H^T + HQH^T + R \\
&= H(\Phi \Sigma_{xx,k} \Phi^T + Q)H^T + R
\end{aligned} \tag{B.7}$$

Inserting these derivations into Equation B.2 yields a conditional estimate of the states:

$$\begin{aligned}
&\hat{\bar{x}}_{k+1} \text{ given } \bar{y}_{k+1} \\
&= \Phi\hat{x}_k + \underbrace{(\Phi \Sigma_{xx,k} \Phi + Q)H^T}_{\text{Kalman gain}} (H(\Phi \Sigma_{xx,k} \Phi^T + Q)H^T + R)^{-1} (\bar{y}_{k+1} - H\Phi\hat{x}_k)
\end{aligned} \tag{B.8}$$

Equation B.8 has important features. $\Phi\hat{x}_k$ is our *a priori* estimate of the future state, $\hat{\bar{x}}_{k+1}$. It is our “prior.” $H\Phi\hat{x}_k$ is our *a priori* estimate of the future measurement $\hat{\bar{y}}_{k+1}$, it is what we expect to see based on the current process trajectory. $(\bar{y}_{k+1} - H\Phi\hat{x}_k)$ is the “surprise,” the difference between expectation and reality. Based on this difference we adjust our estimate of the future state, $\hat{\bar{x}}_{k+1} \text{ given } \bar{y}_{k+1}$. We throttle innovations by the Kalman gain:

$$\begin{aligned}
K &= \underbrace{(\Phi \Sigma_{xx,k} \Phi + Q)H^T}_{\text{Kalman gain}} \underbrace{(H(\Phi \Sigma_{xx,k} \Phi^T + Q)H^T + R)^{-1}}_{\text{Kalman gain}} \\
&= \Sigma_{xx,k+1} H^T (H \Sigma_{xx,k+1} H^T + R)^{-1} \\
&= \Sigma_{xy_{k+1}} \Sigma_{yy_{k+1}}^{-1}
\end{aligned} \tag{B.9}$$

Matrices Q and R can be provided by system interrogation of subspace identification (Appendix 1). The scheme is strongly rooted in probability, but aspects of its implementation are opaque. For example, we do not know, *a priori*, Σ_{xx} . This is the covariance of the estimate. Before any

measurements $\hat{\bar{x}}_k$ is uncertain and thus the estimate covariance is initially large. We can converge a large initial covariance, for example $100*I$, if equipped with an iteration scheme for advancing Σ_{xx} . Consider the update of Σ_{xx} given the last state estimate $\hat{\bar{x}}_k$:

$$\begin{aligned}
\Sigma_{xx,k+1} &= E[(\bar{x}_{k+1} - \hat{\bar{x}}_{k+1})(\bar{x}_{k+1} - \hat{\bar{x}}_{k+1})^T] \\
&= E[((\Phi\bar{x}_k + \bar{q}_k) + \Phi\hat{\bar{x}}_k)((\Phi\bar{x}_k + \bar{q}_k) + \Phi\hat{\bar{x}}_k)^T] \\
&= E[(\Phi(\bar{x}_k - \hat{\bar{x}}_k) + \bar{q}_k)(\Phi(\bar{x}_k - \hat{\bar{x}}_k) + \bar{q}_k)^T] \\
&= E[(\Phi(\bar{x}_k - \hat{\bar{x}}_k) + \bar{q}_k)((\bar{x}_k - \hat{\bar{x}}_k)^T \Phi^T + \bar{q}_k^T)] \\
&= \Phi E[(\bar{x}_k - \hat{\bar{x}}_k)(\bar{x}_k - \hat{\bar{x}}_k)^T] \Phi^T + E[\bar{q}_k \bar{q}_k^T] \\
&= \Phi \Sigma_{xx,k} \Phi^T + Q
\end{aligned} \tag{B.10}$$

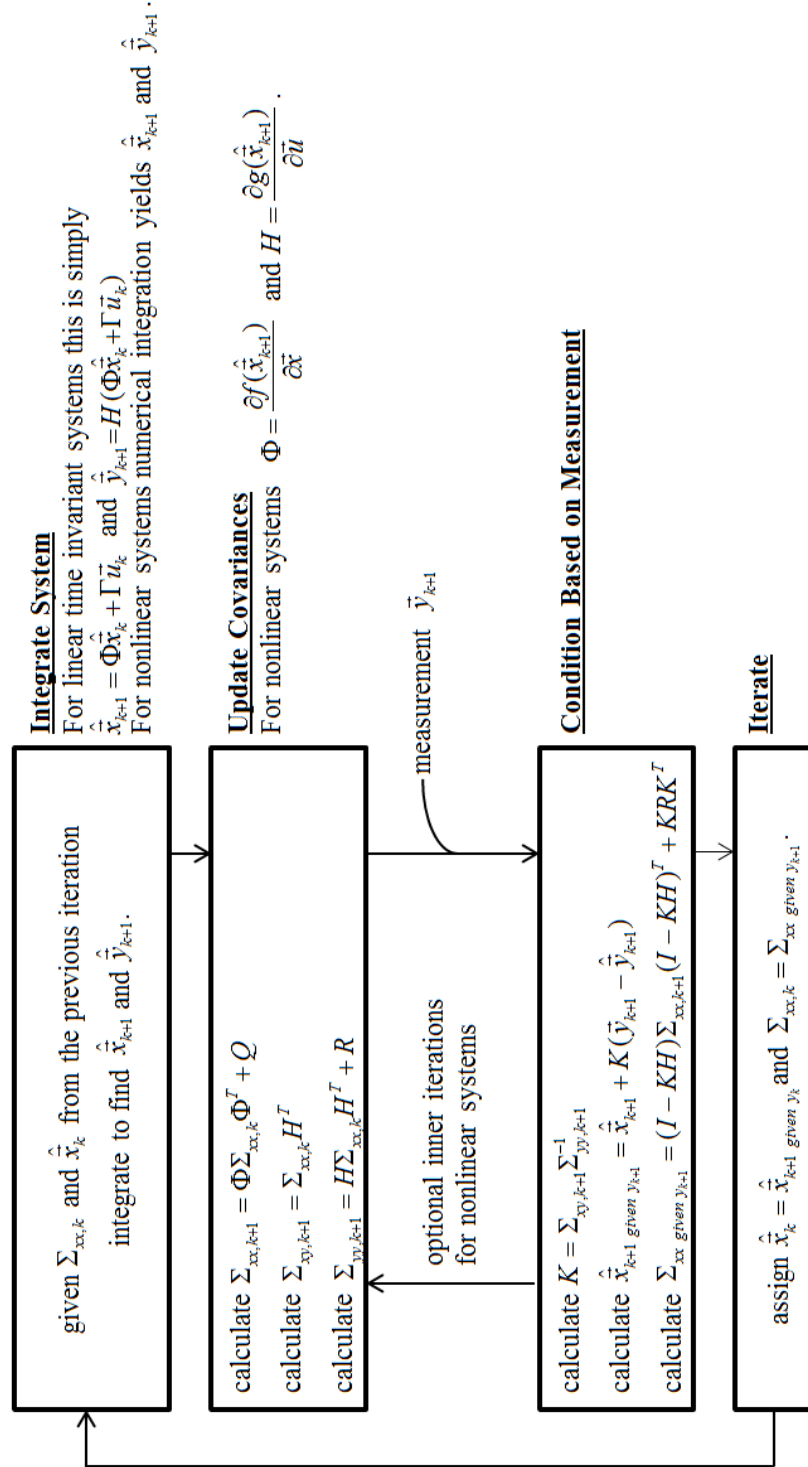
This expression has been underlined in Equation B.8, Equation B.7, and Equation B.6. Equation B.10 is ubiquitous in the preceding calculations. Thus, on a given round of filtering Equation B.10 is calculated first. Once an *a posteriori* estimate of the states ($\hat{\bar{x}}_{k+1}$ given \bar{y}_{k+1}) is available from Equation B.8 the covariance can be updated again:

$$\begin{aligned}
\Sigma_{xx \text{ given } y_{k+1}} &= E[(\bar{x}_{k+1} - \hat{\bar{x}}_{k+1})(\bar{x}_{k+1} - \hat{\bar{x}}_{k+1})^T] \\
&= E[(\bar{x}_{k+1} + K(\bar{y}_{k+1} - (H\bar{x}_{k+1} + \bar{r}_{k+1}))) - (\hat{\bar{x}}_{k+1} + K(\bar{y}_{k+1} - H\hat{\bar{x}}_{k+1}))(\dots)^T] \\
&= E[(\bar{x}_{k+1} + K\bar{y}_{k+1} - KH\bar{x}_{k+1} - K\bar{r}_{k+1} - \hat{\bar{x}}_{k+1} - K\bar{y}_{k+1} + KH\hat{\bar{x}}_{k+1})(\dots)^T] \\
&= E[(\bar{x}_{k+1} - \hat{\bar{x}}_{k+1}) - KH(\bar{x}_{k+1} - \hat{\bar{x}}_{k+1}) - K\bar{r}_{k+1})(\dots)^T] \\
&= E[(\bar{x}_{k+1} - \hat{\bar{x}}_{k+1})(\bar{x}_{k+1} - \hat{\bar{x}}_{k+1})^T] + KHE[(\bar{x}_{k+1} - \hat{\bar{x}}_{k+1})(\bar{x}_{k+1} - \hat{\bar{x}}_{k+1})^T] H^T K^T \\
&\quad - KHE[(\bar{x}_{k+1} - \hat{\bar{x}}_{k+1})(\bar{x}_{k+1} - \hat{\bar{x}}_{k+1})^T] - E[(\bar{x}_{k+1} - \hat{\bar{x}}_{k+1})(\bar{x}_{k+1} - \hat{\bar{x}}_{k+1})^T] H^T K^T \\
&\quad + KE[\bar{r}_{k+1} \bar{r}_{k+1}^T] K^T \\
&= \Sigma_{xx,k+1} + KH\Sigma_{xx,k+1} H^T K^T - KH\Sigma_{xx,k+1} - \Sigma_{xx,k+1} H^T K^T + KRK^T \\
&= (I - KH)\Sigma_{xx,k+1}(I - KH)^T + KRK^T
\end{aligned} \tag{B.11}$$

Equation B.11 is the ‘‘Josef form’’ of the variance update. A complete Kalman filter iteration is shown in Figure B.1. These derivations are substantial. We are iterating in time (k to $k+1$) and

probability (*priori* to *posteriori*), nontrivial tasks. However, the result is an efficient iteration that is readily calculated online.

Figure B.1 The iterative approach of Kalman and nonlinear (“extended”) Kalman filtering.



B.1.2 The Steady State Kalman Filter

Often we wish to avoid Kalman iterations because they can be slow or divergent. In these cases we wish to discover a “steady-state” constant Kalman gain. There are several means of discovering this gain, including the optimal control (co-state) formulation. However, for discrete purposes, it’s simpler to recognize that at steady state: $\Sigma_{xx \text{ given } y_{k+1}} = \Sigma_{xx,k+1} = \Sigma_{xx,k}$.

Thus, we can mix and match all previous equations to find an algebraic statement on the covariance matrix. To start, lets expand our conditioned expression for the covariance:

$$\begin{aligned}
 \Sigma_{xx, \text{given } y_{k+1}} &= (I - KH) \Sigma_{xx,k+1} (I - KH)^T + KRK^T \\
 &= (\Sigma_{xx,k+1} - KH \Sigma_{xx,k+1}) (I - KH)^T + KRK^T \\
 &= (\Sigma_{xx,k+1} - KH \Sigma_{xx,k+1}) (I - H^T K^T) + KRK^T \\
 &= \Sigma_{xx,k+1} - KH \Sigma_{xx,k+1} - (\Sigma_{xx,k+1} - KH \Sigma_{xx,k+1}) H^T K^T + KRK^T \quad \text{B.12} \\
 &= \Sigma_{xx,k+1} - KH \Sigma_{xx,k+1} - \Sigma_{xx,k+1} H^T K^T + KH \Sigma_{xx,k+1} H^T K^T + KRK^T \\
 &= \Sigma_{xx,k+1} - KH \Sigma_{xx,k+1} - \Sigma_{xx,k+1} H^T K^T + KH \Sigma_{xx,k+1} H^T K^T + KRK^T \\
 &= \Sigma_{xx,k+1} - KH \Sigma_{xx,k+1} - \Sigma_{xx,k+1} H^T K^T + K (H \Sigma_{xx,k+1} H^T + R) K^T
 \end{aligned}$$

Then we simplify by inserting for the last Kalman gain and explicitly recognize that, at steady-state, all the covariance matrices are identical:

$$\begin{aligned}
\Sigma_{xx} &= \Sigma_{xx} - KH\Sigma_{xx} - \Sigma_{xx} H^T K^T + K(H\Sigma_{xx} H^T + R)K^T \\
&= \Sigma_{xx} - KH\Sigma_{xx} - \Sigma_{xx} H^T K^T \\
&\quad + K(H\Sigma_{xx} H^T + R) \\
&\quad * \left[\Sigma_{xx} H^T (H(\Phi \Sigma_{xx} \Phi^T + Q)H^T + R)^{-1} \right]^T \\
&= \Sigma_{xx} - KH\Sigma_{xx} - \Sigma_{xx} H^T K^T \\
&\quad + K(H\Sigma_{xx} H^T + R) \\
&\quad * \left[\Sigma_{xx} H^T (H\Sigma_{xx} H^T + R)^{-1} \right]^T \\
&= \Sigma_{xx} - KH\Sigma_{xx} - \Sigma_{xx} H^T K^T \\
&\quad + K(H\Sigma_{xx} H^T + R) \\
&\quad * \left[(H\Sigma_{xx} H^T + R)^{-1} \right]^T \left[\Sigma_{xx} H^T \right]^T \\
&= \Sigma_{xx} - KH\Sigma_{xx} - \Sigma_{xx} H^T K^T \\
&\quad + K(H\Sigma_{xx} H^T + R) \\
&\quad * (H\Sigma_{xx} H^T + R)^{-1} H\Sigma_{xx}^T \\
&= \Sigma_{xx} - KH\Sigma_{xx} - \Sigma_{xx} H^T K^T \\
&\quad + K(H\Sigma_{xx} H^T + R) \\
&\quad * (H\Sigma_{xx} H^T + R)^{-1} H\Sigma_{xx} \\
&= \Sigma_{xx} - KH\Sigma_{xx} - \Sigma_{xx} H^T K^T \\
&\quad + KH\Sigma_{xx} \\
&= \Sigma_{xx} - \Sigma_{xx} H^T K^T \\
&= \Sigma_{xx} - \Sigma_{xx} \left[(H^T K^T)^T \Sigma_{xx}^T \right]^T \\
&= \Sigma_{xx} - (H^T K^T)^T \Sigma_{xx} \\
&= \Sigma_{xx} - KH\Sigma_{xx} \\
&= (I - KH) \Sigma_{xx}
\end{aligned} \tag{B.13}$$

We insert this result back into our iterate (Equation B.10) for the covariance matrix:

$$\begin{aligned}
\Sigma_{xx} &= \Phi \Sigma_{xx} \Phi^T + Q \\
&= \Phi(I - KH) \Sigma_{xx} \Phi^T + Q \\
&= \Phi \left[I - \Sigma_{xx} H^T (H\Sigma_{xx} H^T + R)^{-1} \right] \Sigma_{xx} H \Phi^T + Q \\
&= \Phi \left[\Sigma_{xx} - \Sigma_{xx} H^T (H\Sigma_{xx} H^T + R)^{-1} \Sigma_{xx} \right] H \Phi^T + Q
\end{aligned} \tag{B.14}$$

Equation B.14 is known as the matrix Riccati equation or discrete algebraic matrix equation (DARE):

$$\Sigma_{.xx} = \Phi \left[\Sigma_{.xx} - \Sigma_{.xx} H^T (H \Sigma_{.xx} H^T + R)^{-1} \Sigma_{.xx} \right] H \Phi^T + Q \quad \text{B.14}$$

Solutions to Equation B.14 are nontrivial, especially solutions for which the steady-state Kalman gain converges the system state stably. In the naive case values of the covariance matrix can be solved as a zero problem through Newton iterations. Whatever the case

$$K = \Sigma_{.xx} H^T (H \Sigma_{.xx} H^T + R)^{-1} \quad \text{B.15}$$

B.2. Exercise

B.2.1 Observability

The nonlinear binary flash described in chapter 3 was analyzed for observability where the state and input vectors were:

$$\vec{x} = \begin{bmatrix} M_v \\ y \\ M_L \\ x \\ T \\ x_{in} \\ T_{in} \end{bmatrix} \quad \text{B.16}$$

$$\vec{u} = \begin{bmatrix} F \\ V \\ L \\ Q \end{bmatrix} \quad \text{B.17}$$

Note that the vector \vec{x} refers to states, whereas the scalar x is mole fraction. Our truth model,

$\dot{\vec{x}} = f(\vec{x}, \vec{u})$, was nonlinear:

$$\begin{bmatrix} \dot{M}_v \\ \dot{y} \\ \dot{M}_L \\ \dot{x} \\ \dot{T} \\ \dot{x}_{in} \\ \dot{T}_{in} \end{bmatrix} = \begin{bmatrix} 1 & 0 & 0 & 0 & 0 & 0 & 0 \\ 0 & 1/M_v & 0 & 0 & 0 & 0 & 0 \\ 0 & 0 & 1 & 0 & 0 & 0 & 0 \\ 0 & 0 & 0 & 1/M_L & 0 & 0 & 0 \\ 0 & 0 & 0 & 0 & 1 & 0 & 0 \\ 0 & 0 & 0 & 0 & 0 & 0 & 0 \\ 0 & 0 & 0 & 0 & 0 & 0 & 0 \end{bmatrix} \begin{bmatrix} N_l + N_h - V \\ N_l - yN \\ F - N - L \\ F(x_{in} - x) - N_l + xN \\ C_p F(T_{in} - T) + q - \Delta H_l N_l - \Delta H_h N_h \\ x_{in} \\ T_{in} \end{bmatrix} \quad \text{B.18}$$

x_{in} and T_{in} were added as appended “constant disturbance” states. We assume that a composition analyzer is unavailable. Thus, the measurement vector lacks mole fractions:

$$\vec{y} = \begin{bmatrix} P \\ M_L \\ \rho \\ T \\ T_{in} \\ \rho_{in} \end{bmatrix} \quad \text{B.19}$$

Our measurement model, $\vec{y} = g(\vec{x})$, is nonlinear:

$$\begin{bmatrix} P \\ M_L \\ \rho \\ T \\ T_{in} \\ \rho_{in} \end{bmatrix} = \begin{bmatrix} M_v RT / (v - M_L / \rho) \\ M_L \\ \rho_l x + \rho_h (1 - x) \\ T \\ T_{in} \\ \rho_l x_{in} + \rho_h (1 - x_{in}) \end{bmatrix} \quad \text{B.20}$$

At this point we do not know if hidden states from our measurement model are observable. The observability principle dictates whether or not we can see time evolution of the hidden states.

Observability is the rank of the following matrix:

$$\mathcal{G} = \begin{bmatrix} H \\ H\Phi \\ H\Phi^2 \\ \vdots \\ H\Phi^{n-1} \end{bmatrix} \quad \text{B.21}$$

Where n is the number of system states. The Jacobian of our truth model approximates Φ and the Jacobian of our measurement model approximates H . These Jacobians have the following nonzero entries:

$$\Phi \approx \begin{bmatrix} 1 & 1 & 1 & 1 & 1 & 0 & 0 \\ 1 & 1 & 1 & 1 & 1 & 0 & 0 \\ 1 & 1 & 1 & 1 & 1 & 0 & 0 \\ 1 & 1 & 1 & 1 & 1 & 1 & 0 \\ 1 & 1 & 1 & 1 & 1 & 0 & 1 \\ 0 & 0 & 0 & 0 & 0 & 0 & 0 \\ 0 & 0 & 0 & 0 & 0 & 0 & 0 \end{bmatrix} \quad \text{B.22}$$

$$H \approx \begin{bmatrix} 1 & 0 & 1 & 0 & 0 & 0 & 0 \\ 0 & 0 & 1 & 0 & 0 & 0 & 0 \\ 0 & 0 & 0 & 1 & 0 & 0 & 0 \\ 0 & 0 & 0 & 0 & 1 & 0 & 0 \\ 0 & 0 & 0 & 0 & 0 & 0 & 1 \\ 0 & 0 & 0 & 0 & 0 & 1 & 0 \end{bmatrix} \quad \text{B.23}$$

With Equation B.22 and B.23 we have:

$$\text{rank}(\mathcal{G}) = 7 = n$$

Thus, the rank of the observability matrix equals the number of states. Provisionally our system was observable. However, the states could trespass unobservable conditions.

B.2.2 Simulation Approach

Figure B.2 shows simulation programmatic flow for simulating the nonlinear binary flash from chapter 3. Two hours of process time was simulated and filtered to ascertain true system conditions from noisy measurements. First Gaussian noise was added to the flash inlet and outlet flows, effectively adding noise to all process states (Figure B.3). Noise was also added to the measurements (Figure B.4). Table B.1 summarizes characteristics of the introduced noise. The process and measurement noise covariance matrices were generated by comparing the actual states and measurements to those from an idealized simulation. The condition number of these covariance matrices approached 10^{10} , sizable but below machine precision. No attempt was made at scaling the problem, although this seems advisable.

To test Kalman filter robustness the inlet composition was systematically varied according to the following function:

$$x_{in}(t) = 0.5 + \frac{(Amplitude)t}{7200} \sin\left[\left(\frac{t}{period * 7200}\right) 2\pi\right] \quad B.24$$

In these tests the maximum amplitude and shortest period were achieved after 7200 seconds (two hours). Effectively the disturbance was “ramped up.” Maximum amplitude was consistently 0.15. For stress tests period was 1200 seconds (20 minutes). In all cases the system was sampled at ten second intervals. The choice of sampling period was arbitrary, but likely within the technical limitations of actual flash units.

Filtering was initialized using the steady-state values of all process variables. This seemed a sensible choice given that these numbers are available from steady-state design. Initially covariance of the estimate was:

$$M_v \begin{bmatrix} 20 & 0 & 0 & 0 & 0 & 0 & 0 \\ y & 0 & 0.25 & 0 & 0 & 0 & 0 \\ M_L & 0 & 0 & 400 & 0 & 0 & 0 \\ x & 0 & 0 & 0 & 0.25 & 0 & 0 \\ T & 0 & 0 & 0 & 0 & 50 & 0 \\ x_{in} & 0 & 0 & 0 & 0 & 0 & 0.25 \\ T_{in} & 0 & 0 & 0 & 0 & 0 & 50 \end{bmatrix} \quad B.25$$

These are large covariances, a “diffuse” prior. In all graphs error bars are 95% confidence intervals of the estimate.

The state transition matrix (Φ) and measurement matrix (Γ) were approximated using forward finite differences with a perturbation of (machine precision)^{1/2}. For details see Figure B.1.

Table B.1 process and measurement noise

process variable	noise σ	corner Hz
F	0.25 mol/s	0.011
V	0.05 mol/s	white
L	0.25 mol/sec	0.011
q	2500 mol	0.005
T_{in}	0.25 K	0.011
measured variable	noise σ	corner Hz
P	1000 Pa	white
M_L	25 mol	white
ρ	500 mol/m ³	white
T	0.25 K	white
T_{in}	0.25 K	white
ρ	500 mol/m ³	white

Figure B.2: Simulation workflow.

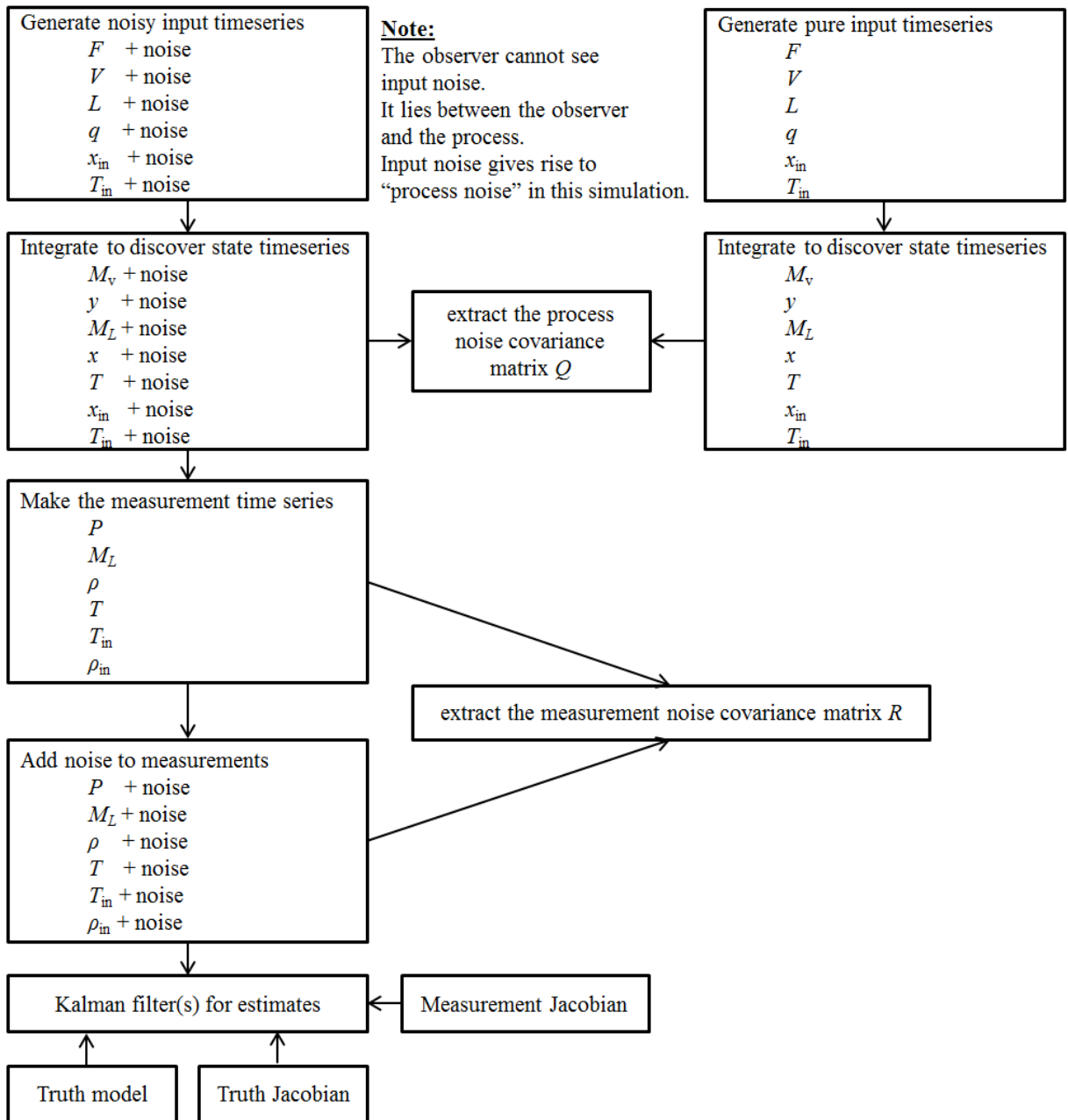


Figure B.3: Example inlet-outlet noise that gives rise to process noise in the model system.

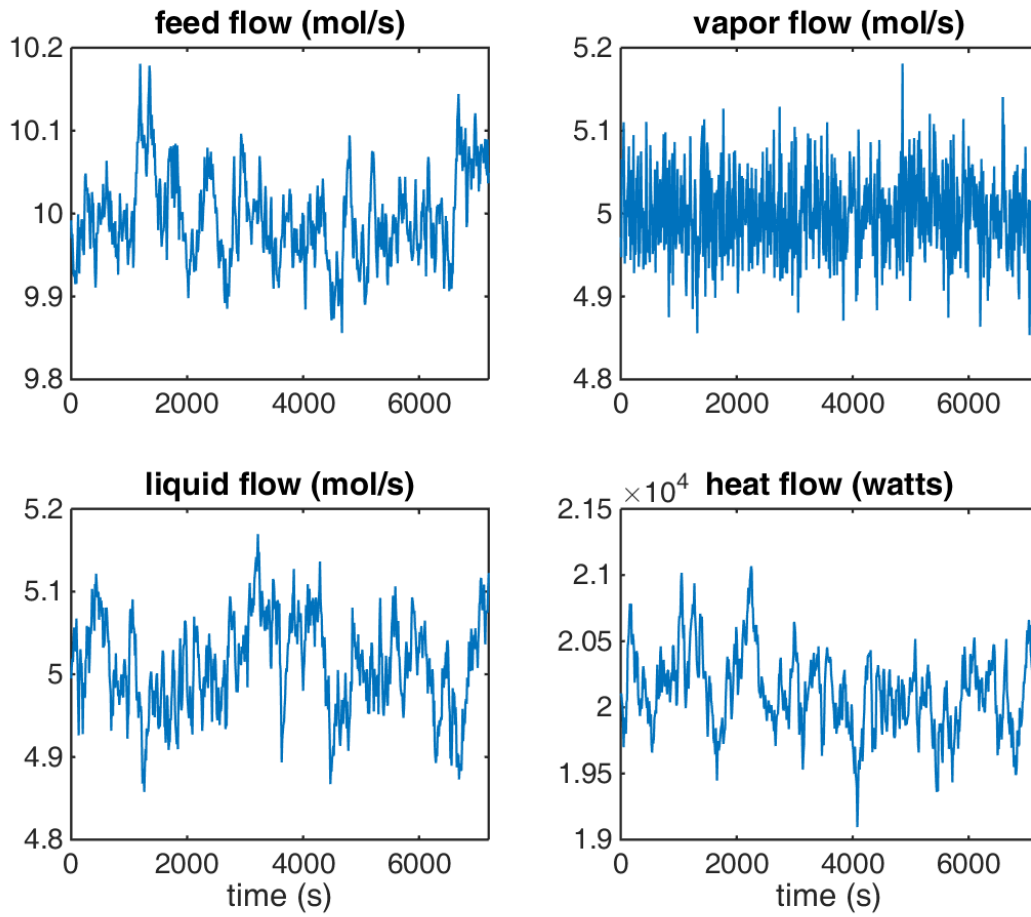
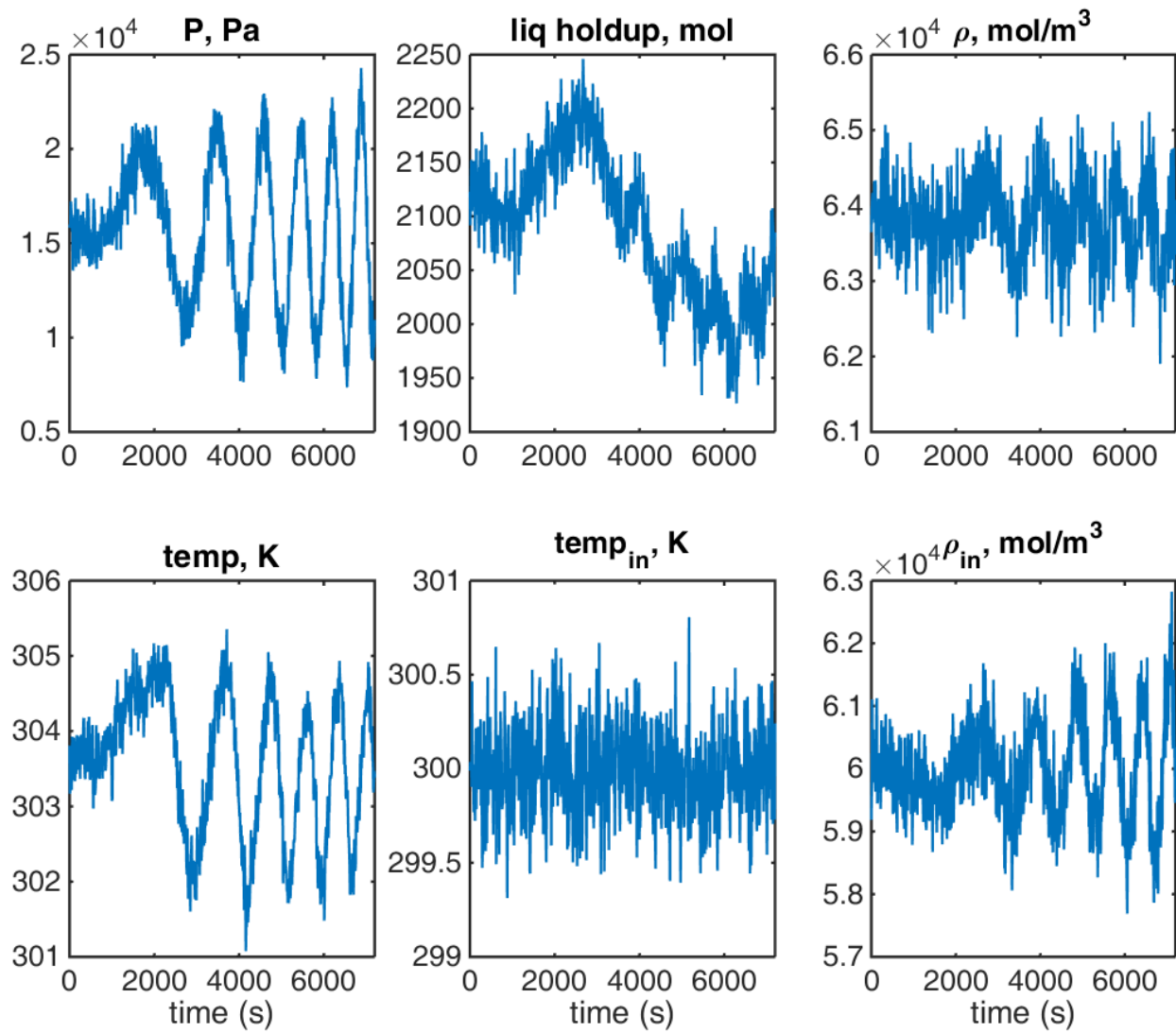


Figure B.4: Measurement noise in the model system. In reduced measurement tests the densities were not available for state estimation.



B.2.3 State Estimation, Base Case

Figure B.5 shows state estimation for two hours of process time and a full measurement vector:

$$\bar{y} = \begin{bmatrix} P \\ M_L \\ \rho \\ T \\ T_{in} \\ \rho_{in} \end{bmatrix} \quad \text{B.19}$$

The Kalman filter successfully tracks truth within the fully observable system. Furthermore, Kalman filter iterations are numerically stable (Figure B.6). The condition number of the estimate covariance matrix appeared bounded.

Figure B.5: The estimator (**black line**) successfully tracks truth (**dashed red line**) in a fully observable system with exact process noise and measurement noise covariance matrices.

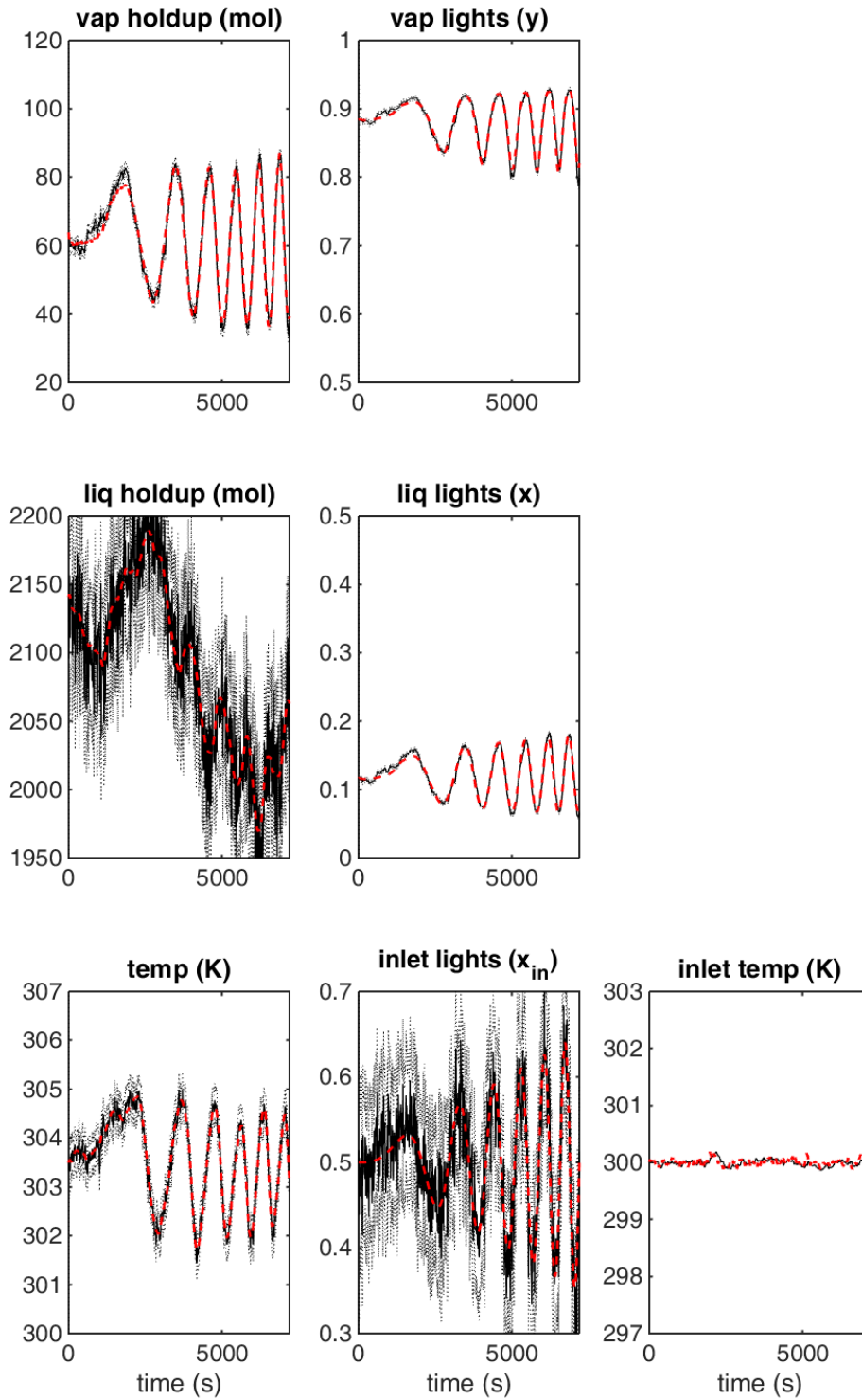
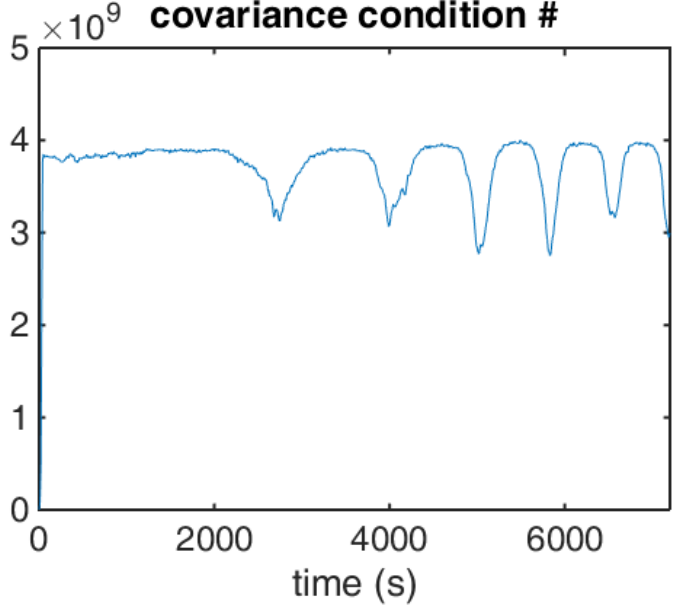


Figure B.6: Condition number of the state estimate covariance matrix over time for a fully observable system. Although the condition number was large, it appeared to be bounded.



B.2.4 State Estimation without Access to the Process Noise Covariance Matrix

Generally the process noise, which lies between the observer and the process, is unknowable. Thus, the process noise covariance matrix, Q , is unavailable. Control practitioners are usually forced to “guess” values in this matrix with their “intuition.”

In the base case the exact process noise covariance matrix was used in the Kalman filter. Here, the process noise covariances were “guessed:”

$$Q = \begin{matrix} M_v \\ y \\ M_L \\ x \\ T \\ x_{in} \\ T_{in} \end{matrix} \begin{bmatrix} 2.5 & 0 & 0 & 0 & 0 & 0 & 0 \\ 0 & 0.025 & 0 & 0 & 0 & 0 & 0 \\ 0 & 0 & 250 & 0 & 0 & 0 & 0 \\ 0 & 0 & 0 & 0.025 & 0 & 0 & 0 \\ 0 & 0 & 0 & 0 & 0.25 & 0 & 0 \\ 0 & 0 & 0 & 0 & 0 & 0.025 & 0 \\ 0 & 0 & 0 & 0 & 0 & 0 & 0.25 \end{bmatrix} \quad \text{B.26}$$

Estimation with the guess was far noisier than estimation with the true process noise covariance matrix (Figure B.7). Error bars were larger and the estimates were highly erratic. This was ameliorated by scaling (“tuning”) the process noise covariance matrix:

$$Q = 0.05 * Q \quad \text{B.27}$$

As shown in Figure B.8 error of the estimate was considerably lower when scaling our guess. In practice values of the process noise covariance could be iterated to maximize our confidence in the estimate. The success of state estimation without an exact process noise covariance matrix suggests that the Kalman filter is somewhat robust.

Figure B.7: The estimator (**black line**) tracks truth (**dashed red line**) despite the use of an inexact, “guessed,” process noise covariance matrix Q . Note the large 95% confidence intervals.

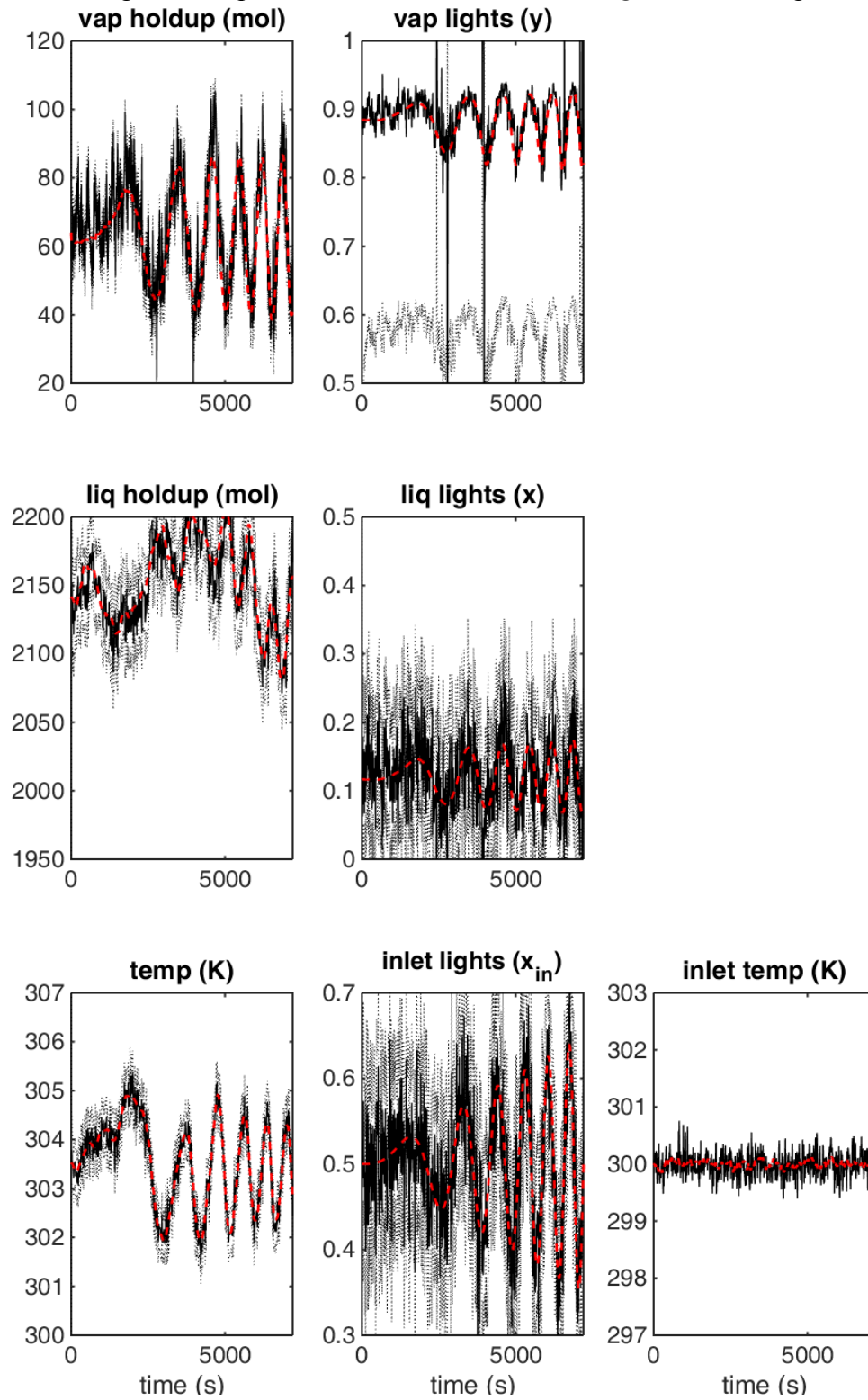
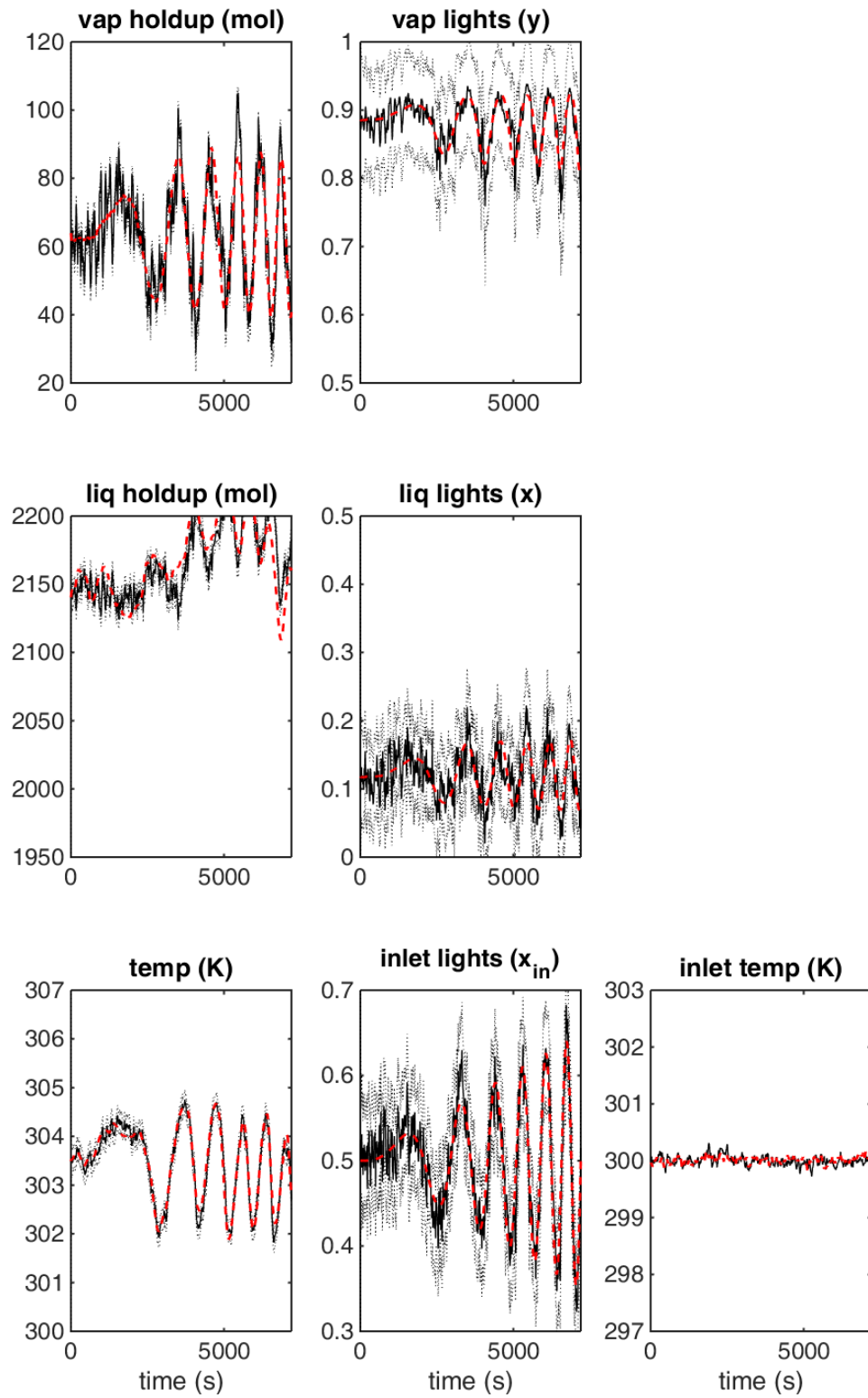


Figure B.8: The estimator (**black line**) tracks truth (**dashed red line**) with a refined, albeit inexact, process noise covariance matrix \mathbf{Q} . Note the improved confidence intervals relative to Figure B.7.



B.2.5 State Estimation with an Unobservable System

To test the limits of Kalman filtering state inference was attempted with only four sensors:

$$\bar{y} = \begin{bmatrix} P \\ M_L \\ T \\ T_{in} \end{bmatrix} \quad \text{B.28}$$

In brief, density measurements were no longer available on the liquid streams. Consequently, the system was no longer observable. However, if errors between the estimate and truth decay quickly (state poles are “fast” and “stable”) unobservable systems can still be processed by the Kalman filter.

Figure B.9 shows that the inlet composition disturbance quickly outpaces our ability to track change. In select cases our estimate diverged from the truth (Figure B.10). This behavior was not seen when the system was observable. Interestingly, during divergence the condition number of the estimate covariance was still bounded (Figure B.11). Thus, divergence likely owes to nonlinearity in the process and not numerical facets of the Kalman filter. There is likely a narrow estimation envelop. If the estimator strays too far from truth the system Jacobian will be evaluated far from the true system state. Consequently, the estimator cannot recover and diverges. A larger measurement vector likely prevents the estimator from drifting substantially from truth. Conversely, a larger measurement vector could endow the estimator with a larger stability envelop.

Figure B.9: The estimator (**black line**) lags the truth (**dashed red line**) when a reduced measurement vector was used.

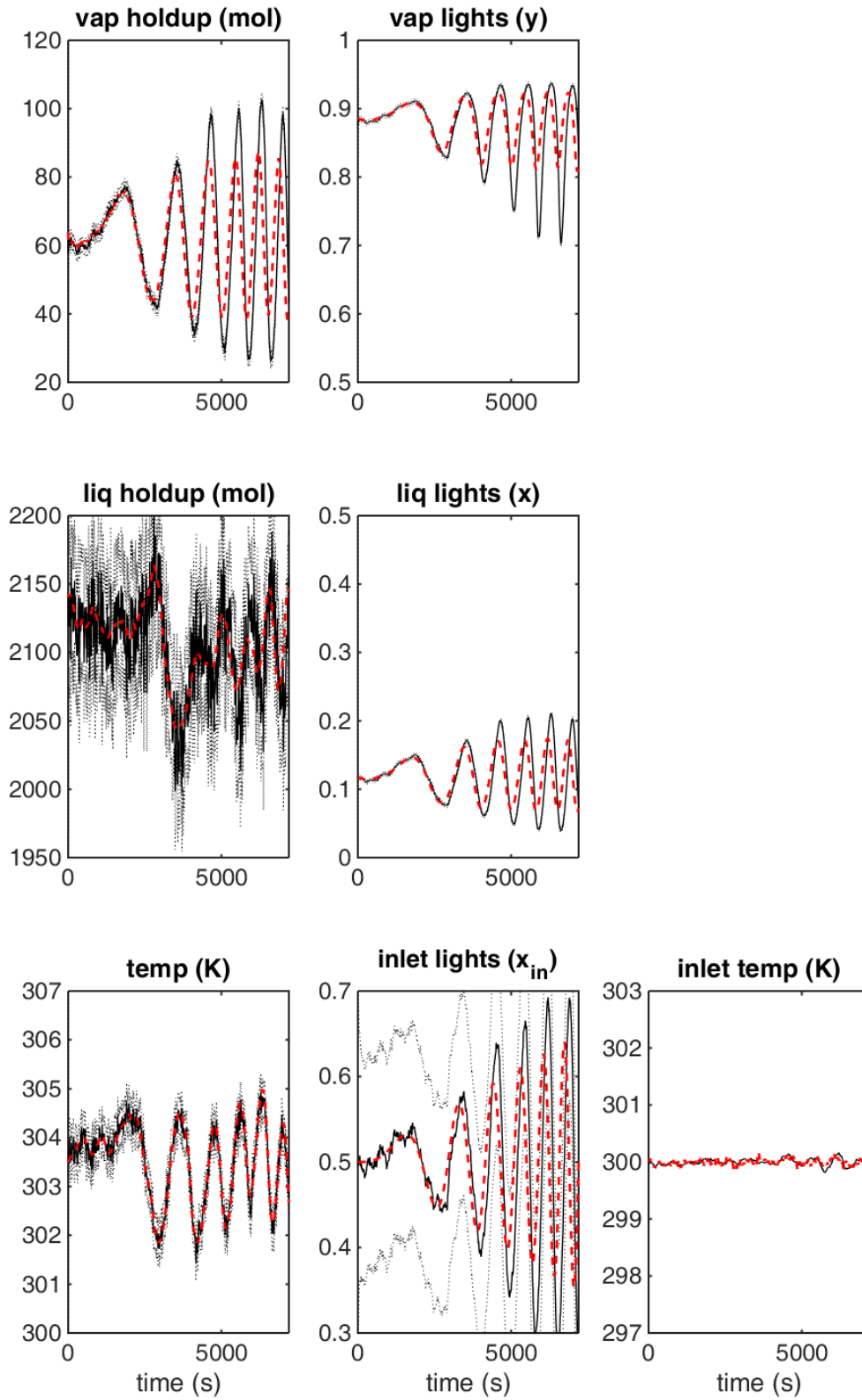


Figure B.10: Occasionally the estimator (**black line**) diverged from the truth (**dashed red line**) when a reduced measurement vector was used.

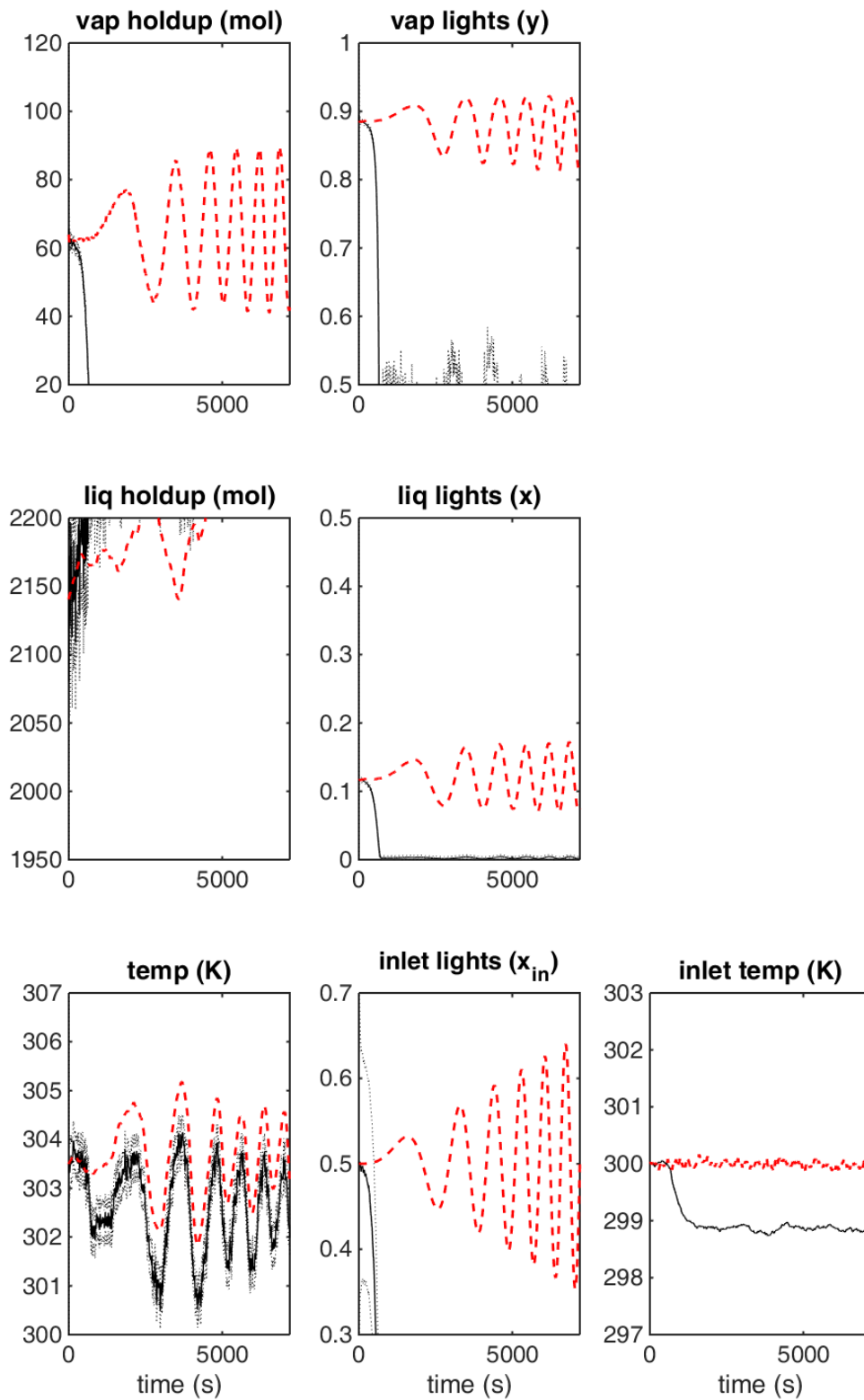
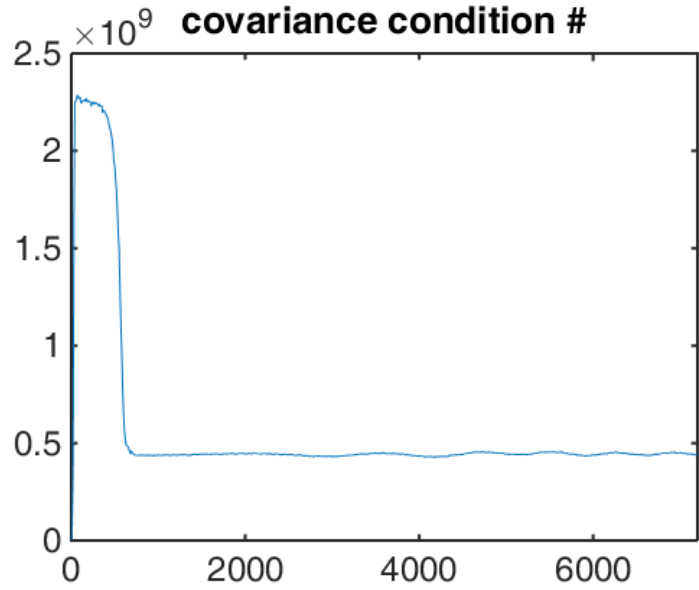


Figure B.11: Condition number of the state estimate covariance matrix over time when the estimate diverged. Note that the covariance matrix became *more* invertible, yet the estimator still diverged.



B.3. Conclusions

The Kalman filter is a means of estimating truth from noise. It is built on a linear view of system dynamics. Given that our process was nonlinear the system was linearized at each sampling time for use in the Kalman filter. This was an “extension” of canonical Kalman filtering. Other extensions include adding process parameters to the state vector.

When supplied with myriad sensor measurements and an observable system the Kalman filter faithfully tracked flash compositions (Figure B.5). Under these conditions the process noise covariance matrix (Q) could be inexact. With an inexact process noise covariance matrix the estimates were erratic, but accurate (Figure B.7). Thus, the Kalman filter is somewhat robust to variation in the process noise covariance matrix.

The Kalman filter occasionally diverged when supplied with a reduced measurement vector (Figure B.10). Likely the estimate strayed to an unrecoverable state when fewer measurements were available. Conversely, the estimator stability envelop was smaller without plentiful sensor measurements. During divergence the estimate covariance matrix became more numerically tractable (Figure B.11). Thus, divergence likely owed to process nonlinearity, not numerical instability.

Kalman filtering with a reduced measurement vector remains an enticing proposition. An expanded view of Kalman filtering, termed Moving Horizon Estimation (“Backwards Smoothing Kalman filtering”), allows for the use of fewer measurement sensors during state estimation. This method revisits past estimates of the system state to refine the current estimate. Research indicates that Moving Horizon Estimation is the most successful and least computationally intense approach to nonlinear filtering.

Appendix C: A Hill Equation for Heat Capacity Calculation

C.1. Introduction

Process engineers commonly rely on computationally efficient and readily implemented thermodynamic models to design, scale, and control chemical process equipment [137]. Thus, although complex *ab initio* methods are now available for accurate thermodynamic predictions, especially for solid specific heat [138, 139], classical thermodynamic models continue to pervade the process industries [140-143]. Notably, despite the current availability of both *ab initio* and classical thermodynamic models for solid specific heat estimation, thermodynamic databanks recommend empirical piecewise polynomials for heat capacity calculation [57, 144]. These empirical models are likely inaccurate outside the fitted data and require the implementation of ungainly lookup tables and case structures in process simulations. To find a feasible alternative, we explored the accuracy of classical thermodynamic models for the prediction of heat capacity across 53 inorganic compounds and technical solids. This included two canonical equations for solid specific heat, the Debye Model and Einstein Solid [145, 146], which were compared against the Hill Equation from biochemistry and an empirical equation for solid specific heat [147].

Recently, a correlation was observed between the Hill Coefficient and the Gibbs energy of interaction in noncovalent binding [148], which suggests that the Hill Equation may capture aspects of covalent bond phenomena. We hypothesized that the Hill Equation could be extended to heat capacity prediction in covalent solids by the substitution of temperature for concentration:

$$\frac{C_v(T)}{3R} = \frac{T^n}{K + T^n} \quad \text{C.1}$$

Where R is the gas constant, $3R$ is the maximum heat capacity for a classical three dimensional solid lattice, T is absolute temperature, K is the dissociation constant, and n is the Hill constant.

The substitution of temperature for concentration is supported by prior derivations that established an equivalence between intensive properties in noncovalent bonding processes [149, 150]. A similar substitution is seen in the Hill Equation and Langmuir isotherm, which share an identical functional form, but depend on concentration and pressure respectively.

The Hill Equation, as posed, satisfies the idealized Dulong-Petit limit [151]:

$$\lim_{T \rightarrow \infty} C_v(T) = 3R \quad \text{C.2}$$

For departures from ideality due to electronic, magnetic, and cooperative modes of thermal energy the constant $3R$ was allowed to vary:

$$C_v(T) = C_{v\max} \frac{T^n}{K + T^n} \quad \text{C.3}$$

Thus, three parameters fit the Hill Equation to specific heat data: $C_{v\max}$, K , and n . In specific heat estimation it was expected that n would always exceed unity ($n > 1$), which is indicative of cooperative binding in noncovalent systems.

The Hill Equation was compared to the Einstein Solid, which is derived from the microcanonical ensemble [145]:

$$\frac{C_v(T)}{3R} = \left(\frac{\varepsilon}{RT} \right)^2 \frac{e^{\varepsilon/(RT)}}{(e^{\varepsilon/(RT)} + 1)^2} \quad \text{C.4}$$

Where ε is the sole quantized energy of oscillation within the solid and all other variables are as previously described.

For departures from ideality due to electronic, magnetic, and cooperative modes of thermal energy the constant $3R$ was allowed to vary:

$$C_v(T) = C_{v\max} \left(\frac{\varepsilon}{RT} \right)^2 \frac{e^{\varepsilon/(RT)}}{(e^{\varepsilon/(RT)} + 1)^2} \quad \text{C.5}$$

Thus, two parameters fit the Einstein Solid to specific heat data: $C_{v\max}$ and ε .

The Einstein Solid often underestimates low temperature specific heat (<100 K) [152], which prompted development of the Debye Model [146]:

$$\frac{C_v(T)}{3R} = 3 \left(\frac{T}{T_D} \right)^{3T/T_D} \int_0^{3T/T_D} \frac{x^4 e^x}{(e^x - 1)^2} dx \quad \text{C.6}$$

Where T_D is the Debye temperature, indicative of the highest energy frequency supported by the solid lattice, and all other variables are as previously described. For departures from ideality due to electronic, magnetic, and cooperative modes of thermal energy the constant $3R$ was allowed to vary:

$$C_v(T) = 3C_{v\max} \left(\frac{T}{T_D} \right)^{3T/T_D} \int_0^{3T/T_D} \frac{x^4 e^x}{(e^x - 1)^2} dx \quad \text{C.7}$$

Thus, two parameters fit the Debye Model to specific heat data: $C_{v\max}$ and T_D .

Typically constant pressure specific heat, not constant volume specific heat, is engineering relevant. The two quantities are related as follows [153]:

$$C_p(T) = C_v(T) + \alpha^2(T)V(T)K_T(T)T \quad \text{C.8}$$

Where α is the coefficient of isobaric thermal expansion, V is the molar volume, and K_T is the isothermal bulk modulus. As has been pursued previously, the last term of equation C.8 was approximated as a linear function with slope m [154]:

$$C_p(T) = C_v(T) + mT \quad \text{C.10}$$

In all cases slope m provided an additional degree of freedom for fitting specific heat data.

The Hill Equation, Einstein Solid, and Debye model were compared to an empirical model, termed the Multilinear Model [147], for heat capacity calculation. The Multilinear Model was shown to be superior to simple polynomial fits for a wide range of solids [147]. It features four fitted parameters: a , b , c , and d :

$$C_p(T) = aT^b e^{cT} e^{d/T} \quad \text{C.11}$$

Like the Hill Equation [155], the Multilinear Model is amenable to logarithmic linearization [147]. For both the Hill Equation and Multilinear Model linear regression was used to initialize a nonlinear optimization for the parameter estimates. Final parameters across all models were discovered through minimization of the L_2 norm between model predictions and experimental data.

C.2. Results

Experimental data for 53 inorganic and technical solids were mined from thermochemical tables and literature reports [57, 118-121, 144, 156-172], data which was fit to the Debye Model, Einstein Solid, Hill Equation, and Multilinear Model [57, 144]. Figure C.1 plots experimental heat capacity against calculated heat capacity for all 53 solids. The correspondence between experiment and prediction appeared strong for the putative fundamental models, especially the Hill Equation, but was variable for the empirical Multilinear Model. Figure C.2 and Figure C.3 show example fits for technical metals and technical ceramics. Generally, the Einstein Solid underestimated heat capacity at low temperatures ($< 100\text{K}$), as has been previously observed [152], while the Hill Equation overestimated specific heat in this range. To further parse model fidelity across the temperature range, absolute relative errors were evaluated:

$$ARE(T_i) = \left| \frac{C_p(T_i) - C_{p,exp}(T_i)}{C_{p,exp}(T_i)} \right| \quad \text{C.12}$$

Where $C_{p,exp}$ is the experimentally measured specific heat at temperature T_i . The average absolute error was determined for each solid over $T \leq 100 \text{ K}$ and $T > 100 \text{ K}$. Figure C.4 shows the results, wherein the Debye Model best minimized relative errors below 100 K. However, the Hill Equation best minimized errors at temperatures above 100 K. Furthermore, the Hill Equation also showed

the lowest standard error across the entire temperature range (Figure C.4), where standard error was calculated as:

$$SE = \sqrt{\frac{\sum_{i=1}^k (C_p(T_i) - C_{p.exp.}(T_i))^2}{k-2}} \quad \text{C.13}$$

For k experimental observations. The Hill Equation showed an average standard error of 0.37 across all the 53 examined solids. Average standard error of the Debye Model and Einstein Solid predictions were 0.45 and 0.81 respectively. Figure C.4 shows that the correlation coefficient, R^2 , was strong for all the putative fundamental models but was inconsistent for the empirical Multilinear Model. Overall, the Hill Equation outperformed alternative representations of heat capacity at temperatures above 100 K.

Prior work has shown a correlation between the Hill coefficient and Gibbs energy of interaction in noncovalent binding [148]. Ostensibly, the enthalpy of fusion is an analogous measure for covalent binding in solids. A correlation between the enthalpy of fusion and the Hill Coefficient could imply a fundamental basis for use of the Hill Equation in solid specific heat estimation. To explore this possibility, estimated Hill Coefficients were plotted against the enthalpy of fusion for alkaline metals and alkaline halides. Figure C.5 shows the results. A linear trend was observed within the alkaline metals and alkaline halide groups, although not across alkaline metals and alkaline halides generally.

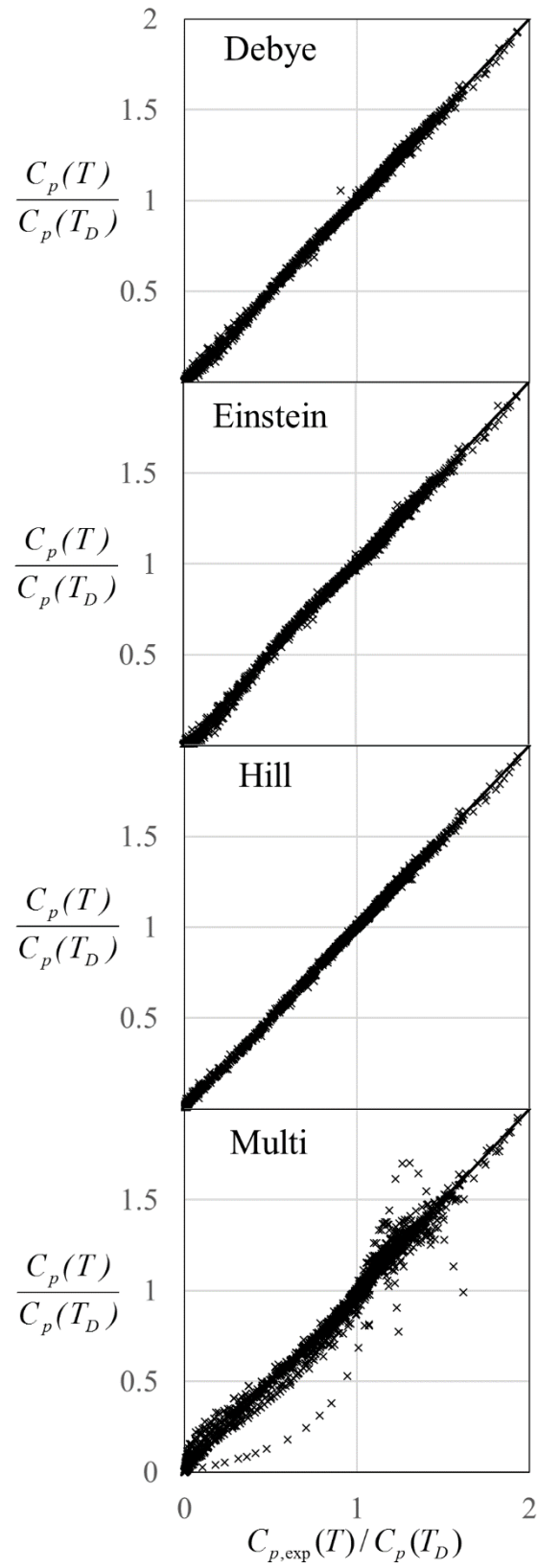


Figure C.1: Accuracy of the specific heat models.

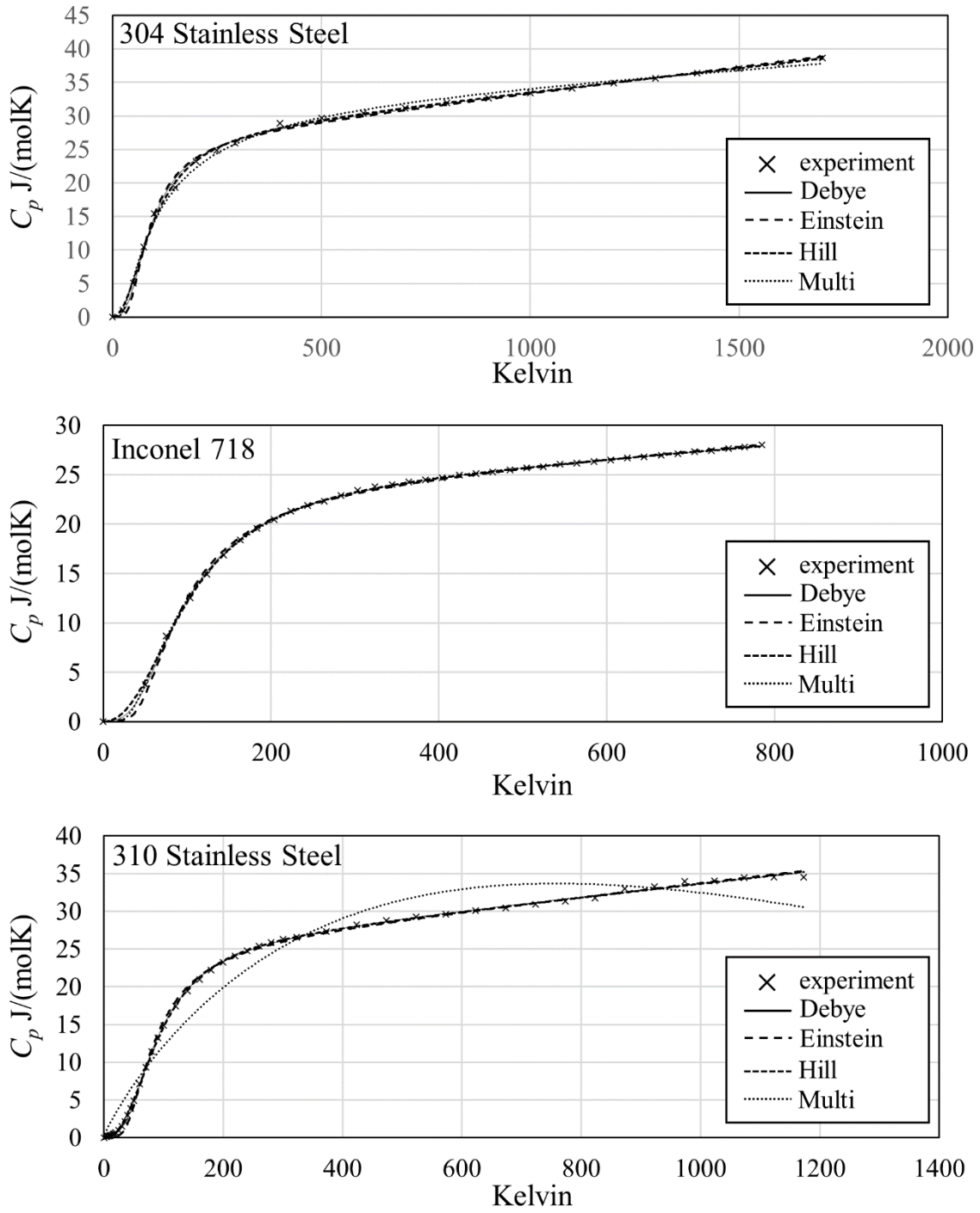


Figure C.2: Model predictions for the specific heat of example technical metals.

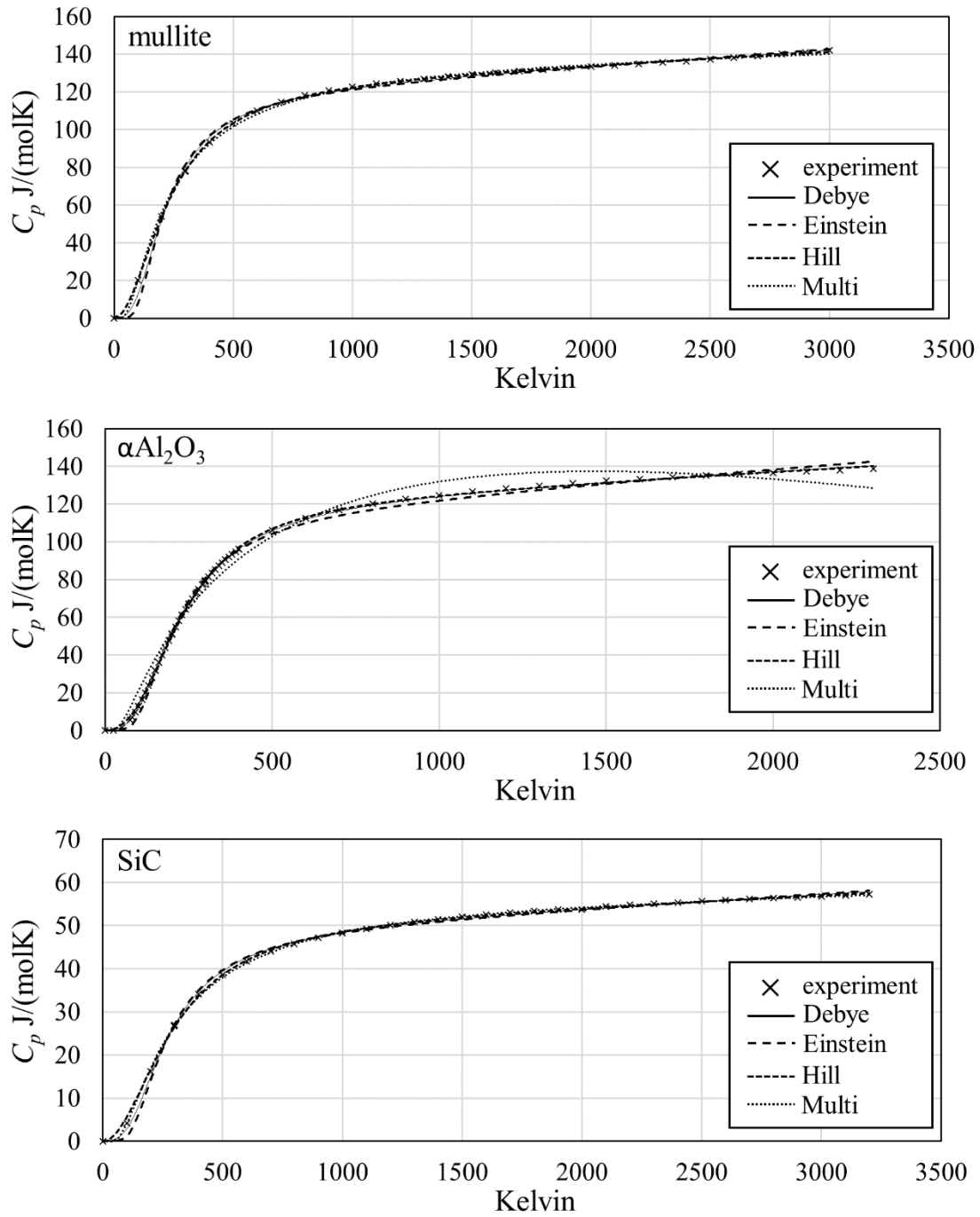


Figure C.3: Model predictions for the specific heat of example technical ceramics.

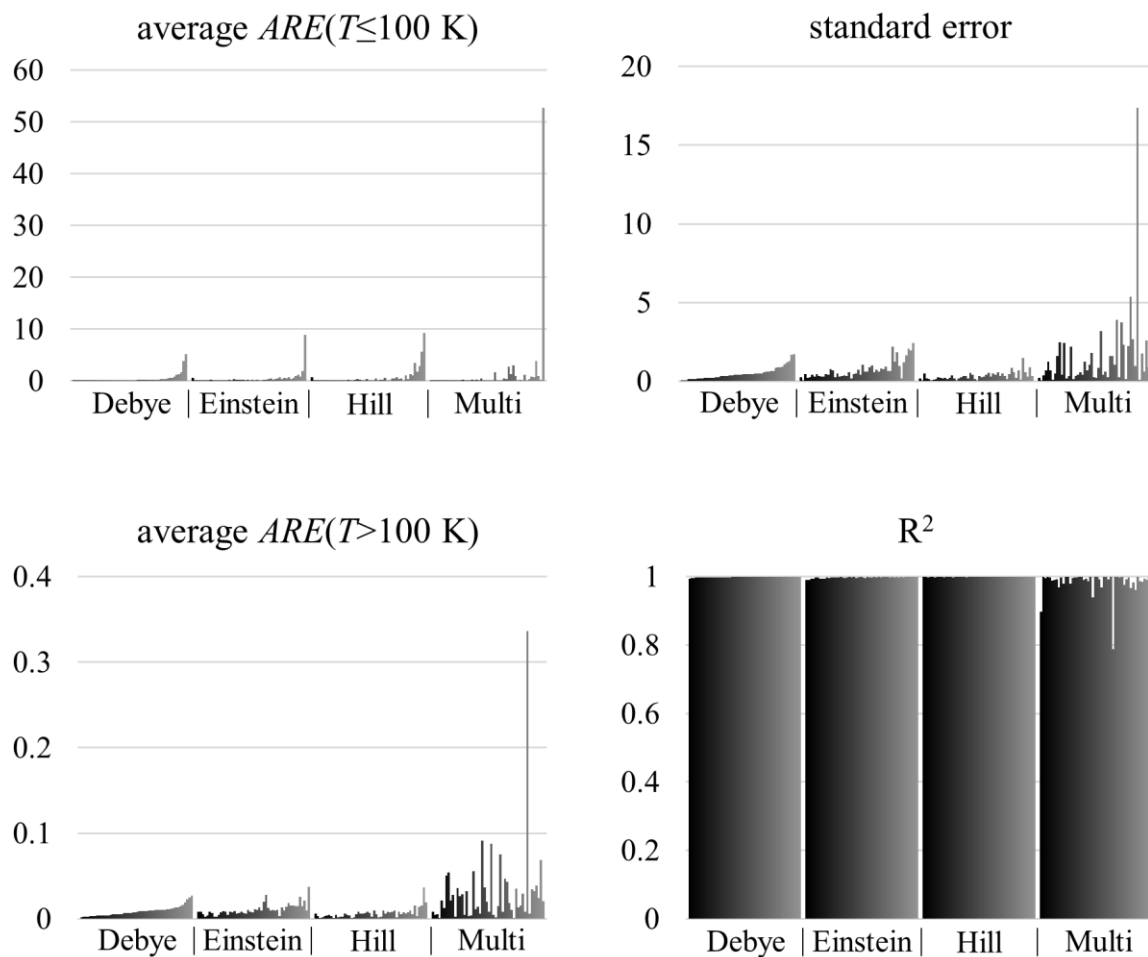


Figure C.4: Enthalpy of fusion and Hill Coefficient correlations for the alkali metals and alkali halides.

C.3 Discussion

The Hill Equation was fit to experimental heat capacity data for 53 inorganic compounds and technical solids. At common chemical process temperatures ($> 100 \text{ K}$ [173]) the Hill Equation predicted specific heat capacity more accurately than the Debye Model, the Einstein Solid, and Multilinear Model. At lower temperatures the Debye Model proved superior. However, the Debye Model requires the evaluation of a numerical integral, which can slow process simulation. Table C.1 shows that use of the Debye Model quintuples computation time relative to the Hill Equation.

Such time inflation would likely add additional computational burden to process engineering problems, which are already resource intensive [174], frequently time sensitive [175], and often NP-hard [176]. Thus, applications for the analytic Hill Equation likely exist at elevated temperatures whenever computational efficiency is essential.

A linear relationship between the Hill Coefficient and enthalpy of fusion was apparent. This result suggests a fundamental basis for specific heat capacity calculation via the Hill Equation. Based on Hill Coefficient trends within periodic groups (Figure C.5) a group contribution method based on the Hill Equation might be tractable [177]. However, sophisticated methods are already available for the *ab initio* prediction of specific heat [138, 139]. Furthermore, a fundamental derivation for use of the Hill Equation in specific heat prediction requires further development. Thus, based on current evidence the Hill Equation represents, at most, an analytic, efficient, and effective expression for heat capacity calculation that is likely useful in chemical process simulation.

Debye	5.06
Einstein	0.96
Hill	1
Multi	0.99

Table C.1: Relative heat capacity computation time for compiled C code on an Intel i5-4690K CPU. Debye integration was by the Trapezoidal Rule with 1 Kelvin granularity.

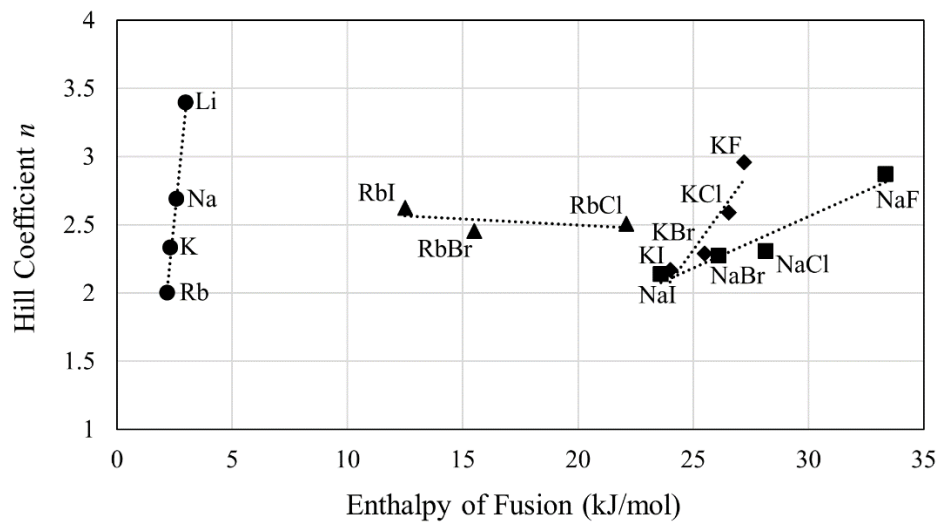


Figure C.5: Enthalpy of fusion and Hill Coefficient correlations for the alkali metals and alkali halides.

Appendix D: Optimized Blocking in Nonlinear Model Predictive Control

D.1. Introduction

Ostensibly, nonlinear model predictive control (NMPC) is closed-loop stable only with a sufficiently long prediction horizon or with the use of output constraints [175]. Constraining the process output is a dubious approach that can yield infeasible control optimizations. Conversely, the prediction horizon can be readily adjusted without complications. In coursework notes Moritz Diehl (University of Freiburg) has described nondimensionalizing time to achieve this goal. Consider a general autonomous plant model:

$$\dot{\bar{x}} = f(\bar{x}, \bar{z}, \bar{u}) \quad \text{D.1}$$

$$0 = g(\bar{x}, \bar{z}, \bar{u}) \quad \text{D.2}$$

where the vector of x contains the differential plant states, the vector of z contains the algebraic plant states, and the vector of u contains the control moves. We nondimensionalize time by scaling to a horizon length Δt :

$$\tau = \frac{t}{\Delta t} \quad \text{D.3}$$

$$\dot{\bar{x}} = \frac{d\bar{x}}{dt} = \frac{d\bar{x}}{(\Delta t)d\tau} = \frac{\dot{\bar{\chi}}}{\Delta t} \quad \text{D.4}$$

The integration bounds are now zero to one:

$$\dot{\bar{\chi}} = (\Delta t)f(\bar{\chi}, \bar{z}, \bar{u}) \quad \text{D.5}$$

$$0 = g(\bar{\chi}, \bar{z}, \bar{u}) \quad \text{D.6}$$

Importantly, we can add Δt as a decision variable in the controls optimization. This can allow the determination of an optimal horizon length that coaxes closed-loop stability.

Chemical processes exhibit dynamics on multiple timescales [103]. Moving too slowly to calm a fast process can yield instability. Moving too quickly to stabilize a slow process causes unnecessary equipment wear. We seek a controller whose responses match the fastest and slowest process dynamics, all while preserving a sufficiently long prediction horizon. To achieve this goal we suggest a parallel multiple shooting method that splits the controls predictions over heterogeneous windows, $\Delta t_1, \Delta t_2 \dots \Delta t_n$. Each processor integrates one window while the overall solver matches the endpoints, optimizes the controls, and optimizes each window length (Figure D.1). We hypothesize that giving the optimizer command over control move duration renders it responsive to process timescales.

Superficially, this is an inefficient computational approach. Integration of the longest windows will determine the overall computation time, degrading the benefits of parallelism. However, when using an adaptive integrator computational efficiency could be preserved. This owes to the qualitative characteristics of control. In brief, control action is usually most intense during rapid system change. Windows in these regions will be small and system integration challenging. Closer to steady-state the control and system dynamics are tamer, the windows are presumably longer, and integration more rapid. Figure D.2 summarizes the hypothesis. It is noteworthy that all the ode integrators in Matlab are adaptive. The availability of inexpensive parallel embedded systems with up to 64 processors could render this approach tenable (Parallella Incorporated).

Figure D.1: The proposed parallel shooting algorithm allocates the prediction to different processors, adjusts the timespan of each control intervention, and adjusts the intensity of each control intervention.

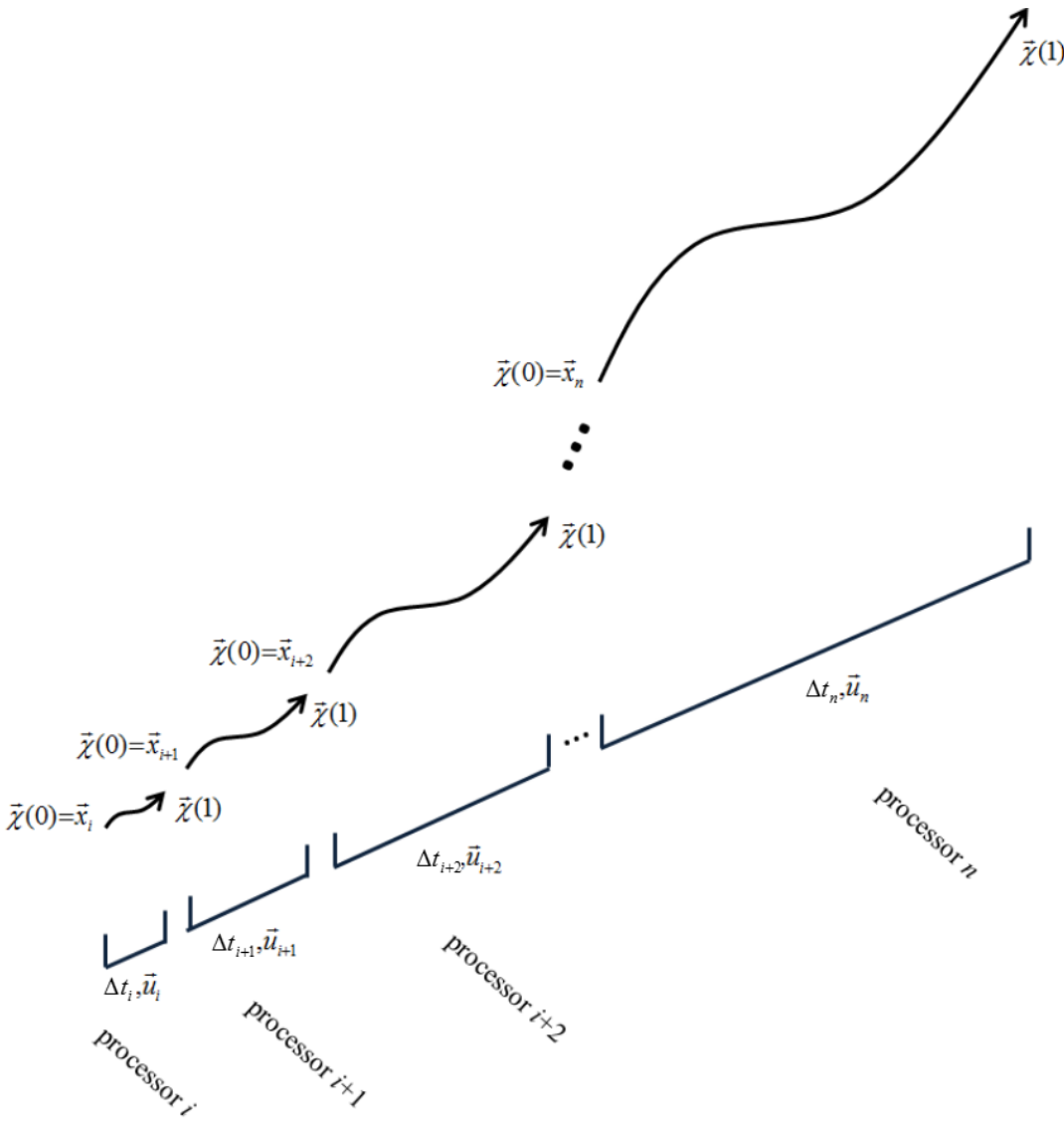
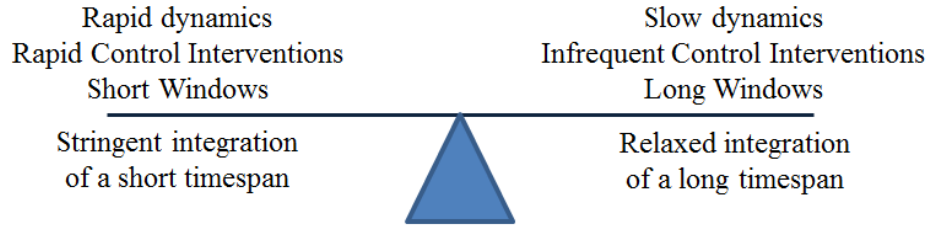


Figure D.2: When using adaptive integrators the proposed algorithm likely balances integration time, preserving the desirable aspects of parallel computation.



We evaluate this approach on a nonlinear predator-prey testbed (Lotka-Volterra equations).

D.2. Multidimensional Shooting

As a prerequisite to parallel shooting for nonlinear model predictive control, we consider the multidimensional shooting method. In engineering math the shooting method is a ubiquitously taught technique for solving boundary constrained differential equations. However, rarely does pedagogy move beyond linear, single-dimension, derivations. NMPC requires more, namely the solution of nonlinear, multidimensional, boundary-constrained differential equations. Here, we elaborate a general shooting method appropriate for NMPC [178-180]. Figure D.3 shows the problem for an \mathbb{R}^2 case.

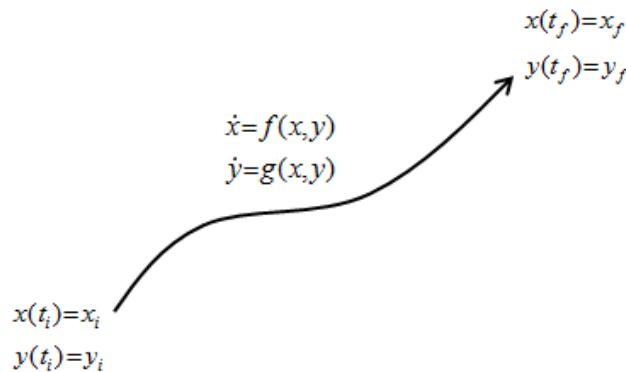


Figure D.3: Boundary constrained differential equations.

We seek a path between t_i and t_f that satisfies both conditions at these boundaries and the differential equations. In the case of trajectory planning we can adjust system states (here, x and y) in hopes of finding a solution. Alternatively, when fitting equations to data we can adjust parameters of the differential system in hopes of finding a solution. Considering the former case we can make the statement:

$$\dot{x} = f(x, y) \quad \text{D.7}$$

$$\dot{y} = g(x, y) \quad \text{D.8}$$

$$h\left(\begin{bmatrix} x(t_i) \\ y(t_i) \end{bmatrix}, \begin{bmatrix} x(t_f) \\ y(t_f) \end{bmatrix}\right) = 0 \quad \text{D.9}$$

Equation D.9 is of special interest. This equation compares the boundary constraints to their actual function values. One is free to choose any sensible function for this comparison (1-norm, 2-norm, etc). If, for example, the system is only constrained at t_f Equation D.9 could be:

$$\begin{bmatrix} x(t_f) \Big|_{x_i, y_i} - x_f \\ y(t_f) \Big|_{x_i, y_i} - y_f \end{bmatrix} = 0 \quad \text{D.10}$$

Here, the initial conditions are free to vary. We seek initial conditions that, after integration to t_f , zero Equation D.10. Starting with a guess for x_i and y_i we can expect some error:

$$h\left(\begin{bmatrix} x_i^k \\ y_i^k \end{bmatrix}, \begin{bmatrix} x(t_f) \\ y(t_f) \end{bmatrix}\right) = \varepsilon \neq 0 \quad \text{D.11}$$

Here, k denotes the iteration of our guess, with $k=1$ initially. Notice that we have explicitly listed the dependencies of h . The question becomes, how do we iterate our guess after acknowledging these dependencies? First it is useful to simplify the nomenclature:

$$\bar{s}^k = \begin{bmatrix} x_i^k \\ y_i^k \end{bmatrix} \quad \text{D.12}$$

$$\bar{z}(t_f; \bar{s}^k) = \begin{bmatrix} x(t_f) \\ y(t_f) \end{bmatrix} \quad \text{D.13}$$

$$\bar{h}(\bar{s}^k, \bar{z}(t_f; \bar{s}^k)) = \varepsilon \quad \text{D.14}$$

Where $z(t_f; s^k)$ is the integration at t_f given the state guess s^k . We seek to drive Equation D.14, a restatement of Equation D.9, to zero. This can be achieved by iterating s^k via a Taylor series expansion:

$$\bar{h}(\bar{s}^{k+1}, \bar{z}(t_f; \bar{s}^{k+1})) = \bar{h}(\bar{s}^k, \bar{z}(t_f; \bar{s}^k)) + \frac{\partial \bar{h}(\bar{s}^k, \bar{z}(t_f; \bar{s}^k))}{\partial \bar{s}} \Delta \bar{s} \quad \text{D.15}$$

with

$$\Delta \bar{s} = \bar{s}^{k+1} - \bar{s}^k \quad \text{D.16}$$

Aspirationally, we always expect that the next iterate of s will zero h . Thus, we set the left side of Equation D.15 to zero and subtract the current value of h :

$$-\bar{h}(\bar{s}^k, \bar{z}(t_f; \bar{s}^k)) = -\frac{\partial \bar{h}(\bar{s}^k, \bar{z}(t_f; \bar{s}^k))}{\partial \bar{s}} \Delta \bar{s} \quad \text{D.17}$$

The result is a “Newton-Raphson” root finding approach that harbors a nontrivial derivative. This derivative can be evaluated with the variational equations. However, a more practical method involves finite differences with small perturbations, δ_j , in each j^{th} direction :

$$\frac{\partial \bar{h}(\bar{s}^k, \bar{z}(t_f; \bar{s}^k))}{\partial \bar{s}} = \begin{bmatrix} \frac{x(t_f)|_{x_i^k + \delta_x, y_i^k} - x(t_f)|_{x_i^k, y_i^k}}{\delta_x} & \frac{x(t_f)|_{x_i^k, y_i^k + \delta_y} - x(t_f)|_{x_i^k, y_i^k}}{\delta_y} \\ \frac{y(t_f)|_{x_i^k + \delta_x, y_i^k} - y(t_f)|_{x_i^k, y_i^k}}{\delta_x} & \frac{y(t_f)|_{x_i^k, y_i^k + \delta_y} - y(t_f)|_{x_i^k, y_i^k}}{\delta_y} \end{bmatrix} \quad \text{D.18}$$

Typically each δ_j is scaled to machine precision:

$$\delta_j = \sqrt{\delta_{\text{machine}}} \quad \text{D.19}$$

Equation D.18 is reminiscent of the Jacobian. It is used in conjunction with Equations D.7 through D.17 to give the iteration system:

$$\begin{bmatrix} x_f - x(t_f)|_{x_i^k, y_i^k} \\ y_f - y(t_f)|_{x_i^k, y_i^k} \end{bmatrix} = \begin{bmatrix} \frac{x(t_f)|_{x_i^k + \delta_x, y_i^k} - x(t_f)|_{x_i^k, y_i^k}}{\delta_x} & \frac{x(t_f)|_{x_i^k, y_i^k + \delta_y} - x(t_f)|_{x_i^k, y_i^k}}{\delta_y} \\ \frac{y(t_f)|_{x_i^k + \delta_x, y_i^k} - y(t_f)|_{x_i^k, y_i^k}}{\delta_x} & \frac{y(t_f)|_{x_i^k, y_i^k + \delta_y} - y(t_f)|_{x_i^k, y_i^k}}{\delta_y} \end{bmatrix} \begin{bmatrix} x_i^{k+1} - x_i^k \\ y_i^{k+1} - y_i^k \end{bmatrix} \quad \text{D.20}$$

In deriving Equation D.20 we have considered the \mathbb{R}^2 case. The general scheme is summarized by Equation D.21:

$$-\bar{h}^k = \begin{bmatrix} \frac{\partial \bar{h}^k}{\partial s_1} & \frac{\partial \bar{h}^k}{\partial s_2} & \dots & \frac{\partial \bar{h}^k}{\partial s_j} & \dots & \frac{\partial \bar{h}^k}{\partial s_n} \end{bmatrix} \Delta \bar{s} \quad \text{D.21}$$

For any explicit system of differential equations:

$$\dot{\bar{z}} = \bar{f}(\bar{s}) \quad \text{D.22}$$

Shooting demands $n+1$ integrations of the differential system, where n is the number of free directions (variables). This holds whether finite differences or the variational equations are employed. However, because the variational equations are cumbersome to derive, general implementations of the shooting method avoid the variational approach.

In the control literature the finite-difference derivatives (Equation D.18) are called “internal numerical differentiation.” When using internal numerical differentiation it is essential to integrate all perturbations simultaneously. Otherwise inconsistent results may arise as adaptive solvers take different steps during sensitivity analysis [180]. Other differentiation approaches also exist, but these are beyond the scope of this introduction (algorithmic differentiation) [181-183].

D.3. Parallel Multiple Shooting

The shooting method is highly unstable, requiring a good initialization to converge [178-180]. This is especially true of the highly nonlinear and stiff systems common in chemical engineering. However, an extension of the shooting method has promise within the field of trajectory optimization. Parallel multiple shooting is more stable than single shooting, an invaluable trait when optimizing control actions in real time [178-180]. Figure D.4 is a starting point for understanding this method.

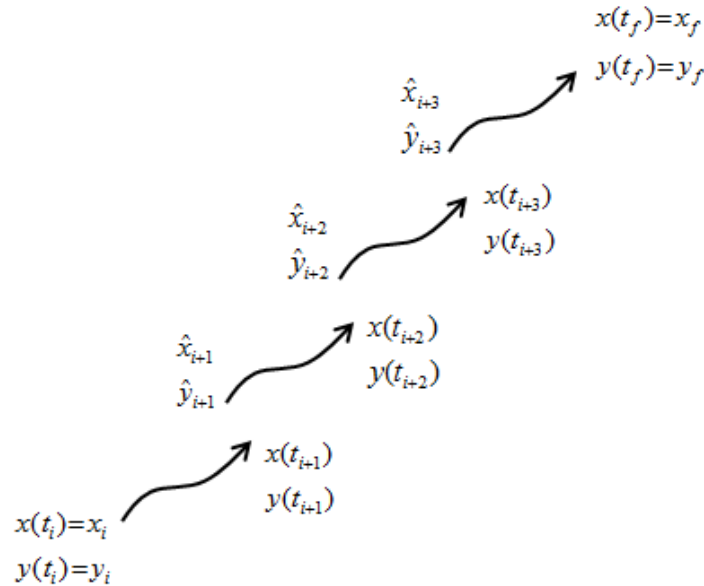


Figure D.4: A first guess in the quest for a unified trajectory in \mathbb{R}^2 .

We begin by guessing select states (\hat{x} and \hat{y}) of a trajectory originating at t_i . It is assumed that the initial state (here, x_i and y_i) is known, either by measurement or an estimator. To match points across the trajectory Equation D.9 is expanded:

$$\bar{h} = \begin{bmatrix} x(t_{i+1}) - x_{i+1} \\ y(t_{i+1}) - y_{i+1} \\ x(t_{i+2})|_{x_{i+1}, y_{i+1}} - x_{i+2} \\ y(t_{i+2})|_{x_{i+1}, y_{i+1}} - y_{i+2} \\ x(t_{i+3})|_{x_{i+2}, y_{i+2}} - x_{i+3} \\ y(t_{i+3})|_{x_{i+2}, y_{i+2}} - y_{i+3} \end{bmatrix} = 0 \quad \text{D.23}$$

As with single shooting, h will not equal zero for a typical guess. Again Newton iterations are employed to refine the guess. However, before proceeding it is useful to develop a nomenclature appropriate for parallel computing. We must define independent subproblems that can be dispatched to different processors in a multicore computer. Consequently, it is convenient to recast the vector of states (Equation D.12):

$$\begin{bmatrix} \bar{s}_{@i+1} \\ \bar{s}_{@i+3} \\ \bar{s}_{@i+3} \end{bmatrix} = \begin{bmatrix} x_{i+1} \\ y_{i+1} \\ x_{i+2} \\ y_{i+2} \\ x_{i+3} \\ y_{i+3} \end{bmatrix} \quad \text{D.24}$$

As a result Equation D.21 becomes:

$$-\bar{h}^k = \begin{bmatrix} \frac{\partial \bar{h}^k}{\partial \bar{s}_{@i+1}} & \frac{\partial \bar{h}^k}{\partial \bar{s}_{@i+2}} & \frac{\partial \bar{h}^k}{\partial \bar{s}_{@i+3}} \end{bmatrix} \begin{bmatrix} \Delta \bar{s}_{@i+1} \\ \Delta \bar{s}_{@i+2} \\ \Delta \bar{s}_{@i+3} \end{bmatrix} \quad \text{D.25}$$

The derivatives within Equation D.25 form a sparse system because each discontinuity in Figure D.4 depends solely on its neighboring states. For the general system of Equation D.22 and d discontinuities the derivative matrix becomes:

$$-\bar{h}^k = \begin{bmatrix} -I & 0 & 0 & 0 & \cdots & 0 \\ Y_{@i+1} & -I & 0 & 0 & \cdots & 0 \\ 0 & Y_{@i+2} & -I & 0 & \cdots & 0 \\ 0 & 0 & Y_{@i+3} & -I & \ddots & \vdots \\ \vdots & \vdots & \ddots & \ddots & \ddots & 0 \\ 0 & 0 & \cdots & 0 & Y_{@i+d} & -I \end{bmatrix} \begin{bmatrix} \Delta \bar{s}_{@i+1} \\ \Delta \bar{s}_{@i+2} \\ \Delta \bar{s}_{@i+3} \\ \vdots \\ \Delta \bar{s}_{@i+d} \end{bmatrix} \quad \text{D.25}$$

Where each matrix Y is given by:

$$Y_i = \begin{bmatrix} \left. \frac{\partial \bar{z}_i(t_{i+1})}{\partial s_1} \right|_{\bar{s}_i} & \left. \frac{\partial \bar{z}_i(t_{i+1})}{\partial s_2} \right|_{\bar{s}_i} & \cdots & \left. \frac{\partial \bar{z}_i(t_{i+1})}{\partial s_j} \right|_{\bar{s}_i} \end{bmatrix} \quad \text{D.26}$$

The bar indicates the derivative of the vector function z at t_{i+1} given a perturbation of s at time t_i .

Y can be easily computed as a matrix subtraction:

$$Y_i = \frac{1}{\sqrt{\delta_{machine}}} \left(\left[\bar{z}_i(t_{i+1}) \right]_{[\bar{s}_i | \cdot | \bar{s}_i] + I \sqrt{\delta_{machine}}} - \left[\bar{z}_i(t_{i+1}) \right]_{[\bar{s}_i | \cdot | \bar{s}_i]} \right) \quad \text{D.27}$$

It is Equation D.27 that can be distributed amongst parallel processors. Each processor solves the same differential system, but with different initial conditions. Figure D.5 shows the programmatic flow for a parallel algorithm. Before exhibiting the parallel implementation of Figure D.5, it's illustrative to write the derivatives within Equation D.25 for the trajectory shown in Figure D.4:

$$\begin{bmatrix}
-1 & 0 & 0 & 0 & 0 & 0 \\
0 & -1 & 0 & 0 & 0 & 0 \\
\frac{x(t_{i+2})|_{x_{i+1}^k+\delta_x, y_{i+1}^k} - x(t_{i+2})|_{x_{i+1}^k, y_{i+1}^k}}{\delta_x} & \frac{x(t_{i+2})|_{x_{i+1}^k, y_{i+1}^k+\delta_y} - x(t_{i+2})|_{x_{i+1}^k, y_{i+1}^k}}{\delta_y} & -1 & 0 & 0 & 0 \\
\frac{y(t_{i+2})|_{x_{i+1}^k+\delta_x, y_{i+1}^k} - y(t_{i+2})|_{x_{i+1}^k, y_{i+1}^k}}{\delta_x} & \frac{y(t_{i+2})|_{x_{i+1}^k, y_{i+1}^k+\delta_y} - y(t_{i+2})|_{x_{i+1}^k, y_{i+1}^k}}{\delta_y} & 0 & -1 & 0 & 0 \\
0 & 0 & \frac{x(t_{i+3})|_{x_{i+2}^k+\delta_x, y_{i+2}^k} - x(t_{i+3})|_{x_{i+2}^k, y_{i+2}^k}}{\delta_x} & \frac{x(t_{i+3})|_{x_{i+2}^k, y_{i+2}^k+\delta_y} - x(t_{i+3})|_{x_{i+2}^k, y_{i+2}^k}}{\delta_y} & -1 & 0 \\
0 & 0 & \frac{y(t_{i+3})|_{x_{i+2}^k+\delta_x, y_{i+2}^k} - y(t_{i+3})|_{x_{i+2}^k, y_{i+2}^k}}{\delta_x} & \frac{y(t_{i+3})|_{x_{i+2}^k, y_{i+2}^k+\delta_y} - y(t_{i+3})|_{x_{i+2}^k, y_{i+2}^k}}{\delta_y} & 0 & -1
\end{bmatrix}$$

Figure D.6 shows Matlab results from coding the multiple shooting algorithm of Figure D.5. It is noteworthy that convergence is linear. Although each processor integrates a fraction of the trajectory, it does so multiple times. Relative to single shooting, no time savings are achieved for simple trajectory integration (Table D.1). However, in multiple shooting solution stability is presumably enhanced.

Figure D.5: A Parallel Shooting Implementation

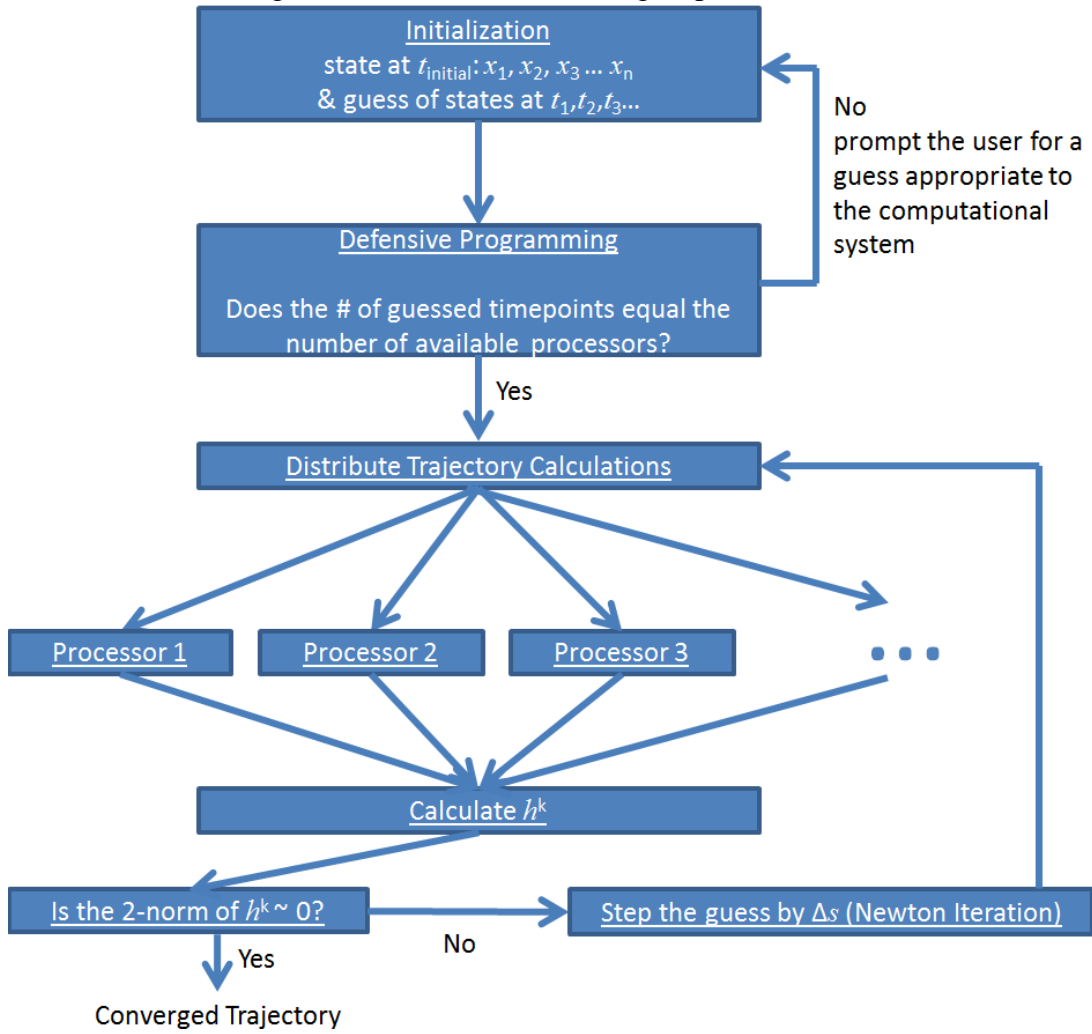
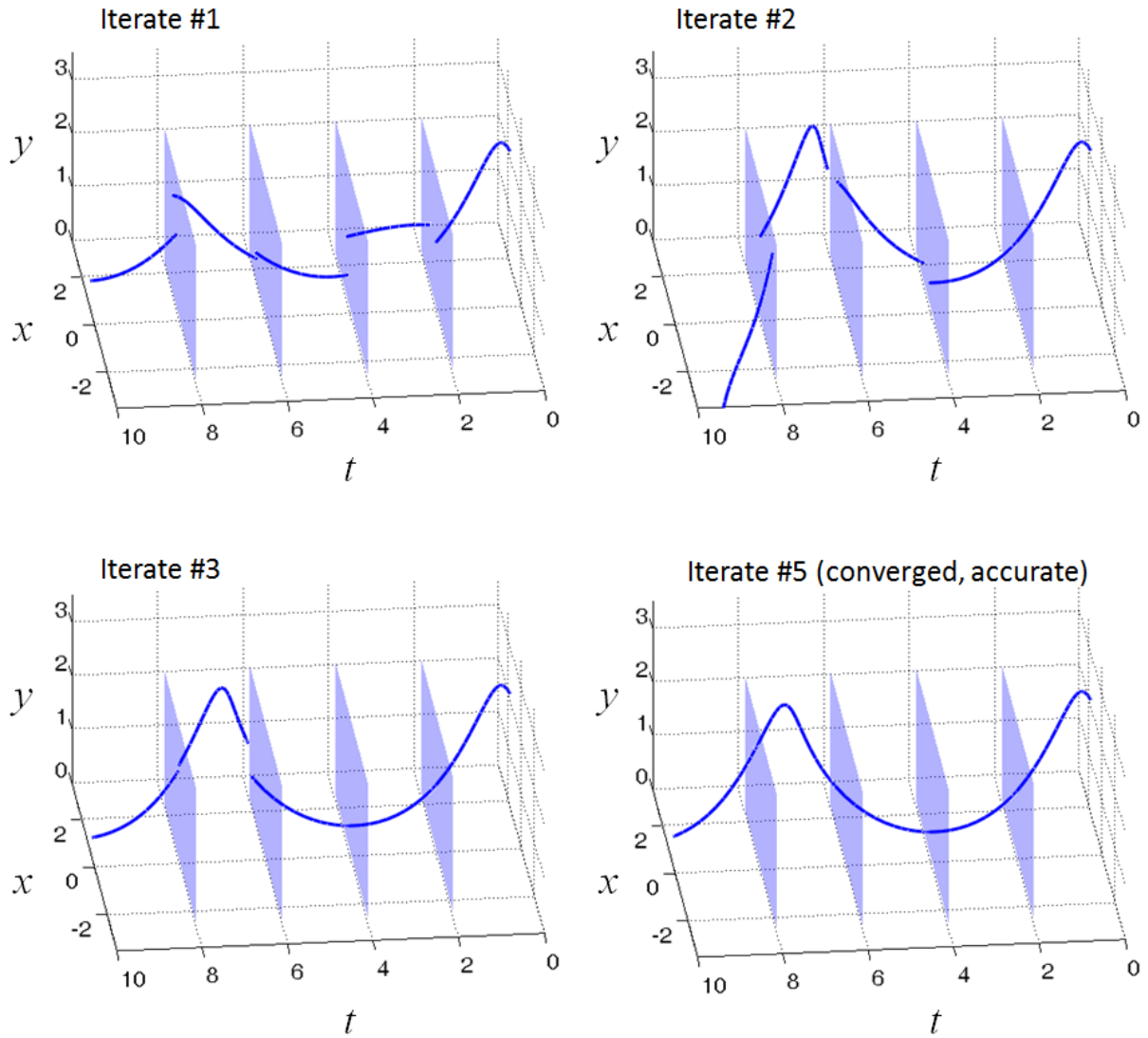


Table D.1

	“Trajectory per processor”	“Number of evaluations”	“Computation Time”
Single Shooting	1	1	1
Multiple shooting	1/(# processors)	(# processors)	1

Figure D.6: The predator prey equations integrated via multiple shooting on four processors.

$$\frac{dx}{dt} = x - xy$$
$$\frac{dy}{dt} = -y + xy$$



D.4. Results

The parallel multiple shooting algorithm was implemented for nonlinear control of the Lotka-Volterra (predator-prey) equations from Figure D.6 [184, 185]:

$$\begin{aligned}\dot{x} &= x - xy \\ \dot{y} &= -y + xy + u \\ \dot{u} &= 0\end{aligned}\tag{D.28}$$

Here, x and y are the states and u is the input. The derivative of u is invariant during a given control block (Figure D.1). Dr. Biegler's IPOPT interior point optimizer and was used to coerce the system to a steady state [186]. In general, this optimizer performs best when the minimization is scaled to $O(1)$. Thus, several dimensionless derived quantities were defined for use in the control objective. Departures from the reference trajectory were normalized elementwise by the nominal steady state operating point:

$$\Delta \vec{y}_k = \frac{(\vec{y} - \vec{Y})_k}{\vec{Y}}\tag{D.29}$$

Where \vec{y}_k is the process output at time k and \vec{Y} is the desired output. The relative time was then defined:

$$\vec{\tau} = \frac{\Delta \vec{t}_{\text{actual control steps}}}{\Delta \vec{t}_{\text{equal spacing for desired horizon}}}\tag{D.30}$$

Where $\Delta \vec{t}$ is a vector that harbors the duration of each blocked control action (Figure D.1). Initially all time steps have an equal spacing, which gives:

$$\vec{\tau} = \begin{bmatrix} 1 \\ 1 \\ \vdots \end{bmatrix}\tag{D.31}$$

The time departure was defined as:

$$\Delta\vec{T} = \frac{\Delta\vec{t}_{\text{actual control steps}} - \Delta t_{\text{equal spacing for desired horizon}}}{\Delta t_{\text{equal spacing for desired horizon}}} \quad \text{D.32}$$

Initially, all time steps have no departure, which gives:

$$\Delta\vec{T} = \begin{bmatrix} 0 \\ 0 \\ \vdots \end{bmatrix} \quad \text{D.33}$$

Finally, the control actions were normalized by the controller span:

$$\Delta\vec{\mu}_k = \frac{\Delta\vec{u}_{\text{applied},k}}{\Delta\vec{u}_{\text{actuator full range}}} \quad \text{D.34}$$

The controls objective function embellished a typical quadratic penalization by throttling changes in the blocked controls, outputs, and $\Delta\vec{T}$:

$$obj = \underbrace{\Delta\vec{y}^T \text{diag}(\vec{\tau})}_{\text{"Q"}} \Delta\vec{y} + \underbrace{\Delta\vec{\mu}^T \begin{bmatrix} 10 & 0 & \dots \\ 0 & 10 & \ddots \\ \vdots & \ddots & \ddots \end{bmatrix}}_{\text{"R"}} \Delta\vec{\mu} + \underbrace{\Delta\vec{T}^T \begin{bmatrix} 0.1 & 0 & \dots \\ 0 & 0.1 & \ddots \\ \vdots & \ddots & \ddots \end{bmatrix}}_{\text{"S"}} \Delta\vec{T} \quad \text{D.35}$$

Here, Q is the output weight matrix, R is the input move suppression matrix, and S weights changes in the control blocking. By placing the relative time along the output weight matrix diagonal we form the integral squared error of process departures irrespective of the actual time blocking. Control was achieved through the minimization of Equation D.35 via parallel multiple shooting.

Figure D.7 shows behavior of the predator-prey system with and without control by the nonlinear objective function (Equation D.35) for a 32 processor implementation of parallel multiple shooting. Figure D.8 compares this response to that of linear model predictive (via state space linearization of the process) and control with $S = 0$ (invariant control blocking). It was

evident that the new optimization approach altered the duration of each control action, especially early in the process trajectory. The initial control move was extended at controller saturation while the remaining moves were compressed to compensate. The result was superior control. Figure D.9 shows that the new controller reduced the integral squared error by 25% relative to a linear model predictive controller and 20% relative to a controller with fixed control blocks.

Figure D.7: The results of control with variable control blocking (solid blue line), versus the uncontrolled response (dotted red line).

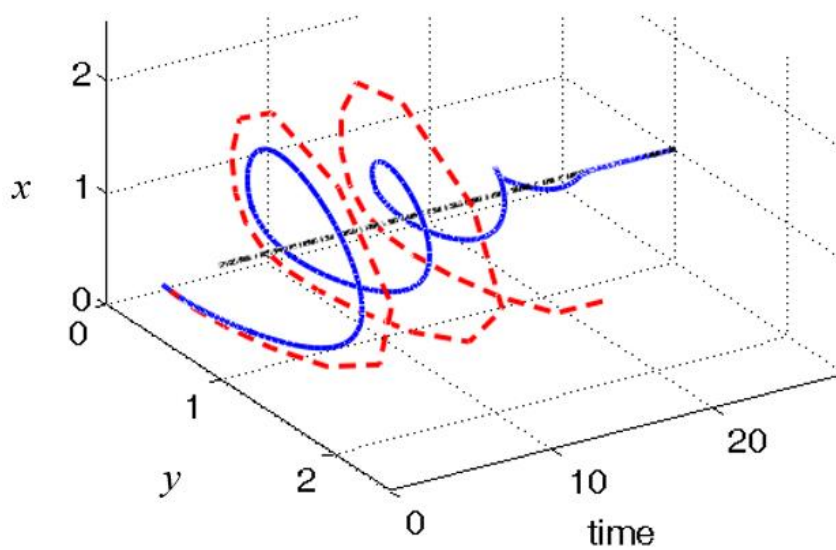


Figure D.8: Behavior of the controllers

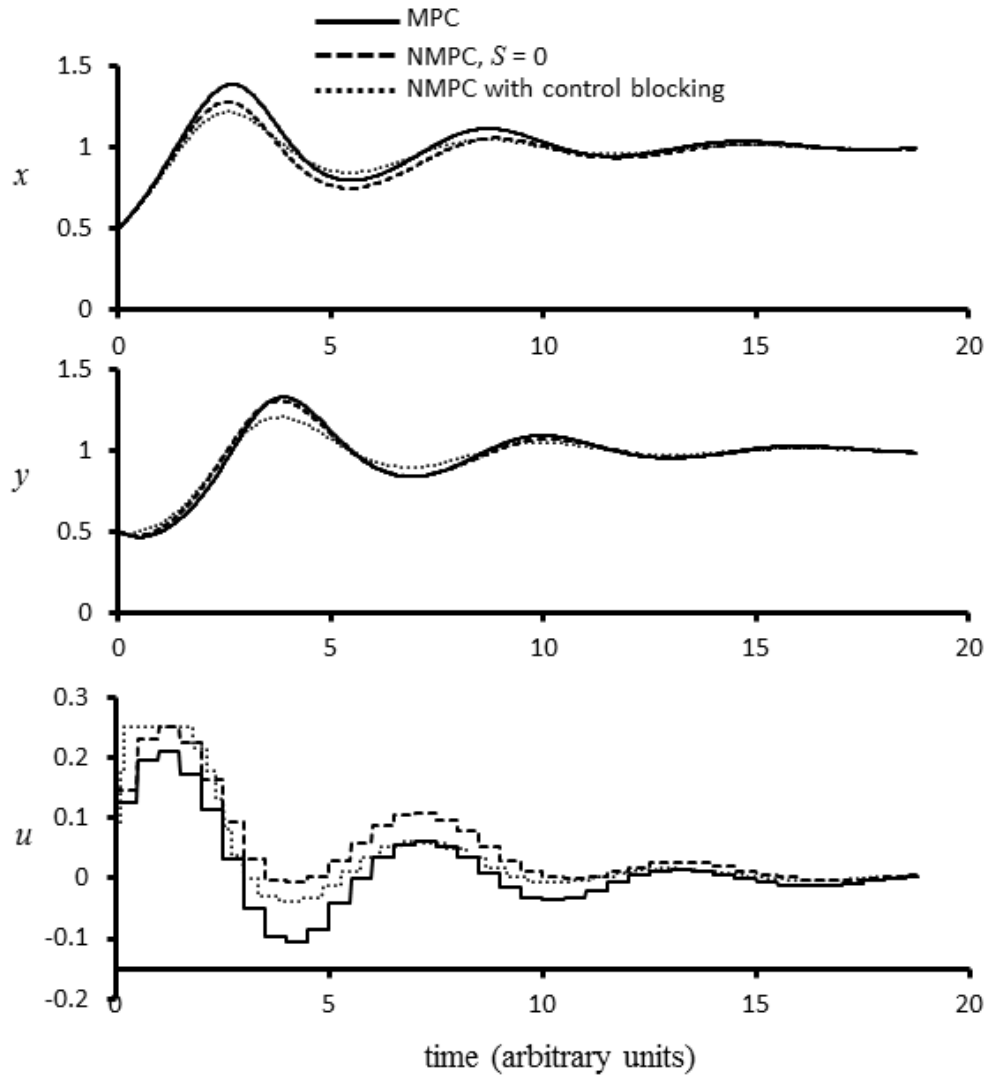
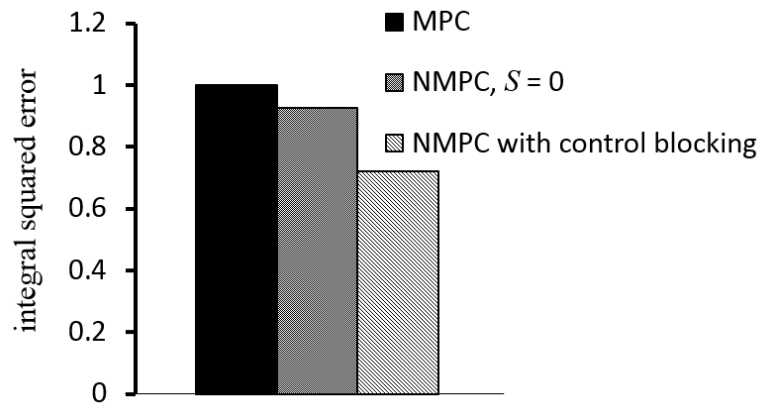


Figure D.9: Integral squared error of the controllers



References

1. Petrasch, J., P. Osch, and A. Steinfeld, *Dynamics and control of solar thermochemical reactors*. Chemical Engineering Journal, 2009. **145**(3): p. 362-370.
2. Muroyama, A., et al., *Modeling of a dynamically-controlled hybrid solar/autothermal steam gasification reactor*. Energy & Fuels, 2014. **28**(10): p. 6520-6530.
3. Saade, E., D.E. Clough, and A.W. Weimer, *Model predictive control of a solar-thermal reactor*. Solar Energy, 2014. **102**: p. 31-44.
4. Roca, L., A. de la Calle, and L.J. Yebra, *Heliostat-field gain-scheduling control applied to a two-step solar hydrogen production plant*. Applied energy, 2013. **103**: p. 298-305.
5. Roca, L., et al., *A control based on a knapsack problem for solar hydrogen production*. Optimal Control Applications and Methods, 2016. **37**(3): p. 496-507.
6. Beschi, M., et al., *Constrained control strategies for disturbance rejection in a solar furnaces*. Control Engineering Practice, 2013. **21**(10): p. 1410-1421.
7. Najafabadi, H.A. and N. Ozalp, *Aperture size adjustment using model based adaptive control strategy to regulate temperature in a solar receiver*. Solar Energy, 2018. **159**: p. 20-36.
8. Zapata, J.I., *Full State Feedback Control of Steam Temperature in a Once-Through Direct Steam Generation Receiver Powered by a Paraboloidal Dish*. Journal of Solar Energy Engineering, 2015. **137**(2): p. 021017.
9. Roeb, M., et al., *Technologies and trends in solar power and fuels*. Energy & Environmental Science, 2011. **4**(7): p. 2503-2511.
10. Simms, D., *Archimedes and the burning mirrors of Syracuse*. Technology and Culture, 1977. **18**(1): p. 1-24.
11. Pifre, A., *A solar printing press*. Nature, 1882. **21**: p. 503-504.
12. Kreith, F. and J.F. Kreider, *Principles of solar engineering*. 1978.
13. *Harnessing Phoebus, Sun Works Machinery, The Modern Substitute for Sun Worship*, in *Egyptian Gazette*. 1913: Cairo, Egypt.
14. Reddy, V.S., et al., *State-of-the-art of solar thermal power plants—A review*. Renewable and Sustainable Energy Reviews, 2013. **27**: p. 258-273.
15. Behar, O., A. Khellaf, and K. Mohammedi, *A review of studies on central receiver solar thermal power plants*. Renewable and sustainable energy reviews, 2013. **23**: p. 12-39.
16. Chen, H., et al., *Progress in electrical energy storage system: A critical review*. Progress in Natural Science, 2009. **19**(3): p. 291-312.
17. Furler, P., J.R. Scheffe, and A. Steinfeld, *Syngas production by simultaneous splitting of H₂O and CO₂ via ceria redox reactions in a high-temperature solar reactor*. Energy & Environmental Science, 2012. **5**(3): p. 6098-6103.
18. Lichty, P., et al., *Rapid high temperature solar thermal biomass gasification in a prototype cavity reactor*. Journal of solar energy engineering, 2010. **132**(1): p. 011012.
19. Muhich, C.L., et al., *Efficient generation of H₂ by splitting water with an isothermal redox cycle*. Science, 2013. **341**(6145): p. 540-542.
20. Wieckert, C., et al., *A 300kW solar chemical pilot plant for the carbothermic production of Zinc*. Journal of Solar Energy Engineering, 2007. **129**(2): p. 190-196.
21. Besarati, S. and D. Goswami, *Supercritical CO₂ and other advanced power cycles for concentrating solar thermal (CST) systems*. Advances in Concentrating Solar Thermal Research and Technology, 2016: p. 157.

22. Loutzenhiser, P.G. and A.P. Muroyama, *A review of the state-of-the-art in solar-driven gasification processes with carbonaceous materials*. Solar Energy, 2017. **156**: p. 93-100.
23. Upham, D.C., et al., *Catalytic molten metals for the direct conversion of methane to hydrogen and separable carbon*. Science, 2017. **358**(6365): p. 917-921.
24. Murray, J.P., A. Steinfeld, and E.A. Fletcher, *Metals, nitrides, and carbides via solar carbothermal reduction of metal oxides*. Energy, 1995. **20**(7): p. 695-704.
25. Feldhoff, J.F. and T. Hirsch. *An approach to DNI transients characterization for system evaluation*. in *AIP Conference Proceedings*. 2017. AIP Publishing.
26. Glaser, P.E., *Engineering research with a solar furnace*. Solar energy, 1958. **2**(2): p. 7-10.
27. Riskiev, T. and S.K. Suleimanov, *Double mirror polyheliostat solar furnace of 1000 kW thermal power*. Solar energy materials, 1991. **24**(1-4): p. 625-632.
28. Douale, P., et al., *Thermal shocks on an electrolytic chromium coating in a solar furnace*. Le Journal de Physique IV, 1999. **9**(PR3): p. Pr3-429-Pr3-434.
29. Rodriguez, G., J. De Damborenea, and A. Vázquez, *Surface hardening of steel in a solar furnace*. Surface and coatings technology, 1997. **92**(3): p. 165-170.
30. Camacho, E.F., et al., *Control of Solar Energy Systems*. Advances in Industrial Control, ed. M. Grimble and M. Johnson. 2012, London, UK: Springer.
31. Morud, J. and S. Skogestad, *Effects of recycle on dynamics and control of chemical processing plants*. Computers & chemical engineering, 1994. **18**: p. S529-S534.
32. Bhargav, K., F. Gross, and P. Schramek, *Life Cycle cost optimized heliostat size for power towers*. Energy Procedia, 2014. **49**: p. 40-49.
33. Bradshaw, R.W., et al., *Final test and evaluation results from the solar two project*. 2002, Sandia National Labs., Albuquerque, NM (US); Sandia National Labs., Livermore, CA (US).
34. Kolb, G.J., et al., *Power tower technology roadmap and cost reduction plan*. SAND2011-2419, Sandia National Laboratories, Albuquerque, NM, 2011. **7**.
35. Vogel, W. and H. Kalb, *Large-scale solar thermal power: technologies, costs and development*. 2010: John Wiley & Sons.
36. Berenguel, M., et al., *An artificial vision-based control system for automatic heliostat positioning offset correction in a central receiver solar power plant*. Solar energy, 2004. **76**(5): p. 563-575.
37. Relloso, S. and E. García, *Tower technology cost reduction approach after Gemasolar experience*. Energy procedia, 2015. **69**: p. 1660-1666.
38. Beschi, M., et al., *Implementation of feedback linearization GPC control for a solar furnace*. Journal of Process Control, 2013. **23**(10): p. 1545-1554.
39. Powell, K.M., et al., *Hybrid concentrated solar thermal power systems: A review*. Renewable and Sustainable Energy Reviews, 2017. **80**: p. 215-237.
40. Wieghardt, K., et al. *SynLight—the world's largest artificial sun*. in *AIP Conference Proceedings*. 2016. AIP Publishing.
41. Bader, R., S. Haussener, and W. Lipiński, *Optical design of multisource high-flux solar simulators*. Journal of Solar Energy Engineering, 2015. **137**(2): p. 021012.
42. Saade, E., D.E. Clough, and A.W. Weimer, *Use of Image-Based Direct Normal Irradiance Forecasts in the Model Predictive Control of a Solar-Thermal Reactor*. Journal of Solar Energy Engineering, 2014. **136**(1): p. 010905.

43. Ackermann, T. and H. Rüterjans, *Kalorimetrische Messungen zur Helix-Coil-Unwandlung von Nucleinsäuren und synthetischen Polypeptiden in Lösung*. Berichte der Bunsengesellschaft für physikalische Chemie, 1964. **68**(8-9): p. 850-856.
44. Pérez-Rábago, C., et al., *Heat transfer in a conical cavity calorimeter for measuring thermal power of a point focus concentrator*. Solar Energy, 2006. **80**(11): p. 1434-1442.
45. Sefkow, E.A.B., *The design of a calorimeter to measure concentrated solar flux*, in *Mechanical Engineering*. 2013, University of Minnesota: Minneapolis, MN.
46. Sparrow, E., *Radiation heat transfer*. 1970, Blemont, CA: Wadsworth Publishing Company.
47. Guillot, E., et al., *Comparison of 3 heat flux gauges and a water calorimeter for concentrated solar irradiance measurement*. Energy Procedia, 2014. **49**: p. 2090-2099.
48. Diver, R., et al., *A New High-Temperature Solar Research Furnace*. Transactions of the American Society of Mechanical Engineers, 1983. **105**: p. 288-293.
49. Sharma, G. and J. Martin, *MATLAB®: a language for parallel computing*. International Journal of Parallel Programming, 2009. **37**(1): p. 3-36.
50. Howell, J.R., M.P. Menguc, and R. Siegel, *Thermal radiation heat transfer*. 2010: CRC press.
51. Fenves, G.L., *Object-oriented programming for engineering software development*. Engineering with computers, 1990. **6**(1): p. 1-15.
52. Phong, B.T., *Illumination for computer generated pictures*. Communications of the ACM, 1975. **18**(6): p. 311-317.
53. Cooper, T. and A. Steinfeld, *Derivation of the angular dispersion error distribution of mirror surfaces for Monte Carlo ray-tracing applications*. Journal of Solar Energy Engineering, 2011. **133**(4): p. 044501.
54. Petrasch, J., *A free and open source Monte Carlo ray tracing program for concentrating solar energy research*. ASME Paper No. ES2010-90206, 2010.
55. Winston, R., J.C. Miñano, and P.G. Benitez, *Nonimaging optics*. 2005: Academic Press.
56. Wendelin, T. *SolTRACE: a new optical modeling tool for concentrating solar optics*. in *Proceedings of the ISEC*. 2003.
57. Daubert, T.E. and R.P. Danner, *Physical and Thermodynamic Properties of Pure Chemicals: Design institute for physical property data, American institute of chemical engineers. vp*. 1989: Hemisphere Publishing Corporation.
58. Prakash, M., S. Kedare, and J. Nayak, *Investigations on heat losses from a solar cavity receiver*. Solar Energy, 2009. **83**(2): p. 157-170.
59. Mori, Y. and W. Nakayama, *Study on forced convective heat transfer in curved pipes:(3rd report, theoretical analysis under the condition of uniform wall temperature and practical formulae)*. International journal of heat and mass transfer, 1967. **10**(5): p. 681-695.
60. Kaya, O. and I. Teke, *Turbulent forced convection in a helically coiled square duct with one uniform temperature and three adiabatic walls*. Heat and mass transfer, 2005. **42**(2): p. 129-137.
61. Steinfeld, A., *Exchange factor between two spheres placed at the foci of a specularly reflecting ellipsoidal cavity*. International communications in heat and mass transfer, 1991. **18**(1): p. 19-26.
62. Rowe, S.C., et al., *Worst-case losses from a cylindrical calorimeter for solar simulator calibration*. Optics Express, 2015. **23**(19): p. A1309-A1323.

63. Kevane, C., *Construction and operation of the Arizona State College solar furnace*. Solar Energy, 1957. **1**(2-3): p. 99-101.
64. Hisada, T., et al., *Concentration of the solar radiation in a solar furnace*. Solar Energy, 1957. **1**(4): p. 14-16.
65. Lewandowski, A., et al., *Performance characterization of the SERI high-flux solar furnace*. Solar Energy Materials, 1991. **24**(1-4): p. 550-563.
66. Riveros-Rosas, D., et al., *Optical design of a high radiative flux solar furnace for Mexico*. Solar Energy, 2010. **84**(5): p. 792-800.
67. Trombe, F. and A.L.P. Vinh, *Thousand kW solar furnace, built by the National Center of Scientific Research, in Odeillo (France)*. Solar Energy, 1973. **15**(1): p. 57-61.
68. Levêque, G., et al., *Experimental and numerical characterization of a new 45 kW el multisource high-flux solar simulator*. Optics express, 2016. **24**(22): p. A1360-A1373.
69. Krueger, K., J. Davidson, and W. Lipiński, *Design of a new 45 kWe high-flux solar simulator for high-temperature solar thermal and thermochemical research*. Journal of Solar Energy Engineering, 2011. **133**(1): p. 011013.
70. Li, Z., et al., *Study on the radiation flux and temperature distributions of the concentrator–receiver system in a solar dish/Stirling power facility*. Applied Thermal Engineering, 2011. **31**(10): p. 1780-1789.
71. Dong, X., et al., *Concentric multilayer model of the arc in high intensity discharge lamps for solar simulators with experimental validation*. Solar Energy, 2015. **122**: p. 293-306.
72. Krueger, K.R., *Design and characterization of a concentrating solar simulator*, in *Mechanical Engineering*. 2012, UNIVERSITY OF MINNESOTA: Mineapolis MN.
73. Gill, R., et al., *Characterization of a 6 kW high-flux solar simulator with an array of xenon arc lamps capable of concentrations of nearly 5000 suns*. Review of Scientific Instruments, 2015. **86**(12): p. 125107.
74. Ballestrin, J., et al., *Systematic error in the measurement of very high solar irradiance*. Solar energy materials and solar cells, 2003. **80**(3): p. 375-381.
75. Krueger, K., W. L., and J. Davidson, *Operational performance of the University of Minnesota 45 kWe high-flux solar simulator*. Journal of Solar Energy Engineering, 2013. **135**(4): p. 044501.
76. Bird, R.B., W.E. Stewart, and E.N. Lightfoot, *Transport phenomena*. 2007: John Wiley & Sons.
77. Palik, E.D., *Handbook of optical constants of solids*. Vol. 3. 1998: Academic press.
78. Nakar, D., et al., *Radiometric characterization of ultrahigh radiance xenon short-arc discharge lamps*. Applied optics, 2008. **47**(2): p. 224-229.
79. Nelder, J.A. and R. Mead, *A simplex method for function minimization*. The computer journal, 1965. **7**(4): p. 308-313.
80. Hsieh, C.K. and K. Su, *Thermal radiative properties of glass from 0.32 to 206 μm* . Solar Energy, 1979. **22**(1): p. 37-43.
81. Thelen, M., *Entwicklung eines optischen Messsystems für Strahlungsfussdichteverteilung und Verifizierung anhand hochkonzentrierter Solarstrahlung*. 2016, Rheinische Fachhochschule Köln.
82. Lee, J.H., M. Morari, and C.E. Garcia, *State-space interpretation of model predictive control*. Automatica, 1994. **30**(4): p. 707-717.
83. Lundström, P., et al., *Limitations of dynamic matrix control*. Computers & Chemical Engineering, 1995. **19**(4): p. 409-421.

84. Maciejowski, J.M., *Predictive control: with constraints*. 1 ed. 2002, Essex, UK: Prentice Hall.
85. Morari, M. and J.H. Lee. *Model predictive control: The good, the bad, and the ugly*. in *Proc. Conf. On Chemical Process Control, CPC-IV*. 1991.
86. Di Ruscio, D., *Closed and open loop subspace system identification of the Kalman filter*. Modeling, Identification and Control, 2009. **30**(2): p. 71.
87. Froisy, J.B., *Model predictive control—building a bridge between theory and practice*. Computers & chemical engineering, 2006. **30**(10): p. 1426-1435.
88. Qin, S.J., *An overview of subspace identification*. Computers & chemical engineering, 2006. **30**(10): p. 1502-1513.
89. Qin, S.J. and T.A. Badgwell, *A survey of industrial model predictive control technology*. Control engineering practice, 2003. **11**(7): p. 733-764.
90. Lee, J.H., *Model predictive control: Review of the three decades of development*. International Journal of Control, Automation and Systems, 2011. **9**(3): p. 415-424.
91. Luenberger, D., *Canonical forms for linear multivariable systems*. IEEE Transactions on Automatic Control, 1967. **12**(3): p. 290-293.
92. Van Dooren, P., *Reduced order observers: A new algorithm and proof*. Systems & Control Letters, 1984. **4**(5): p. 243-251.
93. Radke, A. and Z. Gao. *A survey of state and disturbance observers for practitioners*. in *American Control Conference, 2006*. 2006. IEEE.
94. Wang, L., *Model predictive control system design and implementation using MATLAB®*. 2009: Springer Science & Business Media.
95. Franklin, G.F., J.D. Powell, and M.L. Workman, *Digital control of dynamic systems*. Vol. 3. 1998: Addison-wesley Menlo Park, CA.
96. Grosdidier, P., M. Morari, and B.R. Holt, *Closed-loop properties from steady-state gain information*. Industrial & engineering chemistry fundamentals, 1985. **24**(2): p. 221-235.
97. Morari, M. and J.C. Doyle, *Unifying framework for control system design under uncertainty and its implications for chemical process control*, in *Conference on Chemical Process Control III*. 1986, California Inst. of Tech., Pasadena (USA). Dept. of Chemical Engineering: Asilomar, CA.
98. Nett, C.N. and V. Manousiouthakis. *Euclidean condition and block relative gain: connections, conjectures, and clarifications*. in *American Control Conference, 1987*. 1987. IEEE.
99. Skogestad, S. and M. Morari, *Design of resilient processing plants-IX. Effect of model uncertainty on dynamic resilience*. Chemical engineering science, 1987. **42**(7): p. 1765-1780.
100. Chen, J., J.S. Freudenberg, and C.N. Nett, *The role of the condition number and the relative gain array in robustness analysis*. Automatica, 1994. **30**(6): p. 1029-1035.
101. Datta, B.N., *Numerical methods for linear control systems: design and analysis*. Vol. 1. 2004: Academic Press.
102. Atkinson, A.C. and L.M. Haines, *14 Designs for nonlinear and generalized linear models*. Handbook of statistics, 1996. **13**: p. 437-475.
103. Baldea, M., P. Daoutidis, and A. Kumar, *Dynamics and control of integrated networks with purge streams*. AIChE journal, 2006. **52**(4): p. 1460-1472.
104. Buckley, P.S., *Techniques of process control*. 1964: Wiley.

105. Gaikwad, S. and D. Rivera. *Control-relevant input signal design for multivariable system identification: Application to high-purity distillation*. in *IFAC World Congress*. 1996.
106. Paige, C., *Properties of numerical algorithms related to computing controllability*. *IEEE Transactions on Automatic Control*, 1981. **26**(1): p. 130-138.
107. Höök, M. and K. Aleklett, *A review on coal-to-liquid fuels and its coal consumption*. *International Journal of Energy Research*, 2010. **34**(10): p. 848-864.
108. Lee, J., et al., *Half order plus time delay (HOPTD) models to tune PI controllers*. *AIChE Journal*, 2016.
109. Kruesi, M., Z.R. Jovanovic, and A. Steinfeld, *A two-zone solar-driven gasifier concept: Reactor design and experimental evaluation with bagasse particles*. *Fuel*, 2014. **117**: p. 680-687.
110. Melchior, T., et al., *Solar-driven biochar gasification in a particle-flow reactor*. *Chemical Engineering and Processing: Process Intensification*, 2009. **48**(8): p. 1279-1287.
111. Muroyama, A.P., et al., *Design and demonstration of a prototype 1.5 kW th hybrid solar/autothermal steam gasifier*. *Fuel*, 2018. **211**: p. 331-340.
112. Hathaway, B.J., et al., *Demonstration of a solar reactor for carbon dioxide splitting via the isothermal ceria redox cycle and practical implications*. *Energy & Fuels*, 2016. **30**(8): p. 6654-6661.
113. Hirsch, D. and A. Steinfeld, *Solar hydrogen production by thermal decomposition of natural gas using a vortex-flow reactor*. *International Journal of Hydrogen Energy*, 2004. **29**(1): p. 47-55.
114. Marxer, D., et al., *Solar thermochemical splitting of CO₂ into separate streams of CO and O₂ with high selectivity, stability, conversion, and efficiency*. *Energy & Environmental Science*, 2017. **10**(5): p. 1142-1149.
115. Suresh, D., J. O'Gallagher, and R. Winston, *Thermal and optical performance test results for compound parabolic concentrators (CPCs)*. *Solar Energy*, 1990. **44**(5): p. 257-270.
116. Rowe, S.C., et al., *Experimental evidence of an observer effect in high-flux solar simulators*. *Solar Energy*, 2017. **158**: p. 889-897.
117. Schiesser, W.E., *The numerical method of lines: integration of partial differential equations*. 2012: Elsevier.
118. Touloukian, Y. and E. Buyco, *Thermophysical Properties of Matter, The TPRC Data Series, Specific Heat of Metallic Elements and Alloys, vol. 4, and Specific Heat of Nonmetallic Solids, vol. 5, IFI*. 1970, Plenum, New York, NY.
119. Clark, J. and R. Tye, *Thermophysical properties reference data for some key engineering alloys*. *High temperatures-high pressures*, 2003. **35**(1): p. 1-14.
120. Corsan, J. and N. Mitchem, *The specific heat of fifteen stainless steels in the temperature range 4K-30K*. *Cryogenics*, 1979. **19**(1): p. 11-16.
121. Corsan, J. and N. Mitchem, *The Specific Heat of Stainless Steels Between 4 K and 300 K*, in *International Cryogenic Engineering Conference*, K. Mendelssohn, Editor. 1976, IPC Science and Technology Press: Grenoble.
122. Palumbo, A.W., J.C. Sorli, and A.W. Weimer, *High temperature thermochemical processing of biomass and methane for high conversion and selectivity to H₂-enriched syngas*. *Applied Energy*, 2015. **157**: p. 13-24.
123. Dry, M.E., *The fischer-tropsch process: 1950-2000*. *Catalysis today*, 2002. **71**(3): p. 227-241.

124. De Klerk, A., *Fischer-Tropsch Refining*. 2012: John Wiley & Sons.
125. Espinoza, R., et al., *Low temperature Fischer–Tropsch synthesis from a Sasol perspective*. Applied Catalysis A: General, 1999. **186**(1): p. 13-26.
126. Steynberg, A., *Introduction to fischer-tropsch technology*. Studies in surface science and catalysis, 2004. **152**: p. 1-63.
127. Brosilow, C. and B. Joseph, *Techniques of model-based control*. 2002: Prentice Hall Professional.
128. Bristol, E., *On a new measure of interaction for multivariable process control*. IEEE transactions on automatic control, 1966. **11**(1): p. 133-134.
129. Seborg, D.E., et al., *Process dynamics and control*. 2010: John Wiley & Sons.
130. Andreas, A. and T. Stoffel, *NREL Solar Radiation Research Laboratory (SRRL): Baseline Measurement System (BMS)*. Golden, Colorado (Data); NREL Report No. DA-5500-56488, 1981.
131. Martinek, J. and A.W. Weimer, *Design considerations for a multiple tube solar reactor*. Solar Energy, 2013. **90**: p. 68-83.
132. Konzstowicz, K.J., *Crack growth and acoustic emission in ceramics during thermal shock*. Journal of the American Ceramic Society, 1990. **73**(3): p. 502-508.
133. Coppola, J. and R. Bradt, *Thermal-Shock Damage in SiC*. Journal of the American Ceramic Society, 1973. **56**(4): p. 214-218.
134. Lee, C., et al., *Advanced Fatigue Crack Detection using Nonlinear Self-Sensing Impedance Technique for Automated NDE of Metallic Structures*. Research in Nondestructive Evaluation, 2015. **26**(2): p. 107-121.
135. Van Overschee, P. and B. De Moor, *Subspace identification for linear systems: Theory—Implementation—Applications*. 2012: Springer Science & Business Media.
136. Gibbs, B.P., *Advanced Kalman filtering, least-squares and modeling: a practical handbook*. 2011: John Wiley & Sons.
137. Chen, C.C. and P.M. Mathias, *Applied thermodynamics for process modeling*. AIChE Journal, 2002. **48**(2): p. 194-200.
138. Nath, P., et al., *High-throughput prediction of finite-temperature properties using the quasi-harmonic approximation*. Computational Materials Science, 2016. **125**: p. 82-91.
139. Huang, L.-F., et al., *An efficient ab-initio quasiharmonic approach for the thermodynamics of solids*. Computational Materials Science, 2016. **120**: p. 84-93.
140. Mathias, P.M., *The Gibbs–Helmholtz Equation in Chemical Process Technology*. Industrial & Engineering Chemistry Research, 2016. **55**(4): p. 1076-1087.
141. Kang, J.W., et al., *Quality assessment algorithm for vapor– liquid equilibrium data*. Journal of Chemical & Engineering Data, 2010. **55**(9): p. 3631-3640.
142. Kontogeorgis, G.M. and P. Coutsikos, *Thirty Years with EoS/GE Models • What Have We Learned?* Industrial & Engineering Chemistry Research, 2012. **51**(11): p. 4119-4142.
143. Economou, I.G., et al., *Industrial use of thermodynamics workshop: Round table discussion on 8 July 2014*. Chemical Engineering Research and Design, 2014. **92**(12): p. 2795-2796.
144. Chase Jr, M. and N.-J.T. Tables, *Forth Edition/Chase MW, Jr.* Journal of Physical and Chemical Reference Data, Monograph, 1998. **9**: p. 1951.
145. Einstein, A., *Die plancksche theorie der strahlung und die theorie der spezifischen wärme*. Annalen der Physik, 1906. **327**(1): p. 180-190.

146. Debye, P., *Zur theorie der spezifischen wärmen*. Annalen der Physik, 1912. **344**(14): p. 789-839.
147. Abu-Eishah, S., et al., *A new correlation for the specific heat of metals, metal oxides and metal fluorides as a function of temperature*. Latin American applied research, 2004. **34**(4): p. 257-265.
148. Cattoni, D.I., et al., *Cooperativity in binding processes: new insights from phenomenological modeling*. PloS one, 2015. **10**(12): p. e0146043.
149. Wyman, J., S.J. Gill, and A. Colosimo, *On thermal transitions in biological macromolecules*. Biophysical chemistry, 1979. **10**(3-4): p. 363-369.
150. Gill, S., et al., *Generalized binding phenomena in an allosteric macromolecule*. Biophysical chemistry, 1985. **21**(1): p. 1-14.
151. Dulong, P.L. and A.-T. Petit, *Recherches sur quelques points importants de la theorie de la Chaleur*. 1819.
152. Gopal, E., *Specific heats at low temperatures*. 2012: Springer Science & Business Media.
153. Smith, J., H. Van Ness, and M. Abbott, *Chemical engineering thermodynamics*. Sat, 1996. **18**: p. 1-3.
154. Fei, Y. and S. Saxena, *An equation for the heat capacity of solids*. Geochimica et Cosmochimica Acta, 1987. **51**(2): p. 251-254.
155. Dahlquist, F., *The meaning of scatchard and hill plots*. Methods in enzymology, 1978. **48**: p. 270-299.
156. Archer, D.G., *Thermodynamic Properties of the NaCl+ H2O System I. Thermodynamic Properties of NaCl (cr)*. Journal of physical and chemical reference data, 1992. **21**(1): p. 1-21.
157. Barron, T., W. Berg, and J. Morrison. *On the heat capacity of crystalline magnesium oxide*. in *Proceedings of the Royal Society of London A: Mathematical, Physical and Engineering Sciences*. 1959. The Royal Society.
158. Barron, T. and G.K. White, *Heat capacity and thermal expansion at low temperatures*. 2012: Springer Science & Business Media.
159. Berg, W. and J. Morrison. *The Thermal Properties of Alkali Halide Crystals. I. The Heat Capacity of Potassium Chloride, Potassium Bromide, Potassium Iodide and Sodium Iodide between 2 \cdot 8 and 270 degrees K*. in *Proceedings of the Royal Society of London A: Mathematical, Physical and Engineering Sciences*. 1957. The Royal Society.
160. Collocott, S. and G. White, *Thermal expansion and heat capacity of some stainless steels and FeNi alloys*. Cryogenics, 1986. **26**(7): p. 402-405.
161. Furukawa, G.T., et al., *Thermal properties of aluminum oxide from 0 to 1,200 K*. J Res Nat Bur Stand, 1956. **57**(2): p. 67-82.
162. Huffman, D.R., *Heat Capacity of CaF2 at Low Temperatures*. 1959, The Rice Institute: Houston.
163. Kelley, K. and G. Moore, *The Specific Heats at Low Temperatures of Anhydrous Chlorides of Calcium, Iron, Magnesium and Manganese I*. Journal of the American Chemical Society, 1943. **65**(7): p. 1264-1267.
164. Kirkham, A. and B. Yates, *The low-temperature specific heats and related thermodynamic properties of sodium fluoride and caesium bromide*. Journal of Physics C: Solid State Physics, 1968. **1**(5): p. 1162.
165. Kirkham, A. and B. Yates, *The adiabatic measurement of the specific heats of potassium chloride and rubidium chloride at low temperatures*. Cryogenics, 1968. **8**(6): p. 381-385.

166. Lee, S., S. Kim, and K. Kang, *Effect of heat treatment on the specific heat capacity of nickel-based alloys*. International Journal of Thermophysics, 2006. **27**(1): p. 282-292.
167. Munro, R., *Material properties of a sintered α -SiC*. Journal of Physical and Chemical Reference Data, 1997. **26**(5): p. 1195-1203.
168. Raman, C. *The specific heats of the alkali halides and their spectroscopic behaviour*. in *Proceedings of the Indian Academy of Sciences-Section A*. 1962. Springer.
169. Roberts, L., *The atomic heats of lithium, sodium and potassium between 1.5 and 20 K*. Proceedings of the Physical Society. Section B, 1957. **70**(8): p. 744.
170. Robie, R.A. and B.S. Hemingway, *Thermodynamic properties of minerals and related substances at 298.15 K and 1 bar (10^5 Pascals) pressure and at higher temperatures*. US Geol. Survey Bull., vol. 2131, p. 461-461 (1995). 1995. **2131**: p. 461-461.
171. Smith, S.J., et al., *Heat capacities and thermodynamic functions of TiO₂ anatase and rutile: Analysis of phase stability*. American Mineralogist, 2009. **94**(2-3): p. 236-243.
172. Southard, J. and R. Nelson, *Low Temperature Specific Heats. IV. The Heat Capacities of Potassium Chloride, Potassium Nitrate and Sodium Nitrate I*. Journal of the American Chemical Society, 1933. **55**(12): p. 4865-4869.
173. Broughton, J., *Process Utility Systems: Introduction to Design, Operation and Maintenance*. 2004: IChemE.
174. Charpentier, J.-C., *Among the trends for a modern chemical engineering, the third paradigm: The time and length multiscale approach as an efficient tool for process intensification and product design and engineering*. Chemical Engineering Research and Design, 2010. **88**(3): p. 248-254.
175. Allgöwer, F. and A. Zheng, *Nonlinear model predictive control*. Vol. 26. 2012: Birkhäuser.
176. Grossmann, I., *Enterprise-wide optimization: A new frontier in process systems engineering*. AIChE Journal, 2005. **51**(7): p. 1846-1857.
177. Poling, B.E., J.M. Prausnitz, and J.P. O'connell, *The properties of gases and liquids*. Vol. 5. 2001: Mcgraw-hill New York.
178. Morrison, D.D., J.D. Riley, and J.F. Zancanaro, *Multiple shooting method for two-point boundary value problems*. Communications of the ACM, 1962. **5**(12): p. 613-614.
179. Ascher, U.M., R.M. Mattheij, and R.D. Russell, *Numerical solution of boundary value problems for ordinary differential equations*. 1995: SIAM.
180. Betts, J.T., *Practical methods for optimal control and estimation using nonlinear programming*. 2010: SIAM.
181. Griewank, A. and A. Walther, *Evaluating derivatives: principles and techniques of algorithmic differentiation*. 2008: SIAM.
182. Naumann, U., *The art of differentiating computer programs: an introduction to algorithmic differentiation*. 2011: SIAM.
183. Neidinger, R.D., *Introduction to automatic differentiation and MATLAB object-oriented programming*. SIAM review, 2010. **52**(3): p. 545-563.
184. Volterra, V., *Variazioni e fluttuazioni del numero d'individui in specie animali conviventi*. 1927: C. Ferrari.
185. Lotka, A.J., *Contribution to the theory of periodic reactions*. The Journal of Physical Chemistry, 1910. **14**(3): p. 271-274.

186. Biegler, L.T. and V.M. Zavala, *Large-scale nonlinear programming using IPOPT: An integrating framework for enterprise-wide dynamic optimization*. Computers & Chemical Engineering, 2009. **33**(3): p. 575-582.